Background Investigations of the KATRIN Pre-Spectrometer

Zur Erlangung des akademischen Grades eines
Doktors Der Naturwissenschaften
von der Fakultät für Physik des
Karlsruher Instituts für Technologie (KIT)

genehmigte

DISSERTATION

von

Dipl. Phys. Florian M. Fränkle
aus Karlsruhe

Tag der mündlichen Prüfung: 16.07.2010

Referent: Prof. Dr. G. Drexlin
Institut für Experimentelle Kernphysik, KIT

Korreferent: Prof. Dr. W. de Boer
Institut für Experimentelle Kernphysik, KIT

Hiermit versichere ich die vorliegende Arbeit selbstständig und nur unter Verwendung der angegebenen Hilfsmittel und Quellen verfasst zu haben.

Karlsruhe, den 21. Juni 2010 .....

Abstract

Neutrinos have broad implications for particle physics and cosmology in particular with regard to their absolute mass scale. Until now there is only a lower limit (0.04 eV/c^2 [10]) and an upper limit (2 eV/c^2 [10]) on the neutrino mass. The **KA**rlsruhe **TRI**tium **N**eutrino experiment (KATRIN) is a next-generation, large scale tritium β-decay experiment to determine the mass of the electron anti-neutrino by investigating the kinematics of tritium β-decay with a sensitivity of 200 meV/c^2 (90% CL). In order to achieve this sensitivity a background rate of less than 10^{-2} counts per second (10 mHz) close to the β-decay endpoint at 18.6 keV is required.

A major component within the KATRIN experiment is the electrostatic pre-spectrometer which will act as a pre-filter for β-electrons in the final setup. Presently it is being operated in a test setup as a prototype for the main spectrometer (see chapter 3) and is used for background investigations to test and refine the new electromagnetic design of the KATRIN spectrometers. Additionally, new technologies such as active high voltage (HV) stabilization are tested and developed within the test setup.

The main objective of this thesis has been focused on investigations of the background characteristics at the pre-spectrometer. These investigations are of vital importance for the layout and operation of the large main spectrometer which shares the same conceptual design features as the pre-spectrometer. The main emphasis of the present work has been to develop tools to reduce the background from an initial rate of $> 10^5$ Hz down to a few mHz. As part of this process, new analysis tools were implemented. A time correlation filter, which removes cross talk events, was essential to reduce the intrinsic detector background in the region of interest (15 to 21 keV) by a factor of 5 to 6.3 $\pm$ 0.2 mHz. In addition, pulse shape analysis of the waveforms of single events was used to reliably detect noise events.

Measurements of the pre-spectrometer background characteristics revealed that there are two major background processes in MAC-E filters: Penning discharges (see chapter 4) and Radon emanation processes (see chapter 5 and 6).

A Penning trap is a special configuration of electromagnetic fields that allows the storage of electrically charged particles. The ignition of a Penning discharge in a Penning trap located between ground electrode and the 500 mm flange ($U_{trap} = 5$ kV, volume ≈ 10 l) in the initial pre-spectrometer design, yielded large background rates ($> 10^5$ Hz) at the detector. The successive optimization of the pre-spectrometer electrode system via both extensive Monte Carlo simulations and hardware modifi-

cations has resulted in a major experimental milestone for KATRIN: the complete removal of background resulting from stored particles in Penning-like traps. Within this optimization process it could be shown that even small-volume local Penning traps ($U_{trap} < 1$ kV, volume ≈ 10 cm^3) can generate background rates on the order of kHz. Only by adapting a careful design, precise manufacturing and mounting of the electrodes on a mm level one is able to prevent Penning trap induced background. The experience gained from the pre-spectrometer have yielded important constraints and guiding principles for the design of the main spectrometer electrodes in the region of the ground electrode.

A second class of background events has been identified and eliminated in the framework of this thesis: Radon (Rn) atoms, which emanate from materials inside the vacuum region of the KATRIN spectrometers are able to penetrate deep into the magnetic flux tube so that the final α-decay of Rn contributes to the background. Of particular importance are electrons emitted in processes accompanying the Rn α-decay such as shake off, internal conversion of excited levels in the Rn daughter atoms and Auger electrons. While low-energy electrons directly contribute to the background in the signal region, high-energy electrons can be stored magnetically inside the volume of the spectrometer. Depending on their initial energy, they are able to create thousands of secondary electrons via subsequent ionization processes of residual gas molecules thus creating a time dependent background rate at the detector. For the pre-spectrometer test setup an average Rn induced background rate of 27 ± 6 mHz was determined (see chapter 5 and 6). The emanation of ^{219}Rn from the getter material was determined to be 7.5 ± 1.8 mBq thus being responsible for a large fraction (19 ± 4 mHz) of the average background rate. Based on the results of the pre-spectrometer, the background rate from ^{219}Rn - emanating from 3 km of getter strips - at the main spectrometer is estimated to ≈ 300 mHz, if no countermeasures such as LN2 cooled baffles are taken. The specific background model of various Rn emanation processes (^{219}Rn, ^{220}Rn), which was developed in this thesis, is able to describe all experimental measurements with great precision. It underlines the importance of careful material screening and experimental counter measures which are of vital importance for the success of KATRIN.

Within this thesis the transmission functions of the pre-spectrometer for different flux tube positions and two different retarding potential configurations were measured and compared with corresponding simulations (see chapter 7). The deviation between simulations and measurements is less than 10%. For both retarding potential configurations the effect of early retardation was observed. The pre-spectrometer will be used as a pre-filter for the neutrino mass measurements and therefore early retardation has no negative effect. The transmission measurements showed that the stability of the transmission for low excess energies ($E_e < 100$ eV) is better than 1%.

In concluding one can state that the measurements and analysis methods of this thesis have revealed that an electrostatic retarding spectrometer with a rather large

magnetic shielding is essentially a background-free device, if both the effects from Penning traps and Rn emanation are controlled by careful design and appropriate counter measures (e.g. LN2 baffles).

f

Zusammenfassung

Abhängig von ihrer absoluten Massenskala haben Neutrinos weit reichende Implikationen für Teilchenphysik und Kosmologie. Bisher existiert nur eine untere Grenze (0,04 eV/c^2 [10]) und eine obere Grenze (2 eV/c^2 [10]) für die Neutrinomasse. Das **KA**rlsruher **TRI**tium **N**eutrino Experiment (KATRIN) ist ein Großexperiment zur Bestimmung der Masse des Elektronen-Antineutrinos durch die kinematische Untersuchung des Tritium β-Zerfalls mit einer Sensitivität von 200 meV/c^2 (90% CL). Um diese Sensitivität zu erreichen ist eine Untergrundrate von weniger als 10^{-2} Ereignissen pro Sekunde (10 mHz) im Bereich der Endpunktsenergie des β-Zerfalls bei 18,6 keV erforderlich.

Eine wichtige Komponente innerhalb des KATRIN Experiments ist das Vorspektrometer welches im Endaufbau als Vorfilter für β-Elektronen dienen wird. Gegenwärtig wird es innerhalb eines Testaufbaus als Prototyp für das Hauptspektrometer betrieben (siehe Kapitel 3) und dient Untersuchungen zum Untergrundverhalten sowie zum Testen und Optimieren des neuen elektromagnetischen Designs der KATRIN Spektrometer. Zusätzlich werden neue Technologien wie eine aktive Hochspannungsstabilisierung am Testaufbau entwickelt und getestet.

Die Zielsetzung dieser Arbeit lag schwerpunktmäßig auf der Untersuchung des Vorspektrometer Untergrundverhaltens. Diese Untersuchungen sind von grundlegender Bedeutung für die Auslegung und den Betrieb des großen Hauptspektrometers welches den gleichen konzeptionellen Aufbau wie das Vorspektrometer besitzt. Der Schwerpunkt dieser Arbeit war die Entwicklung von Methoden um den Untergrund von einem anfänglichen Wert von $> 10^5$ Hz auf wenige mHz zu reduzieren. Als Teil dieses Prozesses wurden neue Analysewerkzeuge implementiert. Ein Zeitkorrelationsfilter welcher Ereignisse, erzeugt durch Übersprechen einzelner Pixel, entfernt, ist wesentlich um den intrinsischen Detektor Untergrund im Bereich von 15 bis 21 keV um einen Faktor 5 auf 6,3 $\pm$ 0,2 mHz zu reduzieren. Zusätzlich wird eine Analyse der Signalform von einzelnen Detektorereignissen verwendet um zuverlässig Rauschereignisse zu detektieren.

Messungen des Untergrundverhaltens am Vorspektrometer ergaben das es zwei wesentliche Untergrundprozesse in MAC-E Filtern gibt: Penning Entladungen (siehe Kapitel 4) und Radon Emanationsprozesse (siehe Kapitel 5 und 6).

Eine Penning Falle ist eine spezielle Konfiguration von elektromagnetischen Feldern, welche das Speichern von elektrisch geladenen Teilchen erlaubt. Die Zündung einer Penning Entladung von einer Penningfalle, lokalisiert zwischen Erdelektrode und

500 mm Flansch, ($U_{trap} = 5$ kV, Volumen ≈ 10 l) im anfänglichen Vorspektrometer Design erzeugte eine hohe Untergrundrate ($> 10^5$ Hz) am Detektor. Die sukzessive Optimierung des Vorspektrometer Elektrodensystems durch umfangreiche Monte Carlo Simulationen und Änderungen an einzelnen Elektroden ergaben einen wichtigen experimentellen Meilenstein für KATRIN: Die praktisch vollständige Beseitigung von Untergrund, welcher durch gespeicherte Teilchen in penningartigen Fallen erzeugt wird. Im Verlauf des Optimierungsprozesses konnte gezeigt werden, dass selbst lokale, kleinvolumige Penning Fallen ($U_{trap} < 1$ kV, Volumen ≈ 10 cm^3) eine Untergrundrate in der Größenordnung von kHz erzeugen können. Nur durch ein sorgfältiges Design, eine präzise Fertigung und Einbau der Elektroden im Bereich von mm, kann der durch Penningfallen induzierter Untergrund vermieden werden. Die Erfahrungen vom Vorspektrometer ergaben wichtige Randbedingungen für das Design der Hauptspektrometer Elektroden im Bereich der Erdelektrode.

Eine zweite Klasse von Untergrundereignissen wurde im Rahmen dieser Arbeit identifiziert und eliminiert: Radon (Rn) Atome, welche von Materialien innerhalb des Vakuumbereichs der KATRIN Spektrometer emanieren, können tief in den magnetischen Flussschlauch eindringen so dass deren α-Zerfall zum Untergrund beiträgt. Von besonderer Bedeutung sind Elektronen, die in Prozessen welche den Rn α-Zerfall begleiten wie Shake off, Konversions und Auger Elektronen, freigesetzt werden. Während niederenergetische Elektronen direkt zum Untergrund in der Signalregion beitragen, können hochenergetische Elektronen innerhalb des Spektrometervolumens magnetisch gespeichert werden. Abhängig von ihrer anfänglichen Energie können sie tausende von Sekundärelektronen durch aufeinander folgende Ionisierungsprozesse von Restgasmolekülen erzeugen und somit eine zeitabhängige Untergrundrate am Detektor erzeugen. Für den Vorspektrometer Testaufbau wurde eine durchschnittliche Rn induzierte Untergrundrate von 27 ± 6 mHz bestimmt (siehe Kapitel 5 und 6). Die Emanation von ^{219}Rn aus dem Material der Getter Pumpe (freigesetzte Aktivität $7{,}5 \pm 1{,}8$ mBq) ist verantwortlich für einen Großteil (19 ± 4 mHz) der durchschnittlichen Untergrundrate. Basierend auf den Ergebnissen des Vorspektrometers wurde die Hauptspektrometer Untergrundrate von ^{219}Rn, welches aus insgesamt 3 km an Getter Streifen emaniert, zu ≈ 300 mHz abgeschätzt für den Fall das keine Gegenmaßnahmen, wie z.B. ein LN2 gekühltes Baffle, ergriffen werden. Das spezifische Untergrundmodel für unterschiedliche Rn Emanationsprozesse (^{219}Rn, ^{220}Rn), welches im Rahmen dieser Arbeit entwickelt wurde, ist in der Lage die experimentellen Ergebnisse mit hoher Präzision zu beschreiben. Es unterstreicht die Notwendigkeit einer sorgfältigen Auswahl von Materialien und experimentellen Gegenmaßnahmen, welche von hoher Bedeutung für den Erfolg von KATRIN sind.

Innerhalb dieser Arbeit wurden die Transmissionsfunktionen des Vorspektrometers für unterschiedliche Positionen im Flussschlauch und zwei unterschiedliche Konfigurationen des Retardierungspotentials gemessen und mit entsprechenden Simulationen verglichen (siehe Kapitel 7). Die Abweichungen zwischen Simulationen und Messungen sind geringer als 10%. Für beide Konfigurationen des Retardierungspo-

tentials wurde der Effekt einer frühen Retardierung beobachtet. Für die Neutrinomassenmessungen soll das Vorspektrometer als Vorfilter betrieben werden, daher hat eine frühe Retardierung keinen negativen Einfluss. Die Transmissionsmessungen ergaben das die Stabilität der Transmission für niedrige Überschussenergien ($E_e < 100$ eV) besser als 1% ist.

Als Fazit lässt sich feststellen, dass die Messungen und Analysen dieser Arbeit gezeigt haben, dass ein elektrostatisches Retardierungsspektrometer mit einer vergleichsweise starken magnetischen Abschirmung nahezu untergrundfrei arbeitet, falls die Effekte von Penning Fallen und Radon Emanation durch sorgfältiges Design und geeignete Gegenmaßnahmen (z.B. LN2 gekühltes Baffle) kontrolliert werden.

j

Contents

List of Figures

r

List of Tables

t

1 Introduction

This chapter gives an overview on neutrino physics starting with an historical review. Afterwards the relevance of neutrinos in cosmology and particle physics is discussed. The final section of the chapter deals with massive neutrinos and different methods to determine the mass of the neutrino.

1.1 On the beginning of neutrino physics

At the beginning of the last century, fundamental physical principles were challenged as physicists tried to interpret nuclear β-decay.

After the discovery of radioactivity, one could distinguish three different types of radiation: α-, β- and γ-radiation. The investigation of the energy spectra resulted in discrete lines for α- and γ-radiation. The explanation for this is that the nuclear transformations always releases the same amount of energy and therefore the spectra are discrete. In contrast, the β-spectra show no discrete lines, but a continuous energy spectrum extending to maximum energy. This raised the question how an apparently identical nuclear transformation can produce electrons of different energies. Niels Bohr even speculated that energy and momentum conservation are not valid for the microscopic world of nuclei [8].

In 1930 Wolfgang Pauli solved the problem. He postulated a neutral particle with spin of $\frac{\hbar}{2}$, which he called neutron [76]. The mass of this particle should be of the order of the electron mass, but not larger than 1% of the proton mass. It should be created in the β-decay and should take away the missing energy, which results from the difference between the energy of the electron and the maximum energy at the endpoint of the β-spectra, as well as angular momentum. An experimental proof of the existence of the postulated particle was not possible at that time, because it only interacts weakly with matter.

Already two years later, in 1932, Chadwick discovered a particle with some demanded properties [13], which is nowadays known as the neutron. Further investigations soon revealed, that the particle is much too heavy to be the one postulated by Pauli.

Soon thereafter Enrico Fermi developed his theory on β-decay [35] where the particle suggested by Pauli plays a crucial role. Fermis's theory is still valid today, also his chosen name for the particle: neutrino. For further details on β-decay see section 1.5.2.

Because of the extremely weak interaction of neutrinos with matter, it took more than twenty years until the first successful experimental detection of neutrinos was performed. Operating close to a nuclear power plant in Savannah River (SC), USA, an experiment by Clyde Cowan and Fred Reines [77] detected neutrinos via the inverse β-decay on free protons:

$$\overline{\nu}_e + p \rightarrow n + e^+ \tag{1.1}$$

A cadmium loaded scintillator solution was used to detect the neutrinos in delayed coincidence signature. First, the positron produced in the inverse β-decay annihilates with an electron and produces two γ photons. Then, the neutron capture on Cadmium produces a second gamma photon, so that a position correlated delayed coincidence of the two gammas results.

1.2 Neutrinos in cosmology

The evolution of the universe - as described by present state-of-the-art cosmological models - most likely started with a singularity, the so called "Big Bang". Shortly after the Big Bang the universe was in an extreme dense and hot state which rapidly cooled as the universe expanded. This primordial plasma of the early universe gave birth to a large number of neutrinos. These primordial neutrinos initially were in thermal equilibrium with other particle species, as long as their interaction rate Γ_ν was larger than the expansion rate of the universe (given by the Hubble parameter $H(t)$). At the freeze out condition $\Gamma_\nu < H(t)$ the neutrinos decoupled from the primordial plasma and have kept their thermal distribution at the time of decoupling. Their present day (red-shifted) temperature is $T_\nu \approx 1.95$ K which corresponds to thermal energies in the order of meV. Todays density of relic neutrinos can be calculated to $N_\nu = 336$ cm^{-3} (for all three flavours), which makes neutrinos the most abundant fermionic particle species in the universe. Because these neutrinos have a very small interaction cross section (order of 10^{-54} cm^2), their mean free path is extreme large. Due to this (relativistic) free streaming capability, neutrinos have a strong influence (depending on their mass) on the large scale structure formation. Because neutrinos take away energy from regions of larger density to deposit it in regions of smaller density, they counteract the gravitational clumping of matter.

Figure 1.1 shows the contributions to the total energy density of the universe at the present epoch. Each contribution is normalized to the critical energy density for a flat universe ($\Omega = 1$). The right hand side shows the energy density being dominated of dark energy and dark matter, with ordinary matter accounting only

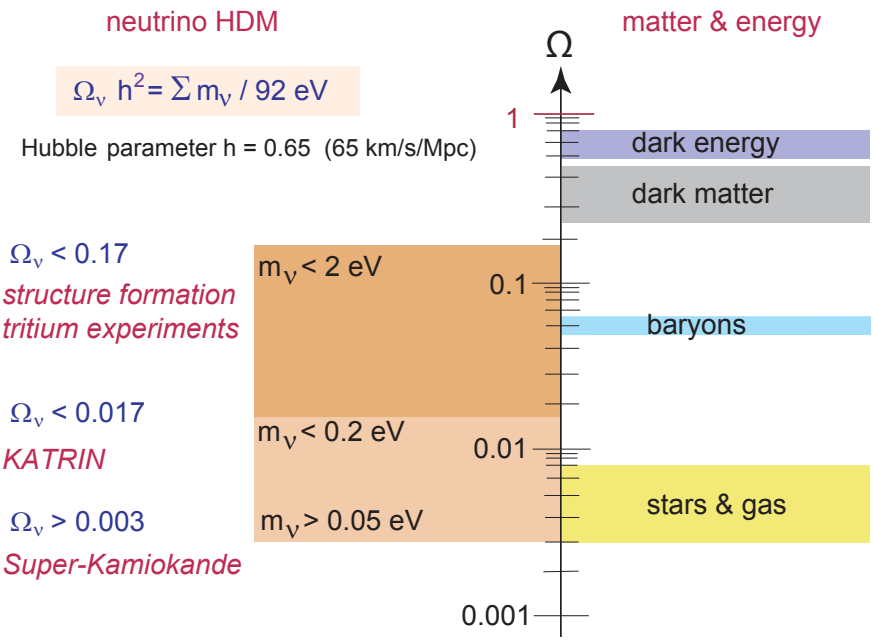

Figure 1.1: Contributions to the total energy density Ω of the universe. The left side shows the possible range of a neutrino mass contribution. Due to their properties neutrinos are classified as hot dark matter. (figure based on [59])

for a small fraction to Ω. The left hand side shows the possible range (up to now there is only a upper and lower limit on the neutrino mass, see below) of a neutrino mass contribution. The KATRIN experiment has a sensitivity of 200 meV/c^2 on m_ν and thus will be able to probe the interesting mass region where neutrinos have a significant influence on the large scale structure formation in the universe.

1.3 Neutrinos in particle physics

The standard model (SM) of particle physics [44] describes the elementary fermionic particles as well as their interactions[1] which are described by bosonic exchange particles. The SM is in excellent agreement with all current data. However, there is widespread belief that it is an approximation of a more fundamental theory.

[1] Gravity is not included in the standard model.

Table 1.1 gives an overview of the fermions in the SM, with quarks and leptons being grouped in three different generations. Each generation has eight members: two quarks, two leptons and their corresponding anti particles. Ordinary matter is made of first generation particles. Second and third generation particles are produced in particle accelerators and air showers.

Table 1.1: elementary spin $\frac{1}{2}$ fermions within the standard model

generation	1	2	3
quarks	u	c	t
	d	s	b
leptons	e^-	μ^-	τ^-
	ν_e	ν_μ	ν_τ

Quarks with an electric charge of either $+\frac{2}{3}$ e (u,c,t) or $-\frac{1}{3}$ e (d,s,b) can only be found in bound states (hadrons). When separating two quarks from each other, the potential of the strong interaction increases until it reaches sufficient energy to create a quark-antiquark pair, thereby creating two (separate) hadrons.

Each generation of leptons is made of an electrically charged (-e) particle and an electrically neutral partner (neutrino). The charged leptons interact both weakly and electromagnetically, whereas neutrinos only interact weakly and thus are very difficult to detect.

1.4 Neutrino sources

Neutrino properties and interactions have played a crucial role in establishing the SM. These investigations have been based on a variety of different neutrino sources, both natural and artificial. The most important neutrino sources are discussed below:

- **Primordial neutrinos**
  According to the Big Bang theory a large number of neutrinos was produced in the early universe (see section 1.2). Their present day number density is $N_\nu = 336$ cm^{-3} (for the sum off all three flavours) and they have thermal energies in the order of meV.

- **Solar neutrinos**
  The nuclear fusion reactions inside the core of the sun produce a large number of neutrinos of different energies. The dominant reaction - which is responsible for 98.4% of the total energy production of the sun - is the pp chain

$$4p \rightarrow {}^4He + 2e^+ + 2\nu_e + 26.73MeV \tag{1.2}$$

  where electron neutrinos are created in successive steps. Figure 1.2 shows the neutrino fluxes from the sun (at the surface of the earth) for different

fusion reactions inside the sun according to the standard solar model (SSM). Dedicated experiments (GALLEX/GNO [45], SAGE [3], Kamiokande [56]) have determined the flux of solar neutrinos to be a factor of about 2 to 3 less than the flux predicted by the standard solar model [6]. This long-standing discrepancy was called "the solar neutrino problem", which could be solved with the discovery of neutrino oscillations (see below).

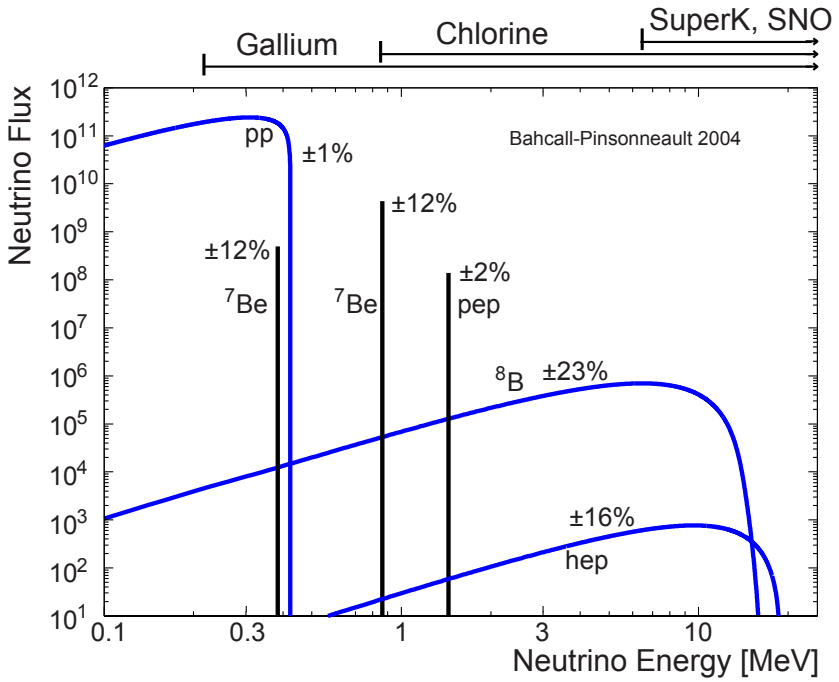

Figure 1.2: Solar neutrino fluxes at the Earth's surface (units are $1/(cm^2 sMeV)$ and $1/(cm^2 s)$ for line sources) for different fusion reactions inside the sun according to the standard solar model (figure from [5]).

- **Supernova neutrinos**
  The final stage in the life of a star is called supernova. Supernovae are classified into two types, depending on the initial mass (M) of the star: Type I ($M < M_c$) and Type II ($M > M_c$) with $M_c \approx 8M_\odot$[2]. Type I supernovae produce no significant number of neutrinos. Type II supernovae result from the gravitational collapse after a star has used up its nuclear fuel. The collapse eventually creates a shock wave which expels the star's outer layers. Shortly after the onset of the collapse the gravitational pressure in the core becomes so large that deleptonisation by electron capture starts

$$e^- + p \rightarrow n + \nu_e \tag{1.3}$$

  whereby a large number of neutrinos is created and the core is turned into a hot ($\approx 10^{11}$ K) and extreme dense neutron star. The thermal cooling of

[2]The mass of the sun is $M_\odot = 2 \cdot 10^{30}$ kg.

the proto-neutron star is due to the emission of neutrinos of all flavours (the mean free path of photons within the neutron star is extreme short). About 90% of all neutrinos emitted during a supernova are emitted in the 10 s long cooling phase. Although a Type II supernova is a bright source in the optical spectrum, about 99% of the energy is released as neutrinos (order of 10^{56} J).

- **Atmospheric neutrinos**
  Cosmic rays (high energetic protons and nuclei accelerated in the shockwave of a SN remnant) interact in the Earth's atmosphere with nuclei of gas molecules (N_2, O_2). In these processes both kaons ($K^{\pm}$) and pions ($\pi^{\pm}$) are created, which subsequently decay into lighter particles:

$$\pi^+, K^+ \rightarrow \mu^+ + \nu_\mu; \quad \mu^+ \rightarrow e^+ + \nu_e + \overline{\nu}_\mu \tag{1.4}$$

$$\pi^-, K^- \rightarrow \mu^- + \overline{\nu}_\mu; \quad \mu^- \rightarrow e^- + \overline{\nu}_e + \nu_\mu \tag{1.5}$$

  These processes create ν_e and ν_μ and their corresponding anti-particles. Atmospheric neutrinos had been used to study neutrino oscillation (e.g. Super-Kamiokande).

- **Geo neutrinos**
  The crust and mantle as well as the core of the Earth has a non-negligible natural abundance of ^{238}U and ^{232}Th. Within the decay chains of these elements (see chapter 6) β^--decays occur, which release electron anti-neutrinos ($\overline{\nu}_e$). The detection of the $\overline{\nu}_e$ produced by Earth's natural radioactivity could yield important geophysical information, e.g. the KamLAND experiment was able to set an upper limit (60TW) on the radiogenic power of U and Th in the Earth [90].

- **Reactor neutrinos**
  Nuclear fission reactors produce a huge amount of $\overline{\nu}_e$ resulting from β^--decays of neutron rich fission products in the reactor core. Each fission reaction creates on average 6 neutrinos with energies between 1 and 10 MeV. The large neutrino flux close to a reactor core (a 2.8 GW reactor produces each second about $5{\cdot}10^{20}$ $\overline{\nu}_e$) has been the reason for the long-standing interest in using reactor neutrinos for experimental studies (at present for Θ_{13}).

- **Accelerator neutrinos**
  In order to create a high energy neutrino beam, a proton beam from a synchrotron is dumped onto a light nuclei target to maximize the production of kaons and pions. With the help of a magnetic horn the particles are separated according to their electrical charge and guided into an evacuated decay tunnel. There they decay into lighter particles (see equations 1.4, 1.5) and form well focused neutrino beams. A beam dump at the end of the decay tunnel is used to stop the muons and the hadronic component of the beam. Depending on the primary proton energy, neutrinos with maximum energies in the order of 100 GeV can be produced.

1.5 Massive neutrinos

In 1958 an important experiment to determine the helicity[3] of neutrinos [47] was performed by M. Goldhaber et al. at Brookhaven National Laboratory, demonstrating that neutrinos have - within the uncertainties of the measurement - negative helicity only. This result implied that neutrinos (with their definite helicity) travel with the speed of light and hence have to be massless. In the standard model of particle physics, neutrinos accordingly entered as massless leptons. This assumption of the SM was proved to be incorrect by the discovery of neutrino oscillations (see below), demonstrating instead that neutrinos have a finite rest mass.

For massive neutrinos the flavour eigenstates (ν_α, $\alpha = e, \mu, \tau$) are generated by a superposition of mass eigenstates (ν_i, $i = 1, 2, 3$). Both representations are connected by an unitary 3×3 mixing matrix (PMNS[4] matrix):

$$|\nu_\alpha\rangle = \sum_{i=1}^{3} U_{\alpha i} \ |\nu_i\rangle \tag{1.6}$$

Until now the absolute mass scale of neutrino masses is unknown, as neutrino oscillation experiments only set a lower limit of 40 meV/c^2 [10] whereas β-decay experiments set an upper limit of 2.3 eV/c^2 [12]. Figure 1.3 shows the neutrino mass eigenvalues m_i (m_i is the eigenvalue to the eigenstate ν_i) as a function of m_1 for normal hierarchy ($m_1 < m_2 < m_3$). Depending on the absolute value of m_1 either a quasi-degenerate or hierarchical ensemble of eigenvalues is formed. For both cases a pattern of neutrino mass eigenstates is shown, including the flavour contribution to m_i for the actual values for $U_{\alpha i}$.

1.5.1 Neutrino oscillations

The PMNS matrix U in the leptonic sector can be parameterized by three mixing angles (Θ_{12}, Θ_{23} and Θ_{13}) and a phase φ, taking into account the possibility that neutrino oscillations violate CP symmetry (φ has not been observed in neutrino oscillation experiments so far). This parametrization is an analogon to the well known CKM[5] matrix, which describes the mixing of quarks. In case that neutrinos are Majorana[6] particles, two additional phases (α_2, α_3) are introduced. The mixing matrix can thus be factorized into 4 parts.

[3] The helicity of a particle is defined as the projection of its spin onto the direction of its momentum.

[4] **P**ontecorvo, **M**aki, **N**akagawa and **S**akata

[5] **C**abibbo, **K**obayashi, **M**askawa

[6] If a particle is identical to its antiparticle it is called Majorana particle. If a particle differs from its antiparticle it is called Dirac particle.

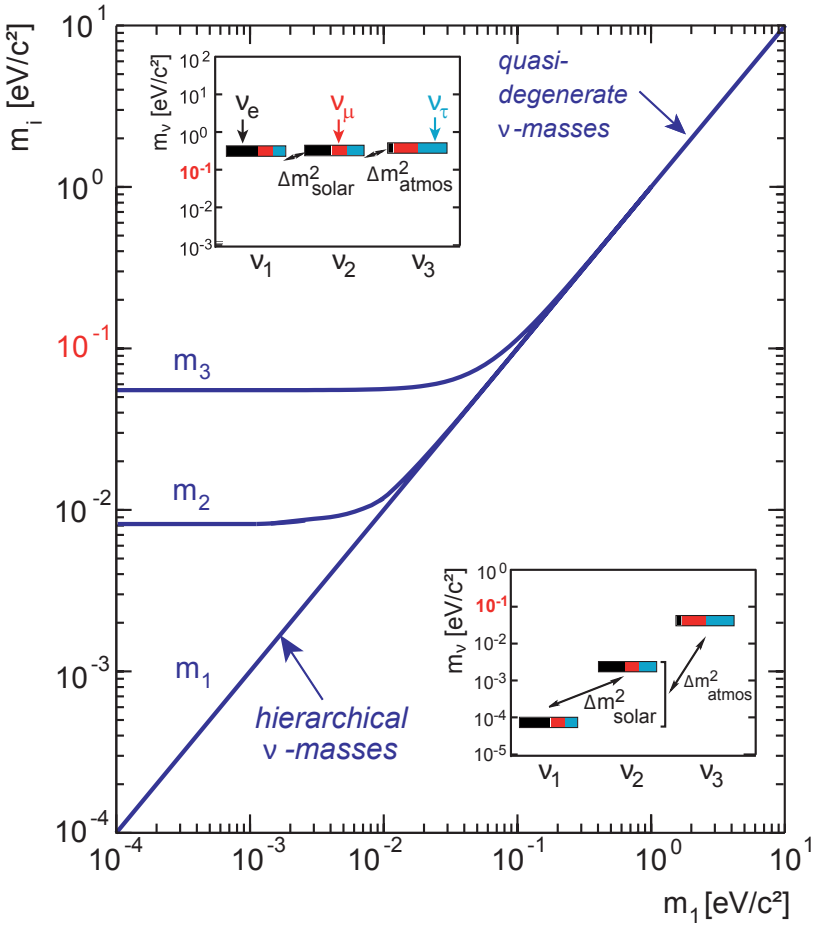

Figure 1.3: Eigenvalues of the neutrino mass eigenstates m_2, m_3 as a function of the lightest mass state m_1 for normal hierarchy ($m_1 < m_2 < m_3$). For $m_1 > 0.1$ eV/c^2 the neutrino mass spectrum is quasi-degenerated with the mass differences Δm^2_{ij} being small compared to m_i^2 (figure from [59]).

$$U = \begin{pmatrix} 1 & 0 & 0 \\ 0 & \cos\Theta_{23} & \sin\Theta_{23} \\ 0 & -\sin\Theta_{23} & \cos\Theta_{23} \end{pmatrix} \cdot \begin{pmatrix} \cos\Theta_{13} & 0 & \sin\Theta_{13}e^{i\varphi} \\ 0 & 1 & 0 \\ -\sin\Theta_{13}e^{-i\varphi} & 0 & \cos\Theta_{13} \end{pmatrix} \cdot \tag{1.7}$$
$$\begin{pmatrix} \cos\Theta_{12} & \sin\Theta_{12} & 0 \\ -\sin\Theta_{12} & \cos\Theta_{12} & 0 \\ 0 & 0 & 1 \end{pmatrix} \cdot \begin{pmatrix} 1 & 0 & 0 \\ 0 & e^{i\alpha_2/2} & 0 \\ 0 & 0 & e^{i\alpha_3/2} \end{pmatrix}$$

After a neutrino flavour eigenstate ν_α is created in a weak interaction, its mass eigenstates ν_i propagate with different phase velocities. This causes periodic flavour oscillation along the flight path of the neutrino. For most existing results on ν oscillations, an effective two-neutrino mixing framework can be used. Within this approximation the oscillation probability P for a baseline L and a neutrino energy

E_ν is given by

$$P(\nu_\alpha \to \nu_\beta) = \sin^2(2\Theta_{ij}) \sin^2\left(\frac{\Delta m^2_{ij} L}{4E_\nu}\right) \tag{1.8}$$

where Θ_{ij} is the mixing angle between the two flavour eigenstates ν_α and ν_β and $\Delta m^2_{ij} = |m^2_i - m^2_j|$ is the difference between the squared mass eigenvalues. Equation 1.8 shows that neutrino oscillation experiments are only sensitive to Θ_{ij} and Δm_{ij} and therefore can not be used to determine the absolute value of neutrino masses.

The parameters of neutrino flavour oscillations have been determined by making use of neutrinos from different sources:

- **Atmospheric neutrinos**
  The first clear experimental evidence of neutrino oscillation was reported in 1998 by the Super-Kamiokande experiment (a 50 kt water Cerenkov detector) [99]. In this case muon neutrinos (ν_μ) created in the upper atmosphere (see equations 1.4, 1.5) travel along different baselines L (between $L_{min} \approx 20$ km and $L_{max} \approx 12800$ km) to the detector. Depending on the actual travel distance L (see equation 1.8) they can oscillate from ν_μ into ν_τ. This causes a pronounced deficit of upward going ν_μ as a function of the incident angle. This zenith angle dependent deficit was measured and found to be in good agreement with simulations assuming neutrino oscillations.

- **Solar neutrinos**
  Further evidence for neutrino oscillations was found by solar neutrino experiments with the final proof of flavour transitions of solar ν being provided by the SNO detector. SNO[7] was a 1000 t heavy-water (D_2O) Cherenkov detector designed to detect neutrinos produced by fusion reactions in the sun. The SNO experiment was sensitive on the flux (Φ) of all three neutrino flavours (ν_α) by using three reactions which have different sensitivities on the different neutrino flavours:

  $$\begin{aligned}
  &\nu_e + d \to p + p + e^- && \text{(CC, charged current)}, && \Phi_{CC} = \Phi_e \\
  &\nu_\alpha + d \to p + n + \nu_\alpha && \text{(NC, neutral current)}, && \Phi_{NC} = \Phi_e + \Phi_{\mu\tau} \\
  &\nu_\alpha + e^- \to \nu_\alpha + e^- && \text{(ES, elastic scattering)}, && \Phi_{ES} = \Phi_e + 0.16\Phi_{\mu\tau}
  \end{aligned}$$

  The results [87] showed that only about one third of the detected neutrinos coming from the sun retain their initial flavour, implying that two third of the neutrinos have oscillated into ν_μ and ν_τ. The total flux of all flavours - as measured by the NC process - is consistent with the prediction of the SSM.

- **Reactor and accelerator neutrinos**
  The advantage of using artificial neutrino sources is that both the baseline L as well as the neutrino energy E_ν can (to some extend) be tuned and thus provide a testbed to investigate neutrino oscillations under laboratory conditions. The

[7] **S**udbury **N**eutrino **O**bservatory

KamLAND[8] experiment makes use of the neutrino flux of a large number of Japanese nuclear power plants within a distance of several hundred kilometres (average distance $L = 180$ km) in order to investigate the oscillation of $\overline{\nu}_e \rightarrow \overline{\nu}_\alpha$ in a "disappearance mode" (the measured flux of one flavour is compared with the expected flux of all flavours).

The actual values [10] of Θ_{ij} and Δm^2_{ij} from the above experiments are summarized in table 1.2.

Table 1.2: actual values of neutrino oscillation parameters [10]

parameter	value
Δm^2_{21}	$(7.59 \pm 0.20) \cdot 10^{-5}$ eV^2
Δm^2_{32}	$(2.43 \pm 0.13) \cdot 10^{-3}$ eV^2
$\sin^2(2\Theta_{12})$	0.87 ± 0.03
$\sin^2(2\Theta_{23})$	> 0.92
$\sin^2(2\Theta_{13})$	< 0.19, CL $= 90\%$

1.5.2 Determination of neutrino masses

Measurements of neutrino oscillation parameters are only sensitive to the ν-mass splittings (Δm^2_{ij})[9] and the mixing strength Θ_{ij} and thus are not able to determine the absolute neutrino mass scale. This section describes different experimental approaches to determine the absolute neutrino masses.

Neutrino mass from β-decay

A nuclear β-decay is a transition of a nuclei where the atomic number (A) changes, but the mass number (N) stays the same:

$$\begin{aligned} {}^N_A X &\rightarrow {}^N_{Z+1} X + e^- + \overline{\nu}_e \quad \beta^-\text{decay} \\ {}^N_A X &\rightarrow {}^N_{Z-1} X + e^+ + \nu_e \quad \beta^+\text{decay} \\ {}^N_A X + e^- &\rightarrow {}^N_{Z-1} X + \nu_e \quad \text{electron capture} \end{aligned} \tag{1.9}$$

The $\beta^\pm$ decays are three-body processes where the released energy is distributed between the components in a statistical fashion. In case of β^--decay the continuous energy spectrum of the released electron is described by the Fermi theory of β-decay (for more details see section 2.2) where the neutrino mass enters as a parameter $m^2_{\overline{\nu}_e}$.

[8] **Kam**ioka **L**iquid-scintillator **A**nti-**N**eutrino **D**etector
[9] It can not be determined which mass eigenvalue is larger.

The experimental observable in β-decay is thus the effective neutrino mass $m^2_{\nu_e}$ [10], which is an incoherent superposition of the mass eigenstates:

$$m^2_{\nu_e} = \sum_{i=1}^{3} |U_{ei}|^2 \cdot m_i^2 \tag{1.10}$$

Figure 1.4 shows the results of different β-decay experiments obtained during the last two decades. Although the sensitivity of the experiments has increased over time, only an upper limit on m_{ν_e} could be determined so far. The actual best limit is $m_{\nu_e} < 2$ eV/c^2 [10] derived by the Mainz and Troitzk experiments.

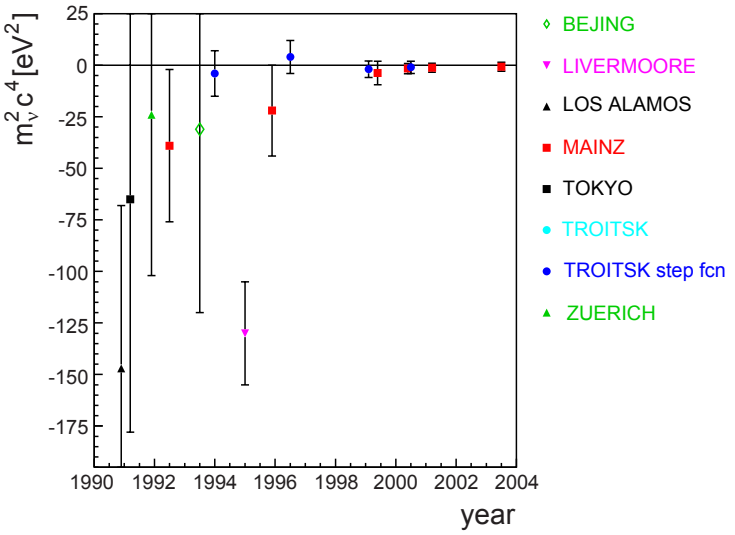

Figure 1.4: results of recent β-decay experiments (figure from [59])

There are three different experimental approaches for measuring $m^2_{\nu_e}$ in kinematic terms via the precise measurement of the electron energy spectrum of β-decay electrons close to the endpoint:

- **Microcalorimeter**
  This approach combines β-source and detector in a micro-bolometer. A sensitive thermistor converts the temperature increase induced by a single β-decay into an electrical signal and thus the entire energy spectrum can be measured in a differential way. The MARE[11] experiment [1] aims to reach a sensitivity of 0.2 eV/c^2 after considerable R&D efforts, using ^{187}Re as β-emitting element.

[10] The eigenvalue m_i^2 of a neutrino mass eigenstate ν_i contributes with a probability given by U_{ei} to the β-decay spectrum, if kinematically allowed. However, the present energy resolution of experiments (0.93 eV for KATRIN) is significantly larger compared to the differences of the mass eigenstates (see table 1.2) and therefore it is sufficient to use the "effective neutrino mass" as the measurement parameter.

[11] **M**icrocalorimeter **A**rrays for a **R**henium **E**xperiment

- **Electromagnetic spectrometer**
  An electromagnetic spectrometer analyses the energy of β-decay electrons (which are magnetically guided), preferably by the decay ${}^3H \rightarrow {}^3He + e^- + \overline{\nu}_e$, by an electrostatic potential. For a detailed explanation see chapter 2.
- **Cyclotron radiation**
  There is a recent proposal to use the cyclotron radiation emitted of β-decay electrons in a magnetic field in order to measure the energy spectrum [71]. The feasibility of this novel approach still needs to be demonstrated in the future.

Neutrino mass from $0\nu\beta\beta$-decay

Double β-decay ($2\nu\beta\beta$) is a second order weak decay process which allows to gain insight to intrinsic ν-properties. It only occurs in even-even nuclei ${}^N_Z X$ when the neighbouring nucleus ${}^N_{Z+1} X$ is heavier and the final state nuclei ${}^N_{Z+2} X$ is lighter than the parent nucleus. In a $2\nu\beta\beta$ process two electrons (or positrons) and their corresponding neutrinos are emitted. In case neutrinos are Majorana particles, and only then, neutrinoless double β-decay ($0\nu\beta\beta$) can occur. In this process a neutrino emitted in one β-decay vertex is absorbed with inverted helicity at the other β-decay vertex. Hence the neutrino has to be in a state of mixed helicity. This is only possible if the neutrino has a finite invariant mass. Because $0\nu\beta\beta$ emits only two particles, the entire decay energy is shared by the two electrons and thus a mono-energetic line at the end of the $2\nu\beta\beta$ electron energy spectrum is created. An observation of this signal would be sensitive to the effective Majorana mass m_{ee} which is a coherent sum of the neutrino mass eigenstates:

$$m_{ee} = |\sum_{i=1}^{3} U_{ei}^2 \cdot m_i| \tag{1.11}$$

In general the elements U_{ei} will be a complex number, so that cancellations could occur. This would mean that a smaller mass value compared to single β-decay experiments (see above) would be measured. The experiment with the best sensitivity on $0\nu\beta\beta$ so far was the Heidelberg-Moscow experiment. A subgroup of the Heidelberg-Moscow collaboration claimed that there is evidence for $0\nu\beta\beta$ at $m_{ee} = 0.32$ eV [49]. While this evidence has been discussed in a highly controversial manner [2], future $0\nu\beta\beta$ experiments (EXO [18], Gerda [81], Majorana [69], Cuore [11]) are being prepared in order to test this evidence.

Neutrino mass from cosmology

Precise observations of the cosmic microwave background (CMB) and large scale structures (LSS) of galaxies can be used to constrain or even probe neutrino masses.

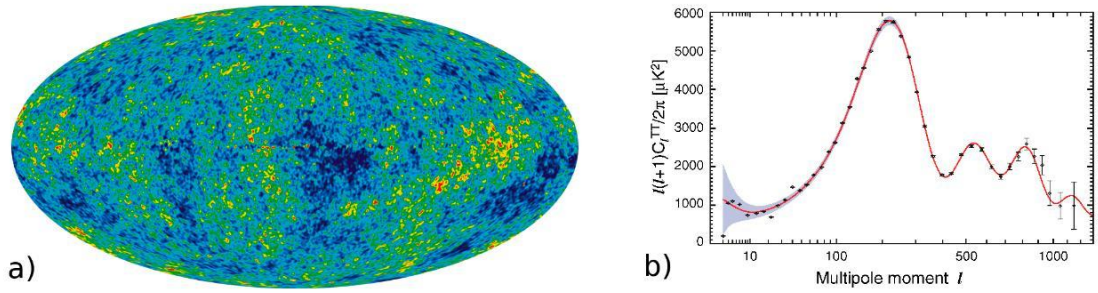

Figure 1.5: **a)** fluctuations of the cosmic microwave background (linear scale from -200 to 200 μK, figure from [97]), **b)** angular power spectrum as a function of the multipole moment ℓ (figure from [15])

Figure 1.5 a) shows the temperature fluctuations of the CMB measured by WMAP[12]. These temperature fluctuations can be decomposed into spherical harmonics

$$\frac{\Delta T}{T}(\Theta, \phi) = \sum_{lm} a_{lm} Y_{lm}(\Theta, \phi) \tag{1.12}$$

and from the coefficients[13] a_{lm} the angular power spectrum (see figure 1.5 b)) can be constructed. Neutrinos leave only a small imprint on the CMB spectrum, the importance of the CMB measurements lies in their ability to constrain a large set of cosmological parameters. A sensitivity on the ν-mass arises from the fact that neutrinos are able to free-stream out of regions of over-density and thus damp acoustic oscillations prior to recombination. This suppresses the peaks in the angular power spectrum to some extend. A fit of the ΛCDM[14] model (including a parameter for the sum of the neutrino masses) to the WMAP data allows to set an upper limit for the sum of the neutrino masses [15]

$$\sum m_\nu < 1.3 \text{ eV } (95\% \text{ CL})$$

This limit can be further constrained by using additional large scale structure data from sky surveys (e.g. SDSS, 2dFGRS), Lyman-α forest and type Ia supernovae measurements. It should be noted in this context that there are some generic inconsistencies between the data sets and the limits on the neutrino mass of these analyses depend on the actual choice of data and priors. It should also be remarked that there might be a degeneracy of parameters of the ΛCDM model (in the standard analysis six different parameters are used), demonstrating and highlighting the importance of direct model independent neutrino mass measurements by kinematic means.

[12] **W**ilkinson **M**icrowave **A**nisotropy **P**robe
[13] For each l value an average value of all $2l+1$ independent m-modes is used.
[14] Λ refers to dark energy and CDM is an abbreviation for **C**old **D**ark **M**atter.

2 The KATRIN Experiment

The international **KA**rlsruhe **TRI**tium **N**eutrino (KATRIN) experiment [59] is a next generation, model independent, large scale tritium β-decay experiment to determine the "mass of the electron anti-neutrino"[1] by investigating the kinematics of tritium β-decay with a sensitivity of 200 meV/c^2.

This chapter is organized in the following way: After motivating the experiment (2.1), tritium β-decay (2.2) and the concept of a MAC-E filter (2.3) are described. Then the experimental setup (2.4) and the functionality of the major system components are presented.

2.1 Motivation of KATRIN

Neutrinos play an important role in the evolution of the large scale structures in the universe. Due to their large abundance (the neutrino density of the universe is 336 ν's cm^{-3} for all three flavours) they affect the evolution of gravitational clustering depending on their mass. Neutrino oscillation experiments imply that neutrinos are massive and set a lower limit of 40 meV/c^2 [10] on the neutrino mass. Experiments investigating the kinematics of β-decay on the other hand set an upper limit on the neutrino mass of 2.3 eV/c^2 [12]. The attempts to determine the absolute neutrino mass from cosmological data strongly depend on the chosen data set and model. The KATRIN experiment uses a model independent method to determine the mass of the electron anti-neutrino ($m_{\overline{\nu}_e}$) by investigating the kinematics of tritium β-decay. With a sensitivity of 200 meV/c^2 it has the potential to probe the entire quasi-degenerated ν-mass scale and the complete mass range of $m_{\overline{\nu}_e}$ where neutrinos have a significant influence on structure formation in the universe.

2.2 Tritium β-decay

In nuclear β-decay a neutron in the atomic nucleus decays into a proton, thereby emitting an electron (e^-) and an electron anti-neutrino ($\overline{\nu}_e$). The energy released in the decay is stored between the e^- and $\overline{\nu}_e$ in a statistical way. The energy spectra

[1] The "mass of the electron anti-neutrino" is used as defined in equation 1.10 as the incoherent sum of the mass eigenvalues m_i.

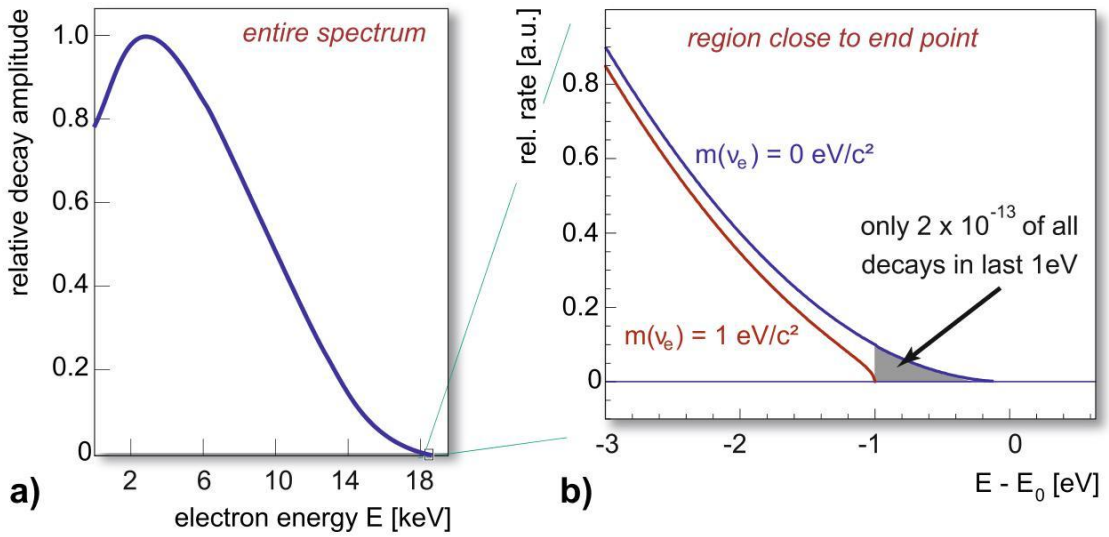

Figure 2.1: **a)** Tritium β-spectrum, **b)** region close to end point, two scenarios for the neutrino mass are shown ($m_{\overline{\nu}_e} = 0$ and 1 eV/c^2)

of the electron is given by the well known Fermi theory of β-decay [35]:

$$\frac{dN}{dE} = \frac{G_F^2}{2\pi^3} \cos^2\Theta_C \, |M|^2 \, F(Z,E) p (E + m_e c^2)(E_0 - E)\sqrt{(E_0 - E)^2 - m_{\overline{\nu}_e}^2 c^4} \quad (2.1)$$

with the following coefficients and parameters:

- G_F: Fermi coupling constant
- Θ_C: Cabibbo angle
- M: nuclear matrix element
- $F(Z,E)$: Fermi function (with Z of the daughter nuclei)
- p: electron momentum
- m_e: electron mass
- E: energy of the electron
- E_0: maximum electron energy for $m_{\overline{\nu}_e} = 0$ (endpoint energy)
- $m_{\overline{\nu}_e}$: mass of electron anti-neutrino

As one can see in equation 2.1, it is the square of the neutrino mass $m_{\overline{\nu}_e}^2$ that enters as a parameter. Its effect on the shape of the spectrum is significant only in a very narrow region close to the endpoint energy (E_0). Figure 2.1 b) shows the energy spectrum of tritium β-electrons for the case of $m_{\overline{\nu}_e} = 0$ eV/c^2 and $m_{\overline{\nu}_e} = 1$ eV/c^2, underlining the importance of the end point regions, where non-relativistic neutrinos are emitted. The KATRIN experiment aims to determine the observable

$m^2_{\overline{\nu}_e}$ by measuring the shape of the β-spectrum close to its endpoint. KATRIN uses molecular tritium as β-emitter because it has several advantages compared to other isotopes:

- **low endpoint energy**: Tritium (T) has the second lowest endpoint energy ($E_0 = 18.59$ keV [72]) of all β-active isotopes. Only ^{187}Re has a lower E_0 of 2.47 keV [4] but has a large life time on the order of 10^{10} y. The low endpoint energy maximizes the event rate close to the endpoint region. Moreover the complexity of the experimental setup is reduced somewhat because the absolute value of the retarding voltage - needed for the precise energy analysis (see section 2.3) of the β-electrons - is below 20 kV.
- **high specific activity**: The specific activity of tritium is $3.6 \cdot 10^{14}$ Bq/g which allows to build a source of high luminosity. This is an important cornerstone for KATRIN in order to measure the energy spectra close to E_0 with sufficient statistics (only $< 10^{-11}$ of all tritium β-decays happen within a few eV below E_0, see figure 2.1b).
- **super-allowed transition**: The nuclear transition of tritium β-decay is super-allowed, hence there are no energy dependent corrections of the nuclear matrix elements.

2.3 MAC-E filter

In order to perform a high precision energy analysis of the β-decay electrons in the KATRIN experiment, the so called MAC-E[2] filter technique [43] is used (for a detailed explanation of the characteristics of a MAC-E filter see chapter 7). The most important property of a MAC-E filter with respect to KATRIN are that it combines high luminosity with a high energy resolution.

In general, a MAC-E filter consists of two solenoids which create a strong guiding magnetic field for electrons[3] (see figure 2.2). This magnetic field B has a minimum B_{min} between the coils and a maximum B_{max} inside the centre of one coil. For adiabatic motion of electrons the magnetic moment μ is constant so that their transversal energy component is transformed into longitudinal energy as they move towards B_{min}. The actual energy analysis is done with an electrostatic retarding potential at B_{min} which is created by an electrode system operated on a (variable) scanning potential U_0. Thus a MAC-E filter acts as an integrating high pass filter (see figure 7.1) with a finite energy resolution ΔE.

[2] **M**agnetic **A**diabatic **C**ollimation combined with an **E**lectrostatic Filter

[3] In principle a MAC-E filter is not limited to electrons and works with any electrically charged particles as long as they are guided adiabatically.

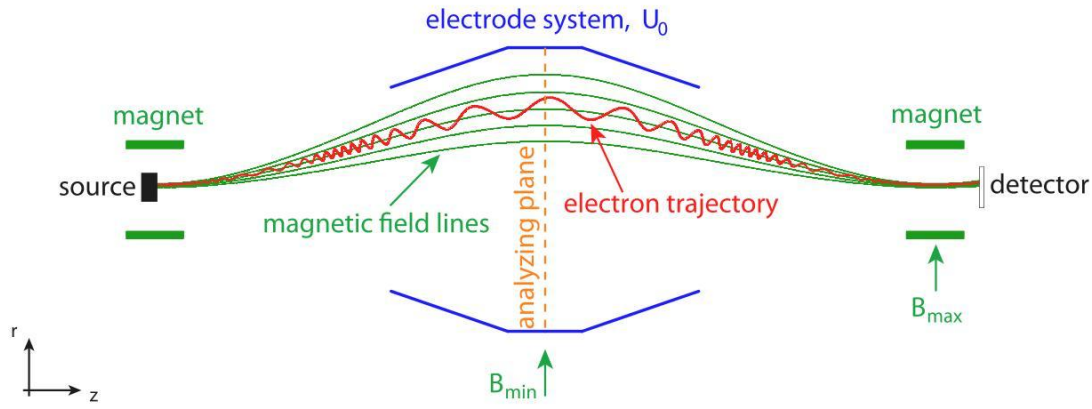

Figure 2.2: Schematic diagram of a MAC-E filter with guiding magnetic field lines, source, electrostatic spectrometer and detector.

2.4 Experimental setup

The KATRIN measurement setup (see figure 2.3) has an overall dimension of ≈ 70 m and consists of a high luminosity windowless gaseous molecular tritium source WGTS (**b**) whose activity is monitored by the rear section (**a**), a differential (**c**) and cryogenic (**d**) tritium pumping and retention section, a tandem spectrometer section with a pre-spectrometer (**e**) and a main spectrometer (**f**) for energy analysis, which is finally followed by a detector system (**g**) for counting the transmitted β-decay electrons. In the following each component is described in more detail.

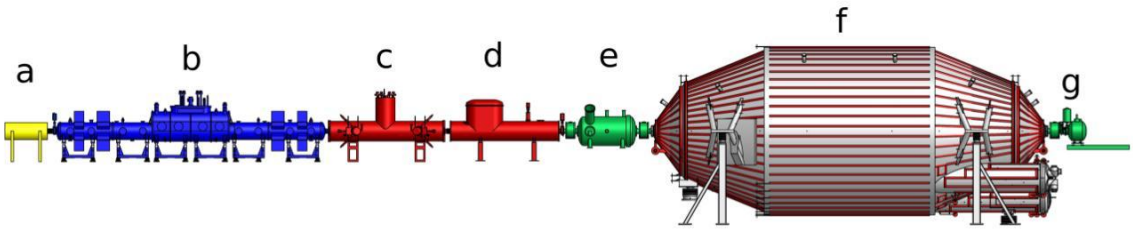

Figure 2.3: Schematic overview of the KATRIN experimental setup, **a** rear section, **b** windowless gaseous molecular tritium source (WGTS), **c** differential pumping section (DPS), **d** cryogenic pumping section (CPS), **e** pre-spectrometer, **f** main spectrometer, **g** detector system. The overall setup has a length of about 70 m

2.4.1 WGTS and rear section

The tritium source consists of a 10 m long stainless steel beam tube with a diameter of 90 mm which is operated at a base temperature of 30 K, maintained by a dedicated

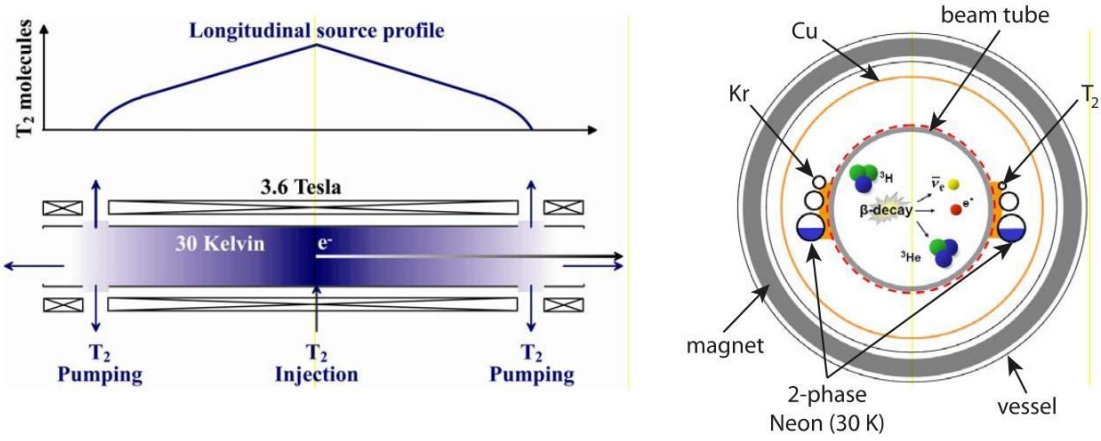

Figure 2.4: windowless gaseous molecular tritium source (WGTS), **Left**: T_2 density profile inside the source. T_2 is injected in the centre and pumped out at the end of the WGTS (figure from [59]). **Right**: Cut of the WGTS, the beam tube is cooled with 2-phase Neon (figure from [16]).

two phase Neon cooling system. Tritium molecules (T_2) are injected into the centre of the tube (injection pressure $3.35{\cdot}10^{-3}$ mbar). While diffusing to the ends of the beam tube tritium decays with a rate of 10^{11} Bq thus providing a sufficient number of β-electrons close to E_0 (see figure 2.1). The activity of the source will be continuously monitored by the rear section. The tritium at the end of the WGTS beam tube is collected via turbomolecular pumps (TMPs) and recirculated via an "inner loop" [88], which removes contaminants (particularly ^{3}He) and is capable to process a throughput of 40 g T_2 per day. Accordingly, a T_2 pressure gradient (see left side of figure 2.4) with a column density of $5{\cdot}10^{17}$ T_2/cm^2 is created within the source. In order to keep the systematic errors of the source on a level comparable to the statistical errors, the column density needs to be stable on a 0.1% level. This implies stringent requirements for the temperature stability and homogeneity of the source of $\Delta T \leq \pm 30$ mK as well as of 0.1% for the injection pressure.

The β-electrons created inside the WGTS are guided via an axial magnetic field of $B_S = 3.6$ T towards the spectrometers. The start angle Θ[4] defines the path length of electrons in the WGTS, meaning that electrons have different probabilities for inelastic scattering on T_2. In order to minimize the number of electrons undergoing inelastic collisions for the neutrino mass measurements, the maximum accepted start angle is limited to $\Theta_{max} = 51°$ via a maximum magnetic field of $B_{max} = 6$ T (pinch magnet, see figure 2.6) which reflects electrons with $\Theta > \Theta_{max}$ due to magnetic mirror effect (see section 4.1.3). The diameter of the WGTS defines the magnetic flux Φ that needs to be transported from the WGTS to the detector system. With an effective source area of $A_S = 53$ cm^2 and a magnetic field of $B_S = 3.6$ T, Φ can

[4] Θ is defined as the angle between electron momentum $\vec{p}$ and magnetic field $\vec{B}$.

be calculated to be $\Phi = 191$ Tcm^2 with

$$\Phi = \int B(r) r dr \approx A_S B_S \tag{2.2}$$

The integral is given in cylindrical coordinates, referring to the axial symmetric setup of the KATRIN experiment. For a homogeneous magnetic field the integral simplifies to a product of magnetic field and area.

2.4.2 Transport and tritium retention section

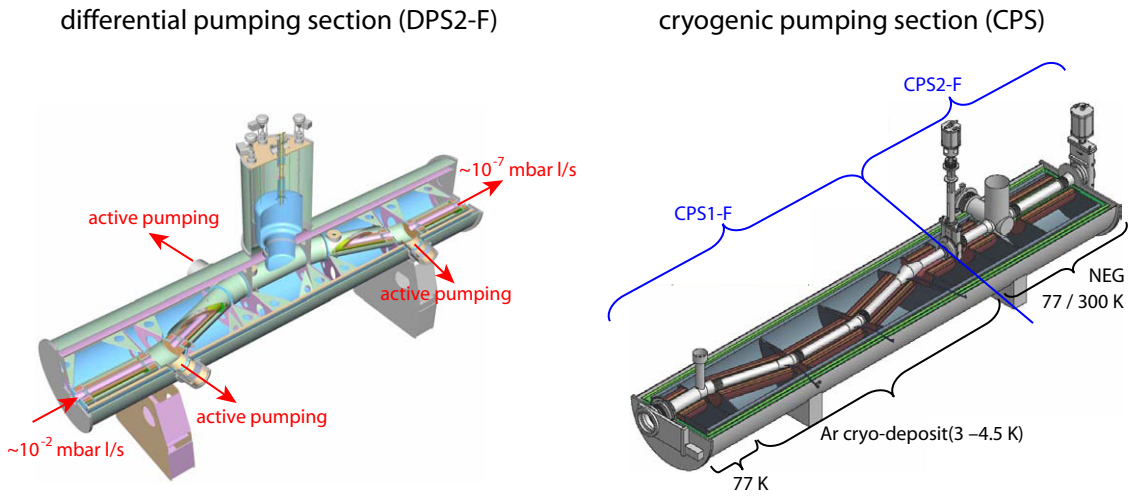

Figure 2.5: **Left**: Differential pumping section (DPS2-F). The tritium flow is reduced a factor of 10^5 by differential pumping with four TMPs. In order to increase the pumping efficiency and to avoid beaming of T_2 molecules the beam tube has four bends of 20° (figure from [59]). **Right**: Cryogenic pumping section. The required tritium retention factor of 10^7 is achieved by a combination of cryo-sorption of T_2 on an Argon frost layer (CPS1-F) and the usage of non evaporable getter strips (CPS2-F), (figure from [58]).

The task of the beam element DPS2-F (see figure 2.5) is to reduce the T_2 partial pressure by a factor of $>10^5$ and to guide the β-electrons via a strong magnetic field of 5.6 T. The beam tube has four bends of 20° to avoid beaming of T_2 molecules towards the spectrometers and to increase the effective pumping speed of the turbomolecular pumps attached there.

Most of the remaining T_2 that passes the DPS2-F is trapped in the cryogenic pumping section (CPS) by a layer of Argon frost frozen on the liquid helium cooled beam tube, which forms a highly efficient and large-area cold surface. The accumulation of tritium on the Argon frost increases the potential of tritium migration

processes. Therefore a refreshment cycle of the Argon frost is foreseen every 2 months. In order to test the concept of cryo-trapping of T_2 on Argon frost a dedicated test experiment was performed. The results showed that a reduction factor of 10^7 by the CPS can be achieved [60].

2.4.3 Spectrometer section

The pre-spectrometer as well as the main spectrometer are operated as electrostatic retarding high pass filters (see above and section 7.1.1). In the final setup the pre-spectrometer will be used as a pre-filter operated on a potential $0 < U_0 < E_0$. A non-zero retarding potential at the pre-spectrometer reduces the flux of β-electrons into the main-spectrometer and thus could reduce the background originating from ionization of residual gas molecules in the volume of the main spectrometer due to β-electrons. Prior to the installation of the pre-spectrometer into the KATRIN beam line, it is currently operated in a stand alone test setup (see chapter 3).

The purpose of the 24 m long main spectrometer (diameter 10 m) is the high precision energy analysis of the β-decay electrons. It features an energy resolution of $\Delta E = 0.93$ eV at 18.6 keV. In order to achieve the desired background rate of < 10 mHz, a double layer inner electrode system made of thin wires which is currently being mounted with submillimeter precision, is required. The wire layers are put on a more negative potential (100/200 V) with respect to the tank voltage in order to electrostatically shield secondary electrons produced in the vessel wall by cosmic particles. The inner electrode system is a contribution of KATRIN collaboration member University Münster. The absolute voltage of -18.6 kV needs to be stable on the 1 ppm level and is monitored with a high precision voltage divider [91] and an independent monitoring and calibration beam line. The main spectrometer is equipped with an air coil system and a magnetic field sensor system [32] for compensating the Earth's magnetic field and for fine-tuning of the magnetic field close to the analyzing plane.

2.4.4 Detector system

The left side of figure 2.6 shows an overview of the detector system. Magnet A (pinch magnet) creates a pinch magnetic field of 6 T - which is the largest magnetic field along the KATRIN beam line - and thus defines Θ_{max} together with B_S (see above). β-electrons that are able to overcome the potential barriers of the spectrometers are detected in a monolithic 148 pixel (see right side of figure 2.6) silicon PIN[5] diode array 90 mm in diameter. The segmentation of the detector is needed to reduce a broadening of the energy resolution caused by inhomogeneities of magnetic field and electric retarding potential in the analyzing plane of the main spectrometer.

[5] **P**ositive **I**ntrinsic **N**egative

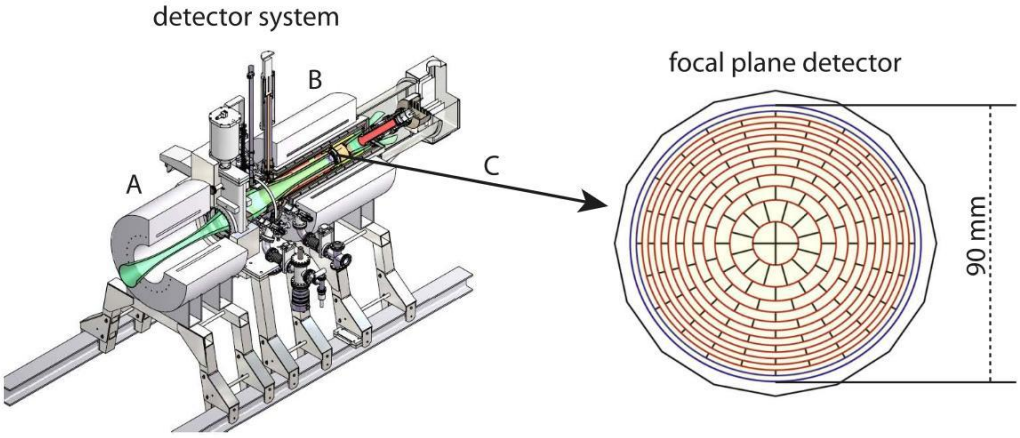

Figure 2.6: focal plane detector (FPD), **A**: pinch magnet (6 T), **B**: detector magnet (up to 6 T), **C**: detector chip (148 pixels of equal area (44.1 mm^2)), figures taken from [74], [16]

Because the actual energy analysis of the β-electrons is done at the main spectrometer, a moderate detector energy resolution of 600 eV FWHM[6] is sufficient for the KATRIN experiment. An extensive quality assurance programme with careful selection of materials, shielding and an active veto are used to keep the intrinsic detector background below 1 mHz [65]. In addition a positive post acceleration voltage of up to 30 kV can be applied in order to move the signal peak to an energy region of low intrinsic detector background. The detector system is a contribution of KATRIN collaboration member University of Washington, Seattle (UW).

[6] **F**ull **W**idth at **H**alf **M**aximum

3 Pre-spectrometer test setup

The framework for this thesis is provided by the pre-spectrometer test setup, consisting of the pre-spectrometer vessel, an ultra high vacuum recipient including an inner electrode system, two super-conducting solenoids (max. 4.5 T), a photoelectric electron source (e-gun) attached at one side and a detector chamber housing a monolithic 64 pixel silicon PIN diode on the other side. A detailed technical description of the pre-spectrometer test setup is available in [50]. The test setup acts as a prototype for the larger main spectrometer in order to test both vacuum concept and the new electromagnetic design of the KATRIN spectrometers. In addition new technologies are tested and developed at the test setup which will later be applied to the KATRIN measurements (e.g. an active HV stabilization, data acquisition system and background suppression).

3.1 Pre-spectrometer

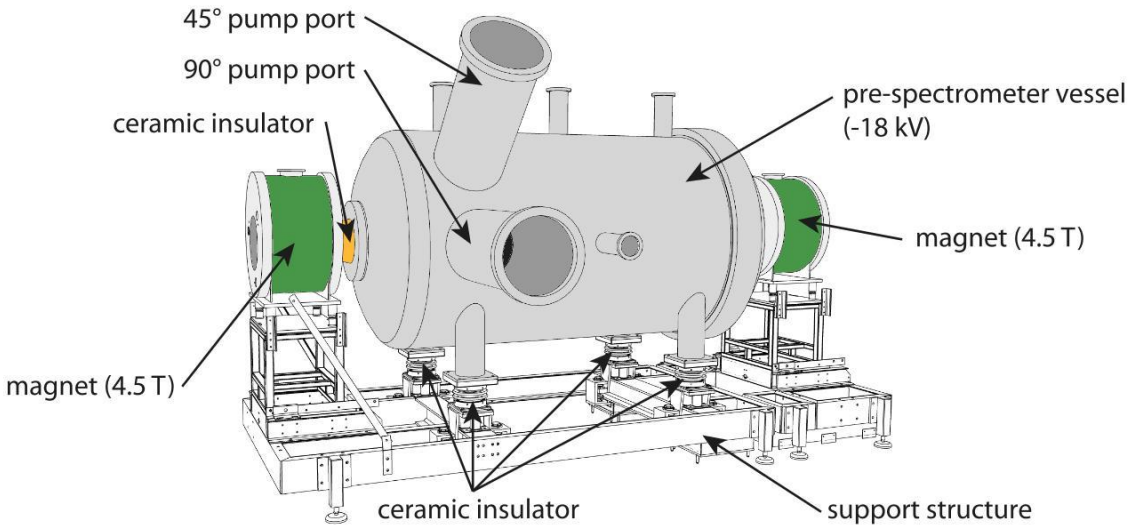

Figure 3.1: The pre-spectrometer vessel is mounted on a stainless steel support structure and is electrically isolated from its surroundings via ceramic insulators. On both sides a superconducting magnet coil is attached, providing an axial field at the centre of the coil of $B = 4.5$ T

Figure 3.1 gives a schematic overview of the pre-spectrometer vessel and the superconducting solenoids. The pre-spectrometer vessel is made of 10 mm thick stainless steel of type 1.4429. It has a length of 3.38 m and an inner diameter of 1.68 m. Two pump ports with a length of 1 m and a diameter of 0.5 m are welded to the vessel at 45° and 90° with respect to the vertical y-axis. The pre-spectrometer vessel is electrically isolated from its surroundings and can be put on high voltage. This is a novel feature compared to predecessor experiments like Mainz and Troitsk.

3.1.1 Vacuum system

The pre-spectrometer vacuum system is intended to routinely maintain pressures of less than 10^{-11} mbar. In order to achieve this ambitious goal a combination of different techniques is used:

- Only UHV[1] compliant materials are used inside the pre-spectrometer vessel.
- The inner surface of the pre-spectrometer vessel was electropolished in order to reduce the surface unevenness to a value of < 0.6 μm. This reduces the inner surface and thus the outgassing rate which is proportional to the surface area.
- In a bake-out process the pre-spectrometer vessel can be heated to temperatures above 200°C and thus removing thin water films. Outgassing from these films is dominant in the residual gas spectrum when pumping down the system after it has been vented.
- A cascaded pumping scheme is used. Two[2] EBARA ET801H turbomolecular pumps (TMPs) are attached to the 90° pump port and are running in parallel. The exhaust flanges are connected to a second stage TMP (Leybold TW290) which creates an intermediate vacuum of 10^{-7} mbar. Attached to the second stage TMP is an Adixen ACP28 fore pump which operates in the 10^{-3} mbar region.
- Inside the 45° pump port a non-evaporable getter (NEG) pump is installed (see also section 5.1). The pump consists of 90 one meter long strips of type SAES[3] ST707. Due to its large pumping power (27000 l/s for H_2) it is able to remove most of the H_2 which dominates the residual gas spectrum after bake-out (see figure 5.27).

In order to measure the pressure inside the pre-spectrometer, two vacuum gauges (MKS I-Mag cold cathode gauge and Leybold Extraktor IE 514 gauge) are attached at the 45° pump port. The composition of the residual gas can be measured with a residual gas analyzer (MKS MicrovisionIP LM92).

[1] **U**ltra **H**igh **V**acuum (pressure region below 10^{-7} mbar)
[2] In September 2009 the EBARA 1 TMP was replaced with a Leybold TMP (MAG W 1300).
[3] SAES Getters S.p.A.

Vacuum measurements performed in 2004 confirmed that the vacuum concept is working and a pressure in the region of 10^{-11} mbar could be achieved [62].

3.1.2 Heating and cooling system

In order to achieve the required pressure of $<10^{-11}$ mbar a dedicated bake out process of the pre-spectrometer is required. The temperature of the pre-spectrometer during bake-out is controlled by a Lauda Kryoheater (KH 350L) system via circulation of thermal oil (Marlotherm LH, Dibenzyltoluol) in tubes welded onto the vessel. Thus the temperature of the pre-spectrometer can be varied between -20 and +220°C. An active cooling of the pre-spectrometer can be used to reduce the outgassing rate of the stainless steel walls and thus to reduce and also stabilize the final pressure inside the pre-spectrometer.

3.1.3 Inner electrode system

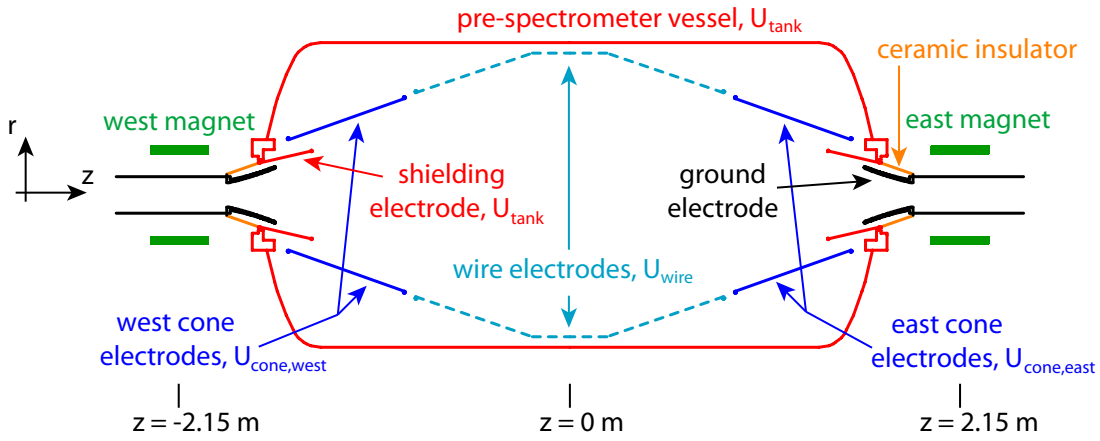

Figure 3.2: schematic overview of pre-spectrometer IV electrode system

Figure 3.2 is a schematic overview of the pre-spectrometer electrode system. The ground electrodes are fixed to ground potential, all other electrodes can be put on high voltage. The shielding electrodes are connected to the tank and thus have the same potential as the pre-spectrometer vessel. There are three sets of inner electrodes[4] (west cone, wire, east cone) which are axial symmetric except a vertical gap of about 5 cm. This gap divides each set into two single electrodes. Each of the six inner electrodes can be powered with an individual voltage. The cone electrodes are made of full metal sheets, each wire electrode is made of 120 wires of 0.5 mm diameter. The inner electrodes can be used for different purposes:

[4]The inner electrodes are a contribution of KATRIN collaboration member UW.

- Fine tuning of potential: The electrodes can be used for a fine tuning of the potential in the analyzing plane and to optimize the transmission characteristics of the pre-spectrometer (see chapter 7).
- Background suppression: The wire electrodes can be operated on a more negative potential with respect to U_{tank}. Thus they are able to shield secondary electrons produced in the tank wall (e.g. by cosmic particles).
- Dipole mode: The inner electrodes can be configured to create an electric dipole field. This dipole field can be turned on periodically to remove trapped particles via an $\vec{E} \times \vec{B}$ drift.

3.1.4 High voltage system

In order to apply stable and precise high voltage values to the pre-spectrometer and its electrodes, different high voltage power supplies are available:

- FuG[5] HCN 140-35000 (FUG4): This device provides a maximum voltage of -35 kV. It is used to supply the pre-spectrometer vessel.
- FuG HCN 140M-35000 (FUG3): The maximum output voltage of this device is -35 kV. It has additional connectors for routing an external high voltage (in the default configuration this is the voltage of FUG4, see figure 3.3). A voltage dependent resistor and a safety circuit limit its output voltage to $|\Delta U| = 5$ kV with respect to the external voltage. This is used as a safety measure to prevent voltage differences > 5 kV between inner electrodes and pre-spectrometer vessel. The output voltage of FUG3 can be distributed via an adapter box to four different devices.
- FuG HCN 35M-5000 (FUG1,2): Two devices of this type are available, each providing a maximum voltage of up to +5 kV as an offset to an external voltage (in the default configuration this is the voltage of FUG3, see figure 3.3). The devices are intended to create an electric dipole (see above) and have a fast rise time (<20 ms) of the offset voltage.
- FuG HCN 35-35000 (FUG e-gun): The maximum output voltage of this device is -30 kV. It is used to supply the photoelectric electron source (see section 3.2).
- Canberra 3102/2 (HV offset): This device is mounted in the rack which is on tank potential (see figure 3.3) and provides an voltage between $\pm$ 1.5 kV (as an offset to U_{tank}) with a precision of 0.1 V. This allows a precise adjustment of the voltage difference between the inner electrodes and U_{tank}.

Figure 3.3 gives a schematic overview of the pre-spectrometer high voltage system. All voltages (except the voltage of FUG e-gun) are available at the distribution panel

[5] FuG Elektronik GmbH

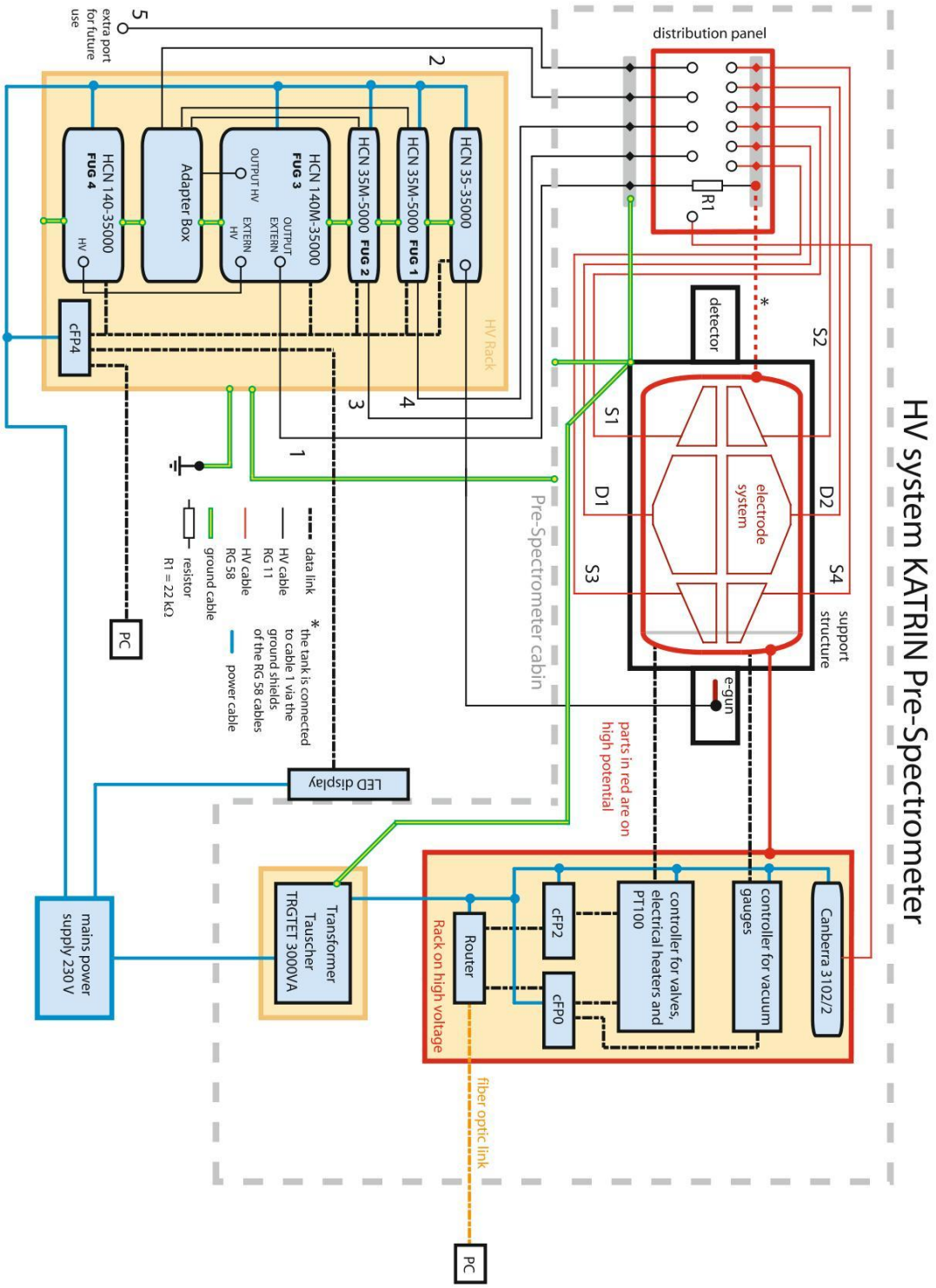

Figure 3.3: schematic overview of pre-spectrometer high voltage system, for details see text

and are distributed via pin plugs to the individual electrodes. This system allows the creation of specific potential configurations for the inner electrodes and thus provides a large flexibility for various kinds of dedicated measurements.

The pre-spectrometer high voltage system includes an active high voltage stabilization of U_{tank} developed at IPE[6]. This stabilization system consists of the following devices [82]:

- Ripple pick-up probe and amplifier: The ripple probe is based on a ceramics HV capacitor (10 nF, 50 kV). It is attached to the pre-spectrometer vessel at one side and - via an amplifier - to the HV post-regulator on the other side. It is used to decouple fluctuations (ripple) from U_{tank}.
- Voltage divider: A Julie Research KV-50 voltage divider is used to monitor the absolute value of U_{tank}.
- HV post-regulator: This device combines the signals of ripple probe and voltage divider and controls the triode shunt.
- Triode: The triode is connected to the pre-spectrometer vessel and creates a leakage current ($\approx$ 0.5 mA at typical operating point) controlled by the post regulator.

The pre-spectrometer voltage U_{tank} is monitored via a ripple probe and a voltage divider. The post-regulator compensates fluctuations of U_{tank} by changing the Triode shunt. Triode and resistor R1 (22 kΩ, see figure 3.3) are creating a voltage divider between the voltage of FUG4 and ground potential. Therefore a change of the resistance of the triode changes the divider ratio and thus U_{tank}. The active high voltage stabilization was able to reduce a 7.3 V peak to peak periodic (50 Hz) fluctuation of U_{tank} [41] (caused by the transformer which powers the devices attached to the pre-spectrometer vessel) to fluctuations below the 50 mV level.

3.1.5 Magnet system

The magnetic field to guide electrons through the pre-spectrometer is created by two Cryogen Ltd. superconducting solenoids. Each magnet generates a maximum magnetic field of 4.5 T at the centre of the coil at a magnet current of 157 A (provided by a FuG NTS 800-5 power supply). On each side of the pre-spectrometer a magnet is mounted with a distance of 2.15 m between the centre of the magnet coil and the analyzing plane (z = 0 m). In order to cool the magnets to superconducting temperatures without cryo-infrastructure a cryogen free system [14] is used.

[6] **I**nstitute of Data **P**rocessing and **E**lectronics, KIT

3.2 Photoelectric electron source

A photoelectric electron source (e-gun) is attached on the east side of the pre-spectrometer test setup. It is used to generate electrons with a dedicated energy in the range of 0 to 30 keV. Figure 3.4 shows a schematic drawing of the e-gun. The intensity of the light produced by the UV lamp (**h**) is controlled via a pneumatic shutter system (**g**). Nine shutters with diameters ranging from 0.2 to 10 mm are available. The light penetrates through a sapphire window (**e**) into a ceramic insulator (**d**) and reaches the gold plated quartz glass tip (**b**) which is fixed with a metal casing (**c**). Here the photons produce free electrons via the photoelectric effect. Taking into account the work function of gold and the energy spectra of the UV lamp (**h**), the start energy of the electrons are expected to be in the range between 0 and 2 eV [41]. The ceramic insulator (**d**) insulates the tip (**d**) electrically from the rest of the e-gun, so high voltage can be applied via the high voltage connector (**f**) to the tip. The potential difference between tip (**b**) and ground electrode (**a**) then accelerates the electrons. The original design of the e-gun was developed at KATRIN collaboration member INR[7] Troitzk [100].

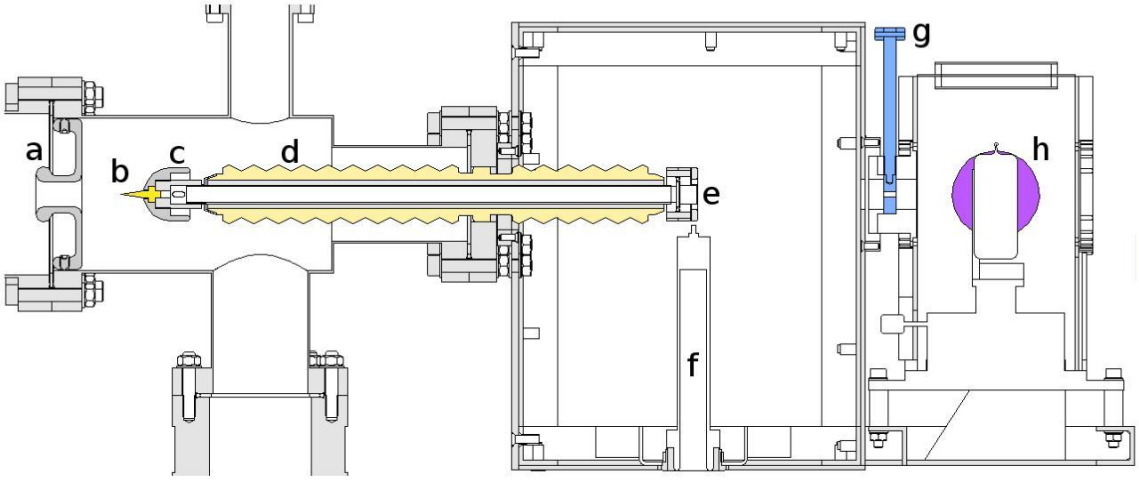

Figure 3.4: schematic drawing of photoelectric electron source, **a:** ground electrode, **b:** gold plated quartz glass tip, **c:** metal casing, **d:** ceramic insulator, **e:** sapphire window, **f:** high voltage connection, **g:** pneumatic shutter system, **h:** deuterium UV lamp (Hamamatsu L6565)

In order to be able to start electrons at different positions within the flux tube, the e-gun is mounted on a pneumatic driven manipulator. It allows to move the e-gun on a sphere[8] up to $\pm 23°$ into x (horizontal) and y (vertical) direction. This moves the e-gun tip on a radius of 1.06 m around the point $z = 2.4$ m, $r = 0$ m (pre-spectrometer coordinates).

[7] Institute for Nuclear Research of the Russian Academy of Sciences
[8] Therefore the positions of the e-gun are given in degrees.

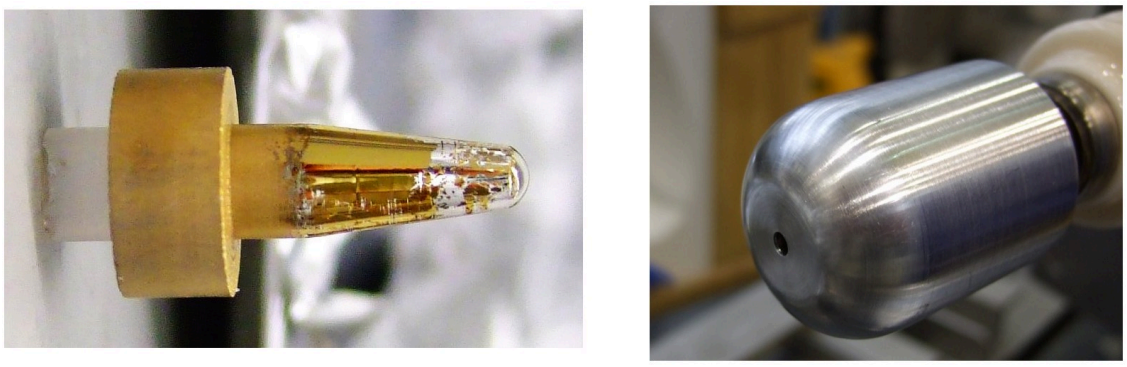

Figure 3.5: **left**: damaged e-gun tip, **right**: metal casing of the new e-gun design

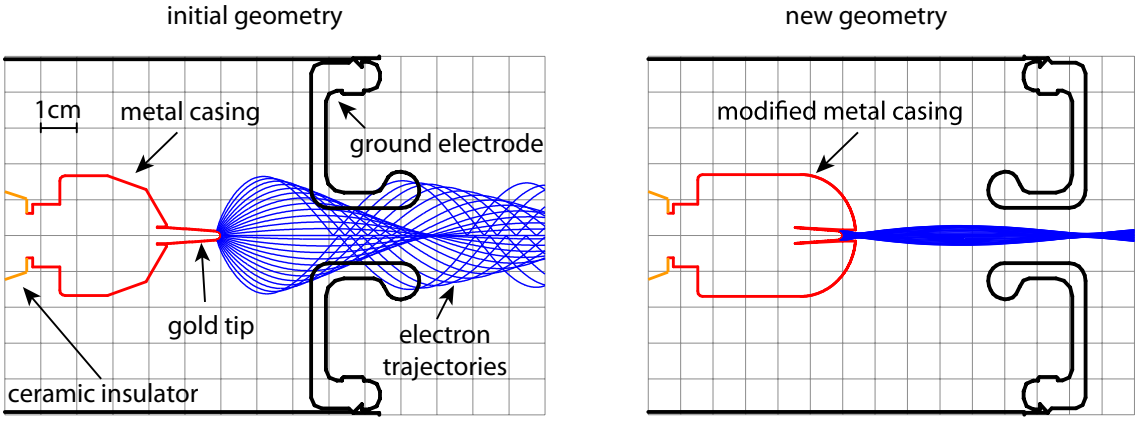

Figure 3.6: **left**: simulation of the initial e-gun geometry, most of the electrons hit the ground electrode, **right**: simulation of new geometry, the electron beam is much better collimated.

During the initial commissioning phase of the e-gun, the gold layer of the tip was severely damaged two times (see left side of figure 3.5). The following processes could have caused the damage of the tip:

- **bake out**: In order to improve the pressure inside the e-gun, the system is baked out. However, the observed maximum temperatures (about 150°C) are well below values which would harm the gold coating of the tip.
- **discharge**: Experiments using a full metal tip instead of the gold plated tip showed that electrical discharges happened inside the e-gun [37]. Because the distance between e-gun tip and ground electrode (see left side of figure 3.6) is small (about 30 mm), high electric fields occur in this region. Thus it is very likely that discharges are happening in this region. The electric current during a discharge can locally heat the thin gold layer and evaporate it. However, discharges do not necessarily imply a damage of the gold layer [38].

- **ion bombardment**: Electrons emitted from the tip can scatter with residual gas molecules and create positive charged ions. These ions are accelerated towards the tip and can remove gold atoms there via sputtering. Microscopic images of the tip after removing the gold layer indeed show small craters which may be caused by ion bombardment [96].

In the scope of this work, simulations of six different e-gun geometries were performed in order to improve the stability of the e-gun operation [19]. The left side of figure 3.6 shows the emission characteristics of the initial e-gun geometry. Most of the electrons starting at the gold tip hit the ground electrode (there was no stop condition in the tracking program in case an electron hits an electrode, therefore there are also trajectories inside the electrodes shown). The right side of figure 3.6 shows the new improved design of the e-gun. This geometry has two major modifications. The metal casing was elongated such that the gold tip now resides 4 mm inside. The ground electrode was moved about 30 mm further away from the tip and (for technical reasons) mirrored. In this way the very large electric field strength (6.4 MV/m at U_{e-gun} = -12 kV) at the gold tip of the initial geometry could be reduced considerably thereby protecting the tip from electrical discharges and (to some extent) from ion bombardment. Another advantage of the new geometry is a better collimation of the electron beam and a higher efficiency of the e-gun. The rate - measured at the detector - has been increased by a factor of about 2 for the same shutter setting. Nevertheless, there is also a drawback of the new geometry. The angular distribution (Θ) of electrons emitted from the e-gun in the centre of the east magnet, is not isotropic anymore. The simulations reveal that preferably electrons with small Θ are emitted. As will be shown later, the angular distribution of the e-gun is important for the transmission function measurements (see chapter 7). With the new geometry the operation of the e-gun is stable (for an accumulated operating time of several months) and no damage of the tip occurred anymore.

3.3 Detector system

In order to detect electrons from the e-gun in the framework of transmission studies or from the pre-spectrometer itself (background studies), a detector system is attached at the west side of the pre-spectrometer. It consists of a vacuum chamber and a manipulator which is movable in x, y and z direction. Two kinds of detectors were mounted on the manipulator: first a microchannel plate (MCP) and later a segmented silicon detector (64PD).

3.3.1 Microchannel plate (MCP)

An MCP is made of a large number of very thin, conductive glass channels, usually 6 to 25 μm in diameter (see right side of figure 3.7). By applying a voltage (U_{MCP})

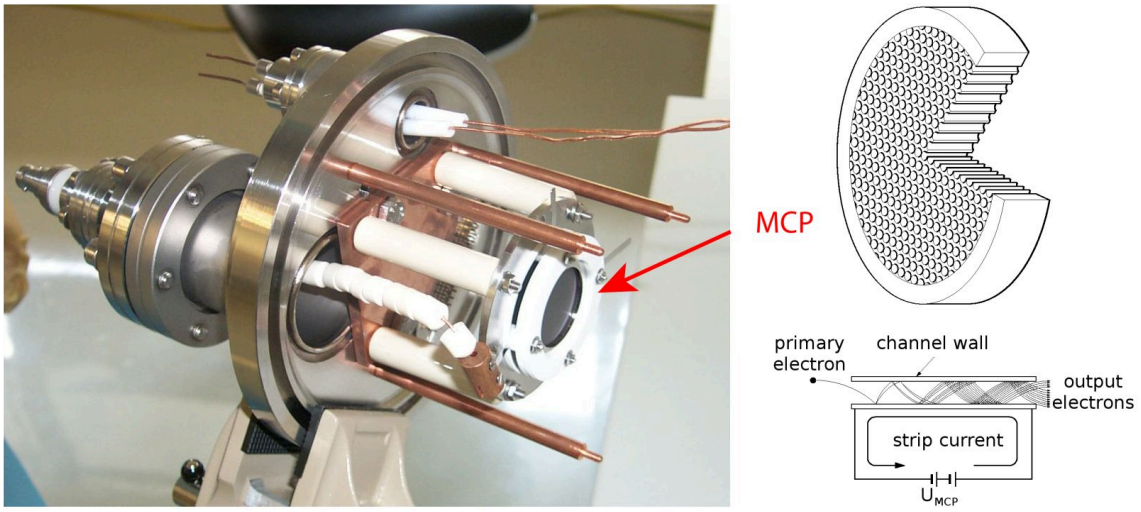

Figure 3.7: **left**: MCP used for the pre-spectrometer test setup, **right**: schematic of a MCP detector, figure taken from [51]

between the front and the rear side of the MCP, a potential gradient along the channel walls is created. If an electron - coming from the front side of the MCP - hits the channel wall, several secondary electrons are produced. These electrons are accelerated by the potential gradient and hit the channel wall, releasing more secondary electrons. Thus each channel acts as an independent electron multiplier. An MCP is able to detect electrons, ions and photons. The minimum energy for detection is given by the work function of the channel wall material (several eV). For the initial measurements with the pre-spectrometer test setup an MCP (Hamamatsu F2223-21) detector with the following properties was used:

- diameter: 27 mm (sensitive area 5.7 cm^2)
- channel diameter: 12 μm
- charge amplification for an incident electron at $U_{MCP} = 2.1$ kV: 10^6

The operation of an MCP detector at this setup has several advantages and disadvantages:

- **pros**:
  - the detection of very low energetic ($\approx$ 10 eV) electrons is possible
  - detection of electrons, ions, UV light, x-rays and γ-rays
  - relatively cheap (order of 1 k€) and easy to replace
- **cons**:
  - no energy resolution
  - no spatial resolution

– no discrimination of incident particles

For these reasons, the MCP was used only in the initial start-up phase of the measurements.

3.3.2 Segmented silicon detector (64PD)

The 64PD detector [83] chip is a large quadratic monolithic silicon PIN diode (sensitive area 16 cm^2) which is segmented into 8 × 8 individual pixels. The detector chip was manufactured by Canberra[9] and has a thickness of 200 μm including a 100 nm dead layer. On the front side of the detector chip there is an n^{++} doped layer whereas at the rear side there is a segmented p^{++} layer which defines the pixels. The bulk material in between is made of n doped silicon. Between n^{++} and p^{++} layer a depletion voltage of 12 V is applied. Incident electrons or x-rays create electron-hole pairs which are separated due to the electric field and amplified via JFETs[10] which are mounted on a ceramics (Al_2O_3) plate at the rear side of the detector in the UHV region (see figure 5.30) and connected to the individual pixels. The JFETs are connected via a 100 pin feed through - which separates the UHV region of the detector from the ambient air region - to preamplifiers which provide the signal for the data acquisition (DAQ) electronics. In order to reduce thermal noise, the detector and the JFETs on the ceramics plate are cooled with liquid nitrogen (LN2) via a copper (Cu) cooling ring (see figure 3.8) to temperatures in the range -100°C and -60°C.

The position of the 64PD can be adjusted in all directions with a manipulator in order to be able to cover 100% of the flux tube. The default measurement position of the detector is at x = -0.3 cm, y = 0.35 cm, z = 40 cm. The coordinates are given in the system of the manipulator. The z component can be translated into the pre-spectrometer coordinate system with $z_{ps} = -2.7m + z_{det}$. At the default measurement position the detector is located at a magnetic field of 3.4 T and covers 28.5% of the flux tube (see figure 3.8). A detailed characterization of the 64PD [78] showed that all pixels have similar behaviour for linearity and energy resolution except pixels E5, F5 and F7. Their energy resolution is a factor of about two worse and they show an increased noise level. In the analysis of the 64PD data these pixels are usually excluded.

The operation of the 64PD detector has two major advantages compared to the MCP detector (see above). It offers energy discrimination with an energy resolution (≈ 4 keV FWHM [78]) and, most importantly, offers spatial resolution (64 pixel). A drawback of the 64PD is its rather high threshold, so that only electrons with energies > 10 keV can be detected.

[9] Canberra Industries, Inc
[10] **J**unction **F**ield **E**ffect **T**ransistor

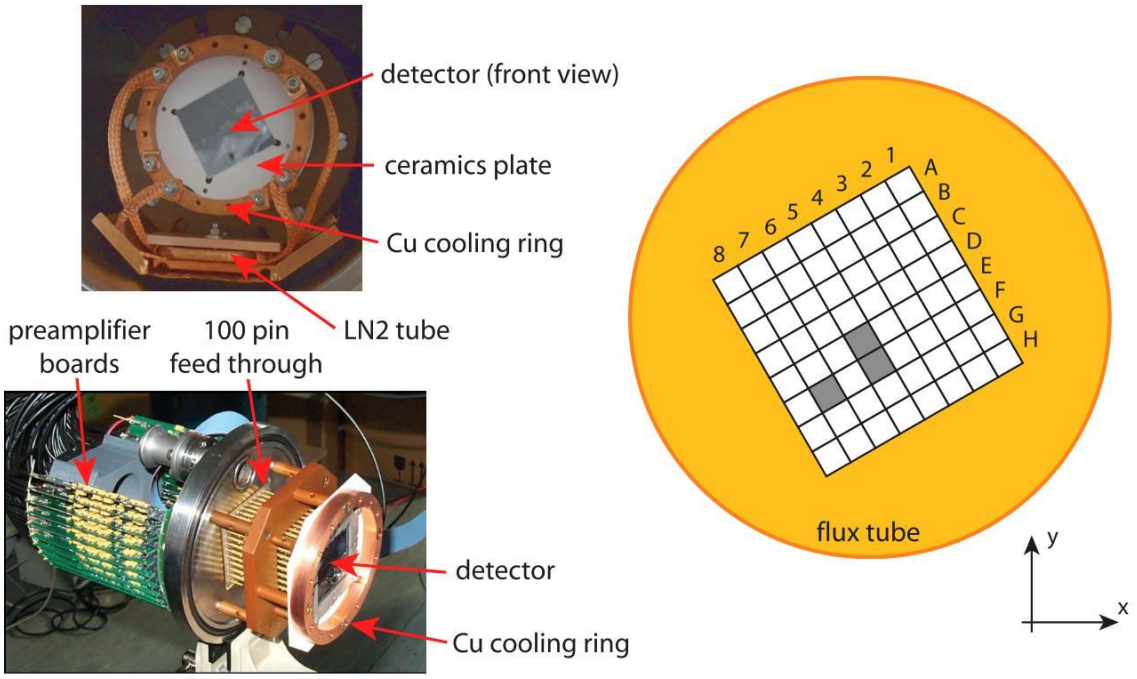

Figure 3.8: Segmented pixel detector (64PD). The right side of the figure shows the position and orientation of the detector inside the flux tube at the default (x = -0.3 cm, y = 0.35 cm, z = 40 cm) measurement position as seen from the pre-spectrometer. The centre of the flux tube is at pixel D4 (see also right side of figure 5.26).

3.4 Pre-spectrometer data acquisition

This section gives an overview of the data acquisition (DAQ) system in use at the pre-spectrometer.

Figure 3.9 characterzizes the data flow at the pre-spectromter test setup. This flow line can be separated into three data chains:

1. **Detector data**
   The analog output signals of the detector (64PD or MCP) are digitised via a dedicated DAQ electronics. At the pre-spectrometer test setup, two different DAQ electronics were in operation. Until October 2008 a system developed at the University of Washington, Seattle (UW) was used. Afterwards a DAQ electronics system developed at IPE (IPE version 3, IPE3) was used. A detailed description and characterization of the IPE electronics is available in [65]. The IPE3 electronics is the predecessor of the IPE4 electronics which will be used for the detector system of the KATRIN setup. The DAQ electronics is controlled via the DAQ software ORCA[11] which has been used already in other

[11] **O**bject oriented **R**eal-time **C**ontrol and **A**cquisition, ORCA is a contribution of KATRIN col-

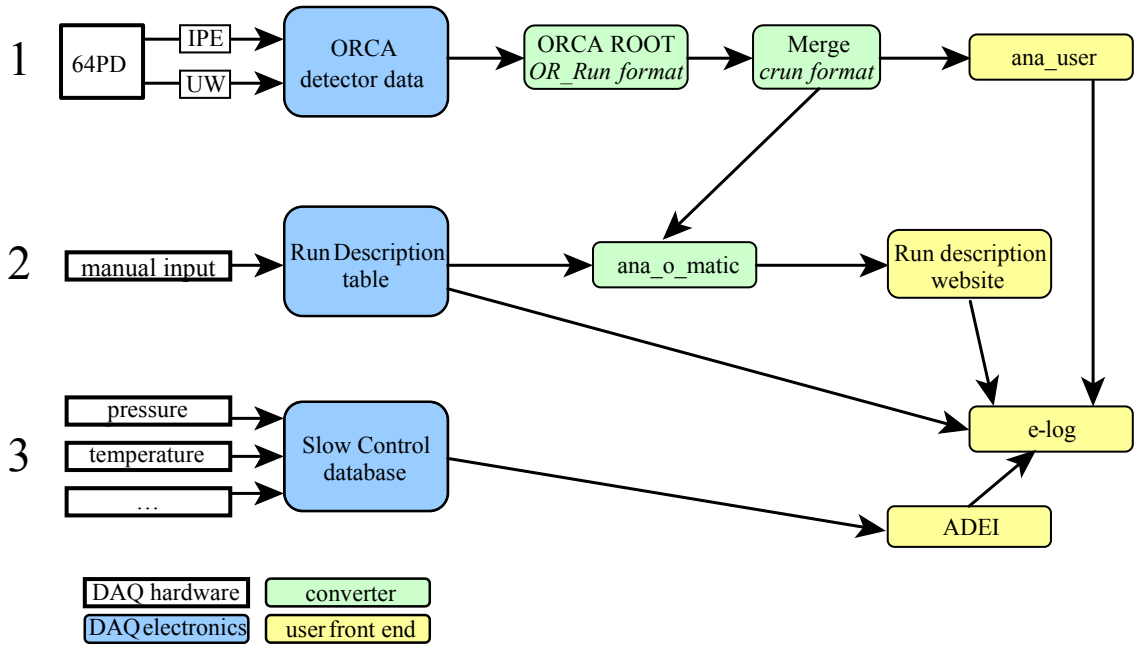

Figure 3.9: overview of pre-spectrometer data acquisition system, there are three different data chains (see text)

experiments like SNO [52] and which will also be used for the final KATRIN setup. The ORCA detector data has a binary format and is converted via ORCARoot into a ROOT [9] tree (OR_Run format). The structure of this tree depends on the DAQ electronics and therefore the data is converted in a second step into crun format (also a ROOT tree) which is independent of the actual DAQ electronics. The default analysis tool ana_user (see below) works with the crun format and thus does not need to be adapted in case the DAQ electronics changes.

2. **Run descriptions**
   All important parameters (e.g. configuration of the inner electrodes, magnet currents, comments on the measurement,...) during a measurement run are stored in a table. The data of the table is combined with the detector data via a semiautomatic converter (ana_o_matic) and published on a website [40]. The website allows a filtering of the data by various experimental parameters (e.g. high voltages, magnetic fields, e-gun settings,...) and displays the energy spectrum, pixel distribution and time series of the detector data for each measurement run. This data chain was implemented within the scope of this work.

laboration member University of North Carolina at Chapel Hill (UNC).

3. **Slow control data**
   The data of the slow control system, which monitors and controls practically all parameters of the pre-spectrometer test setup (vacuum system, high voltage system, heating/cooling system, e-gun,...), are stored in an SQL[12] database. The data is available via the ADEI[13] website. This data chain was implemented by IPE.

The physical relevant results of the measurements including data of all three data chains are usually published to the KATRIN collaboration via an electronic logbook (e-log).

The experience gained with the pre-spectrometer DAQ system had a strong influence on the final DAQ system that will be used for the main spectrometer commissioning phase and further for the final KATRIN setup. The new DAQ system is currently under development and will integrate all data chains in a fully automatic way and will make all data available on a single website.

3.5 Pre-spectrometer data analysis

This section describes the analysis tool ana_user which is used for most of the analysis steps of the pre-spectrometer detector data presented here. The program was created within the scope of this work and has several features:

- **data calibration:** The detector data are stored in the crun format (see above) in an uncalibrated state. Ana_user applies an energy calibration of the detector data by using a specific calibration file, where each pixel is calibrated individually.
- **definition of pixel groups:** Each pixel of the 64PD can be seen as an individual detector. Ana_user allows the combination of several pixels in pixel groups with up to 64 pixels. For each pixel group individual energy cuts can be applied.
- **data cuts:** Time and energy cuts can be applied to the detector data.
- **data filtering:** Three kind of filters (see below) can be applied to the detector data.
- **display of data:** Ana_user provides different plots of the data (event rate, pixel distribution, time separation plot, energy spectra and energy over time plot) for each pixel group and also provides overview plots showing all pixel groups.

[12] **S**tructured **Q**uery **L**anguage
[13] **A**dvanced **D**ata **E**xtraction **I**nfrastructure

- **export of data as plain text:** Energy spectra and event rates can be exported as plain text and thus be used for further analysis or in combination with slow control data.
- **easy configuration:** All parameters of ana_user can be configured via a text file, thus no modification of the source code is necessary.

In order to remove noise events or cross talk events, ana_user has implemented three different kind of filters which are described below.

3.5.1 Burst filter (BF)

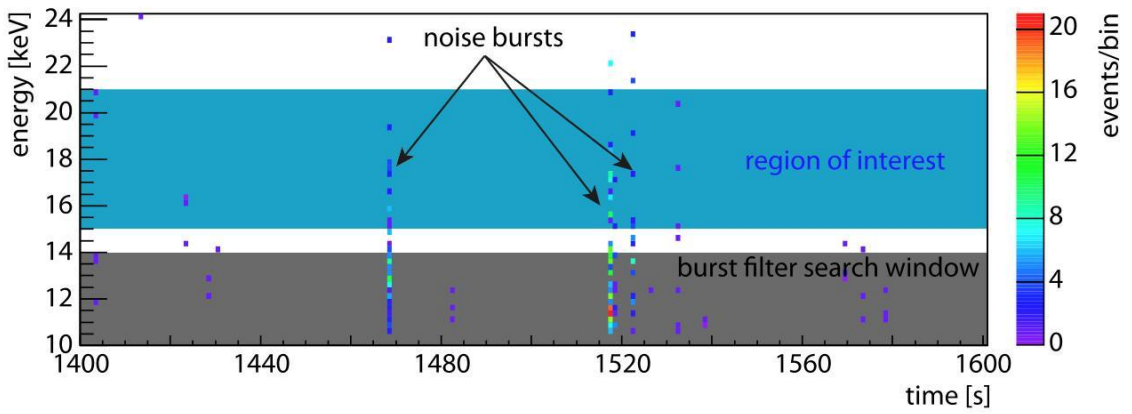

Figure 3.10: Energy over time plot of a detector background measurement (run 10523). From time to time noise bursts occur.

Figure 3.10 shows an energy over time plot of a detector background measurement (run 10523). Three major noise bursts are observed. Although most of the noise events occur at low energies[14] (< 14 keV), some noise events leak into the region of interest (ROI), which is defined as the energy region between 15 and 21 keV for typical pre-spectrometer measurements. The burst filter has three parameters: minimum (E_{min}) and maximum energy (E_{max}) for the search window and minimum number of events (N_{min}) needed to detect a noise burst for an one second bin within the search window. The filter searches within the search window for a time bin (1 s) where the number of events is larger N_{min}. This time bin is then excluded - over the complete energy range - from the further analysis of the run. The disadvantages of this filter are a large dead time in case of a run with many noise bursts and the possibility that real events are removed[15] which coincide with the excluded time bin.

[14] The energy spectra of noise events declines exponentially to higher energies.

[15] For the calculation of the rate within the ROI this is irrelevant, but the statistical uncertainty of the rate will increase.

3.5.2 Time correlation filter (TCF)

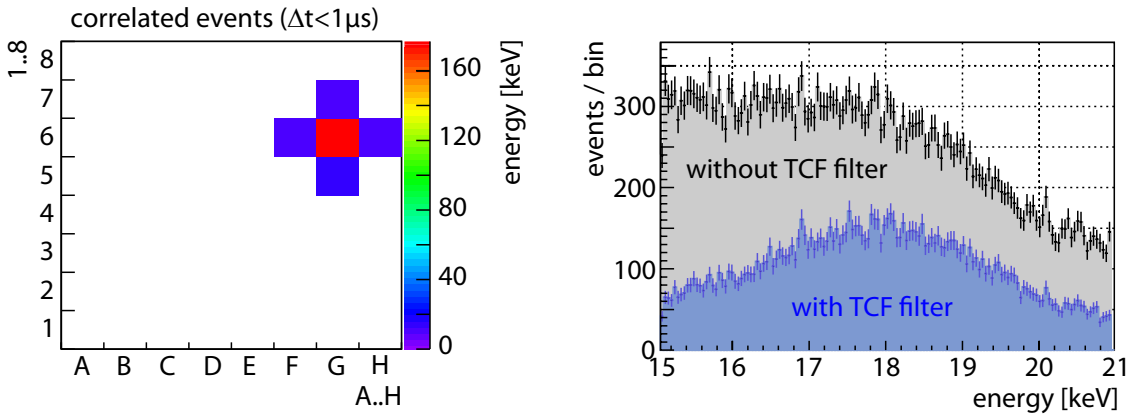

Figure 3.11: **left:** example of five correlated events as they are typical for the intrinsic detector background, **right:** energy spectrum (in the region of interest) of a pre-spectrometer background measurement with and without TCF filter

Measurements of the intrinsic detector background revealed that about 80% of all events in the region of interest are correlated in time (the time difference Δt between the single events is smaller 2 μs, which is less than the shaping length of the IPE3 DAQ electronics of 3.2 μs). The left side of figure 3.11 shows the pixel distribution of five correlated events. Pixel G6 is hit by a high energetic particle (energy $>$ 177 keV)[16]. At the same time (Δt $<$ 1 μs) also events with an energy between 10 and 15 keV are detected at four adjacent pixels. This signature (one high energetic event and several low energetic events at adjacent pixels) is typical for the correlated events. A possible explanation of this behaviour is crosstalk (an incident high energetic particle induces a signal on adjacent pixels). The right side of figure 3.11 shows the effect of the TCF filter in the ROI for a pre-spectrometer background measurement (measurement 7, see section 5.4.8). After the filter is applied, a peak at 18 keV (this corresponds to U_{tank} = -18 kV) becomes visible. The behaviour of the TCF filter is controlled via a parameter dt which defines the maximum time difference between two events in order to be identified as correlated events. The default value of dt is 2 μs. For a random source (e.g. e-gun) with an average rate of 1 kHz the probability that the TCF filter removes two events with the default value of dt can be calculated to $2 \cdot 10^{-6}$. This probability increases with the rate but is still much smaller (more than a factor 100) compared to the loss of events due to dead time effects of the DAQ electronics.

[16]This energy is already within the overflow peak (see figure 5.8) and is therefore only a lower limit on the energy of the incident particle.

3.5.3 Pulse shape analysis filter (PSA)

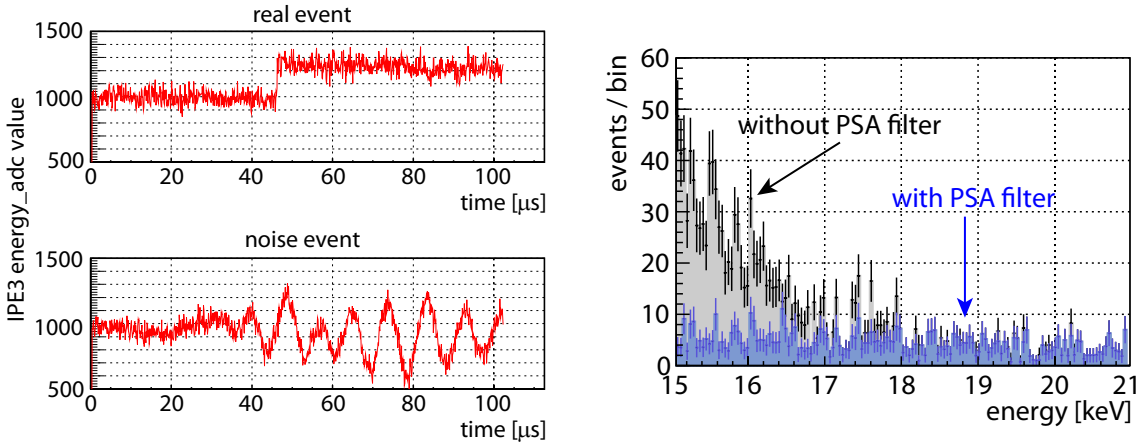

Figure 3.12: **left:** waveform of a real event and a noise event, **right:** energy spectrum in the region of interest with and without PSA filter

The expected background rate at the pre-spectrometer is in the order of mHz. Therefore it is important to identify any noise event in the region of interest in order to gain reliable results of the background rate. The IPE3 DAQ electronics provides the possibility to take data in waveform mode. In this mode for each event the trace (typically 1024 bins with a bin width of 0.1 μs) is stored. The maximum number of events that can be processed and read out in waveform mode is about 300 each second. This is sufficient for typical background measurements with rates < 1 Hz within the total energy range (10 to 180 keV). The left side of figure 3.12 shows two examples of measured waveforms (one real event caused by an incident particle and a noise event). In order to identify noise events ana_user provides a pulse shape analysis filter. It performs a discrete Fourier transform using the FFTW[17] library. In the frequency domain, cuts are defined that determine whether an event is real or noise. The PSA filter was extensively tested with an e-gun run (run 1464) containing about $8{\cdot}10^4$ events of 18 keV electrons. Only one of those events in the region of interest was misleadingly classified as noise. The reason for this singular mis-classification was a pronounced slope of the baseline as a result of the high e-gun rate (2.1 kHz) for this particular event. Although such a behaviour is not expected within a background run, the probability for a real event being misleadingly classified as noise is defined to be in the order of 10^{-5} [18]. The right side of figure 3.12 shows the effect of the PSA filter in the region of interest. The PSA filter has the advantage that no deadtime is created (unlike the BF filter), in case that a noise event is detected.

[17] **F**astest **F**ourier **T**ransform in the **W**est

[18] The systematic error caused by misleading classifications of real events is only 1% of the statistical error of a 4 month measurment, assuming a background rate of 10 mHz in the region of interest.

4 Pre-spectrometer background from trapped particles

This chapter describes the background characteristics of the pre-spectrometer setups I to IV which were characterized by different levels of background resulting from trapped particles. In particular it describes the hardware modifications which were instrumental in reducing the background rate by many orders of magnitude via the successive optimisation of the pre-spectrometer electrode system. The first section (4.1) introduces the concept of Penning traps and discusses other storage conditions of electrically charged particles such as magnetic trapping. The following sections (4.2 to 4.5) are organized in a similar way: First the electrode system of the actual setup is described, then the results of the background measurements are presented and finally the corresponding simulations of the electromagnetic properties of the pre-spectrometer setup are discussed.

4.1 Penning traps and storage conditions

4.1.1 Penning trap

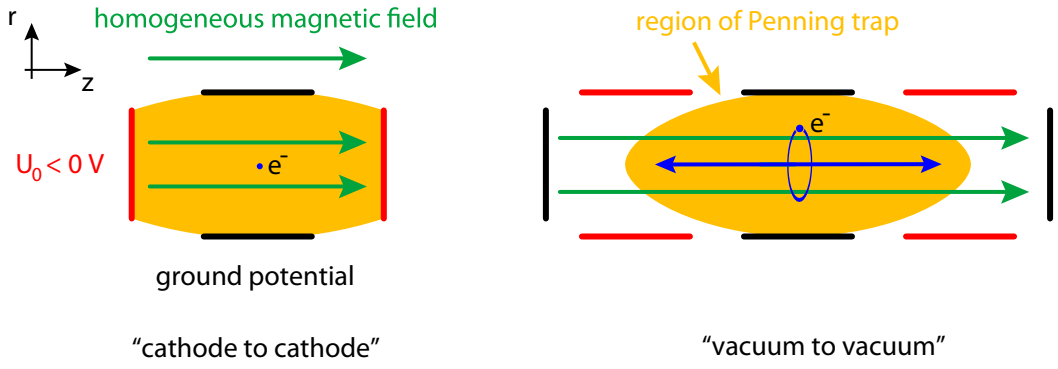

Figure 4.1: schematics of a Penning trap for an electron, **left:** Cathode to cathode type, **right:** Vacuum to vacuum type, figure based on [29]

In a Penning trap it is possible to store charged particles in a specific configuration of magnetic and electric fields. Figure 4.1 shows two exemplary configurations for

an electron Penning trap. In order to explain the trapping mechanism one generally assumes an electron with zero start energy at the centre of the cathode to cathode configuration[1]. It can not move in z-direction because of the more negative potential of the electrodes on the left and right side. A movement in r-direction is also not possible because a perpendicular motion with respect to the magnetic field would cause a Lorentz force that deflects the electron back to its start position. Therefore the electron is trapped in this position.

Assuming that the electron has a start energy $0 < E_0 < q \cdot U_0$ and starts at an arbitrary position inside the Penning trap (see right side of figure 4.1), its motion can be split in two components with respect to the magnetic field:

- transversal: The electron moves in a cyclotron motion around a guiding magnetic field line.
- longitudinal: This component is not influenced by the magnetic field. The electron moves along the z-direction until it is reflected from the more negative electrodes and thus oscillates in z-direction.

The resulting track is a spiral around a guiding magnetic field line between a minimal and a maximal z value. In case the magnetic field is not homogeneous but axially symmetric around the z-axis, as it is the case for the KATRIN spectrometers, the gradient of $\vec{B}$ causes an azimuthally drift (called magnetron drift) of the electron and thus it has an additional motion component on a circle around the z-axis (see figure 5.6).

The same description of the trapping mechanisms described above is also valid for the storage of positively charged particles if $U_0 > 0$.

4.1.2 Penning discharge mechanism

In the presence of storage conditions for a charged particle, a self-sustained discharge process is expected to start. The occurrence of a Penning discharge is discussed on the basis of figure 4.2. For the following discussion a very low pressure p is assumed such that the mean free path of an electron is much larger than the characteristic dimensions of the cathode to cathode configuration.

In order to start a discharge, a primary source of electrons is needed. In the configuration of figure 4.2 this could be the emission of low energy electrons from the cathode electrode surface due to natural radioactivity or cosmic particles (1). These electrons are accelerated from the electric field and follow the magnetic field lines to the opposing cathode electrode (electron a). If they lose some energy on their way via scattering processes or cyclotron radiation, they are not able to reach the cathode electrode and consequently are trapped inside the Penning trap (electron b) where they oscillate in z-direction (2). Sooner or later they will ionize a residual

[1] The following is also true for the vacuum to vacuum configuration.

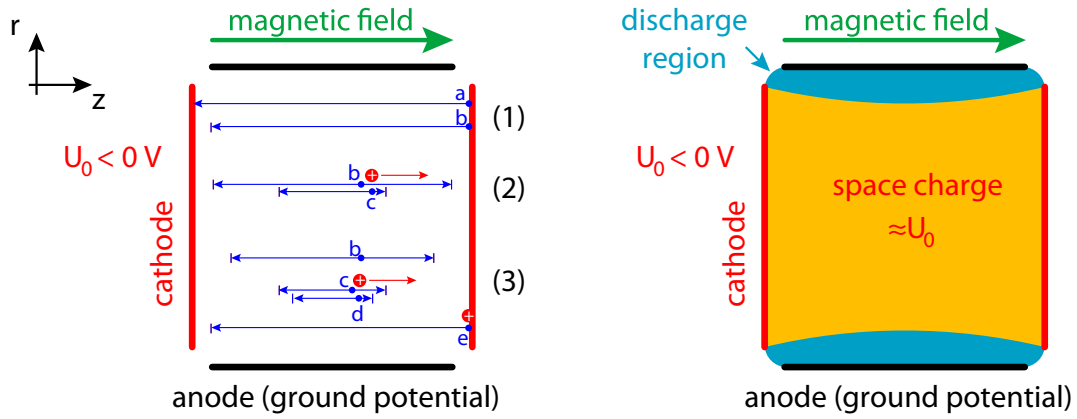

Figure 4.2: **left:** start of Penning discharge (details see text), **right:** stable Penning discharge

gas molecule and thus create a secondary electron (electron c) and a positive ion. The low-energy electron created in the ionization is also trapped. Depending on the position of the ionization it can gain sufficient energy and thus further ionize residual gas molecules (3). The maximal number of secondary electrons (and ions) that can be produced of a primary electron in this way is given by

$$N_{max} = 2^{\frac{e \cdot U_{trap}}{E_{ion}}} - 1 \tag{4.1}$$

with U_{trap} describing the absolute value of the difference between the minimal and maximal electric potential within the region of the Penning trap and E_{ion} representing the ionization energy of the residual gas molecules. The positive ions are accelerated towards the cathode electrodes and there create secondary electrons (3) which are also trapped with a certain probability (electron e). If the product of this probability and the average number of ions produced of a primary electron is equal or larger one, a self-sustained Penning discharge starts. Because positive ions leave the trap whereas the secondary electrons are trapped, a negative space charge starts to build up (right side of figure 4.2). This decreases U_{trap} and only electrons in a small region close to the anode can gain sufficient energy for ionization of residual gas molecules [61]. If electron loss processes such as radial drift and creation processes such as secondary electrons due to ion impact at the cathode reach an equilibrium, a stable Penning discharge occurs.

4.1.3 Magnetic trapping of electrically charged particles

In a Penning trap such as described above (see figure 4.1) a charged particle is confined in z-direction via an electrostatic potential barrier and in r-direction via the magnetic field. In case of magnetic trapping the particle is completely confined

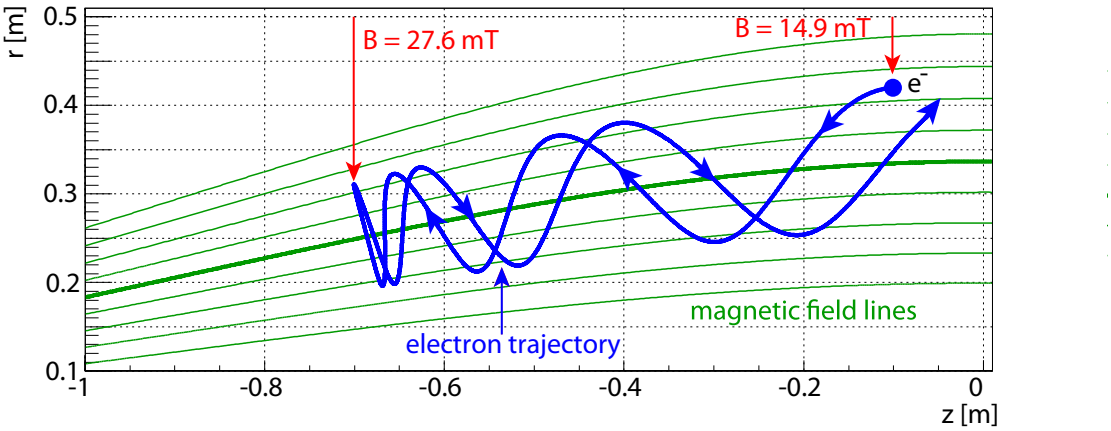

Figure 4.3: example of the magnetic mirror effect for an electron in the magnetic field of the pre-spectrometer, electron start conditions: z = -0.1 m, r = 0.42 m, Θ = 130 °, E_0 = 200 keV

to a volume due to magnetic fields. This is only possible for inhomogeneous magnetic fields.

If the motion of a charged particle in a magnetic field $\vec{B}$ is adiabatic, the magnetic moment $\mu = E_t/|\vec{B}(\vec{r})|$ is conserved[2]. Therefore any change of $B = |\vec{B}(\vec{r})|$ causes a transformation of E_t to E_l or vice versa and thus changes the angle Θ (for a definition of Θ see figure 4.4). For a particle that starts at position $\vec{r}_0$ in a magnetic field $\vec{B}(\vec{r}_0)$ with Θ_0, the corresponding angle Θ at a position $\vec{r}$ can be calculated with:

$$\Theta(\vec{r}) = \arcsin\left(\sqrt{\frac{|\vec{B}(\vec{r})|}{|\vec{B}(\vec{r}_0)|}} \cdot \sin(\Theta_0)\right) \tag{4.2}$$

If the particle moves into the direction of an increasing magnetic field B (e.g. it moves towards a magnet coil), the angel Θ increases according to equation 4.2. For a sufficiently large increase of the magnetic field, Θ becomes 90° (all energy is stored in E_t) and thus the particle is reflected. Another view to describe the magnetic mirror effect is the following: Let's look at the transversal motion component (cyclotron motion). Due to the gradient of B there is a radial component of the magnetic field. This causes a component of the Lorentz force pointing towards lower magnetic field and thus decelerates the transversal motion of the particle. Figure 4.3 shows an example of a magnetically reflected electron in the magnetic field of the pre-spectrometer.

Assuming an axial symmetric configuration of two magnet coils (1, 2) aligned axially on a common z-axis, the magnetic field of each magnet along the z-axis is

[2]Actually $\gamma\mu$ is conserved (with the Lorentz factor γ).

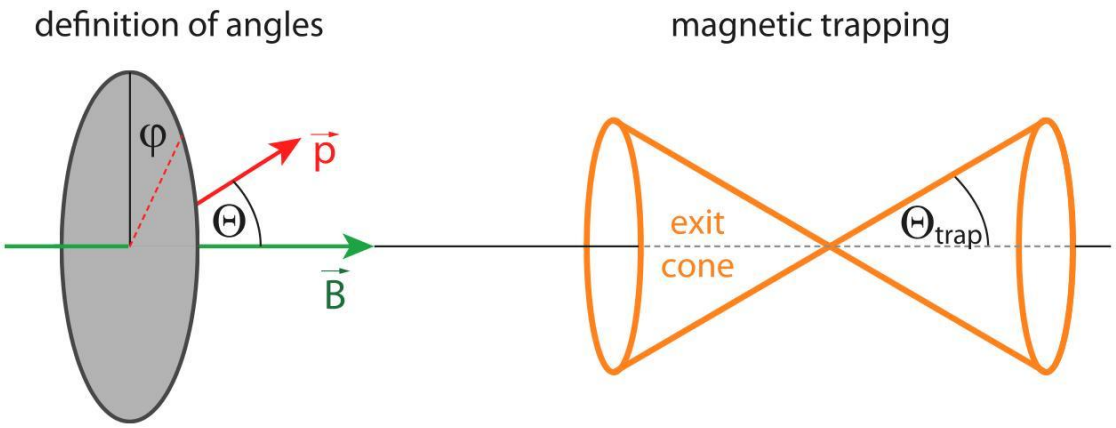

Figure 4.4: **left:** definition of angles, Θ is the polar angle between magnetic field and momentum vector, φ is the azimuthal angle around the magnetic field vector, **right:** schematic drawing of Θ_{trap} and the exit cone for magnetic trapping

maximum at the centre of each coil ($B_{1,max}$ at z_1, $B_{2,max}$ at z_2). The angle $\Theta_{1,2}$ of an charged particle, starting at a position between z_1 and z_2 in a magnetic field of B_0, at the position $z_{1,2}$ can be calculated with equation 4.2. If $\Theta_{1,2} < 90°$ the particle exits the region between z_1 and z_2, otherwise it is reflected. If reflections occur at both sides, the particle is trapped magnetically. The minimum angle Θ_{trap} (pitch angle) that is required for a particle in order to be trapped is defined as:

$$\Theta_{trap} = \arcsin\left(\sqrt{\frac{B_0}{B_{max}}}\right) \tag{4.3}$$

whereas B_{max} is the minimum of $B_{1,max}$ and $B_{2,max}$. This is graphically illustrated in figure 4.4. All particles with $\Theta < \Theta_{trap}$ leave the magnetic trap independent of the azimuthal angle φ. However, the trapping of particles in a magnetic trap is not stable on long time scales. Due to cyclotron radiation the particle loses transversal energy and thus Θ decreases until $\Theta < \Theta_{trap}$. In case the particle is trapped in a volume with finite pressure, it will also scatter on residual gas molecules and thus a change of Θ can occur. Also non-adiabatic motion could change Θ such that the particle leaves the trap.

4.2 Background of pre-spectrometer I setup (PS1)

This section describes the background characteristics of the initial pre-spectrometer test setup (PS1). In this configuration the detector chamber was equipped with a MCP detector (see section 3.3). Without the non-evaporable getter (NEG) pump a

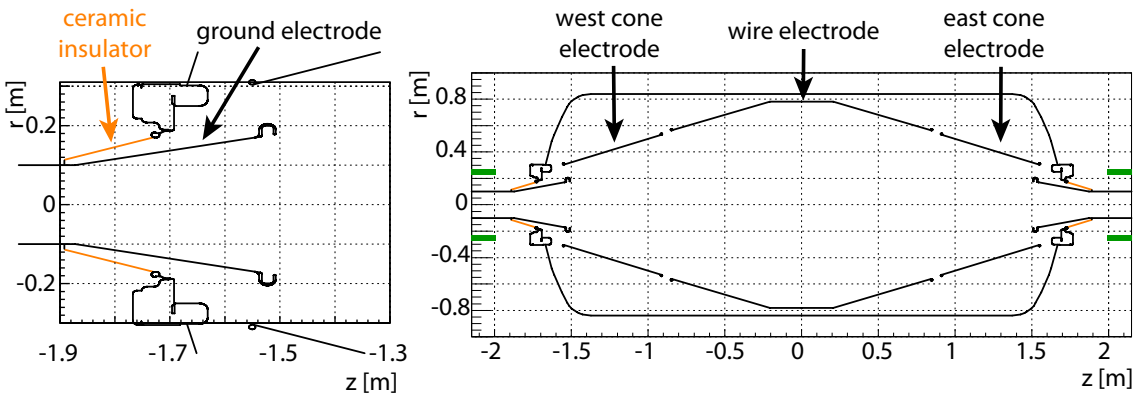

Figure 4.5: schematic of the initial pre-spectrometer test setup, the system is rotational symmetric but for better illustration it is mirrored at r = 0 m, **left:** region of the ground electrode, **right:** overall setup

rather moderate initial pressure in the region of 10^{-9} mbar was reached. A schematic drawing of the setup is shown in figure 4.5.

4.2.1 Measurements

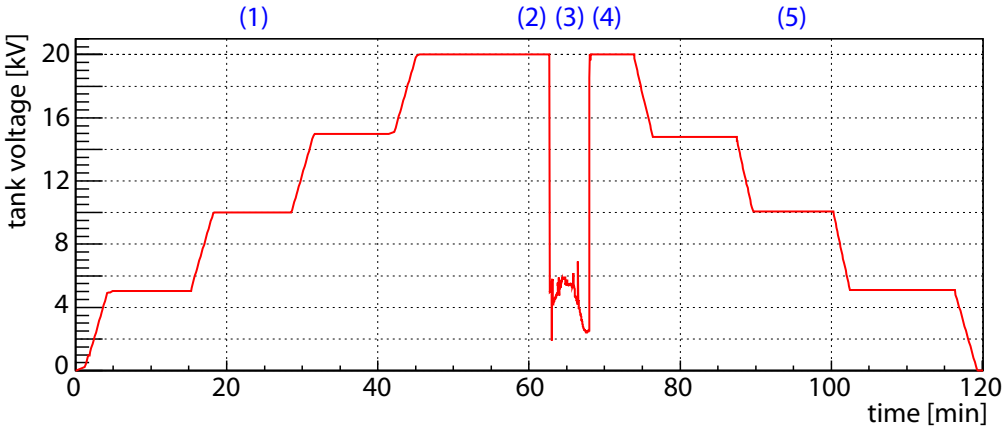

Figure 4.6: Tank high voltage during simultaneous operation of magnets. When the magnets reached 0.23 T (magnet current 8 A) a breakdown of the tank voltage with a concurrent increase of pressure ($3.5*10^{-9}$ to $1.7*10^{-6}$ mbar) was observed.

After completion of the major parts of the pre-spectrometer test setup the high voltage system and the magnets were successfully commissioned independently. Figure 4.6 shows the tank voltage during the first attempt to run high voltage (tank

and inner electrodes connected to the same power supply) and magnetic field simultaneously:

(1) The tank voltage was slowly ramped to -20 kV in 5 kV steps. At each step a check was performed whether the voltage is stable.

(2) In a second step, the ramping of both pre-spectrometer magnets from 0 T (0 A) to 0.23 T (8 A) was initiated.

(3) When the magnets reached $B = 0.23$ T, a sudden breakdown of the tank voltage was observed. This breakdown can be explained by a large increase of the pre-spectrometer conductivity[3]. This effect increases the current of the power supply until it reaches current limitation (1.6 mA) and therefore the voltage drops. At the same time a major increase of pressure (from $3.5*10^{-9}$ to $1.7*10^{-6}$ mbar) inside the pre-spectrometer was observed.

(4) After breakdown, both magnets were ramped down to 0 T (0 A), correspondingly, the breakdown of high voltage ends and the pressure normalizes.

(5) Ending the initial cycle, the tank voltage was ramped down to 0 kV in 5 kV steps.

The fact that the breakdown of high voltage is coincident with a pressure increase points to a process inside the spectrometer which increases the conductance of the pre-spectrometer in presence of a magnetic field. A viable explanation of this behaviour is the presence of a Penning trap in the region of the ground electrode. In case of a Penning discharge, (see section 4.1.2) a non-neutral plasma is created which significantly increases the conductance in the region of the Penning trap.

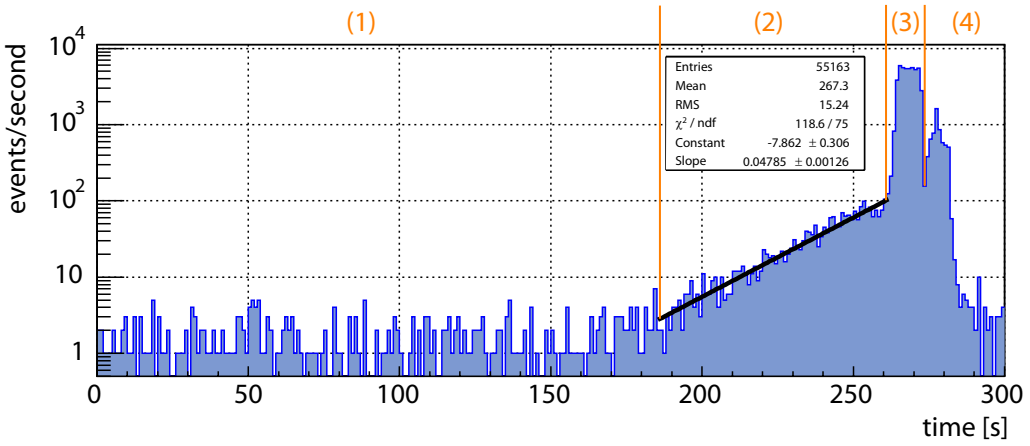

Figure 4.7: Rate at MCP detector for the configuration $U_{tank} = U_{wire} =$ -1.3 kV, $U_{cone} =$ -1.4 kV and symmetric magnetic field (0.29 T). The exponential increase in (2) is typical for a Penning discharge.

[3]This is the conductivity between pre-spectrometer tank and ground potential.

In order to investigate the initial hypothesis of a Penning trap further measurements involving the MCP detector were performed. Figure 4.7 shows the rate[4] at the detector for the following experimental configuration: symmetric magnetic field (0.29 T, 10 A), pre-spectrometer tank and wire electrode -1.3 kV, cone electrodes -1.4 kV. These parameters had been reached at the start of the run (0 s). The plot can be divided into four regions (1-4) which are characteristic for a Penning discharge:

(1) The rate is at the level of the intrinsic detector background for 180 s. Such a region is expected in case of a Penning discharge, because the initial electron is usually created in a statistical process such as natural radioactivity or via a cosmic ray induced event (see section 4.1.2).

(2) An exponential increase of the rate for a time interval of about 1 min is observed. This is due to the fact that the beginning Penning discharge follows a power law (see figure 4.2, equation 4.1).

(3) The rate increases now much faster (due to dead time effects of the electronics the maximum rate is limited to about 6 kHz). This can be attributed to the following process: The Penning discharge creates positive ions which hit the metal surface of the electrodes or tank wall. Due to the impact they release gas molecules which cover the metal surface. This causes a local increase in pressure and such boosts the Penning discharge.

(4) Tank and electrode potentials were ramped to 0 V and the Penning discharge stops.

Additional measurements at specific configurations of magnetic field and potential distributions of tank and inner electrodes were performed in order to investigate the properties of the Penning discharge in more detail. For more information see references [31], [50] and [95].

4.2.2 Simulations

In order to localize the region of the Penning trap within the pre-spectrometer, calculations of the magnetic field and electric potential inside the pre-spectrometer were performed [30], [95], [28]. Figure 4.8 shows the calculated electric potential[5] - for $U_{tank} = U_{wire} = U_{cone}$ = -18 kV and maximum magnetic field (4.5T, symmetric) - along five selected magnetic field lines (a-e) in the region of the ground electrode:

a This field line crosses the ground electrode three times. Between z = -1.66 and -1.54 m the potential increases from 0 up to 2.8 kV thus creating a Penning trap

[4] The MCP detector has essentially no energy resolution therefore the rates are given for the sum of all adc channels.

[5] Although the tank is on negative potential, the absolute values of the potential are shown. This makes it more intuitive to recognize a Penning trap for electrons as a dip in the potential along a magnetic field line.

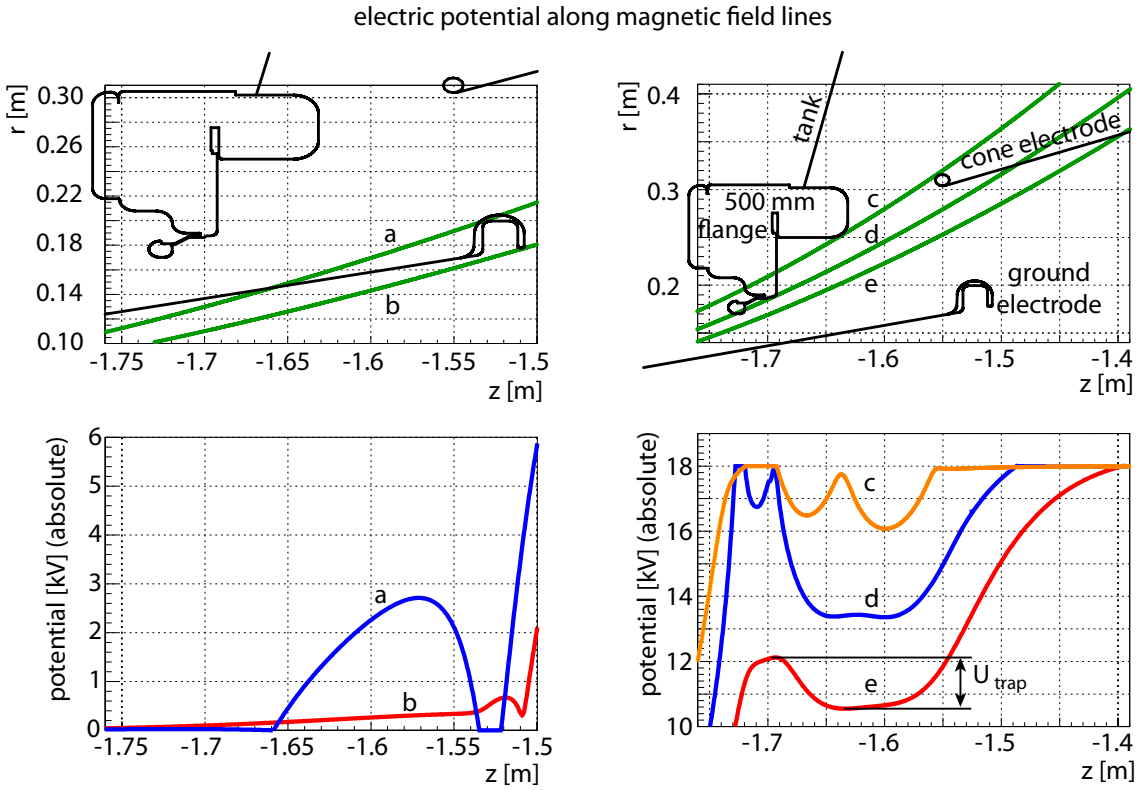

Figure 4.8: Electric potential along selected magnetic field lines in the region of the ground electrode. For a discussion of the different field lines see text.

for positively charged particles. Simulations of positive charged hydrogen ions (protons) at maximum magnetic field showed that the trapping is not stable in this region. After a short time (2 μs for a proton started at z = -1.57 m, r = 0.17 m), the ions leave the trap due to non adiabatic motion. Between z = -1.54 and -1.52 m the field line is within the ground electrode and thus the potential is zero. Further following the field line into positive z direction, the potential increases steeply towards the tank potential (18 kV).

b Along this field line two minor Penning traps (one for positively charged particles between z = -1.53 and -1.51 m and one for negatively charged particles around z = -1.51 m) are present. Compared to traps at other regions (e.g. **a**, **d**) they are orders of magnitude smaller in volume (the traps stretch 2π in azimuthal direction) and depth (U_{trap}) and therefore can be excluded to be the primary source of the observed Penning discharge.

c This field line stretches from the 500 mm flange to the cone electrode. Two Penning traps for negatively charged particles with a maximum depth of 2 kV are visible.

d Along this field line two Penning traps for negatively charged particles are visible. A relatively small (U_{trap} = 1.2 kV) trap is located between z = -1.72 and -1.7 m. Between z = -1.7 and -1.49 m a large (U_{trap} = 4.8 kV) Penning trap of cathode to cathode type is present.

e This field line is closer to the ground electrode as compared to line **d**. The potential around z = -1.7 m does not reach the value of the tank potential anymore and thus the depth of the large Penning trap already mentioned in **d** decreases (U_{trap} depends on the minimum of the electrostatic potential barrier)

As conclusion one can say that a large Penning trap ($U_{trap} \approx$ 5 kV) for negative charged particles (electrons) is present in the region between ground electrode, 500 mm flange and cone electrode. It is of the type "cathode to cathode" Penning trap. Therefore, a Penning discharge as described in section 4.1.2 could start in this region and produce the effects observed in the measurements (see section 4.2.1).

4.3 Background of pre-spectrometer II setup (PS2)

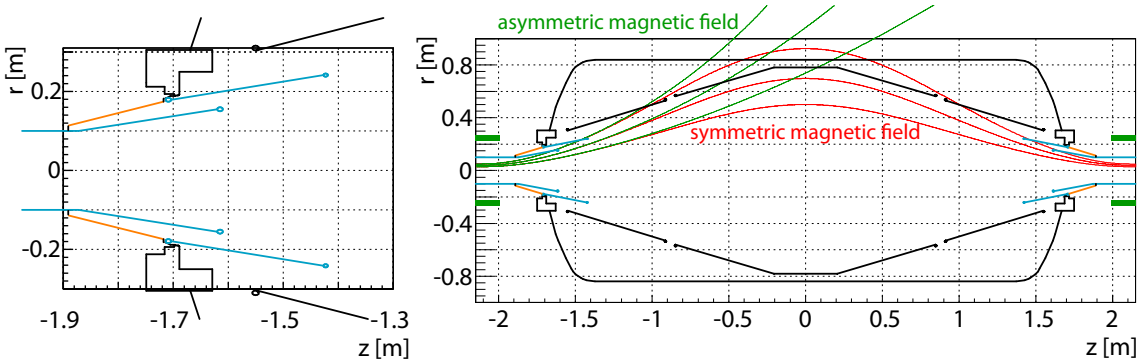

Figure 4.9: schematic drawing of the pre-spectrometer test setup after installation of the shielding electrodes and new ground electrodes (blue), the system is rotational symmetric but for better illustration it is mirrored at r = 0 m, **left:** region of the ground electrode, **right:** overall setup, the magnetic field lines for a symmetric magnetic field (east magnet = west magnet = 4.5 T) and an asymmetric magnetic field (east magnet = 0 T, west magnet 4.5 T) are shown

This setup has several major improvements compared to the previous one (see section 4.2):

- On each side of the pre-spectrometer a shielding electrode and a new ground electrode had been mounted in order to remove the previous Penning trap in the region of the 500 mm flange (see section 4.3.1).

- The detector chamber was equipped with a 64 pixel silicon detector (64PD) which provides both spatial resolution and energy resolution (see section 3.3).
- A NEG pump was installed and after bake-out a much lower pressure on the order of 10^{-11} mbar was achieved.

Figure 4.9 shows a schematic drawing of the pre-spectrometer test setup II (PS2).

4.3.1 Electrode design

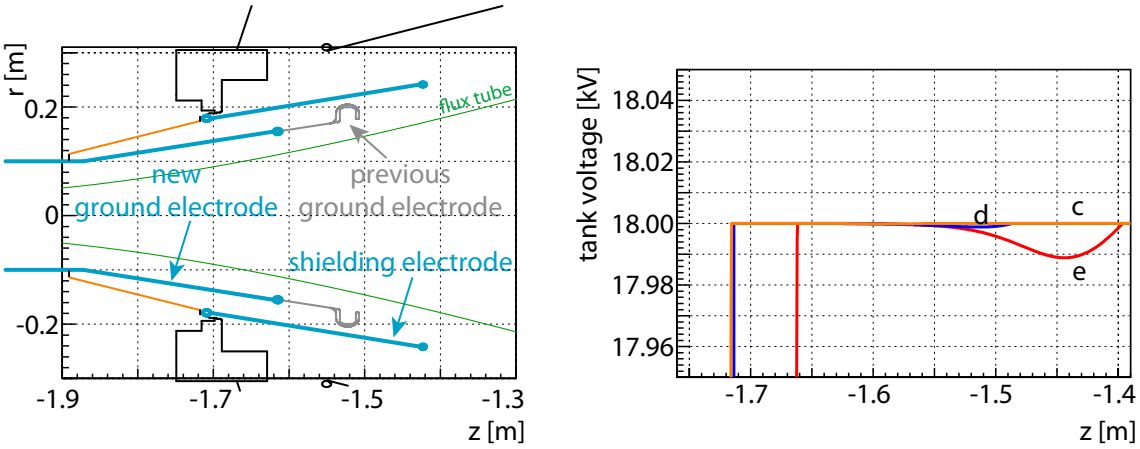

Figure 4.10: **left:** schematic drawing of new shielding electrode and modified ground electrode, for better comparison the previous ground electrode is also shown, **right:** potential along magnetic field lines (see right side of figure 4.8), only a 10 V deep Penning trap remains.

In order to remove the Penning trap described above (section 4.2.2) a set of two novel electrodes on each side of the pre-spectrometer was designed:

- **shielding electrode:** The influence of the ground electrode potential in the region of the 500 mm flange creates a Penning trap there. In order to remove it an additional electrode on tank potential - which shields the region of the 500 mm flange form the influence of the ground potential (and is therefore called shielding electrode[6]) - was designed (see figure 4.10). There are two constraints that had to be taken into account for the design of the electrode:
  - The electrode has to be mounted via the 500 mm flange from the outside of the pre-spectrometer and thus its diameter is not allowed to exceed this value.
  - For the neutrino mass measurements the pre-spectrometer needs to transport the complete flux tube of 191 T/cm^2. This limits the length of the electrode because it is not allowed to shadow the flux tube volume.

[6] In some references this electrode is also called Anti-Penning electrode.

- **new ground electrode:** The previous ground electrode would have been too close ($\approx$ 1 cm) to the shielding electrode, thereby creating electric field strengths much larger than 10 MV/m. This would have caused field emission as a major additional background source. Therefore a completely new ground electrode was designed that had to meet the following requirements:
  - The maximum electric field strength should not exceed the values of the previous setup (1.1 MV/m at 500 mm flange[7], 0.53 MV/m ground electrode [30]).
  - The distance to the flux tube boundary has to be larger than 1 cm.
  - The transmission conditions have to be fulfilled, especially an early retardation should be avoided (for a detailed description of the transmission characteristics see chapter 7).

  The final design is a well-balanced compromise of meeting these requirements. The maximum field strength at the shielding electrode (cathode) is 0.97 MV/m [30] and the distance to the flux tube is 1.7 cm [30].

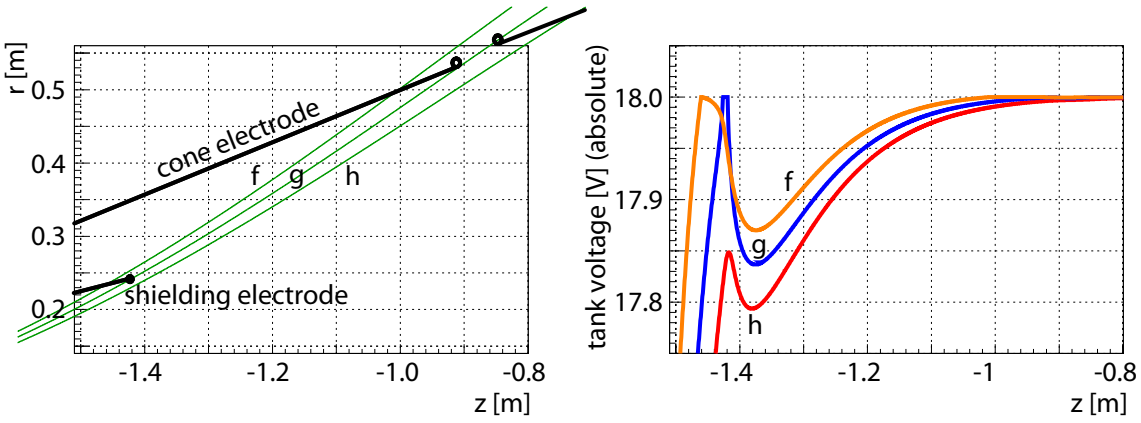

Figure 4.11: Electric potential along three selected magnetic field lines (f-h) in the region between the new shielding electrode and cone electrode for equal potential of tank and inner electrodes (-18 kV). A Penning trap for negative charged particles ($U_{trap} \approx 0.17$ kV) is present between z = -1.42 and -1.0 m. Its depth can be varied with U_{cone} and completely disappears for this potential configuration at U_{cone} = -18.5 kV.

Although the new electrodes were designed with the intention to completely remove Penning traps, it is possible to create a Penning trap in the region between the new shielding electrode and the cone electrode with an appropriate potential distribution. This trap has a depth of $U_{trap} = 0.17$ kV with all electrodes and tank at -18 kV. The depth can be fine tuned with U_{cone} and becomes 0 for $U_{cone} <$ -18.5 kV

[7] This is the more important value because field emission electrons are emitted from the cathode.

and so makes it an ideal test bed for the investigation of background created from Penning traps. Due to its position close to the cone electrodes the trap is called east/west trap.

4.3.2 Measurements

In order to investigate the merits of the new configuration after the installation of shielding electrode and new ground electrode, in particular with regard to preventing a major Penning discharge inside the pre-spectrometer, a measurement at symmetric magnetic field (2.3 T, 80 A) and a potential of -25 kV (tank and inner electrodes) was performed [33]. No increase in pressure or leakage current (see figure 4.6) was observed and thus it can be concluded that the new electrodes work as intended. As no strong Penning discharge is expected anymore, all further background measurements were performed with the 64PD.

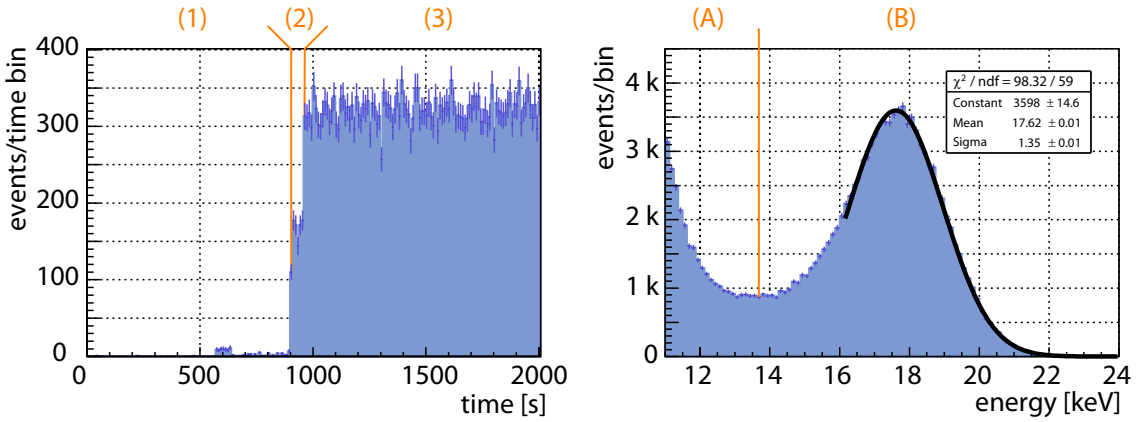

Figure 4.12: **left:** typical two stage ignition of "high B-field background", each histogram bin has a width of 10 s, **right:** typical energy spectrum after ignition

Figure 4.12 shows the event rate at the detector for the measurement configuration B_{max} = 3.4 T and $U_{tank} = U_{wire} = U_{cone}$ = -18 kV. Prior to this measurement the high voltage was ramped to -18 kV and the magnet current was increased from 1 A to 120 A (3.4 T). At t = 0 s the magnets reached the set point of 120 A. Within the first 900 s (1) the rate is at the level of 100 mHz. In (2) the rate increases to 15 Hz and after about 60 s a further increase to about 30 Hz (3) is observed. The rate within region (3) (R_{HBB}) is stable until the end of the measurement. The right side of figure 4.12 shows the energy spectrum for (3). A peak around U_{tank} (B) is clearly visible. Another feature of the spectrum is a tail[8] towards lower

[8]This tail is not due to detector noise. Measurements at larger pre-spectrometer potential (U_{tank} < -24 kV) showed that the low energy tail is part of a negative ion peak [50].

energies (A). In order to investigate this background many measurements at different parameters for magnetic field, pressure, electric potential and electrode configuration were performed. A detailed description of these measurements can be found in [50]. Below, the results are summarized:

1. The background only appears above a magnetic field of $B \approx 2$ T (≈ 7 mT at analyzing plane). Due to this behavior it is also called "high B-field background" (HBB).
2. For magnetic fields of $B > 3.5$ T R_{HBB} is independent of B (within 10%).
3. A strong dependence of HBB on U_{tank} is observed. Changing U_{tank} from -4 kV to -18 kV increases R_{HBB} about two orders of magnitude [57].
4. HBB is independent of east/west trap (see figure 4.11) [24].
5. Electric dipole fields have no effect on HBB [20].
6. R_{HBB} increases towards larger flux tube radii.
7. There is a strong correlation between R_{HBB} and the pressure p inside the pre-spectrometer ($R_{HBB} \propto p$, see [26]).
8. R_{HBB} is stable on long time scales (>16 h, see [22]).
9. The events of R_{HBB} are distributed randomly in time (no correlated events) [22].
10. HBB emits photons [39].
11. HBB emits negative ions (H^-) [23].
12. HBB is also present with asymmetric magnetic field configuration (west magnet 4.5 T, east magnet 0 T) [22] .

The characteristics of the background described above can be explained with the hypothesis of trapped particles. A trapped particle can ionize residual gas molecules (if it has sufficient energy) and thus creates more particles. This process depends linear on the pressure[9] as it is observed in item 7. Inelastic scattering on residual gas molecules can create an excited state of an atom and therefore photons are created. This is observed in item 10.

The complete pre-spectrometer - if operated at high voltage and high magnetic field - is a huge Penning trap (ion trap) for positive ions with $U_{trap} \approx |U_{tank}|$. A discharge of this trap could be a possible explanation of HBB. An argument in favour of this hypothesis is item 1. Because of the large cyclotron radius of protons ($r_c \approx 0.3$ m at the analyzing plane for maximum magnetic field), a high magnetic field is needed to provide stable storage conditions for ions with energies in the keV region. Simulations showed that hydrogen ions (protons) up to an energy of about 2.5 keV [21] can be stored in the pre-spectrometer at maximum magnetic

[9] As long as the mean free path is larger than the characteristic dimensions of the pre-spectrometer.

field (4.5 T). Anyhow, an electric dipole field should be able to remove the ions and thus stop the discharge. According to item 5 this is not observed. In addition, the magnetic field configuration of item 12 removes the storage conditions but HBB is still observed. Therefore item 5 and item 12 rule out a discharge of the ion trap as a possible source for HBB. In order to detect other possible storage conditions, detailed simulations had been performed.

4.3.3 Simulations

Measurements of the high B-field background (see above) showed that the background is caused of trapped particles. The east/west trap as well as the ion trap could be excluded as possible sources of the background. Measurements with asymmetric magnetic[10] field point out that the source of the background is in the region of the ground electrode. The identification of the background source is of high importance for the KATRIN experiment because the main spectrometer geometry in the entrance region is comparable to the one of the pre-spectrometer and thus the same background effects (HBB) could occur.

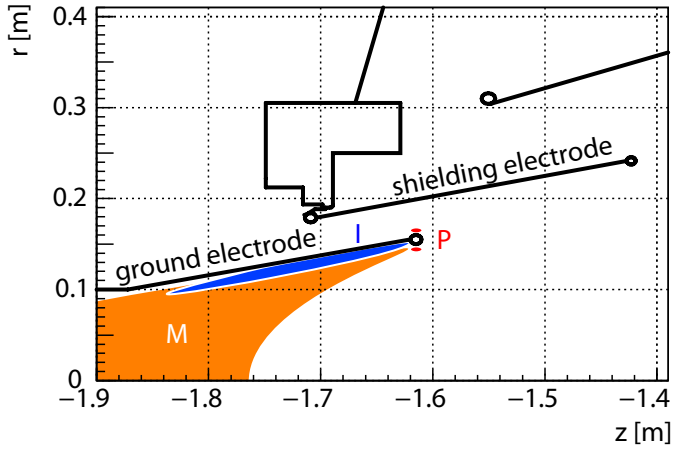

Figure 4.13: Three different storage conditions as possible sources of HBB, **P**: two Penning traps for negatively charged particles, **I**: storage condition for positively charged particles, **M**: storage condition for negatively charged particles

Until now storage conditions were identified as dips in the potential along magnetic field lines. In order to determine the source of HBB a more general approach was used. In a Monte Carlo (MC) simulation, electrons ($>10^6$) and protons ($>10^5$) were started randomly in the volume of the pre-spectrometer. Their tracks were calculated with a modified version of the tracking program traj [95]. If the track

[10] For a comparison of asymmetric and symmetric magnetic field at the pre-spectrometer see figure 4.11.

length exceeded 10 m (about three times the length of the pre-spectrometer) the particle was assumed to be trapped. The simulation was performed with equal potential of tank and inner electrodes of -18 kV for three different magnetic field settings (west magnet 1.7, 3.2 and 4.5 T, east magnet 0 T). As a result of the simulation three different storage conditions could be identified (see figure 4.13) which are discussed in detail below.

Penning traps (inner/outer ring trap)

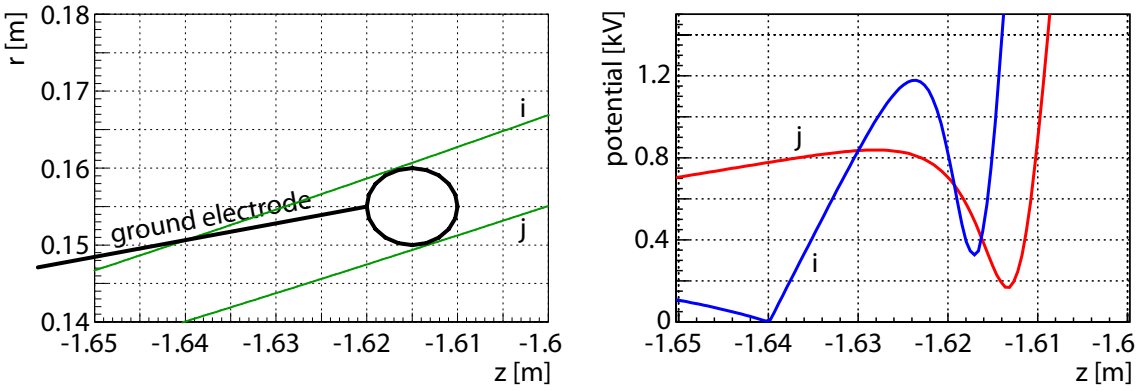

Figure 4.14: Electric potential along two selected magnetic field lines (i, j) at the end ring of the ground electrode. Along each field line a Penning trap is present (i: $U_{trap} = 0.9$ kV, j: $U_{trap} = 0.6$ kV).

There are two[11] Penning traps present at the end ring of the ground electrode (see figure 4.14). According to their position relative to the end ring they are called inner ring trap (j) and outer ring trap (i). These traps are created due to the influence of the end ring potential on nearby magnetic field lines. Their volume is on the order of 10 cm^3 which is about three orders of magnitude less compared to the Penning trap that caused the large discharge described in section 4.2.1. In addition, U_{trap} is more than a factor of 5 smaller.

The fact that both ring traps are of vacuum to vacuum type (see right side of figure 4.1) makes it more unlikely to create a self-sustained Penning discharge because a positive feedback mechanism is needed to inject electrons into the volume of the trap. Unlike the case of a cathode to cathode Penning trap where positive ions create a positive feedback, positive ions created in the ring traps are accelerated towards the shielding electrode, where they produce secondary electrons. However,

[11] The one at smaller radius was detected directly from the MC simulation, the other one was discovered after more detailed simulations of this region [68].

these electrons follow the magnetic field lines and do not go to the volume of the Penning traps[12].

Ground electrode ion trap

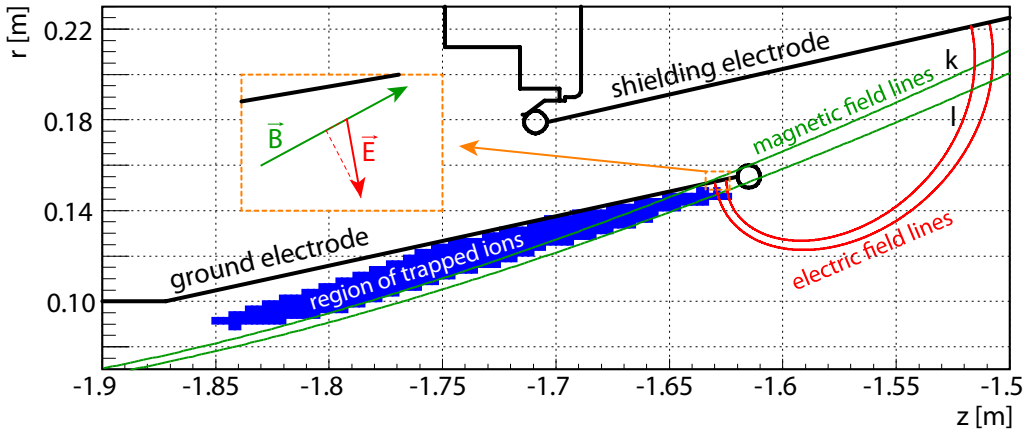

Figure 4.15: Storage condition for positive ions. On the left side ions are confined due to more positive potential. On the right side ions are confined of an electric field component along magnetic field lines.

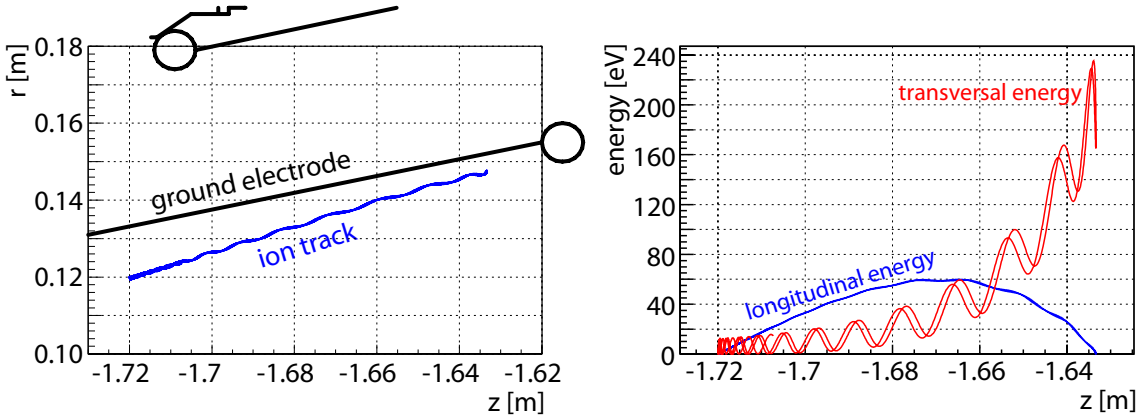

Figure 4.16: **left:** Track of a trapped ion started at z = -1.72 and r = 0.12 m, **right:** Longitudinal and transversal energy component along the track of the trapped ion.

Figure 4.15 shows a storage volume for positively charged particles (protons). Due to the potential gradient in the volume bordered of the ground electrode (along the z-axis the potential changes from -30 V (z = -1.9 m) to -6 kV (z = -1.61 m)) a Penning

[12]Even if they do, their energy is too large to be trapped.

trap along magnetic field lines (e.g. k, l) close to the ground electrode is created. Towards smaller z values the potential increases because the influence of the tank potential becomes smaller. In the other direction the potential first decreases, but as the field lines get close to the ground electrode it increases again. Anyhow, due to the potential gradient and the large mass of a proton (compared to an electron) it can not be expected that the proton follows exactly a magnetic field line. A microscopic tracking of protons in the expected trapping region is needed in order to see whether the trapping conditions are stable. The left side of figure 4.16 shows the track of a proton - started at z = -1.72 and r = 0.12 m - within the expected region of trapped ions. On the right side the transversal (E_t) and longitudinal (E_l) energy components along the track are shown. The large fluctuation of the transversal energy component is due to the potential gradient within one cyclotron step. The total energy (E_l + E_t) is maximum close to the reversal point at $z \approx$ -1.63 m (or the electric potential along the track is minimal). In order to understand why the proton turns around at (almost) minimal potential (and does not follow the potential gradient further) let's have a closer look at the magnetic and electric fields at the reversal point (see figure 4.15). The angle between z-axis and magnetic field ($\vec{B}$) is larger than the angle between ground electrode and z-axis. The electric field ($\vec{E}$) close to the ground electrode is almost perpendicular to the ground electrode and thus it has an component along $\vec{B}$, pointing to smaller z values. This component reduces E_l (see figure 4.16) until the proton turns around.

In order to create a discharge of this trap a positive feedback mechanism is needed. For this special configuration it could look like this: A trapped ion could ionize a residual gas molecule. The released electron follows the magnetic field line and hits the ground electrode where it could create a positive ion via ionization of a gas molecule on the surface of the electrode. This ion is accelerated by the electric field and trapped inside the ion trap. However, for this mechanism it needs to be considered that charge transfer processes[13] ($p + H \rightarrow H + p$) are much more likely than ionization. For protons with energies $<$ 3 keV the cross section for charge transfer is more than 2 orders of magnitude larger than the one for ionization [36]. In case of a Penning trap (e.g. the pre-spectrometer ion trap, see section 4.3.2) the trapped protons lose most of their energy - without creating other charged particles - due to charge exchange processes and end up in the region of the potential minimum with energies too low for ionization. For the ground electrode ion trap this is different. If a low energetic positive ion inside the trapping volume is created it gains energy due to the potential gradient. Simulations showed that trapped protons are able to regain energies up to several hundred eV if their energies are randomly set to zero[14]. The regain of energy is connected to a drift of the protons and thus to a change of the trapping volume. The simulations also showed that protons can regain energy up to 40 times before they leave the trap.

[13] In charge transfer processes the incident proton keeps most of its energy and thus becomes a fast neutral particle after charge transfer.

[14] This imitates a charge transfer process.

MAC-E filter trap

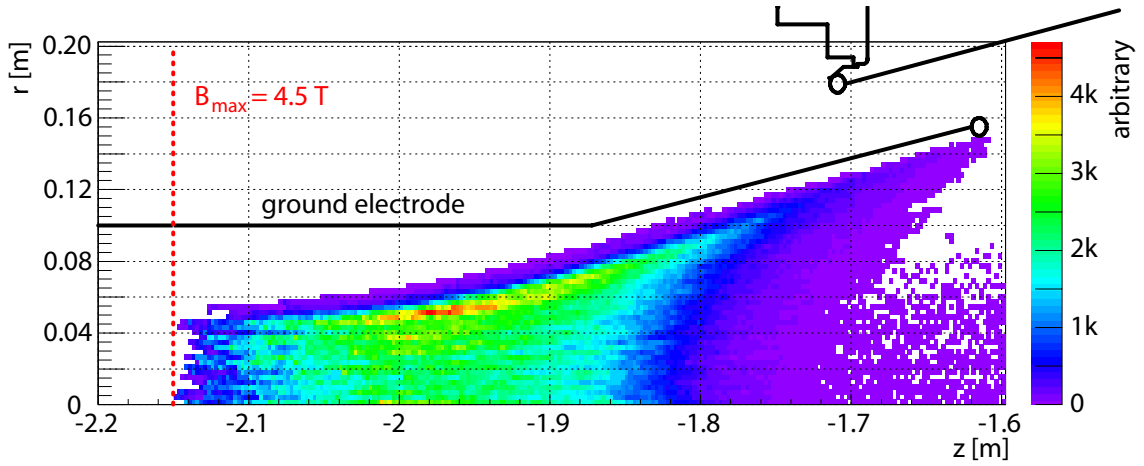

Figure 4.17: Region of trapped electrons (maximum start energy 320 eV). A superposition of tracks of trapped electrons is shown. This can be seen as the probability to find a trapped electron at a given position.

Figure 4.17 shows the storage region of electrons (start energy up to 320 eV) started inside the ground electrode. Towards larger values of z they are reflected of the increasing electric potential. Towards smaller z values they are reflected due to magnetic mirror effect of the increasing magnetic field (see section 4.1.3). This kind of trap is an intrinsic feature of MAC-E filters and thus can not be avoided. The storage probability for electrons in this trap increases with the start energy of the electrons. Due to the potential gradient in z direction electrons gain a fixed amount of longitudinal energy (depending on their start position). This decreases Θ and if $\Theta < \Theta_{trap}$ the electron is not trapped. For larger start energies the relative change of Θ becomes smaller and thus the trapping probability increases.

The MAC-E filter trap is of vacuum to vacuum type. For any positive feedback mechanism electrons need to be created inside the volume of the trap. Electrons from the ground electrode can not enter the region of the trap due to effective magnetic shielding (B at the z-position of the end ring is 0.44 T for $B_{max} = 4.5$ T) and a more negative potential inside the ground electrode. Electrons created inside the pre-spectrometer ($|z| < 1.6$ m) are either trapped magnetically around the analyzing plane (see section 5.2.1) or accelerated of the tank potential such that $\Theta < \Theta_{trap}$ (the chance that such an electron scatters on residual gas molecules and thus changes Θ in a way that it is trapped is smaller 10^{-8} for a pressure of 10^{-10} mbar). The only remaining process is ionization of residual gas molecules by ions or photons, but there is no positive feedback of electrons that leave the trap on the ground potential side and the creation of a sufficient number of ions or photons.

Conclusion

Simulations described above revealed three possible storage conditions for charged particles as potential sources of the high B-field background. Although the discharge of each storage condition seems to be unlikely if considered separately there is an overlap of different storage conditions (e.g. ground electrode ion trap and MAC-E filter trap). This could give rise to more complicated feedback mechanisms and thus trigger a discharge.

4.4 Background of pre-spectrometer III setup (PS3)

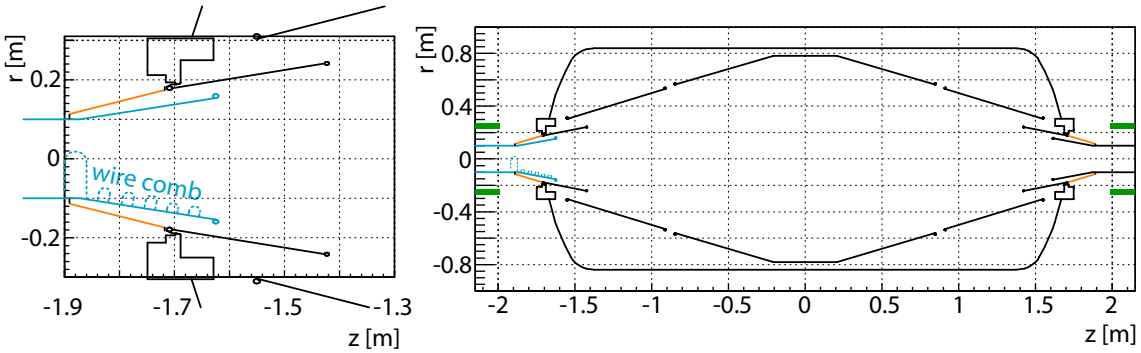

Figure 4.18: schematic drawing of the pre-spectrometer test setup after installation of modified ground electrode including a wire comb (blue) on the west (detector) side of the system, the system (except the wire comb) is rotational symmetric but for better illustration it is mirrored at r = 0 m, left: region of the ground electrode on the west side of the system, right: overall setup

This setup is intended to determine the source of the high B-field background observed at the previous setup (see section 4.3). On the west (detector) side a modified ground electrode (see section 4.4.1) including a wire comb was installed, otherwise the test setup remained unchanged. Figure 4.18 shows a schematic drawing of the pre-spectrometer test setup III (PS3).

4.4.1 Electrode design

In order to identify the storage condition responsible for the high B-field background experimentally, the ground electrode on the west (detector) side[15] was slightly mod-

[15]The HBB is also present at asymmetric magnetic field, therefore it is sufficient for measurements to exchange only one side.

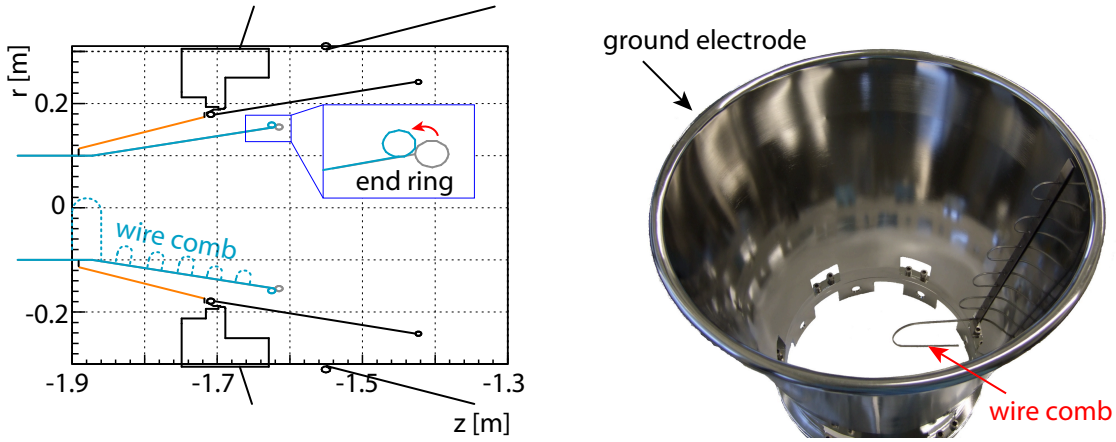

Figure 4.19: modified ground electrode and wire comb, the end ring of the ground electrode was shifted in order to reduce the number of Penning traps in this region

ified. The end ring was shifted in a way that the inner ring trap disappears but at the same time the outer ring trap is enlarged (U_{trap} = 2.4 kV after modification). In addition, a "wire comb" was manufactured and installed. The wire comb consists of six U-shaped metal strips (width: 2 mm, thickness: 1 mm) [27] and is attached to the ground electrode. The largest U-strip is intended to break the storage conditions of the MAC-E filter trap. It is placed at a position where most of the trapped electrons are expected (see figure 4.17). Due to magnetron drift these electrons rotate in azimuthal direction with frequencies $>$ 1 kHz and thus hit the wire comb (and hence are removed from the trap) after $<$ 1 ms. The smaller U-strips are intended to disturb the storage conditions of the ground electrode ion trap. The idea is that the electric field inside the ground electrode is enhanced close to the U-strips. The non-adiabatic motion of ions in this region[16] could weaken the storage conditions.

4.4.2 Measurements

Figure 4.20 shows energy spectra and event rates of pre-spectrometer II and III setup for identical measurement parameters[17] (west magnet 4.5 T, east magnet 0 T, U_{tank} = -18 kV, $U_{cone,west}$ = U_{wire} = -18.5 kV, $U_{cone,east}$ = -17.5 kV). The rate increased about two orders of magnitude from 26 Hz to 6.7 kHz. The PS2 energy spectra shows the typical HBB features, a peak at U_{tank} and a low energy tail (presumably due to negative ions). The PS3 energy spectra is dominated of a non

[16] The U-strips are on ground potential therefore positive ions are not able to hit them as it is the case for electrons.

[17] The more negative potential of $U_{cone,west}$ and U_{wire} compared to U_{tank} and $U_{cone,east}$ prevents low-energy electrons - created at the cone electrode or shielding electrode at the east side of the pre-spectrometer - from reaching the detector.

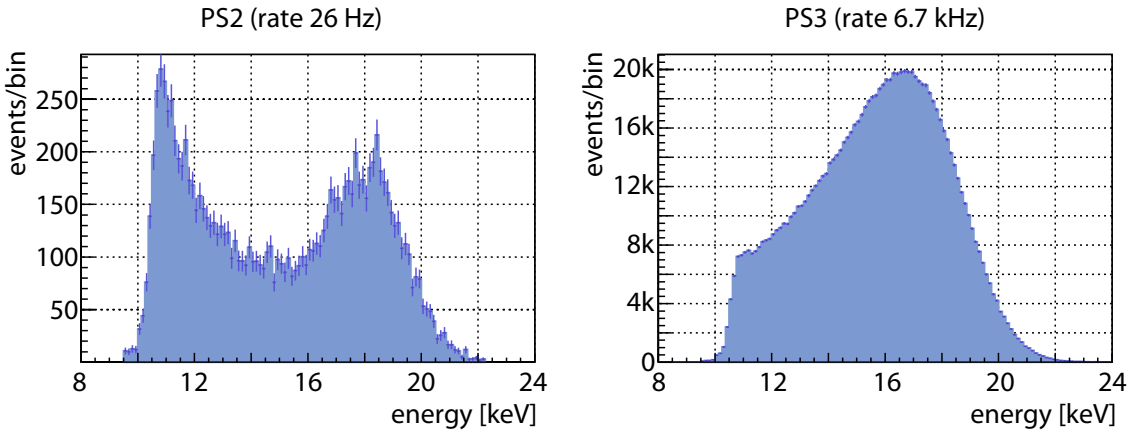

Figure 4.20: energy spectra of high B-field background for PS2 (left, Run 887) and PS3 (right, Run 902) for identical experimental parameters: asymmetric magnetic field (west magnet 4.5 T, east magnet 0 T), U_{tank} = -18 kV, $U_{cone,west} = U_{wire}$ = -18.5 kV, $U_{cone,east}$ = -17.5 kV

Gaussian peak at 17 keV. In order to investigate the PS3 background, further measurements at different parameters for magnetic field, pressure, electric potential and electrode configuration were performed. A detailed description of these measurements is available in [63]. The results are summarized below:

1. The background only appears above a magnetic field of $B \approx 1.7$ T (≈ 6 mT at analyzing plane).
2. For magnetic fields of $B > 3.5$ T the background rate R_{BG} is independent of B (within 10%).
3. R_{BG} is independent of U_{tank} for $|U_{tank}| > 22$ kV and $B_{max,west} = 4.5$ T. For lower magnetic fields ($B_{max,west} = 2.0$ T) a decrease in rate (more than a factor of 2 when changing U_{tank} from -18 to -30 kV) is observed.
4. R_{BG} is independent of east/west trap (see figure 4.11).
5. R_{BG} increases towards larger flux tube radii.
6. There is a strong correlation between R_{BG} and the pressure p inside the pre-spectrometer ($R_{BG} \propto p^2$).
7. The events of R_{BG} are distributed randomly in time.
8. The background process emits negative ions (H^-).

The background characteristics are very similar to the ones observed at the PS2 setup (see section 4.3.2) and therefore it is concluded that the same background process is responsible for the observed background at this setup. The modified ground electrode and the wire comb removed the storage conditions for the MAC-E filter trap and the inner ring trap. Because HBB is still present, these storage

conditions are excluded as possible sources. The outer ring trap and the ground electrode ion trap remain as possible sources. The ground electrode modification increased the depth (U_{trap}) of the outer ring trap by a factor of about 3. The strength of a Penning discharge is expected to follow a power law depending on U_{trap} (see equation 4.1). Because the observed rate increased two orders of magnitude after the modification of the ground electrode the outer ring trap is most likely the source of the high B-field background.

4.5 Background of pre-spectrometer IV setup (PS4)

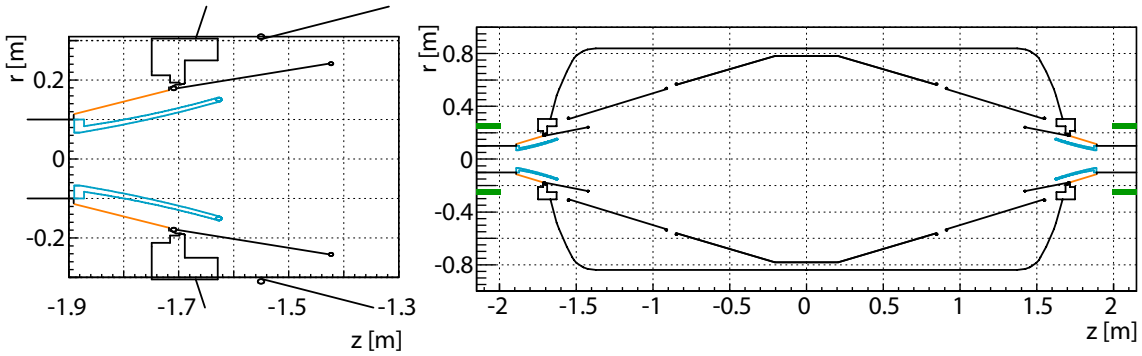

Figure 4.21: schematic drawing of the pre-spectrometer test setup after installation of aluminium ground electrodes (blue) on both sides of the system, the system is rotational symmetric, but for better illustration it is mirrored at r = 0 m, left: region of the ground electrode, right: overall setup

Figure 4.21 shows a schematic drawing of the pre-spectrometer test setup IV (PS4). On each side an aluminium ground electrode (see section 4.5.1) was installed in order to remove all storage conditions for electrically charged particles in this region. In addition, a small Penning trap at the end ring of the shielding electrode (z = -1.7 m) [53] was removed with the installation of an additional metal sheet at this region. Otherwise, there are no essential changes compared to the pre-spectrometer III setup.

4.5.1 Electrode design

In order to remove all storage conditions for trapped particles at the ground electrode (see section 4.3.3), a new pair of ground electrodes was designed. The design has to meet the following requirements:

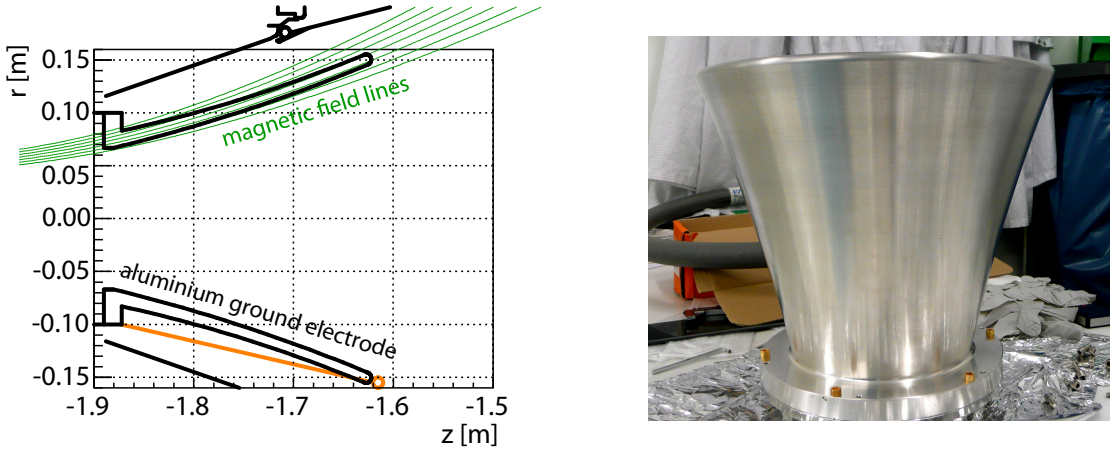

Figure 4.22: The aluminium ground electrode is designed to follow the magnetic field lines and thus avoids any storage conditions (except the MAC-E filter trap) for charged particles. The ground electrode was manufactured at KATRIN collaboration member University of Münster.

- The maximum electric field strength should not exceed the values of the PS1 setup (1.1 MV/m at 500 mm flange, 0.53 MV/m ground electrode [30]).
- The distance to the flux tube boundary has to be larger than 1 cm.
- Storage conditions (except the MAC-E filter trap) for electrically charged particles have to be avoided.

Figure 4.22 shows the design of the new ground electrode. Its shape is designed to follow the magnetic field lines. The angle between the inner side (smaller r) of the electrode and the z-axis (α_{el}) is larger than the angle between magnetic field line and z-axis (α_{mag}) for any z value between -1.88 and -1.63 m. Thus the ground electrode ion trap is avoided completely. The angle α_{el} is smaller than α_{mag} at the outer side (larger r) of the ground electrode for any z value between -1.87 and -1.63 m. Thus the potential along the magnetic field lines from the outer side of the ground electrode to the shielding electrode is monotonic decreasing and Penning traps are avoided. The radius at the end of the ground electrode ($z \approx$ -1.63 m) is 5 mm. This avoids a too strong (>0.5 MV/m) electric field in this region. In addition, a small Penning trap ($U_{trap} < 0.6$ kV, volume in the order of 10 cm^2) at the end ring of the shielding electrode [53] ($z =$ -1.7 m) was removed with the installation of an additional metal sheet at this region[18].

[18] An even smaller Penning trap between the insulator (volume in the order of 1 cm^2, $U_{trap} < 0.2$ kV [46]) still remains.

4.5.2 Measurements

Measurements at maximum magnetic field (B_{max} = 4.5 T) and the potential configuration U_{tank} = -18 kV, U_{wire} = U_{cone} = -18.5 kV, at a pressure of 10^{-10} mbar resulted in an average background rate - originating from the pre-spectrometer - of 17 ± 0.4 mHz in the energy window 15 to 21 keV and the observed fraction of the flux tube (28.5%). At identical measurement parameters this is five orders of magnitude less than the average background rate of the pre-spectrometer II setup (if the high B-field background had ignited) and more than seven orders of magnitude less compared to the pre-spectrometer III setup. The characteristics of the remaining background (for a detailed description see chapter 5) shows no evidence that the background is caused by a Penning discharge.

4.6 Conclusion

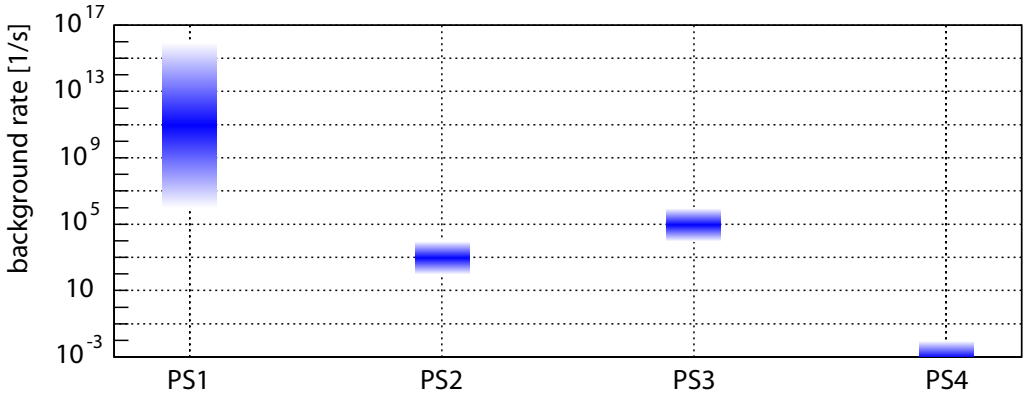

Figure 4.23: pre-spectrometer background rate for the setups PS1 to PS4. For PS1 only a lower limit (MCP measurement) and an upper limit (leakage current limitation of high voltage power supply, 1.6 mA correspond to 10^{16} ionizations/second) could be determined. The optimization of the electrode system on the mm scale could reduce the background rate many orders of magnitude to values < 10 mHz for PS4

Figure 4.23 summarizes the order of magnitude of the pre-spectrometer background rate for the four different setups. The Penning discharge of a large Penning trap (U_{trap} = 5 kV, volume ≈ 10 l) at the pre-spectrometer I setup caused a breakdown of the tank high voltage and a background rate far beyond (>6 kHz) the limits of the data acquisition system. This Penning trap could be removed with the installation of an additional electrode (shielding electrode) and a new ground electrode. The modified setup (PS2) showed a characteristic background behaviour (high B-field background, background rate in the order of kHz) that only appeared above

$B_{max} = 2$ T. Measurements showed that this background is due to trapped particles and could trace back its origin to the region of the ground electrode. Extensive simulations of this region revealed four possible storage conditions for electrons and positive ions. Measurements with a modified pre-spectrometer setup (PS3) - which removed two of the storage conditions - showed that the high B-field background is most likely caused by a small Penning trap ($U_{trap} = 0.9$ kV, volume ≈ 10 cm^2) at the end ring of the ground electrode. A new ground electrode - made of aluminium - removed all storage conditions and after installation at the pre-spectrometer (PS4) the background rate was in the order of 10 mHz with no evidence that the remaining background is caused by a Penning discharge.

The measurements showed that discharges as a result of the presence of storage conditions for charged particles are a major background source in the pre-spectrometer and thus have to be avoided. This requires a careful design, precise manufacturing and accurate mounting of the electrodes on a mm level, especially at the entrance region of the spectrometer where strong magnetic and electric fields are present. Small deviations of the optimal electrode shape could increase the background rate several orders of magnitude. The experience gained from the pre-spectrometer have yielded important constraints and guiding principles for the design of the main spectrometer electrodes in the region of the ground electrode.

5 Pre-spectrometer Radon background measurements

This chapter describes the background characteristics of the KATRIN pre-spectrometer after the installation of the aluminium ground electrodes (see section 4.5.1). The first section 5.1 describes the NEG pump installed in the pre-spectrometer which could be a possible background source due to the emanation of ^{219}Rn. Afterwards (5.2) the behaviour of high energetic (order of 100 keV) trapped electrons inside the pre-spectrometer is discussed on the basis of simulations. Due to the fact that the background event rate of the pre-spectrometer is at the same level as the intrinsic detector background, a dedicated section (5.3) describes the nature of the detector background. The actual background measurements are presented in section 5.4 whereas the focus is on the measurements and not on their interpretation. Section 5.5 summarizes the results of the measurements and discusses several background models. After a check of their plausibility, a conclusive background model is presented.

5.1 ^{219}Rn emanation from NEG strips

In order to meet the vacuum requirements ($p < 10^{-11}$ mbar) for the KATRIN spectrometers the usage of non-evaporable getter (NEG) pumps is needed. The pre-spectrometer is equipped with 90 m (1.8 kg) of NEG strips of the type SAES ST707. This material consists of Zirconium (70%), Vanadium (24.6%) and Iron (5.4%) [84].

Prior to the installation into the pre-spectrometer, the specific activity of the getter material was measured. Figure 5.2 shows the ^{219}Rn activity of different getter samples. The material used for the pre-spectrometer is "standard (10/2001)". From that the ^{219}Rn activity during the low background measurement phase (end 2009 to beginning 2010) can be determined to about 8 Bq. For the main spectrometer the "low activity (07/2005)"[1] material will be used. Due to the large surface of the getter material (0.15 m^2/g [85], 270 m^2 total) and the fact that Rn is a noble gas, a considerable amount of ^{219}Rn could emanate and decay inside the volume of the pre-spectrometer. Figure 5.1 shows two microscopic photos (taken with a SEM[2]) of

[1] This material is identical to "low activity (07/2008)".
[2] **S**canning **E**lectron **M**icroscope

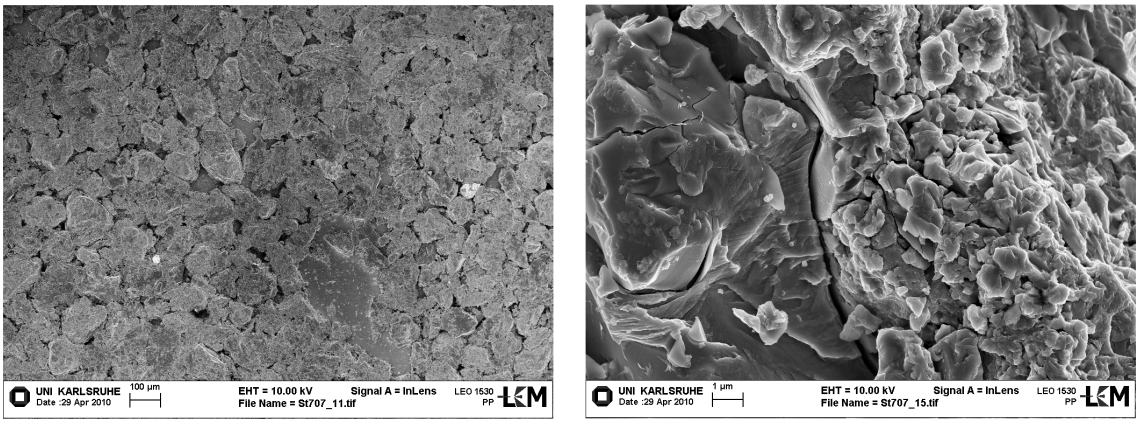

Figure 5.1: Microscopic pictures of the getter strips, **left**: grains of the getter material with a typical size of 100 μm are visible, **right**: close-up view of a getter grain

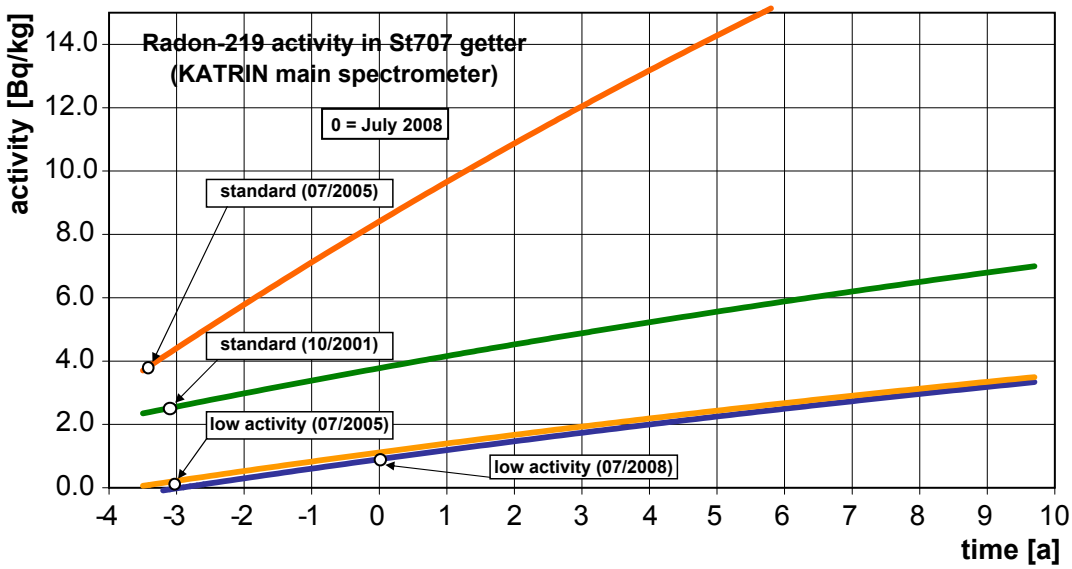

Figure 5.2: ^{219}Rn activity vs. time for different getter samples. One kg of getter corresponds to 50 m of St707 NEG strips. For the pre-spectrometer the "standard(10/2001)" material is used. The main spectrometer NEG pump will use the "low activity" material. Taken from [25]

the getter strips. On the left side grains of the getter material with a typical size of 100 μm are visible.

The activities shown in figure 5.2 increase over time. To understand this feature, the decay chain of ^{235}U needs to be considered (see figure 6.2). Protactinium (^{231}Pa) and Actinium (^{227}Ac) is produced within the decay chain. Due to the production process of the ST707 getter material most of the ^{227}Ac is removed and thus cuts off the short-lived (combined half-lives about 1 month) chain containing ^{219}Rn. Over time the α-decay of ^{231}Pa fills the reservoir of ^{227}Ac and thus increases the ^{219}Rn activity.

5.2 Simulations concerning Radon background processes

This section discusses the behaviour of electrons that could be created in radioactive decay processes (see section 6.3) inside the volume of the pre-spectrometer.

5.2.1 Storage of electrons in the pre-spectrometer

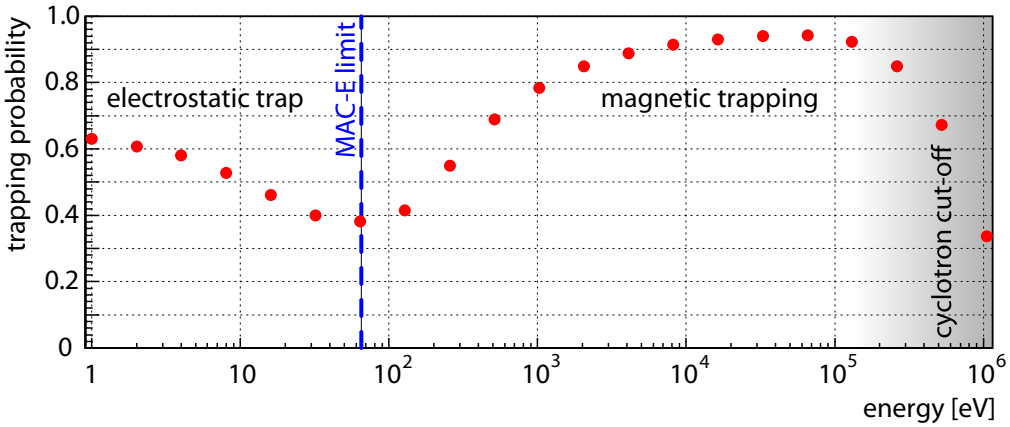

Figure 5.3: trapping probability (ratio between started and trapped electrons) for the pre-spectrometer configuration with maximum magnetic field (4.5 T), tank potential -18 kV and inner electrode potential -18.5 kV, for more details see text

Figure 5.3 shows the probability for an electron to be trapped inside the volume of the pre-spectrometer. For each energy 10^5 electrons had been started isotropically inside the pre-spectrometer flux tube volume with a random distribution of the start momentum vector. The tracks of the electrons were calculated and if they were

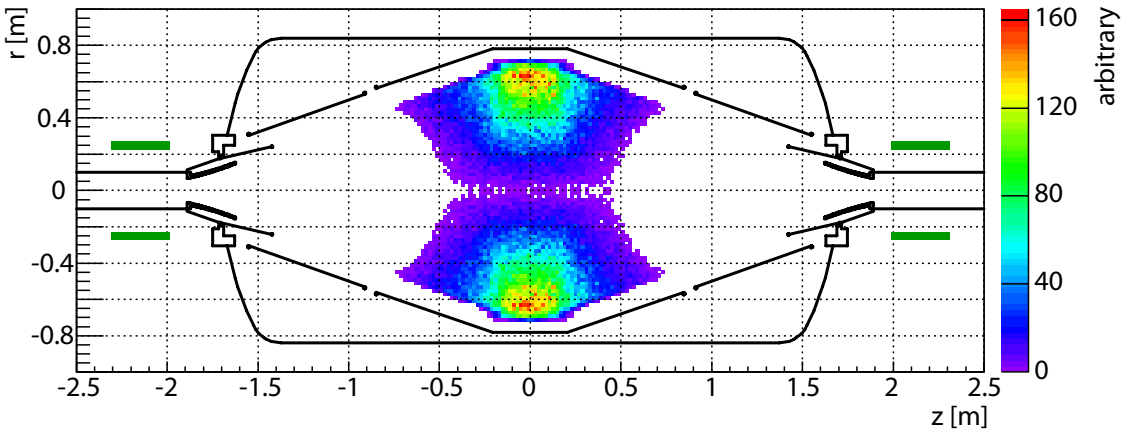

Figure 5.4: Region of trapped electrons with a start energy of 4 eV (electrostatic trap). 10^5 electrons were started isotropically in the volume of the pre-spectrometer with a random angular distribution (Θ, φ) and their track was calculated. If they were tracked for $>$ 20 m (about 6 times the length of the pre-spectrometer) they were assumed to be trapped. The plot shows the end position of such electrons which corresponds to the trapping volume. For better illustration the distribution was mirrored at r = 0 m.

tracked for $>$ 20 m[3] (about 6 times the length of the pre-spectrometer) they were assumed to be trapped. For this simulation the same electromagnetic settings (tank potential: -18 kV, inner electrode potential: -18.5 kV, maximum magnetic field of the pre-spectrometer magnets B_{max} = 4.5 T) as for the background measurements (see section 5.4) were used.

The trapping probability shows different features:

- **electrostatic trap**: The wire electrode is not able to shield the 500 V more positive tank potential completely and thus the potential in the centre region (around the analyzing plane) increases compared to the potential created of the full metal cone electrodes (which are able to shield the tank potential more effectively). This configuration creates a Penning trap for electrons in the centre part of the pre-spectrometer which is U_{trap} = 4 V deep for r = z = 0 m. The depth increases in radial direction (z = 0) up to 40 V at the position of the flux tube boundary. The presence of this trap explains the large trapping probability ($\approx$ 60%) for low energy (1 to 10 eV) electrons. Figure 5.4 shows the trapping region for electrons with 4 eV start energy. Although the maximum depth of the Penning trap is 40 V, electrons of larger energies (depending on Θ) can still be stored because the electric field of the trap only influences the

[3]This value was increased to 50 m for energies above 10^5 eV in order to take into account strong non adiabatic motion of the electrons.

longitudinal component of the electron energy.

- **MAC-E filter limit**: In a MAC-E filter the longitudinal energy component (E_l) is transferred into the transversal component (E_t) and vice versa (for a detailed description see section 7.1.1). The maximum transversal energy at the analyzing plane for a transmitted electron is ΔE. Turning this argument around, one can say that each electron that is created in the volume of the spectrometer with an energy E_s leaves the spectrometer if $E_s < \Delta E$ (and thus is not trapped). The value of ΔE is 67 eV for the pre-spectrometer configuration of figure 5.3.
- **magnetic trapping**: If $E_s > \Delta E$, electrons can be reflected due to magnetic mirror effect (see section 4.1.3) caused by the increasing magnetic field towards larger absolute values of z. In this case the electron is trapped in a magnetic trap because the magnetic field is mirror symmetric around $z = 0$ m. Although the magnetic trapping probability is independent of the electron energy (as long as its motion is adiabatic) it increases towards larger energies. This is due to the presence of an electric field created by the retarding potential (see figure 7.4) of the pre-spectrometer which accelerates electrons in the region of the ground electrode. Because this acceleration increases the longitudinal energy (E_l) component, Θ decreases and if $\Theta < \Theta_{trap}$ (see equation 4.3) the electron is not trapped. The gain of E_l (pre-spectrometer potential) is fixed and therefore the relative change of Θ decreases with larger E_s and thus the trapping probability increases. Unlike the electrostatic trap - which the electron in general[4] can not leave due to energy conservation - the magnetic trap is not stable on long time scales (order of several hours). The electron scatters on residual gas molecules and emits synchrotron radiation. Thus it loses energy until its energy is smaller than ΔE and then exits the trap.
- **cyclotron cut-off**: For large energies (>100 keV) the cyclotron radius r_c (0.3 m for a 1 MeV electron at $z = 0$ m) increases to values in the order of the pre-spectrometer radius ($r_{PS} = 0.85$ m) and thus the probability that an electron hits the inner electrode - and therefore is not trapped - increases. The absolute maximal energy of an electron trapped in the pre-spectrometer is 4.1 MeV for $r_c = r_{PS}$ and $z = 0$ m.

[4]There is one scenario that would allow the electron to exit the trap: If $E_s > e * U_{trap}$ and $E_l < e * U_{trap}$ but $E_l > e * U_{trap}$ after scattering on a residual gas molecule, the electron leaves the trap.

5.2.2 ^{219}Rn decay events

If a ^{219}Rn atom decays inside the volume of the pre-spectrometer electrically charged particles with different masses and energies are created:

- **α-particle:** Due to its high energy (5.74 to 6.55 MeV) and large mass ($m_\alpha \approx 7500 * m_e$) it is practically not influenced from electric and magnetic fields within the pre-spectrometer and thus flies on a straight track until it hits the vessel wall or inner electrode. As a result of the impact, secondary electrons are produced. Anyhow, these electrons are not able to penetrate into the flux tube due to magnetic shielding and therefore are of less concern.
- **^{215}Po:** The recoil energy of ^{215}Po - which can have a charge between -2·e and +10·e (or even more) - is in the range between 107 and 122 keV. It can remain up to 12 μs[5] inside the volume of the pre-spectrometer which is much less than its lifetime of 2.57 ms. Thus the probability that ^{215}Po decays in the volume of the pre-spectrometer is $< 0.5\%$ an can therefore practically be neglected.
- **shake-off, Auger and Coster-Kronig electrons:** These electrons can have energies up to 59.7 keV in case of an Auger electron for a K vacancy. The probability that this happens is rather small (only 0.07% of all ^{219}Rn decays produce a K vacancy (internal conversion) that emits an Auger electron). Most of the time these electrons have energies in the region of keV or less. In this energy region there is a good chance that they are trapped in the volume of the pre-spectrometer (see figure 5.3). Once trapped, they can ionize residual gas molecules and thus create secondary electrons (up to 25 secondary electrons due to ionization of H_2 molecules for each keV of primary energy assuming an average energy loss of 40 eV [25] for each ionization event and no other energy losses e.g. synchrotron radiation or inelastic scattering).
- **conversion electrons:** They appear with a probability of 3.25% for each ^{219}Rn decay and can have energies up to 501 keV whereas 178 keV (1.27%) and 254 keV (0.74%) are the most likely ones. The probability to be trapped is close to 100% and due to their high energy they have the potential to create thousands of secondary electrons. The behaviour of a trapped 178 keV electron is discussed in detail below.
- **γ-rays:** They are not influenced by the electric or magnetic fields and can only produce secondary electrons inside the vessel wall or inner electrodes which are of less concern (see α-particle).

Figure 5.5 shows an interaction map for a 178 keV conversion electron. The electron was started close to the analyzing plane (z = -0.095 m) at a radial position of 0.33 m. It is trapped magnetically and thus oscillates in z-direction with a frequency of 35.3 MHz. This motion is overlapped with an azimuthal magnetron drift

[5] This is the time that ^{215}Po needs for travelling the length of the pre-spectrometer (3.4 m) with minimum recoil energy.

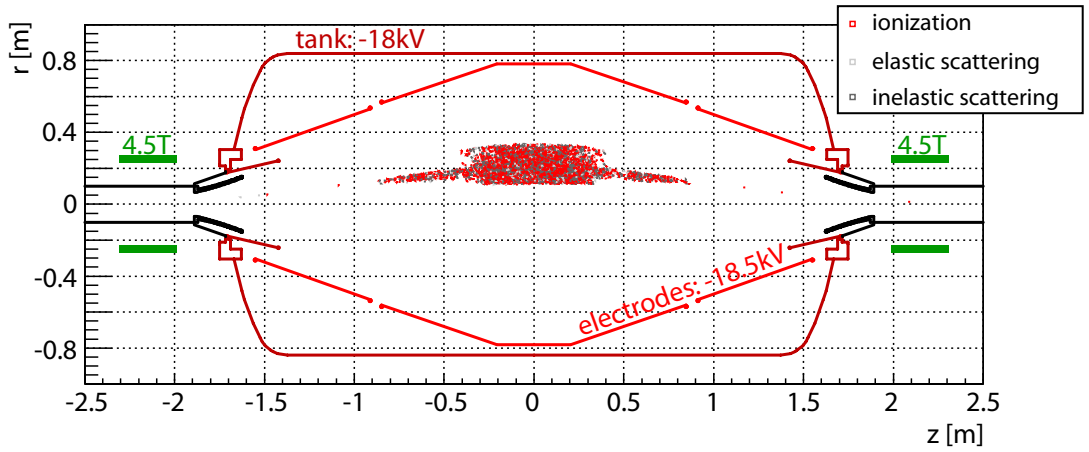

Figure 5.5: interaction map of a 178 keV electron, start conditions: x = 0.31 m, y = -0.10 m, z = -0.095 m, $\Theta = 67.2°$, $\varphi = 244°$, the pre-spectrometer is rotational symmetric but for better illustration it is mirrored at r = 0 m

of 1.8 MHz. Although the pressure inside the pre-spectrometer is on the level of 10^{-10} mbar the trapped electron interacts with residual gas molecules[6]:

- elastic scattering
- inelastic scattering
- ionization

Each interaction changes the angle Θ ($\Delta\Theta$) of the trapped electron and thus the volume where the electron is trapped changes dynamically over time. Although $\Delta\Theta$ is usually small ($<1°$) for electron energies above 10 keV, there is a small chance that the trapped electron - after the interaction - has a sufficiently small Θ to leave the magnetic trap without depositing all of its energy via ionization or inelastic scattering inside the volume of the pre-spectrometer.

In case of ionization a secondary electron is created with a start energy of typically a few eV. According to figure 5.3 it has a 60% chance to be trapped inside the electrostatic trap and thus only a 20% chance to leave the pre-spectrometer on the detector side. In this case it is accelerated by the tank potential to an energy of up to 18.5 keV and detected at the detector[7]. The left side of figure 5.6 shows the pixel distribution of all secondary electrons produced in figure 5.5 that arrive at the detector. Because of magnetron drift of the trapped primary electron, secondary electrons are produced on a concentrical ring that is diffuse due to cyclotron motion of the trapped electron and the dynamic change of the trapping volume. The left

[6]For the simulation only the scattering of electrons on H_2 molecules - which are dominant in the residual gas (see figure 5.27) - is included.

[7]This is true if it is created inside the fraction of the flux tube (28.5%) that is covered by the detector.

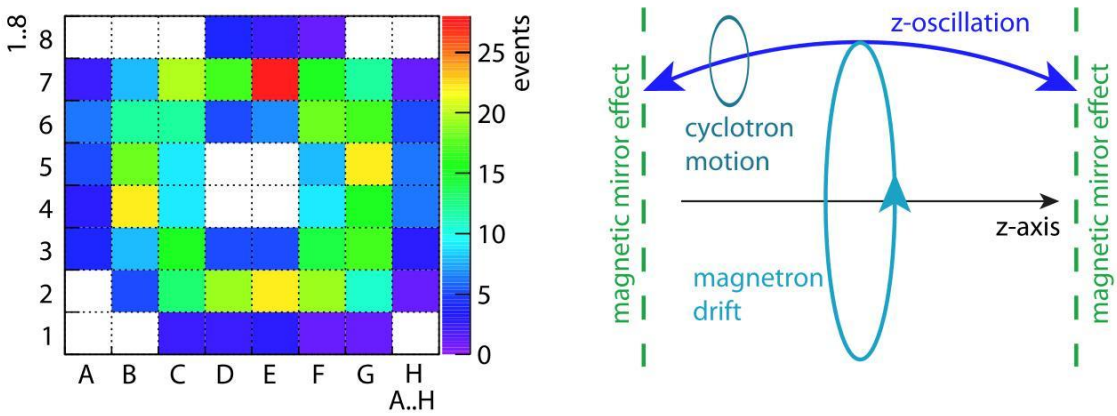

Figure 5.6: **left:** Simulated pixel distribution of secondary electrons produced by a magnetically trapped 178 keV conversion electron (see figure 5.5), that arrive at the detector, **right:** motion components of a magnetically trapped electron

side of figure 5.7 shows the simulated event rate of secondary electrons - produced by a trapped 178 keV electron - at the detector. Towards the end the rate increases (Bragg peak). This is due to the fact that the cross section for ionization increases with lower energies (see right side of figure 5.7).

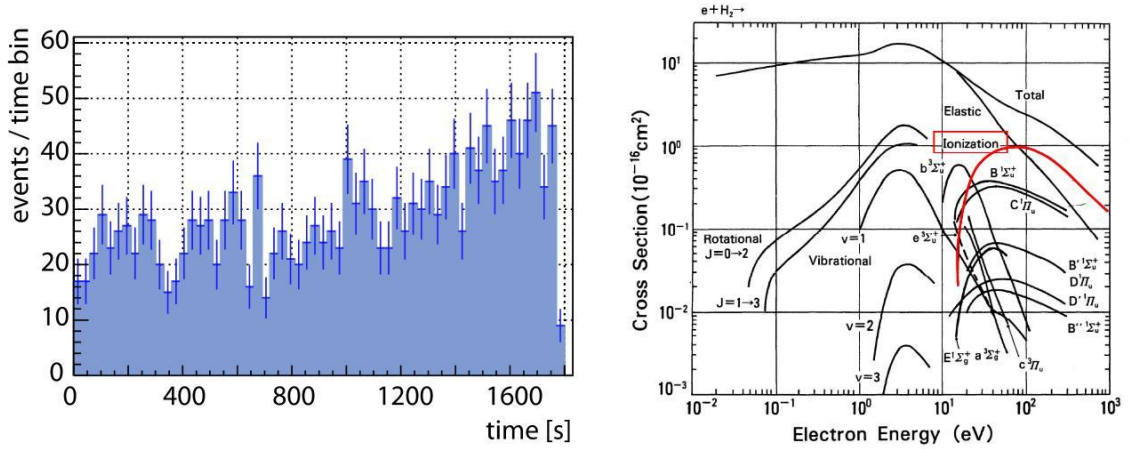

Figure 5.7: **left:** Simulated event rate of secondary electrons - produced via ionization of a trapped 178 keV electron - that arrive at the detector, **right:** cross sections for the interaction of electrons on H_2, data taken from [48]

5.3 Detector background characteristics

The expected background rate originating from the pre-spectrometer is in the order of a few counts per 1000 seconds. In order to be able to distinguish between the spectrometer signal and detector background, a detailed characterization of the intrinsic detector background is needed. For this reason, six background measurements (see table 5.2) were performed at three different configurations (see table 5.1). For all of them the pre-spectrometer was kept on ground potential.

Table 5.1: Configurations for detector background measurements, configuration: label of configuration, valve: status of valve between detector and pre-spectrometer, z-position: z-position of the detector in detector coordinates, B: magnetic field at the detector position

configuration	valve	z-position [cm]	B [T]
A	closed	0.5	0
B	open	40	3.4
C	open	0.5	0.4

Table 5.2: detector background measurements, events and rates given in the region of interest (15 to 21 keV), configuration: measurement configuration (see table 5.1), events: number of events in region of interest, correlated: number of correlated events (time difference between events < 2 μs), time: measurement time, rate: rate in events/1000 s, runs: corresponding run numbers

configuration	events	correlated	time [s]	rate [1/1000s]	runs
A	1938	1428	57591	33.7 $\pm$ 0.8	1237 - 1240
A	4494	3239	133095	33.8 $\pm$ 0.5	10523 - 10531
B	1828	1473	57599	31.7 $\pm$ 0.7	1287 - 1290
B	2319	1856	72035	32.2 $\pm$ 0.7	1469 - 1473
C	2212	1801	57609	38.4 $\pm$ 0.8	1251 - 1254
C	2932	2372	72611	40.4 $\pm$ 0.8	10532 - 10534

Figure 5.8 shows a typical background energy spectrum with and without TCF filter (see section 3.5.2). Several features are observed:

- **Overflow peak:** The energy spectrum in figure 5.8 is the sum of the energy spectra of 61 pixel[8]. Because each pixel has a slightly different energy calibration, the overflow energy is slightly different. In addition, the trapezoidal filter can produce varying results depending on the noise of the baseline. Both

[8] Although the detector has 64 Pixel, the pixels E5, F5, F7 are normally excluded from the analysis due to an increased noise level and worse energy resolution [78].

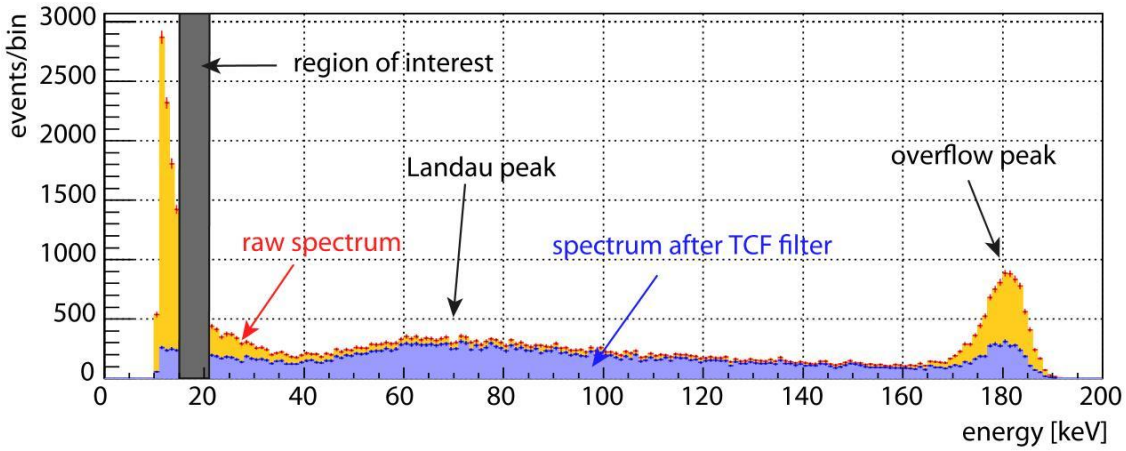

Figure 5.8: energy spectra of 64PD for measurement configuration B, orange spectrum: only PSA noise filter applied, blue spectrum: PSA and TCF filter applied

effects cause a broadening and instead of a single overflow bin an overflow peak is created.

- **Low energy tail:** Between 10 and 40 keV the number of events increases by an order of magnitude towards lower energies in case of the raw spectrum. Most of these events are correlated in time (the time difference between the events is $<$ 2 μs[9]) and space (the events appear only in adjacent pixels). This behaviour can be explained with crosstalk between the pixels in case the detector is hit by a high energetic (>170 keV) particle. After removal of the correlated events using the TCF filter, a slight increase of events towards lower energies is observed. This could be caused by fluorescence light of the surrounding material (see [86]).
- **Landau peak:** The fluctuations of energy loss by ionization of a charged particle in a thin layer of matter (detector thickness: 200 μm [78]) can be described with a Landau distribution [64]. Characteristic features of a Landau distribution are a narrow peak and a long tail towards positive values. A Landau fit to the accumulated data between 40 and 160 keV of all detector background measurements in configuration A is shown in figure 5.9. Because the fitted Landau distribution matches the data well it can be argued that most of the background events in this energy window are due to high energetic charged particles (cosmic radiation).

Table 5.3 contains the background rates for all three different measurement configurations. Important for the measurements in section 5.4 is R^*_{64PD} for configuration B.

[9]This is less than the shaping length of the DAQ electronics (3.1 μs).

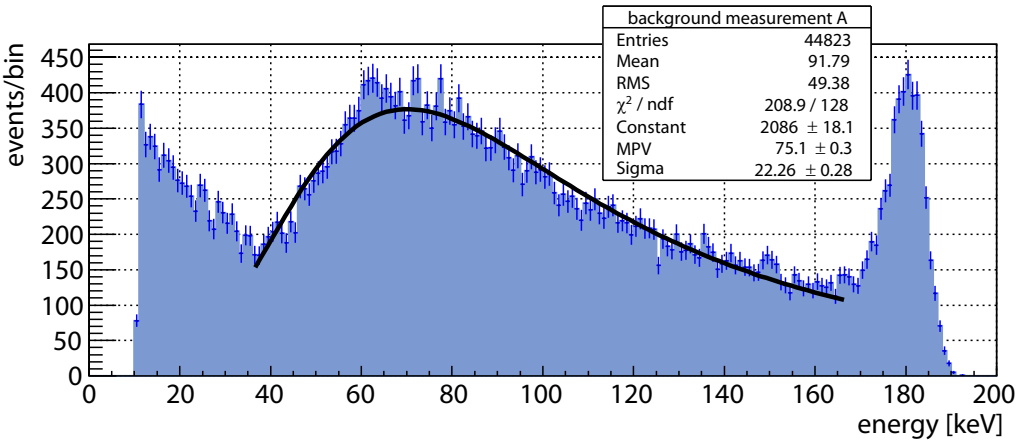

Figure 5.9: Accumulated energy spectra for all background measurements of configuration A. A Landau distribution is fitted to the data in the region between 40 and 160 keV

Table 5.3: combined detector background measurements, R_{64PD}: event rate in the region of interest [1/1000 s], R^*_{64PD}: event rate in the region of interest after applying TCF filter [1/1000 s], T: measurement time in hours

configuration	R_{64PD}	R^*_{64PD}	T [h]
A	33.7 ± 0.4	9.3 ± 0.2	53
B	32.0 ± 0.5	6.3 ± 0.2	36
C	39.5 ± 0.4	7.5 ± 0.2	36.2

5.4 Pre-Spectrometer background measurements

With the successful installation of aluminium ground electrodes at the pre-spectrometer an elevated background component ("high B-field background") in the kHz regime could be removed (see chapter 4). In order to investigate the nature of the remaining background of the actual pre-spectrometer setup, several measurements with different settings (see table 5.4) were performed. For all measurements described below, the following parameters were identical:

- detector (segmented silicon detector with 64 pixels, 64PD) position at z = 40 cm (detector coordinates, 28.5% of entire flux tube visible at detector)
- pressure gauges off to avoid additional background (the pressure p was measured before and after each background measurement)
- active stabilization of pre-spectrometer tank high voltage (-18kV)
- inner electrodes 500V more negative with respect to tank voltage in order to prevent ignition of east/west Penning trap and to use electrostatic shielding of the wire electrode

- unless stated else, only one TMP (Ebara) was used
- rates are given in events/1000 s, synonymously the unit mHz[10] is used
- unless stated else, all plots and rates given are within the region of interest E_{ROI} = 15 to 21 keV - after application of PSA and TCF filter (see section 3.5) - inclusive $R^{*}_{64PD} = 6.3 \pm 0.2$ mHz

The background measurements are organized in the following way:

- **Measurement:** During a measurement no experimental parameter was changed. Each measurement is divided into many subsequent runs that are merged into a single file. All times given are relative times since the start of the first run.
- **Run:** A run is an ORCA Run with a length of 8 hours. In order to be able to cut noise events with the PSA filter the data is taken in "energy and trace" mode of the IPE3 electronics.

Table 5.4: overview of pre-spectrometer background measurements, #: label of measurement, B_{max}: maximum magnetic field inside the coils, 64PD x/y: position of the detector in detector coordinates, runs: corresponding run numbers, T: measurement time in hours, comment: short comment on measurement

#	B_{max} [T]	64PD x/y [cm]	runs	T [h]	comment
1a	4.5	-0.3/0.35	1504 - 1509	49.5	default configuration
1b	4.5	-0.3/0.35	1511 - 1516	48.0	default configuration
2	0.11	-0.3/0.35	1638 - 1645	57.6	low magnetic field
3	4.5	-0.3/0.35	1772 - 1777	43.3	dipole mode
4	4.5	-0.3/0.35	6659 - 6669	88.0	increased pressure
5	4.5	-2.5/0.5	8423 - 8435	91.1	detector shifted
6	4.5	-0.3/0.35	10418 - 10429	88.6	heated getter
7	4.5	-0.3/0.35	10535 - 10564	232.6	cooled getter
8a	4.5	-0.3/0.35	10568 - 10587	157.4	no getter
8b	4.5	-0.3/0.35	10588 - 10599	96.0	e-gun valve closed
8c	4.5	-0.3/0.35	10600 - 10620	168.0	Ebara valve closed
8d	4.5	-2.5/0.55	10621 - 10630	72	detector shifted
9	4.5	-0.3/0.35	10637 - 10788	158	pressure rise
10	4.5	-2.5/0.5	10470 - 10474	20	e-gun

Table 5.4 contains an overview of low background measurements performed at the pre-spectrometer. Each measurement is described in detail below.

[10] In this case the usage of Hz does not imply a periodic behaviour of the events.

5.4.1 Background measurement 1a (default configuration)

For this measurement the maximum symmetric magnetic field (4.5 T inside coil) was used. The total measurement time was about 50 h at a pressure of $1*10^{-10}$ mbar.

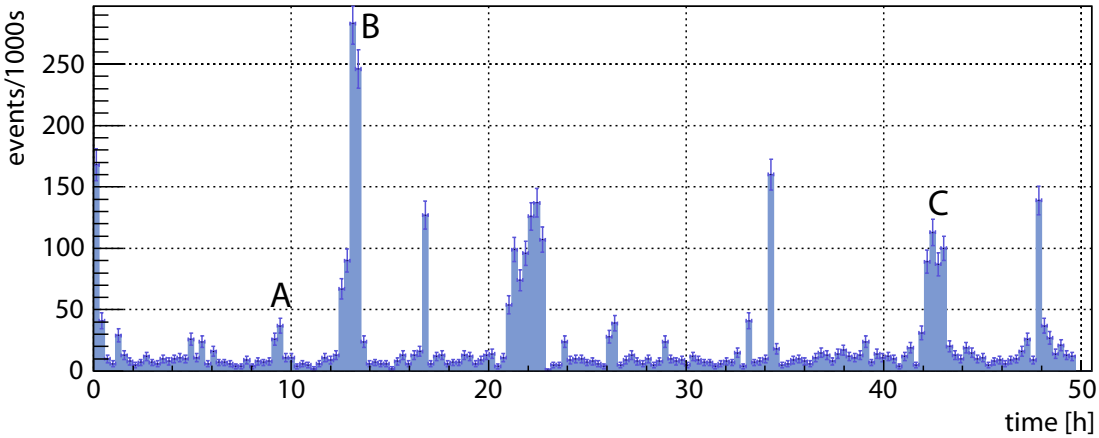

Figure 5.10: Rate over time plot for measurement 1a, PSA and TCF filter applied, each histogram bin has a width of 1000 s. The pixel distributions for the intervals of elevated rate A to C are shown in figure 5.11.

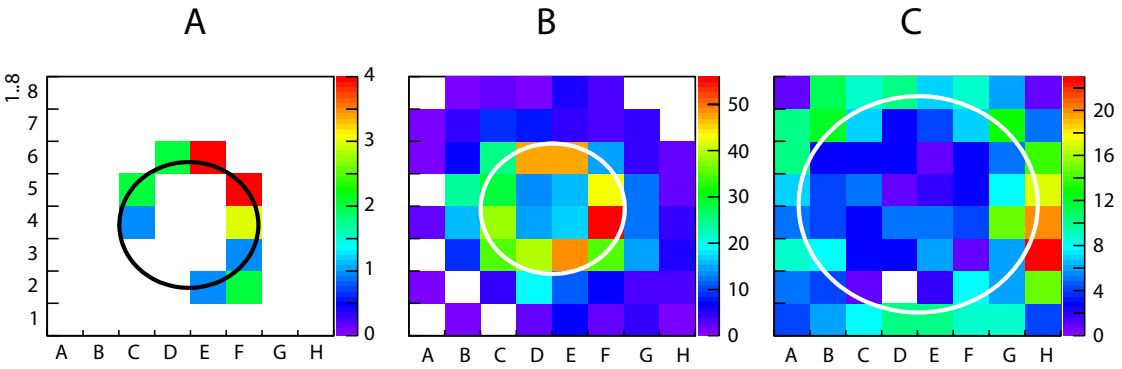

Figure 5.11: Pixel distributions for different intervals of elevated rate (see figure 5.10) together with the ring radius resulting from a fit. At the centre of the pre-spectrometer the radius for the C period is about r = 0.243 m.

Figure 5.10 shows the rate over time at the detector. The average rate coming from the spectrometer is $R_{BG} = 23.3 \pm 0.4$ mHz (including R^*_{64PD}), but the events are not distributed equally: There are shorter intervals (15 to 120 min) of elevated rate (up to 250 mHz) and longer intervals where the rate is at the level of 10 mHz. Figure 5.11 displays the pixel distributions of three different intervals of elevated rate (A,B and C). Each pixel distribution shows a distinct ring structure but the radii of

the ring structures differ for each interval of elevated rate. The corresponding energy spectra are showing peaks around 18 keV (see figure 5.12). This implies that the events which create the rings are real physical events coming from the spectrometer and are no artefacts of the detector. Between the intervals of elevated rate no rings in the pixel distribution or peaks in the energy spectra are observed.

The number of events that create the ring structures ranges over two orders of magnitude (from 10 to 726 in this measurement). In order to classify the ring structures four event classes are defined (see table 5.5). The definition of the event classes is to some extend arbitrary and is only intended to cover an order of magnitude for each class. Class *0* events are in most cases not detectable as ring structures due to low statistics, but they could contribute as a diffuse background component to the total pre-spectrometer background.

Table 5.5: definition of the ring structure event classes, event class: label of event class, number of events: number of events that create a ring structure (without detector background), primary energy: order of magnitude of the initial energy of a trapped electron in the pre-spectrometer that could create the "number of events" via subsequent ionization of residual gas molecules.

event class	number of events	primary energy
0	1 .. 9	0.1 keV
I	10 .. 50	1 keV
II	51 .. 500	10 keV
III	501 .. 5000	100 keV

Table 5.6 shows the number of events for event class *I* to *III* for this measurement. Most events occur in class *I* but due to the low number of electrons of each class *I* event the contribution to the average pre-spectrometer background rate R_{BG} is rather small (1.1 ± 0.1 mHz). After subtracting the class *I* to *III* contributions and the intrinsic detector background R^*_{64PD} from R_{BG}, a background rate of 3.2 ± 0.3 mHz (possible class *0* contribution) remains.

Table 5.6: number of events in each event class for measurement 1a, events: occurrence of events during the measurement, event rate: rate of events in events/day, background rate: contribution to the average pre-spectrometer background rate in mHz, the error originates from the statistical error of the number of all "ring" events.

event class	events	event rate	background rate
I	10	4.8 ± 1.5 1/d	1.0 ± 0.1 mHz
II	5	2.4 ± 1.1 1/d	4.9 ± 0.2 mHz
III	2	1.0 ± 0.7 1/d	7.8 ± 0.2 mHz

5.4.2 Background measurement 1b (default configuration)

The intention of this measurement is to check whether the background behaviour observed in the previous measurement 1a (see above) is reproducible. Therefore identical measurement parameters were chosen. The time dependence of R_{BG} is similar to measurement 1a: Most of the time R_{BG} is at the level of the intrinsic detector background and there are time intervals of elevated rate with different length (1 to 90 min) and amplitude (up to 250 mHz). The events for the event classes *I* to *III* are summarized in table 5.7. No statistical significant deviation of the event rate compared to 1a is observed.

Table 5.7: number of events in each event class for measurement 1b

event class	events	event rate	background rate
I	7	3.5 ± 1.3 1/d	0.7 ± 0.1 mHz
II	2	1.0 ± 0.7 1/d	2.3 ± 0.1 mHz
III	2	1.0 ± 0.7 1/d	8.3 ± 0.2 mHz

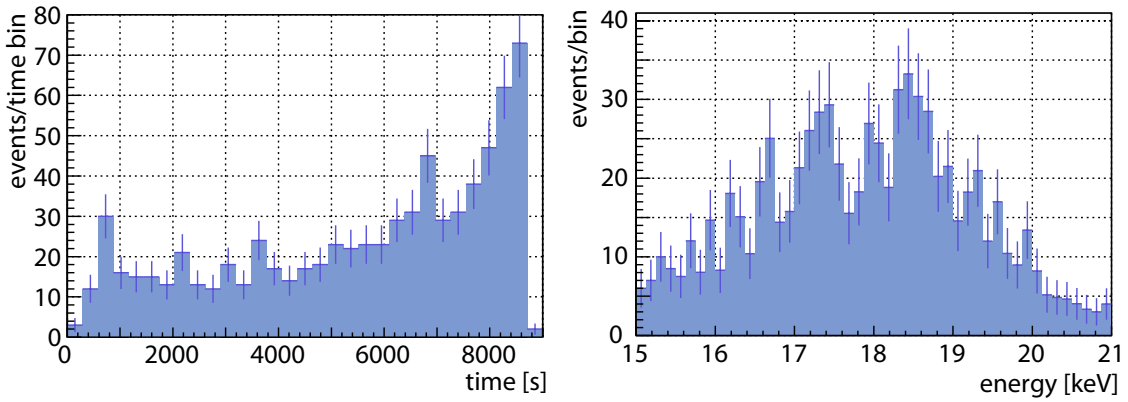

Figure 5.12: **left:** rate over time for an interval of elevated rate (bin width 300 s), **right:** corresponding energy spectrum

Figure 5.12 shows the energy spectrum and time series of a class *III* event. The energy spectrum of E_{ROI} has a mean value of 17.9 keV. This is consistent with the hypothesis that the electrons are created in the volume of the pre-spectrometer and are accelerated with the tank potential to about 18 keV. The time series shows a sudden increase in rate at the beginning, followed by a plateau of about 15 events/time bin (50 mHz) for 6000 seconds. Towards the end the rate increases up to 70 events/time bin (220 mHz) and then suddenly drops to the level of the detector background. This behaviour is observed for most of the class *II* and *III* events[11].

[11] Class *I* events have too few events for a statistical significant statement about the time dependence of the rate.

5.4.3 Background measurement 2 (low magnetic field)

In order to investigate the magnetic field dependence of the intervals of elevated rate the magnetic field was lowered by a factor of 40 - from $B_{max} = 4.5$ T to 0.11 T. This adjusts the magnetic field strength in the pre-spectrometer analyzing plane (0.4 mT) to the field in the main spectrometer and significantly changes the storage condition for high-energy electrons, as only low-energy particles can be stored in such a weak field (the cyclotron radius of a 9 keV electron is already at the dimension of the pre-spectrometer and thus the electron hits the wall or inner electrodes).

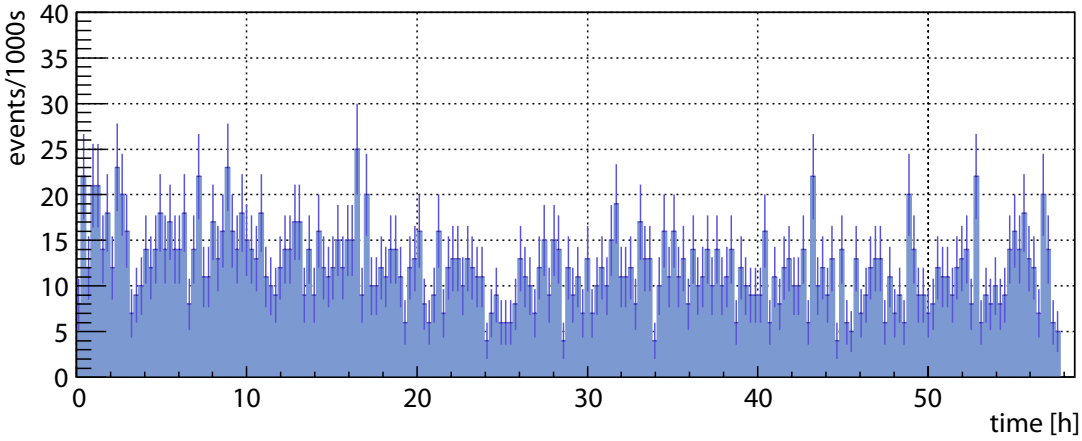

Figure 5.13: Rate over time plot for measurement 2, PSA and TCF filter applied, each histogram bin has a width of 1000 s.

Figure 5.13 shows the rate over time plot of this measurement. The average rate is 11.8 ± 0.2 mHz and no obvious intervals of elevated rate are observed. A detailed analysis revealed three short (<1 s) regions of elevated rate, but the time structure and the pixel distribution is completely different compared to the previous measurement. All events arrive within a narrow interval of 60 μs and no ring structure is observed. This behaviour is similar to measurements at zero magnetic field [42] where such burst events were detected. The origin of these bursts is most likely related to micro discharges inside the pre-spectrometer. Because of the weak magnetic shielding in this measurement, such bursts could still be visible on the detector.

5.4.4 Background measurement 3 (dipole mode)

The aim of this measurement is to check if an electric dipole field has an effect on the intervals of elevated rate. The segmented inner electrode system of the pre-spectrometer can be configured to create an electric dipole field to remove stored particles via $\vec{E}\times\vec{B}$ drift. For this particular measurement, the following settings were used: dipole 1 (electrodes: S1/S3/D1), voltage +2 kV, duration 0.5 s and dipole 2

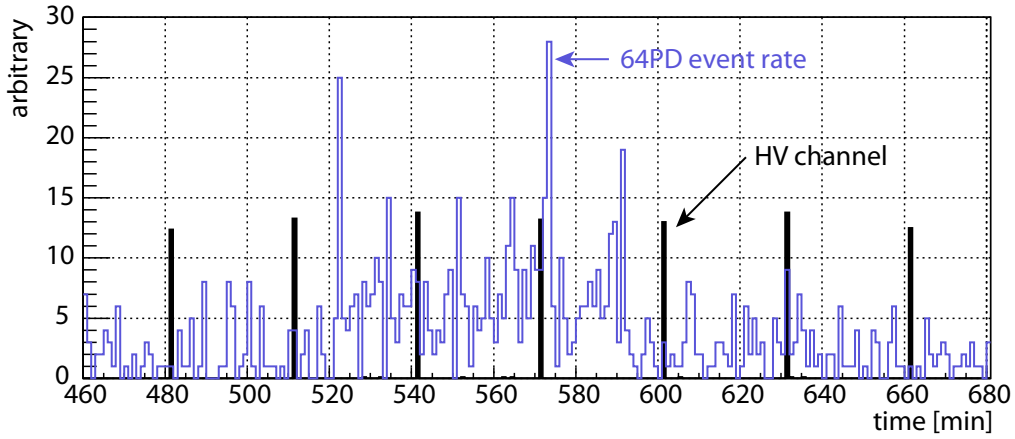

Figure 5.14: Rate at the detector (blue) and HV channel (black) for an interval of elevated rate (520 to 600 min). The periodic HV signal (T ≈ 30 min) is induced of the dipole mode.

(electrodes S2/S4/D2), +2 kV, 0.5 s, immediately after dipole 1. The dipole voltage was applied every half an hour. In addition, the stability of the pre-spectrometer tank HV was monitored with the IPE3 crate in order to investigate whether the intervals of elevated rate coincide with times of elevated tank HV instabilities.

In this 40 h measurement two intervals of elevated rate could be identified. In figure 5.14 a time interval with elevated rate (520 to 600 min) is shown (blue histogram) and superimposed with the HV channel (black histogram). The dipole pulses are clearly visible in the HV channel, because at the moment when the dipole pulse is applied to the inner electrodes, a signal is induced on the tank HV via capacitive coupling. As one can see in figure 5.14 the dipole has no effect on the region of elevated rate. For the hypothesis of a stored high energetic electron this is expected. Corresponding simulations [94] have shown that an electric dipole field can not remove such high energetic electrons.

5.4.5 Background measurement 4 (increased pressure)

In order to further validate the hypothesis of stored high energetic electrons, the pressure inside the pre-spectrometer was artificially increased via the injection of Argon gas from an initial value of $1*10^{-10}$ to $2*10^{-9}$ mbar. For these conditions one expects that the intervals of elevated rate should become shorter in time and the rate should increase. This results from the fact that almost the entire energy of the primary electrons is used for ionizing collisions with the residual gas. As the ionizing energy of H_2 (15.5 eV) is comparable to the ionizing energy of Argon (15.8 eV) the same number of secondary electrons is expected for these runs.

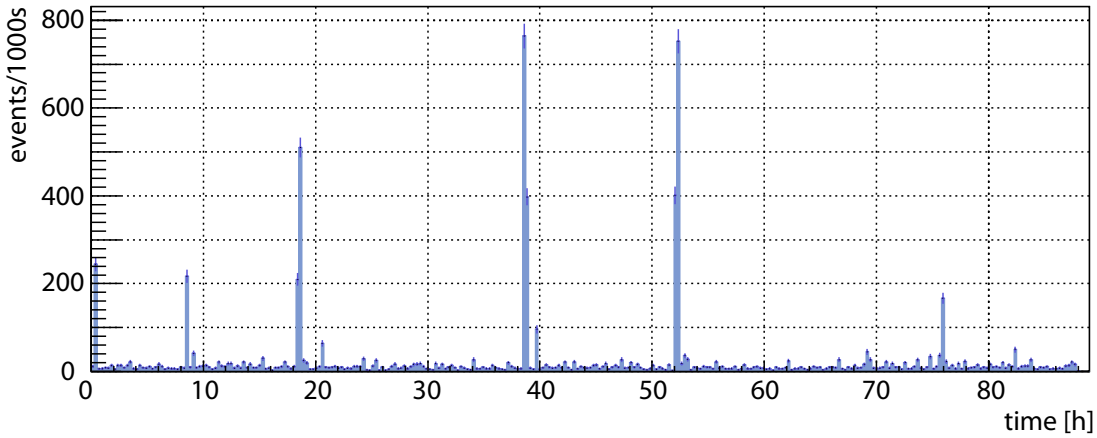

Figure 5.15: Rate over time plot for measurement 4, PSA and TCF filter applied, each histogram bin has a width of 1000 s.

Figure 5.15 shows the rate over time at the detector for this 88 hour measurement. Several intervals of elevated rate are clearly visible. In contrast to the measurement at the $1*10^{-10}$ mbar level (see figure 5.10), the rates within the intervals are about a factor 10 higher and the intervals are an order of magnitude shorter. This supports the hypothesis of stored high energetic electrons because the total number of ionizations should stay the same, but due to the higher pressure more ionizations happen within a given time interval.

Table 5.8: number of events in each event class for measurement 4

event class	events	event rate	background rate
I	20	5.5 ± 1.2 1/d	1.1 ± 0.1 mHz
II	3	0.8 ± 0.5 1/d	1.6 ± 0.1 mHz
III	3	0.8 ± 0.5 1/d	10.1 ± 0.2 mHz

Table 5.8 summarizes all events in this measurement. Most of the class *I* events happen within 4 seconds. The total number of class *I* events are 20, which correspond to a rate of 5.5 ± 1.2 events/day in the observed fraction of the flux tube.

5.4.6 Background measurement 5 (detector shifted)

This measurement aims to answer the question whether the observed ring events are distributed isotropically. As mentioned in the beginning of this section, the detector only covers about 30% of the total flux tube in the pre-spectrometer. However, the detector can be moved in x and y direction and therefore is able to cover 100% of the flux tube radius. As the events create ring structures, 100% of the flux tube can be observed indirectly via the detection of ring segments.

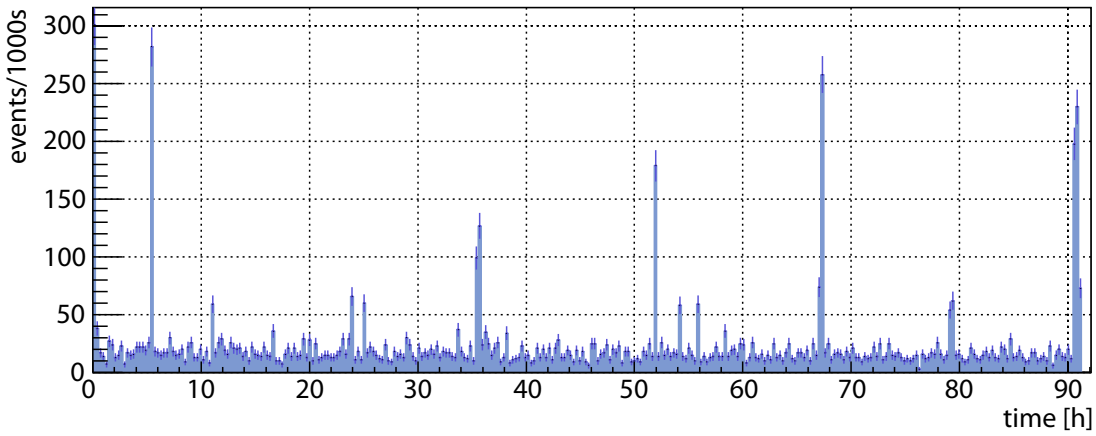

Figure 5.16: Rate over time plot for measurement 5, PSA and TCF filter applied, each histogram bin has a width of 1000 s.

For this measurement the same parameters as in the previous measurement (see subsection 5.4.5) were used, but the detector was moved from x = -0.3 cm / y = 0.35 cm to -2.5 / 0.5 cm. The centre pixel in this configuration is B8, the outer most pixel is H1. Figure 5.16 shows the rate at the detector and figure 5.17 shows the pixel distribution of two intervals of elevated rate. As expected, ring segments are observed. There are 10 class *II* events and 6 class *III* events in this measurement. This is about 3 times more compared to the previous run (see table 5.8) and in good agreement with the expectation because the observed flux tube is also a factor 3 larger. The detection of class *I* events in this particular measurement configuration is very difficult because of the reduced number of events at the detector, e.g. assuming a class *I* event with 14 events and a large radius such that only 30% of the events arrive at the detector. This would result in 4 events on the detector which practically can not be distinguished from intrinsic background events. Therefore only 4 class *I* events could be identified in this run.

Table 5.9: number of events in each event class for measurement 5

event class	events	event rate	background rate
I	4	1.1 ± 0.5 1/d	0.15 ± 0.02 mHz
II	15	4.0 ± 1.0 1/d	2.2 ± 0.1 mHz
III	5	1.3 ± 0.6 1/d	3.7 ± 0.1 mHz

An increase in rate for class *II* + *III* events from 1.6 ± 0.7 1/d (measurement **4**, about 60% of the flux tube radius) to 5.3 ± 1.2 1/d is observed. This increase in rate is - within the statistical uncertainties - compatible with the assumption that the ring events are distributed isotropically and thus should increase by a factor of 2.8.

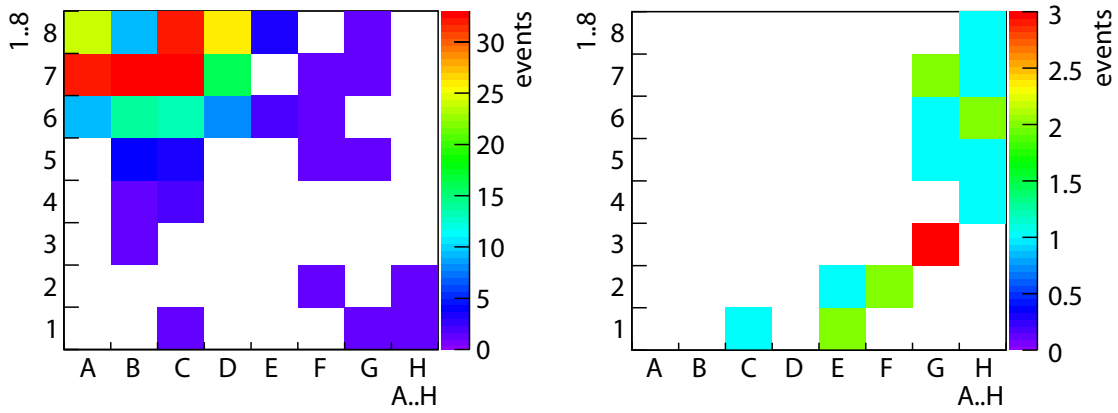

Figure 5.17: pixel distribution for two events, ring segements around the centre pixel B8 are observed

5.4.7 Background measurement 6 (heated getter)

A possible source of the observed background features could be the ^{219}Rn emanation from the NEG strips (see section 5.1). In order to check if the temperature of the getter pump has an effect on the ^{219}Rn emanation, the 45° pump port was electrically heated to about 90 °C. Via radiative heating the temperature of the getter pump was increased to about 70 °C (see figure 5.18). In order to have a good signal to noise ratio (about 100:1) for the detection of intervals of elevated rate the pressure was artificially increased via the injection of Argon to about 2*10^{-9} mbar.

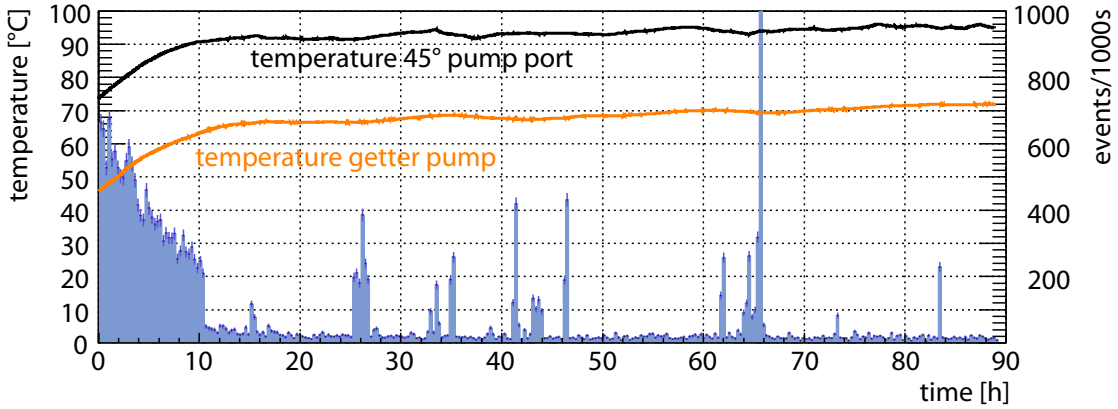

Figure 5.18: Rate over time plot for measurement 6, PSA and TCF filter applied, each histogram bin has a width of 1000 s. In addition, the temperatures of the getter pump and the 45° pump port are shown. The high rate within the first 10 h is presumably due to a conditioning effect.

Figure 5.18 shows the event rate at the detector over time. A remarkable feature is the high rate within the first 10 hours that decreases slowly from 700 to 200 mHz and then abruptly drops to 20 mHz[12]. Such a background behaviour was only observed in this measurement and as it shows no ring structure in the pixel distribution it might be argued that it is connected to an incident that happened prior to the measurement: With the tank at ground potential but the inner electrodes at -500 V the Argon partial pressure was increased to values $> 1*10^{-5}$ mbar. This caused a small discharge that could have changed the surface properties of the tank and electrodes. After the tank was elevated to -18 kV field emission could have started and caused the increased background in the beginning of this measurement.

Table 5.10: number of events in each event class for measurement 6

event class	events	event rate	background rate
I	8	2.2 ± 0.8 1/d	0.51 ± 0.04 mHz
II	5	1.4 ± 0.6 1/d	4.30 ± 0.12 mHz
III	2	0.5 ± 0.4 1/d	3.93 ± 0.11 mHz

Within this measurement several class *I* to *III* events could be observed (see table 5.10. Within the statistical uncertainties the event rates are compatible with the previous measurements.

5.4.8 Background measurement 7 (cooled getter)

In order to further investigate the background behaviour in dependence on the spectrometer and getter temperature, the pre-spectrometer was cooled to temperatures below 0 °C. Figure 5.19 shows the temperature distribution during the measurement. Most of the cooling power was used to cool the 45° pump port which reached temperatures below -5 °C. For technical reasons it is not possible to install thermal insulation at the east side of the spectrometer while at the same time applying high voltage to the system, therefore the temperature in this region is > 0 °C (about 10 °C). During this 10 day measurement the pressure inside the pre-spectrometer was increased to $2*10^{-9}$ mbar via the injection of Argon.

The rate at the detector for this measurement is shown in figure 5.20. The typical background behaviour is observed: long periods of low background (about 10 mHz inclusive R^*_{64PD} interrupted from intervals of elevated rate (class *I* to *III* events)). Due to the long measurement time (233 h) this measurement shows the smallest statistical uncertainties for the event rates of the single event classes (see table 5.11).

[12]This behaviour was much larger for pixel H1, H2 and H3 (up to 5 Hz), therefore those pixels were not taken into account for the analysis of this run.

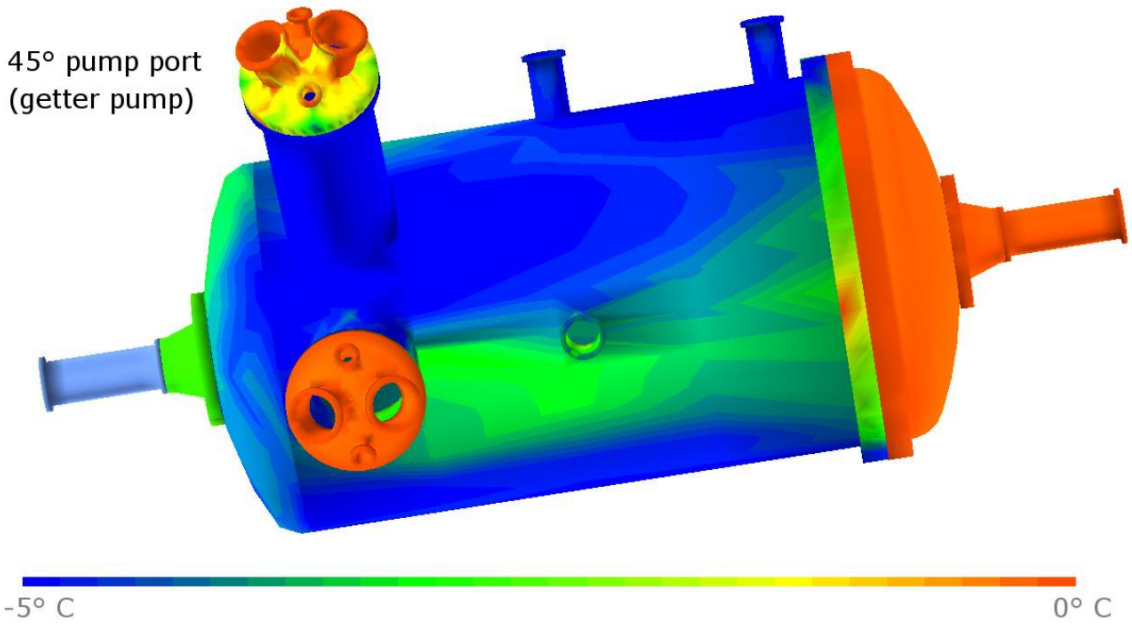

Figure 5.19: Temperature distribution of the pre-spectrometer while cooling the getter below 0° C.

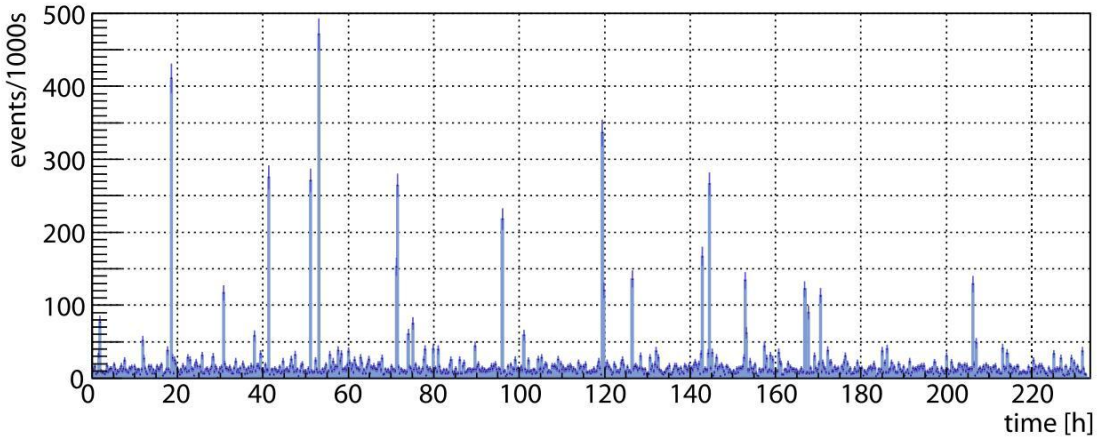

Figure 5.20: Rate over time plot for measurement 7, PSA and TCF filter applied, each histogram bin has a width of 1000 s.

Table 5.11: number of events in each event class for measurement 7

event class	events	event rate	background rate
I	49	5.1 ± 0.7 1/d	1.1 ± 0.04 mHz
II	13	1.3 ± 0.4 1/d	2.88 ± 0.06 mHz
III	0	0 ± 0 1/d	0 ± 0 mHz

5.4.9 Background measurement 8a (no getter)

Prior to this measurement the getter pump had been removed from the 45° pump port. In order to achieve a low pressure ($< 10^{-8}$ mbar) without the need of a bake out of the pre-spectrometer, the spectrometer vessel was cooled to values below 0° C. In addition both turbo molecular pumps (Ebara and Leybold) were running. In this configuration a pressure in the region of 10^{-10} mbar could be achieved. The measurement was performed at a pressure of $1*10^{-9}$ mbar (opening the valve between detector and spectrometer increases the pressure). Unlike measurements 4 to 7 no Argon was injected into the pre-spectrometer.

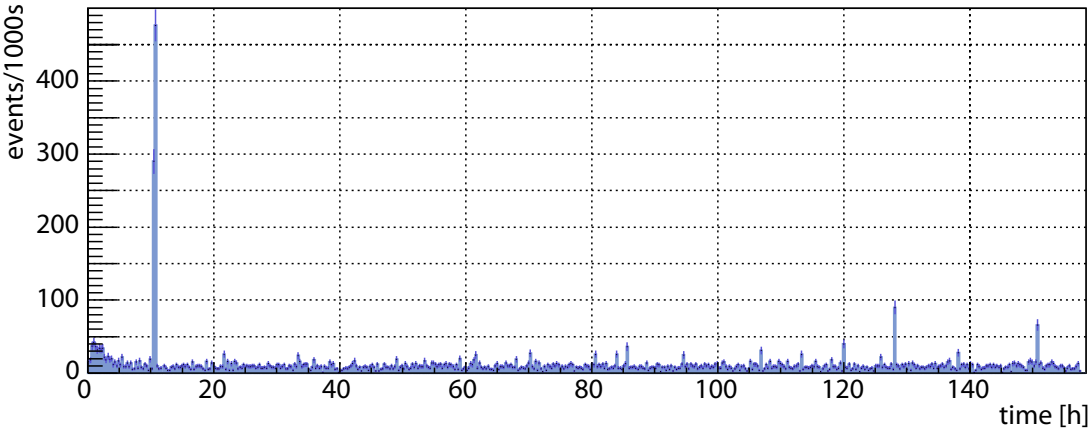

Figure 5.21: Rate over time plot for measurement 8a, PSA and TCF filter applied, each histogram bin has a width of 1000 s.

Figure 5.21 shows the time series of the detector rate. Only one major interval of elevated rate (class *III* event) is observed after 10 h. A detailed analysis showed the existence of class *I* to *III* events (see table 5.12). The event rates are smaller for all classes compared to previous measurements, especially the combination of class *II* and *III* shows a factor of about 4 times less events.

Table 5.12: number of events in each event class for measurement 8a

event class	events	event rate	background rate
I	15	2.3 ± 0.6 1/d	0.49 ± 0.03 mHz
II	1	0.2 ± 0.2 1/d	0.17 ± 0.02 mHz
III	1	0.2 ± 0.2 1/d	1.38 ± 0.05 mHz

5.4.10 Background measurement 8b (e-gun valve closed)

This measurement is a continuation of 8a with closed e-gun valve in order to exclude the e-gun chamber as a source of the background events. Until now all previous measurements (1a to 8a) were performed with open e-gun valve[13]. The occurrence of class *I* to *III* events is summarized in table 5.13. No significant change of event rate compared to measurement 8a is observed.

Table 5.13: number of events in each event class for measurement 8b

event class	events	event rate	background rate
I	6	1.5 ± 0.6 1/d	0.37 ± 0.03 mHz
II	1	0.3 ± 0.3 1/d	0.30 ± 0.03 mHz
III	2	0.5 ± 0.4 1/d	5.92 ± 0.13 mHz

5.4.11 Background measurement 8c (Ebara valve closed)

This measurement continues measurement 8b with only one turbo molecular pump (Leybold) running (the valve between pre-spectrometer and Ebara TMP was closed) in order to investigate whether the remaining background events are correlated with the pumping speed. Table 5.14 gives an overview of the observed class *I* to *III* events.

Table 5.14: number of events in each event class for measurement 8c

event class	events	event rate	background rate
I	22	3.1 ± 0.7 1/d	0.71 ± 0.03 mHz
II	3	0.4 ± 0.2 1/d	0.33 ± 0.02 mHz
III	0	0 ± 0 1/d	0 ± 0 mHz

[13] Although the e-gun was not used for the background measurements, the e-gun chamber was pumped via the pre-spectrometer because the operation of a turbo molecular pump (Leybold TW 70) at the e-gun chamber is not possible due to the high magnetic field of about 30 mT.

5.4.12 Background measurement 8d (detector shifted)

This measurement is the equivalent of measurement 5 (detector shifted to cover 100% of the flux tube radius) but without getter pump. The number of observed events is summarized in table 5.15.

Table 5.15: number of events in each event class for measurement 8d

event class	events	event rate	background rate
I	10	3.3 ± 1.0 1/d	0.53 ± 0.04 mHz
II	4	1.3 ± 0.7 1/d	0.33 ± 0.04 mHz
III	1	0.3 ± 0.3 1/d	1.50 ± 0.08 mHz

5.4.13 Background measurement 9 (pressure rise)

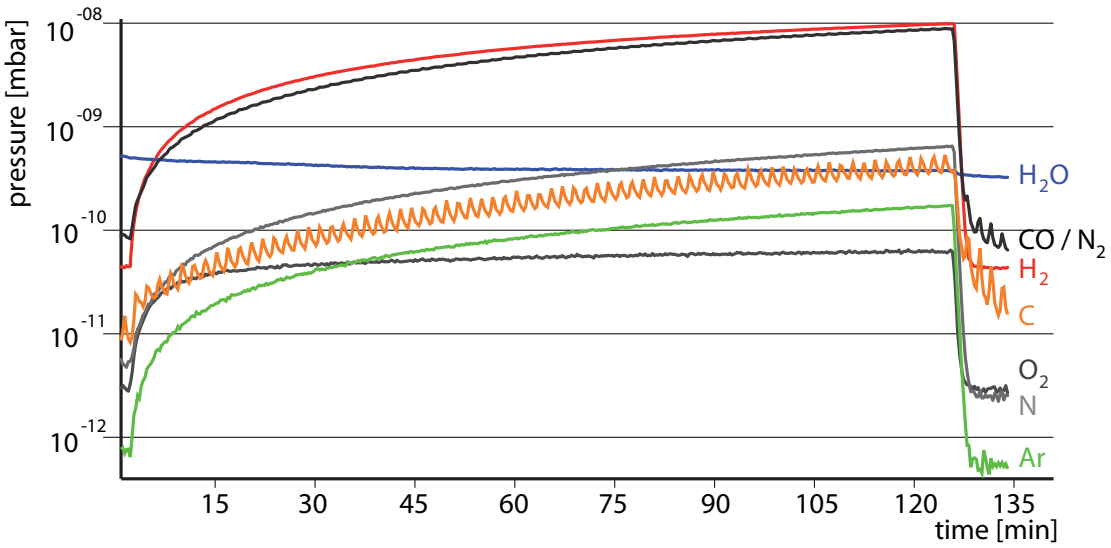

Figure 5.22: Partial pressures of common gases during a 2 h pressure rise measurement. The pressure values are not calibrated and are only intended for a qualitative analysis.

The aim of this measurement was to check if class *I* events depend on the pumping speed of the vacuum system, therefore the pumping speed of the turbo molecular pumps (TMPs) was reduced to zero via closing the valves between the TMPs and the pre-spectrometer for 95% of the time. In order to avoid a too strong increase in pressure ($> 10^{-6}$ mbar) one valve (Ebara) was opened periodically for 5 minutes after a 2 hours pressure rise. After closing both valves the pressure inside the pre-

spectrometer rises with a speed of about 1.3*10^{-11} mbar/s [14] resulting in a maximum pressure of about 1.0*10^{-7} mbar after 2 h. A scan of the residual gas spectrum (see figure 5.22) showed that the increase of pressure is mainly due to H_2 (this is expected because no getter pump is installed) and N_2/CO.

Table 5.16 shows the occurrence of class *I* to *III* events during this measurement. A significant increase (4.4 σ) of class I events compared to measurement 8c is observed.

Table 5.16: number of events in each event class for measurement 9

event class	events	event rate	background rate
I	52	7.9 ± 1.1 1/d	0.58 ± 0.03 mHz
II	2	0.3 ± 0.2 1/d	0.42 ± 0.03 mHz
III	2	0.3 ± 0.2 1/d	1.27 ± 0.05 mHz

5.4.14 Background measurement 10 (e-gun)

The aim of this measurement is to proof that high energetic (about 10 keV) electrons (produced with the e-gun) can be trapped in the pre-spectrometer. This is not a typical background measurement, but as the background events observed in measurement 1a to 9 are most likely connected to trapped high energetic particles this measurement is described here.

Figure 5.23 shows the principle of this measurement. The following experimental parameters were used:

- Detector position: x = -2.5 cm/y = 0.5 cm (centre pixel B8)
- Tank potential: -18 kV, inner electrodes: -18.5 kV
- Pressure inside pre-spectrometer increased with the injection of Argon to 2*10^{-9} mbar
- E-gun position: x = 0°/y = 15° (shooting electrons to a position next to the detector)
- E-gun potential: U_{e-gun} = -30 kV
- Periodic modulation of e-gun UV light with the shutter system: maximum intensity (10 mm shutter) for 10 s, afterwards shutter closed for 30 s
- Measurement time: 4 h (about 350 e-gun cycles)

With a small probability (order of 10^{-6}) electrons scatter on residual gas molecules on their way from the e-gun to the detector chamber. If the scattering happens close

[14] Because all pressure gauges are turned off during the actual measurement, this value was determined from a pressure rise measurement prior to the measurement.

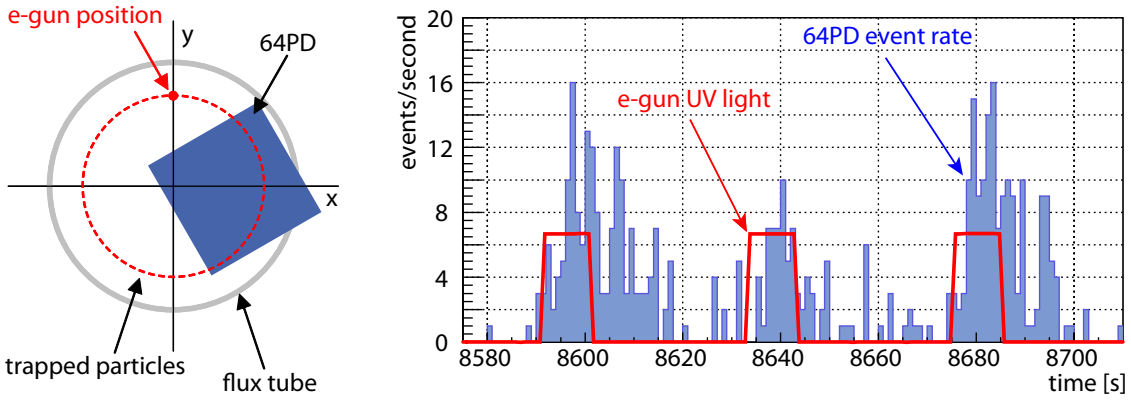

Figure 5.23: **left:** principle of the measurement, 30 keV electrons from the e-gun are injected into the pre-spectrometer and indirectly observed from the detector (64PD) via secondary electrons that they produce if trapped inside the pre-spectrometer, **right:** the e-gun UV light was periodically turned on/off and at the same time the event rate at the detector was measured

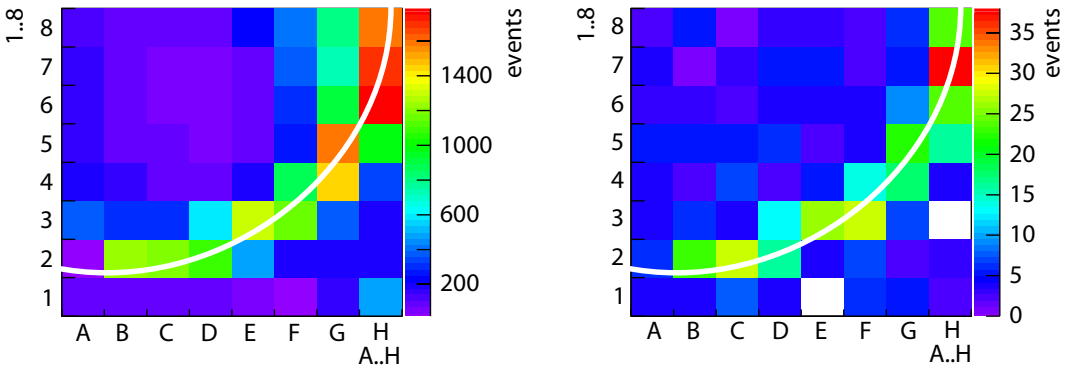

Figure 5.24: accumulated pixel distribution of this measurement, **left:** energy window 15 to 21 keV (secondary electrons), **right:** energy window 27 to 33 keV (primary electrons)

to the analyzing plane and the change of the momentum vector ($\vec{p}$) of the electron is sufficiently large - the angle Θ between $\vec{p}$ and $\vec{B}$ (see figure 4.4) is larger than Θ_{trap} (see equation 4.3) - the electron can be trapped magnetically inside the pre-spectrometer with an energy of 11.5 keV. Anyhow, because Θ is close to Θ_{trap} the electron has a large probability to exit the magnetic trap after an interaction with residual gas molecules. Due to magnetron drift the electron moves in azimuthal direction on a circle within the flux tube. The trapped electron can produce secondary electrons via ionization of residual gas molecules. These electrons are accelerated from the pre-spectrometer potential to an energy of 18.5 keV and can be detected if they are produced in the detector's field of view.

On the right side of figure 5.23 the event rate at the detector and the status of the e-gun shutter is shown. If the e-gun is turned on (10 mm shutter open) the event rate at the detector increases although the detector is not directly hit from the e-gun. After the e-gun is turned off (shutter closed) the event rate decreases again on time scales of several seconds.

Figure 5.24 shows the accumulated pixel distribution of this measurement for two energy windows:

- **left:** 15 to 21 keV (secondary electrons)
- **right:** 27 to 33 keV (primary electrons)

Both distributions show a ring segment at the position where stored particles are expected. The large number of events in the primary window could be explained with a high escape probability of the trapped electrons. As described above, the primary electrons are trapped with Θ close to Θ_{trap} and therefore the probability that Θ is decreased below Θ_{trap} as a result of an interaction with residual gas molecules is relatively high.

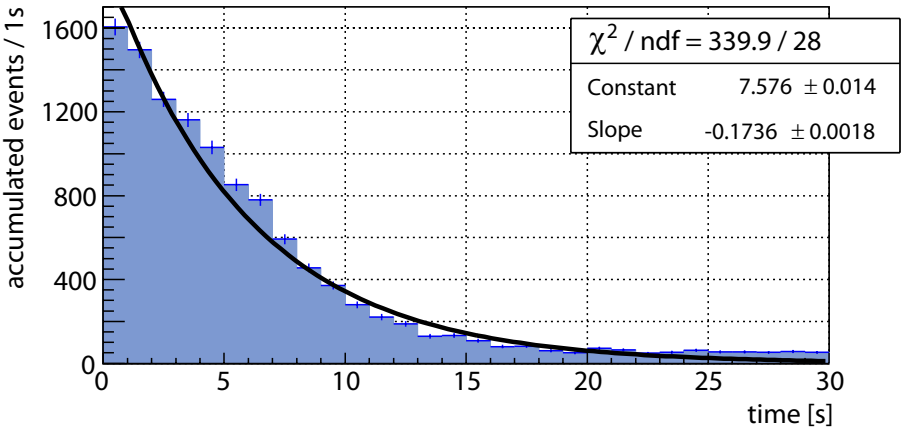

Figure 5.25: accumulated events since the e-gun was turned off, the time constant (storage time) is 5.76 ± 0.06 s

The accumulated number of events in each second for the time period when the e-gun is turned off is shown in figure 5.25. The rate decreases in good approximation exponentially and hence a lifetime of the trapped electrons of 5.76 ± 0.06 s can be determined.

5.5 Background measurement results and conclusions

This section summarizes the background measurements described in 5.4 and discusses several models of the background.

5.5.1 Summary of background measurements

The results of each measurement are presented below:

1a (default configuration) The pre-spectrometer background is not constant over time. Time intervals (up to 2 h) of elevated rate (up to 250 mHz) are observed. Within these intervals the pixel distribution shows ring structures made of 10 to 726 detector events. In order to classify the intervals of elevated rate 4 event classes have been defined (see table 5.5). Between these intervals the average spectrometer background rate (R_{PS}) is 3.2 ± 0.3 mHz.

1b (default configuration) This measurement shows the same background behavior as **1a**, therefore it can be stated that the observed background characteristic is reproducible.

2 (low magnetic field) With a magnetic field of about 2.5 % of the maximum field (4.5 T) no class *I* to *III* events are observed.

3 (dipole mode) This measurement shows two things:

1. The electric dipole mode has no effect on class *III* events.
2. There is no correlation between high voltage instabilities (fluctuations of the tank voltage <1 V) and regions of elevated rate.

4 (increased pressure) For this measurement the pressure was increased with the injection of Argon into the pre-spectrometer from $1*10^{-10}$ mbar to $2*10^{-9}$ mbar. The occurrence of class *I* to *III* is - within the statistical uncertainties - not larger compared to measurement **1**, thus it seems that their occurrence is not connected to the absolute value of the pressure. R_{PS} is 3.4 ± 0.3 mHz and in very good agreement with measurement **1a** (3.2 ± 0.3 mHz), therefore it can be stated that R_{PS} has no strong correlation with the absolute pressure.

5 (detector shifted) The indirect observation of 100% flux tube showed an increase in rate for class *II* + *III* events[15] from 1.6 ± 0.7 1/d (measurement **4**,

[15]This measurement has a low efficiency for the detection of class *I* events, therefore only *II* and

about 60% of the flux tube radius) to 5.3 ± 1.2 1/d. The increase in rate is - within the statistical uncertainties - compatible with the assumption that the ring events are distributed isotropically and thus should increase by a factor of 2.8.

6 (heated getter) The heating of the getter pump (70° C) and the 45° pump port (90° C) showed no significant influence on the occurrence of class *I* to *III* events.

7 (cooled getter) In this measurement the getter pump and most parts of the spectrometer were cooled below 0° C. No significant change in rate (event class *I* to *III*) was observed between this measurement (6.4 ± 0.8 1/d) and measurement **4** (7.1 ± 1.4 1/d).

8a (no getter) This and the following measurements (except **10**) were performed without getter pump, but with active cooling of the pre-spectrometer vessel (around 0° C) in order to reduce the out gassing of the stainless steel walls. A significant reduction (4.8 σ) in rate (event class *I* to *III*) from 6.4 ± 0.8 1/d (measurement **7**) to 2.6 ± 0.6 1/d (this measurement) is observed.

8b (e-gun valve closed) In this measurement the valve between e-gun and pre-spectrometer was closed. As no significant change in R_{I-III} (2.3 ± 0.8 1/d for this measurement, 2.6 ± 0.6 1/d measurement **8a**) was observed, the e-gun chamber as a potential source of the remaining background can be excluded.

8c (Ebara valve closed) The valve in front of one (Ebara) of the two pre-spectrometer TMPs was closed and thus the pumping speed was reduced by a factor of about 2. A rate of $R_{I-III} = 3.6 \pm 0.7$ 1/d was observed.

8d (detector shifted) This measurement is comparable with measurement **5** as it covers 100% of the flux tube radius. The rate of class *II* and *III* events in this measurement (1.6 ± 0.8 1/d) is a factor 3.3 lower compared with measurement **5** (5.3 ± 1.2 1/d).

9 (pressure rise) A significant (5.4 σ) increase of class *I* events (7.9 ± 1.1 1/d) compared to the combination of measurement 8a and 8b (2.0 ± 0.4 1/d) is observed. For class *II* and *III* events no increase is observed.

10 (e-gun) This measurement with the e-gun showed that 11.5 keV electrons can be trapped within the pre-spectrometer with a characteristic time scale of 5.76 ± 0.06 s. Due to systematic effects of this measurement (Θ close to Θ_{trap}) this does not exclude much longer storage times.

III are considered.

5.5.2 Background measurements conclusions

Combining the results of different measurements the following conclusions can be made:

1. The occurrence of class *I* to *III* events is due to the storage of (at least one) high energetic electron (e_t^-) in the pre-spectrometer (measurements **1a** to **10**). This explains the following features observed in the measurements:
   - ring structures: Due to magnetron drift a trapped particle moves in azimuthal direction on a concentrically track within the flux tube and produces secondary electrons - that are observed at the detector with a certain probability - via ionization of residual gas molecules (see also section 5.2).
   - magnetic field dependence: In measurement **2** no *I* to *III* events are observed. At magnetic fields used for this particular measurement (2.5% of $B_{max} = 4.5$ T) the cyclotron radii of e_t^- can be larger than the diameter of the pre-spectrometer (1.6 m for a 9 keV electron at the analysing plane) and hence no e_t^- is trapped. In addition, non adiabatic effects could change Θ of e_t^- in a way that it can exit the pre-spectrometer after a short time.
   - pressure dependence: The number of ionizations N_{ion} of e_t^- for a given start energy can be seen as constant[16]. Because the ionization probability linearly increases with the pressure, the duration of the events should decrease with the same factor while the event rate at the detector should increase accordingly. This is observed e.g. in the comparison of measurement **1a** and **4**.
   - time structure: For a typical event an increase in detector rate towards the end of the event is observed (see figure 5.12). This can be explained with an increase of the cross section (see figure 5.7) for interactions of e_t^- with residual gas molecules as it loses more and more energy - via ionization and inelastic scattering - over time.
   - dipole mode: Simulations for the Mainz spectrometer [94] showed that the dipole mode[17] is not able to remove e_t^- with large energies (>10 keV) via $\vec{E} \times \vec{B}$ drift. This is observed in measurement **3**.
2. The rate of class *I* to *III* events is independent of the absolute pressure in the pre-spectrometer.
3. The occurrence of class *I* to *III* events is distributed isotropically in the (observed) volume of the pre-spectrometer. The left side of figure 5.26 shows the

[16] For single events N_{ion} fluctuates because ionization is a statistical process, but the average value is constant.

[17] The maximum dipole voltage at the pre-spectrometer is 5 kV.

distribution of fitted ring radii [79] for all class *I* to *III* events of measurements with installed NEG pump. A linear increase towards larger radii is observed (for radii > 20 mm (detector edge length 40 mm) the rings became larger than the detector and thus the ring detection efficiency decreases). This is expected for an isotropic distribution because the volume element increases with rdr.

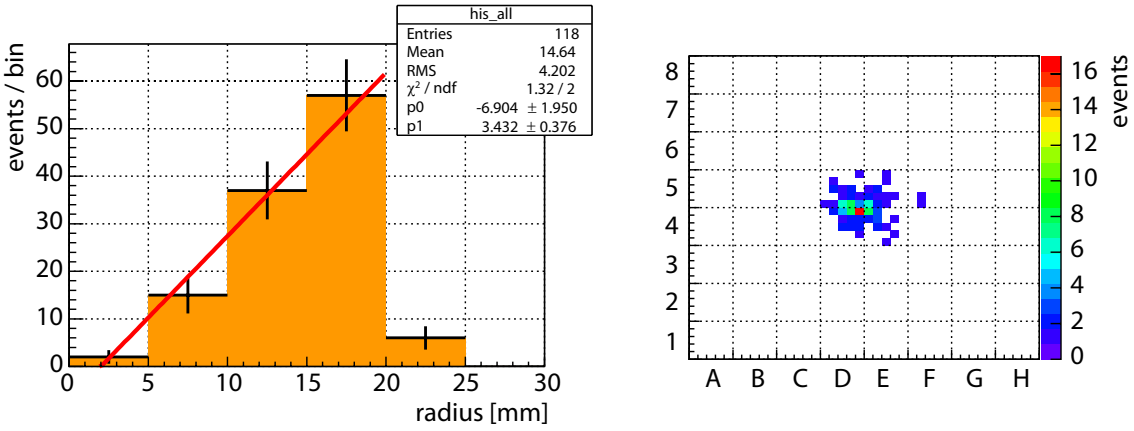

Figure 5.26: **left:** Distribution of fitted ring radii for all class *I* to *III* events of measurements with installed NEG pump. The bin size corresponds to the width of a detector pixel (5 mm). **right:** Distribution of ring centres in sub-pixel resolution (1 mm), the mean value is at the position of pixel D4. This agrees with e-gun measurements that were used to determine the centre pixel for this detector position.

4. The temperature of the getter has no influence on the rate of class *I* to *III* events.
5. Removing the getter pump has an influence on the rate of class *I* to *III* events.
6. The rate of class *I* events depends on the pumping speed of the pre-spectrometer vacuum system (see figure 5.28).

5.5.3 Discussion of different background models

In order to explain the background characteristics of the pre-spectrometer several models are discussed below and their plausibility is tested on the basis of the measurements.

A Penning discharge: It is known from previous measurements (see chapter 4) that Penning discharges can produce ring structures in the pixel distribution. Although the potential configuration for the background measurements was selected carefully with respect to Penning traps, a small trap in the centre of the pre-spectrometer can not be avoided (see section 5.2.1). A Penning

discharge of this trap as the source of class *I* to *III* events can be excluded for several reasons:

- Class *I* to *III* events had been observed close to the centre of the flux tube where the Penning trap depth is < 10 eV. Since this is below the ionization energy of H_2, H_2O and Ar, no Penning discharge is expected.
- The dipole mode has no effect, although it should be able to remove electrons stored inside this trap.
- This hypothesis is in contradiction to conclusions 3, 5 and 6.

B cosmic particles: Cosmic particles could penetrate into the flux tube due to their high energy. Inside the spectrometer volume they could interact with residual gas molecules and thus produce high energetic electrons. Without the need of going into details of such processes, it can be concluded that this kind of background should strongly correlate with the absolute pressure inside the pre-spectrometer. However, no pressure dependence of the background is observed (conclusion 2) therefore this hypothesis can be ruled out.

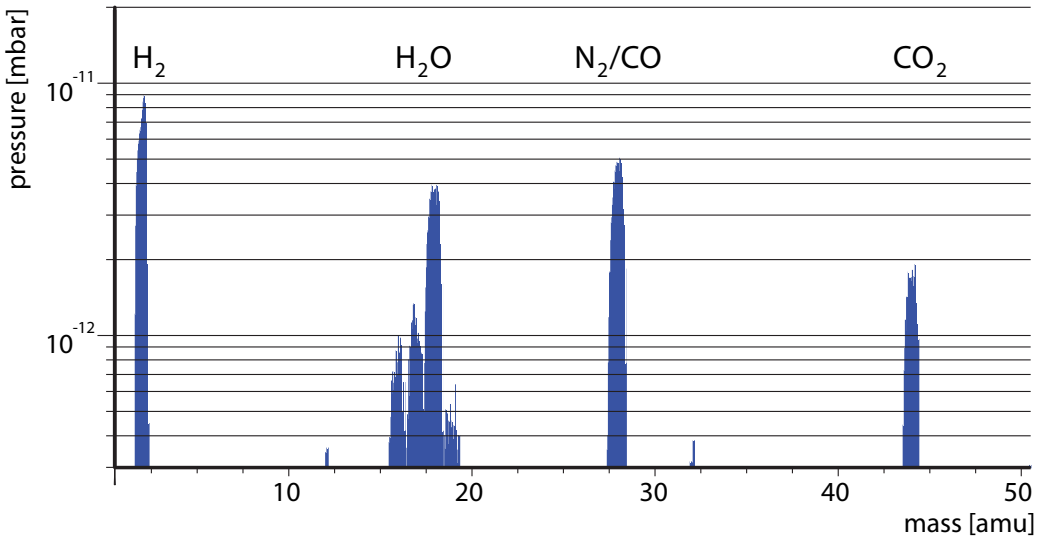

Figure 5.27: Residual gas spectrum after getter activation and bake out of the pre-spectrometer at an absolute pressure of $4*10^{-11}$ mbar (valve between detector and pre-spectrometer closed).

C ^{14}C: In β-decay of ^{14}C an electron with a maximal energy of 156 keV can be produced. This covers the energy range needed to explain the occurrence of class *I* to *III* events. Figure 5.27 shows a residual gas spectrum of the pre-spectrometer. The dominant fraction is H_2 but there are significant contributions of CO and CO_2 originating from the stainless steel of the pre-spectrometer vessel walls. Although the RGA is not calibrated, the amount of

gas containing C can not exceed the total pressure of $4*10^{-11}$ mbar. From this the ^{14}C activity inside the pre-spectrometer can be calculated to $3*10^{-8}$ mBq. This is eight orders of magnitude lower then the observed activity and therefore this hypothesis as source of the background is ruled out.

D ^{39}**Ar**: For the measurements with artificially increased pressure (**4** to **7**) Argon gas (purity 6.0[18]) was injected into the pre-spectrometer. The β-decay of ^{39}Ar releases an electron with a maximum energy of 565 keV and thus makes it a possible candidate for the source of class *I* to *III* events. However, with a natural abundance of $8*10^{-16}$ [73] relative to ^{40}Ar and a lifetime of 269 years the ^{39}Ar activity in the pre-spectrometer at an Argon partial pressure of $2*10^{-9}$ mbar is $2.7*10^{-8}$ mBq. As this is eight orders of magnitude lower then the observed background this hypothesis can be excluded.

E **Radon**: It is known from activity measurements of the getter material (see section 5.1) that it has a ^{219}Rn activity of 8 Bq. Although most of the ^{219}Rn decays inside the getter material, a small fraction could emanate and decay in the pre-spectrometer volume. Due to internal conversion or shake-off processes, high energetic electrons could be released and thus producing class *I* to *III* events. Anyhow, after removal of the getter class *I* to *III* events still occur (but on a lower level) therefore the getter is not the only source of ^{219}Rn. Because this hypothesis is not ruled out, it is discussed in detail below (section 5.5.4).

5.5.4 Radon background model

This model assumes that the pre-spectrometer background (class *0* to *III* events observed in the measurements in section 5.4) is caused by α-decay of different Radon (Rn) isotopes and the accompanying emission of electrons due to internal conversion, Auger transitions or shake-off processes (see section 6.3). The model takes into account the following Rn isotopes of different sources:

- $^{219}\mathrm{Rn}_G$: ^{219}Rn emanating from the NEG pump (see section 5.1)
- $^{219}\mathrm{Rn}_B$: ^{219}Rn emanating from the pre-spectrometer
- $^{220}\mathrm{Rn}_B$: ^{220}Rn emanating from the pre-spectrometer

It is assumed that a possible ^{222}Rn contribution to the observed background can be neglected due to its small decay probability (order of 10^{-5}) inside the pre-spectrometer (see table 5.17). ^{220}Rn emanation of the getter material (activity 19 ± 4 mBq/kg) is not taken into account because it is much less compared to the ^{219}Rn activity (4.4 Bq/kg).

Table 5.17 shows the decay probabilities of ^{219}Rn, ^{220}Rn and ^{222}Rn inside the pre-spectrometer for different pumping speeds. In case of pump configuration "0" (see

[18] 6.0 means that 99.9999% of the gas is Argon.

Table 5.17: Radon decay probabilities inside the pre-spectrometer for different pumping speeds, m: index of measurement, pump: 0 = no pump (see section 5.4.13), E = Ebara, L = Leybold, pumping speed: effective pumping speed for ^{220}Rn in l/s, τ_p: pre-spectrometer (V = 8.5 m^3) pump out time in s, ^{219}Rn: decay probability of ^{219}Rn in the pre-spectrometer volume in %, ^{220}Rn: decay probability for ^{220}Rn, ^{222}Rn: decay probability for ^{222}Rn

m	pump	pumping speed [l/s]	τ_p [s]	^{219}Rn [%]	^{220}Rn [%]	^{222}Rn [%]
d	0	9.2	924	99.5	96.9	2.16
a	E	194	43.8	88.5	35.3	$9.2*10^{-3}$
c	L	208	40.9	87.7	33.8	$8.6*10^{-3}$
b	E+L	402	21.1	78.7	20.8	$4.4*10^{-3}$

measurement **9**) average values[19] for pumping speed and τ_p are given. The decay probabilities were calculated as weighted averages. The large decay probability of ^{219}Rn is due to its rather short life time (5.7 s) compared to τ_p.

Figure 5.28 summarizes the rates of class *I* to *III* events for different pumping speeds and distinguishes whether the NEG pump was installed or not. It is assumed that class *I* events are caused by trapped Auger electrons originating from a M vacancy which is caused by a shake-off process of the emitted α-particle and thus class *I* events are an indicator of the total Rn decay activity independent of the isotope. For class *II* and *III* events a large number of secondary electrons is produced therefore high energetic primary electrons are needed which occur as internal conversion electrons in the decay of ^{219}Rn with a probability of 3.25% (for ^{220}Rn and ^{222}Rn the probability for internal conversion is $< 0.1\%$). Hence class *II* and *III* events can be seen as an indicator of ^{219}Rn activity.

In order to determine the activity of the three Rn contributions a system of linear equations of the following type was created for class *I* events:

$$r_{I,m} = \sum_{i=1}^{3} Rn_i \cdot p_{i,m} \tag{5.1}$$

$r_{I,m}$ is the measured rate of class *I* events for one of the four measurements in figure 5.28, m is the index of the measurement (a to d), Rn_i is the activity of the different Rn contributions (^{220}Rn$_B$, ^{219}Rn$_B$, ^{219}Rn$_G$) and $p_{i,m}$ the decay probability of Rn isotope i for measurement m (see table 5.17).

The system is overdetermined (3 parameters and 4 measurements), therefore the parameters were determined in a fit with a user defined function using the ROOT TMinuit framework. The results of the fit are shown in table 5.18 and figure 5.28.

[19] During the measurement time of 158 h there had been 75 valve cycles.

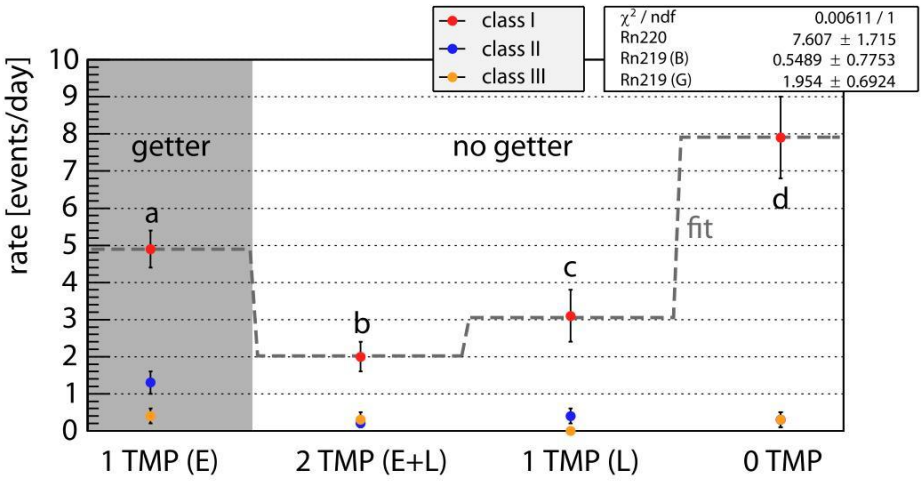

Figure 5.28: dependence of the rate of class *I* to *III* events on pumping speed (see table 5.17)

The good agreement of the fit and the measured data is remarkable and a first test of the consistency of the model. The decay probabilities $p_{i,m}$ are calculated for the specific life times of the Rn isotopes. If there was a contribution of another radioactive isotope with a different life time, no such good agreement is expected.

A further test of the model can be done if the ratio of class *I* to class *II*+*III* events for ^{219}Rn is considered. The probability of a class *I* event (creation of a M shell vacancy) is 3.7 ± 0.5 % for each ^{219}Rn decay. The probability for *II*+*III* events is 3.25% (internal conversion) thus the expected ratio is 1.1. A fit of the measured ratio of all 4 measurements gives a value of 1.1 ± 0.5 which is within the statistical uncertainties in good agreement with the expected value.

A similar system like equation 5.1 was defined for the combination of the rates of class *II* and *III* events in order to obtain values for $^{219}\mathrm{Rn}_B$ and $^{219}\mathrm{Rn}_G$ from independent measurement values. Afterwards the activity values of $^{219}\mathrm{Rn}_B$, $^{219}\mathrm{Rn}_G$ were combined with the ones obtained from class *I* events (see table 5.18).

Table 5.18 shows the activities of the different radon sources in the pre-spectrometer. The activity for $^{220}\mathrm{Rn}_B$ was calculated from the occurrence of class *I* events under the assumption that a Rn decay creates a class *I* event with a probability of 3.7 ± 0.6 % (this is the probability for the creation of a M shell vacancy and a subsequent emission of an Auger electron). The activities for the ^{219}Rn isotopes were calculated from a combination of the results obtained from class *I* and class *II*+*III* events. For the calculation of the activities of *II*+*III* it is assumed that class *II* and *III* events are due to internal conversion after a ^{219}Rn decay which occurs with a 3.25% probability. In order to calculate the total activity it was taken into account that the detector covers only 28.5% of the flux tube and that the flux tube volume (2.13 m^3) is only 25% of the pre-spectrometer volume (8.5 m^3).

Table 5.18: Pre-spectrometer Radon activities, source: Radon isotope, class: event class taken into account, rate: rate of events defined in class, corrected for pumping effects in the observed fraction of the flux tube, activity: Radon decay activity in the observed fraction of the flux tube, total activity: expected Radon decay activity in the complete volume of the pre-spectrometer.

source	class	rate [1/d]	activity [mBq]	total activity [mBq]
$^{219}Rn_B$	I	0.5 ± 0.8	0.2 ± 0.3	2 ± 4
$^{219}Rn_G$	I	1.9 ± 0.7	0.6 ± 0.2	8 ± 3
$^{219}Rn_B$	II+III	0.55 ± 0.14	0.2 ± 0.05	2.7 ± 0.7
$^{219}Rn_G$	II+III	1.4 ± 0.4	0.5 ± 0.15	7 ± 2
$^{219}Rn_B$	I to III	-	0.2 ± 0.15	2.4 ± 2.0
$^{219}Rn_G$	I to III	-	0.55 ± 0.13	7.5 ± 1.8
$^{220}Rn_B$	I	7.6 ± 1.7	2.4 ± 0.7	33 ± 9

Assuming that the decay chains of ^{219}Rn (^{235}U, see table 6.2) and ^{220}Rn (^{232}Th, see table 6.1) are in equilibrium the ratio ^{232}Th/^{238}U can be calculated to 2.0 ± 1.7. This is in the range of the natural abundance of the isotopes.

Table 5.19: summary of background rates, m: index of measurement, rate: measured rate at the detector after applying PSA and TCF filter, rate_{I-III}: average contribution to the rate from class *I* to *III* events, rate_u: contribution to the rate after subtracting rate_{I-III} and detector background (6.3 ± 0.2 mHz), rate_0: possible contribution to the rate from class *0* events.

m	rate [mHz]	rate_{I-III} [mHz]	rate_u [mHz]	rate_0 [mHz]
a	20.1 ± 0.1	7.86 ± 0.07	5.9 ± 0.3	0.92 ± 0.18
b	12.1 ± 0.1	3.77 ± 0.06	2.0 ± 0.3	0.38 ± 0.10
c	8.8 ± 0.1	1.04 ± 0.04	1.4 ± 0.3	0.58 ± 0.16
d	20.4 ± 0.2	11.29 ± 0.14	2.8 ± 0.3	1.48 ± 0.32

Table 5.19 gives an overview of the average event rates at the detector for the four measurement configurations. After subtracting the detector background and the known contribution of class *I* to *III* events a rate of < 6 mHz remains. From section 6.3 it is known that after each ^{220}Rn[20] α-decay the daughter atom has a charge between -2*e and +10*e (or even more), but in most cases (>90%) it is neutral and thus has emitted two electrons. These electrons can have energies in the order of 10 eV and hence their probability that they escape at the detector side - where they are detected as class *0* events - is 30% (assuming the minimal trapping probability of 40%). From the activities of the Rn isotopes (see table 5.18 and their

[20]Because ^{219}Rn has the same atomic shell structure, a similar behaviour is assumed.

decay probability inside the pre-spectrometer (see table 5.17) the rate originating from class *0* events was calculated (see column rate_0 in table 5.19). Because $\text{rate}_0 < \text{rate}_u$ for all measurements this is another successful test of the model.

5.5.5 Pre-spectrometer Radon sources

In the previous section the activities of three different Radon sources inside the pre-spectrometer were determined. Anyhow, except of $^{219}\text{Rn}_G$ - which emanates from the getter material (see section 5.1) - the sources can not be derived from the background measurements. This section will discuss several possible sources of $^{219}\text{Rn}_B$ (2.4 ± 2.0 mBq) and $^{220}\text{Rn}_B$ (33 ± 9 mBq).

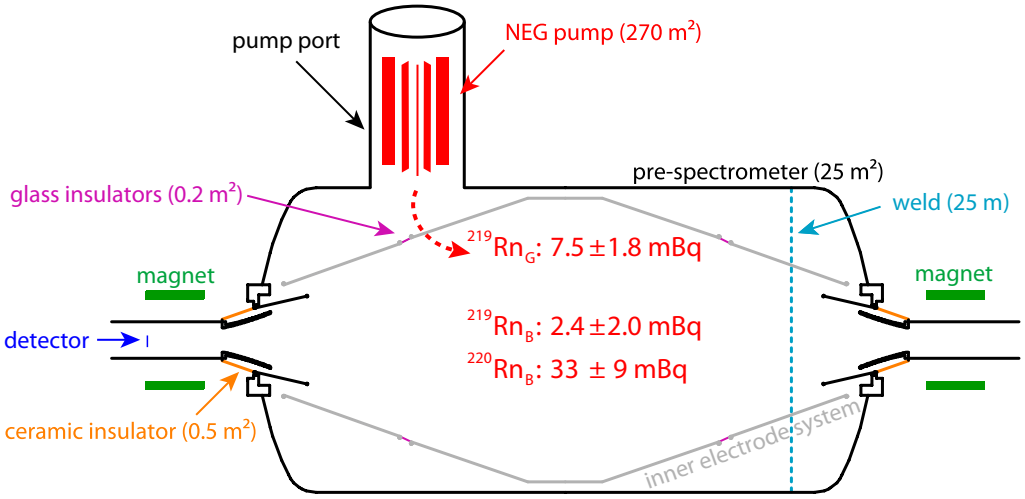

Figure 5.29: overview of possible pre-spectrometer Radon sources

Figure 5.29 gives an overview of possible Radon sources inside the pre-spectrometer. From simulations performed with SRIM [55] it is estimated that Radon only emanates from a 30 nm thick layer below the surface of the material. Therefore the source needs to have a large surface or a high specific activity.

- pre-spectrometer vessel: With a surface of 25 m^2 a specific activity of 5.6 Bq/kg would be needed for the observed $^{220}\text{Rn}_B$ activity. The expected value for steel is 0.071 ± 0.001 Bq/kg [86] and thus about two orders of magnitude smaller. This makes it unlikely that the pre-spectrometer vessel is the dominant Radon source.
- welds: Due to the small surface of the welds (≈ 0.25 m^2) compared to the tank surface the specific activity needed to explain the observed $^{220}\text{Rn}_B$ activity increases to 550 Bq/kg. This would correspond to a Thorium (Th)

contamination of the weld on the level of 10^{-4} g/g. In case a thoriated tungsten welding rod (Th content usually 1 to 2% [92]) was used for welding this level might have been achieved. Anyhow - according to the manufacturer of the pre-spectrometer tank (SDMS) - only Th free welding rods (TUNGSTENE CERIUM or LANTHANE) had been used. It remains the possibility that devices attached to the pre-spectrometer (e.g. HV feed throughs, Thermocouple, vacuum gauges,...) contain a thoriated weld.

- ceramic insulators: The ceramic insulators on both sides of the pre-spectrometer are covered with a 0.1 mm thick glass layer. An activity measurement of the glass gave a value of 5 Bq/kg for ^{220}Rn [54]. From this activity only 0.17 mBq are released into the pre-spectrometer which is 2 orders of magnitude less then the observed activity.
- glass insulators: Each of the inner electrodes can have an individual potential. Glass insulators are used in order to separate the electrodes electrically from each other and from the pre-spectrometer tank. The activity of the glass insulators was measured and gave a total activity of 1.7 ± 0.8 Bq/kg. Due to a small surface of 0.2 m^2 only a activity of 0.02 mBq is released into the pre-spectrometer which is three orders of magnitude less than the observed value.
- detector: The first stage of detector electronics (64 JFETs) is directly mounted on a ceramics plate beyond the silicon detector inside the UHV region (see figure 5.30). In addition 40 heating resistors and 4 PT1000 temperature sensors are mounted on the ceramics. Assuming a ^{220}Rn activity of 0.91 ± 0.09 Bq/device [86] an activity of 7.4 mBq would be released into the pre-spectrometer. This is at the same order of magnitude as the observed activity.

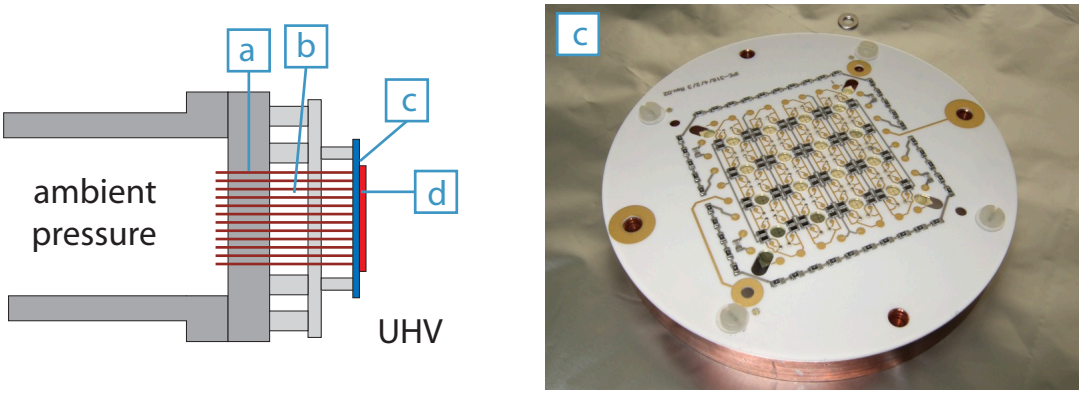

Figure 5.30: **left**: Schematics of the detector (64PD), a: DN100 flange with 100 signal feedthrough pins, b: connector pins, c: ceramics plate with electronic devices, d: silicon wafer, **right**: Backside of ceramics plate, pictures taken from [50]

From the estimation of the possible contribution of different parts of the pre-spectrometer test setup to the measured Rn activity it seems that the detector electronics on the ceramics plate could be the dominant Rn source. Anyhow, further investigations to determine the Rn source(s) are necessary in order to make a quantitative prediction of the Rn induced background at the main spectrometer.

6 Radon emanation processes in MAC-E filter

Radon emanation can be a major background source in MAC-E filters. Because Radon is a neutral noble gas, it is not affected by the magnetic shielding of a MAC-E filter and thus is able to decay inside the volume of a MAC-E filter. The Radon decay process releases electrons with energies up to several 100 keV, which can produce a large number of secondary electrons via subsequent ionization of residual gas molecules, in case they are magnetically trapped inside the MAC-E filter.

6.1 Introduction: Pre-spectrometer background

Measurements of the KATRIN pre-spectrometer background characteristics showed that there are two major background processes in MAC-E filters: discharges of electromagnetically trapped particles (see chapter 4) and Radon emanation processes (see chapter 5).

Storage conditions for electrically charged particles (e.g. Penning traps) are created due to the presence of strong magnetic and electric fields within a MAC-E filter. In case the storage conditions cause a discharge, large background rates (> 1 kHz) were observed at the pre-spectrometer. A careful design and precise manufacturing (mm level) of the pre-spectrometer electrodes in the region of strong electric fields could remove the storage conditions and thus prevent any discharge.

The KATRIN spectrometers are designed in a way that the spectrometer vessel itself can be put on high voltage (U_{tank}) in order to create the retarding potential. Low energetic (order of 10 eV) secondary electrons created at the inner surface of the vessel can be produced by various processes including, but not limited to, cosmic rays, natural radioactivity and photoelectric effect. If theses electrons reach the flux tube, they are accelerated by U_{tank} and arrive at the detector with the same energy as the signal electrons from β-decay (and therefore can not be distinguished from β-electrons). The guiding magnetic field of a MAC-E filter provides an intrinsic protection against such background electrons (magnetic shielding). In order to reach the flux tube, electrons originating from the vessel wall have to move perpendicular to the guiding magnetic field lines. This motion causes a Lorentz force that reflects the electrons back to the vessel wall. Measurements at the pre-spectrometer using an x-ray tube to artificially create background electrons, showed that the magnetic

shielding is working very well already at low magnetic fields (2% of the maximum magnetic field[1] at the pre-spectrometer) [63].

The very effective magnetic shielding of the pre-spectrometer prevents low energetic electrons (secondary electrons have typical energies < 50 eV) from entering the flux tube[2]. Higher energetic electrons and negative ions could penetrate into the flux tube and produce background electrons via ionization of residual gas molecules. This kind of background should have a radial dependence and should increase towards larger flux tube radii. Anyhow, the low pressure inside the KATRIN spectrometers (order of 10^{-11} mbar) would require a strong source of high energetic electrons or negative ions in order to produce a background on the mHz level. Such a source can not (only) be explained with natural radioactivity or cosmic rays.

Electrically neutral particles such as photons or gas molecules are not affected of magnetic or electric fields and therefore are able to reach any point within the spectrometer. Of concern with regard to background is Radon, which is produced within the decay chains of natural radioactivity (see below) and could emanate from materials within the spectrometer. As a neutral gas particle it would decay isotropically in the volume of the spectrometer. Electrons, released in the decay can produce a large number of background electrons via subsequent ionization of residual gas molecules in case they are magnetically trapped inside the spectrometer. This kind of background was observed at the pre-spectrometer with an average background rate of 27 ± 6 mHz (see chapter 5).

6.2 Decay chains of ^{232}Th, ^{235}U and ^{238}U

The natural abundance of ^{232}Th, ^{235}U and ^{238}U yields three different radioactive decay chains. Within each decay chain the initial atomic nuclei decays through a sequence of α and β-decays until a stable Lead (Pb) nucleus is created.

The decay chains are shown below. Each table shows the sequence of *parent and daughter* nuclei for the most likely *branching ratio* (usually 1 or close to 1). The column *Decay* indicates the decay channel for the corresponding branching ratio. *N(atoms)* is the number of atoms of each isotope, assuming the decay chain is in equilibrium (all isotopes have the same activity *A(Bq)*).

For MAC-E filters the emanation of Radon is important with regard to background processes. As a noble gas, Radon is able to penetrate into the flux tube and thus decay inside the volume of a MAC-E filter.

[1] This corresponds to 0.3 mT in the analysing plane of the pre-spectrometer which is comparable to the magnetic field of the main spectrometer at the analyzing plane.

[2] This is true for an axially symmetric magnetic field. For non-axially symmetric magnetic fields, trapped electrons could slowly (in the order of 1 m/s) drift into the flux tube [66].

6.2.1 ^{232}Th decay chain (thorium series)

Parent+Daughters	Half-life	Branching Ratio	Decay	N(atoms)	A(Bq)
90 Th232	1.4E10 y	1; 1.00E-05; 1.40E-11; 2.78E-12; 2.78E-12	α; ß-,ß-; SF; Ne24/Ne26; Ne26	6.4E+20	1000.0
88 Ra228	5.75 y	1	ß-	2.6E+11	1000.0
89 Ac228	6.15 h	1	ß-	3.2E+07	1000.0
90 Th228	1.91 y	1; 1.13E-13	α; O20	8.7E+10	1000.0
88 Ra224	3.64 d	1; 4.00E-11	α; C14	4.5E+08	1000.0
86 Rn220	55.8 s	1; 1.00E-05	α; ß-,ß-	8.0E+04	1000.0
84 Po216	150 ms	1; 1.00E-05	α; ß-,ß-	2.2E+02	1000.0
82 Pb212	10.64 h	1	ß-	5.5E+07	1000.0
83 Bi212	1.01 h	0.64056; 3.59E-01; 1.40E-04	ß-; α; ß-,α	5.2E+06	1000.0
84 Po212	298 ns	1	α	0.0E+00	0.0
82 Pb208 Stable	stable			3.2E+16	0.0
81 Tl208	3.05 m	1	ß-	9.5E+04	359.3
2 He4 Stable	stable			0.0E+00	0.0

Figure 6.1: ^{232}Th decay chain (Thorium series), data from [17]

Figure 6.1 shows a table of the thorium series. Within this series ^{220}Rn is produced. Measurements at the pre-spectrometer showed that this isotope dominates the Rn activity inside the pre-spectrometer test setup.

6.2.2 ^{235}U decay chain (actinium series)

The actinium series is summarized in figure 6.2. Within this series ^{219}Rn is produced. Measurements of the NEG material used for the pre-spectrometer NEG pump showed that the NEG material has a specific ^{219}Rn activity of 4.4 Bq/kg (see section 5.1).

6.2.3 ^{238}U decay chain (radium series)

Figure 6.1 shows a table of the radium series. Within this series ^{222}Rn is produced. ^{222}Rn is of less concern for the KATRIN spectrometers regarding background. Because of its long half-life (3.82 d) it is usually pumped out before it decays in the volume of the spectrometer. For the pre-spectrometer the probability that a ^{222}Rn atom decays in the volume of the pre-spectrometer (before it gets pumped out) is on the order of 10^{-5}.

Parent+Daughters	Half-life	Branching Ratio	Decay	N(atoms)	A(Bq)
92 U235	7.0E8 y	1; 7.20E-11; 8.00E-12; 8.00E-12; 8.00E-12	α; SF; Ne20; Ne25; Mg28	3.2E+19	999
90 Th231	1.06 d	1; 4.00E-13	ß-; α	1.3E+08	999
91 Pa231	3.3E4 y	1; 1.34E-11; 3.00E-12; 9.90E-15	α; Ne24; SF; F23	1.5E+15	999
89 Ac227	21.79 y	0.9862; 1.38E-02	ß-; α	9.9E+11	999
90 Th227	18.72 d	1	α	2.3E+09	985
88 Ra223	11.43 d	1; 8.90E-10	α; C14	1.4E+09	999
86 Rn219	3.96 s	1	α	5.7E+03	999
84 Po215	1.78 ms	1; 4.00E-06	α; ß-	2.6E+00	999
82 Pb211	36.1 m	1	ß-	3.1E+06	999
83 Bi211	2.17 m	0.99727; 2.73E-03	α; ß-	1.9E+05	999
81 Tl207	4.77 m	1	ß-	4.1E+05	996
82 Pb207 Stable	stable			3.0E+16	0
87 Fr223	21.8 m	0.99994; 6.00E-05	ß-; α	2.6E+04	14
2 He4 Stable	stable			0	0

Figure 6.2: ^{235}U decay chain (Actinium series), data from [17]

Parent+Daughters	Half-life	Branching Ratio	Decay	N(atoms)	A(Bq)
92 U238	4.5E9 y	0.999945; 5.46E-07; 2.20E-12	α; SF; ß-,ß-	2.0E+20	998
90 Th234	24.09 d	1	ß-	3.0E+09	998
91 Pa234 m	1.17 m	0.9985; 1.50E-03; 1.00E-12	ß-; IT; SF	1.0E+05	998
92 U234	2.5E5 y	1; 1.70E-11; 1.40E-13; 9.00E-14; 9.00E-14	α; SF; Mg28; Ne24/Ne26; Ne26	1.1E+16	997
90 Th230	7.5E4 y	1; 5.60E-13; 2.50E-13	α; Ne24; SF	3.4E+15	997
88 Ra226	1.6E3 y	1; 1.00E-05; 2.60E-11	α; ß-,ß-; C14	7.3E+13	997
86 Rn222	3.82 d	1	α	4.8E+08	997
84 Po218	3.1 m	0.99981; 1.90E-04	α; ß-	2.7E+05	997
82 Pb214	26.8 m	1	ß-	2.3E+06	997
83 Bi214	19.9 m	0.99979; 2.10E-04; 3.00E-05	ß-; α; ß-,α	1.7E+06	997
84 Po214	1.6E2 µs	1	α	0.0E+00	0
82 Pb210	22.17 y	1; 1.90E-08	ß-; α	1.0E+12	997
83 Bi210	5.01 d	0.999999; 1.32E-06	ß-; α	6.2E+08	997
84 Po210	1.4E2 d	1	α	1.7E+10	997
82 Pb206 Stable	stable			3.0E+17	0
2 He4 Stable	stable			0.0E+00	0

Figure 6.3: ^{238}U decay chain (Radium series), data from [17]

6.3 Electron emission following α-decay

The α-decay is a transition of a nucleus (X) with atomic number Z and mass number A to a nuclei (Y) with Z-2 and A-4 while emitting a He nuclei (α-particle):

$$ {}^{A}_{Z}X \rightarrow {}^{A-4}_{Z-2}Y + {}^{4}_{2}He \tag{6.1} $$

In addition to the α-particle, electrons of different energies (order of 1 eV to 100 keV) can be released due to processes accompanying the α-decay (see below).

6.3.1 Internal conversion electrons

Internal conversion is an electromagnetic decay process. Inner-shell electrons[3] have a finite probability to be at the position of the nucleus and thus an excited nucleus is able to transfer its energy to such an electron in a first order process. This process of de-excitation competes with the emission of γ-rays. The ratio between the rate of emitted electrons and the rate of emitted γ-rays is defined as the conversion coefficient α. In addition, partial conversion coefficients are defined for the different atomic shells (e.g. α_K, α_L,...). The conversion coefficient α increases with Z and decreases rapidly with increasing transition energy [93]. Therefore, internal conversion is the dominant process for low-energy nuclear transitions in heavy-Z nuclei.

Conversion electrons are emitted as mono energetic electrons. Compared to the energy of the accordant γ-ray, the energy of the conversion electron is reduced with its binding energy.

6.3.2 Shake-off electrons

Any nuclear transition that changes the charge Z or charge distribution in the central core of the atom (e.g. internal conversion) is accompanied with a restructuring process of the atomic shells. Within this process, electrons can be emitted. The probability of the electron emission increases with $(\Delta Z)^2$. In addition, the emission probability depends on the atomic shell and increases from the K shell towards the valence shell. For α-decay the overall probability is nearly unity[4] [34].

Table 6.1 shows the relative emission probabilities of electrons in different shells for the decay of ^{216}Rn. The emission probability of an M electron is already on a percent level. The total number of emitted electrons in case of ^{220}Rn decay is shown in figure 6.1.

[3] essentially K and L shell electrons

[4] Each α-decay is accompanied with the emission of (at least) one electron.

Table 6.1: electron emission probabilities per ^{216}Rn α-decay, data taken from [34]

atomic shell	emission probability
K	$1.88 \pm 0.15 * 10^{-6}$
L	$7.9 \pm 0.4 * 10^{-4}$
M	$2.3 \pm 0.3 * 10^{-2}$

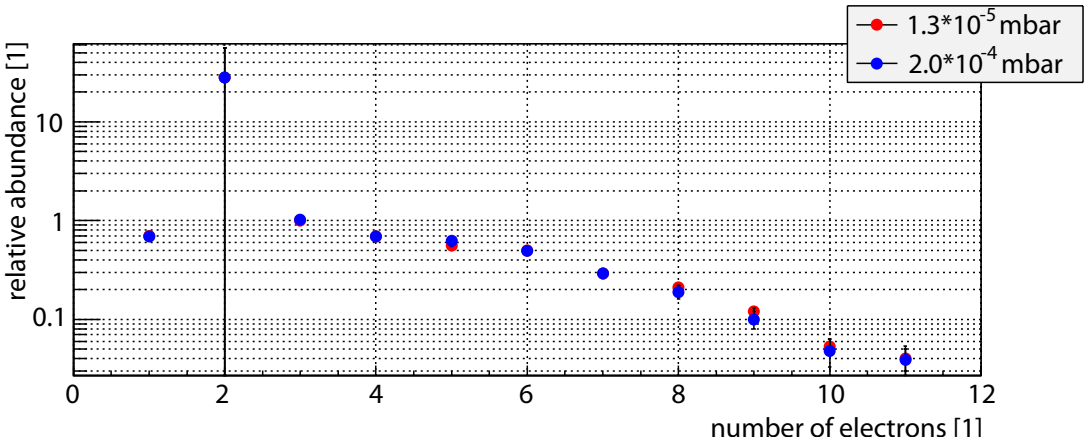

Figure 6.4: number of electrons released during α-decay of ^{220}Rn normalized to the emission of 3 electrons, data obtained from the measurement of the charge of ^{216}Po, measured for two different pressures, data from [89]

6.3.3 Auger and Coster-Kronig electrons

Internal conversion or shake-off processes can produce a vacancy in inner shells. If an electron from a higher energetic level fills the vacancy, energy is released. The energy can be emitted in different processes which are shown in figure 6.5 for the example of a L shell vacancy:

- **γ-ray fluorescence**: The energy is released as a photon.
- **Auger transition**: The vacancy is filled with an electron of a larger principal quantum number. Afterwards, the released energy is transferred to another electron of larger principal quantum number which is ejected from the atom with a discrete energy. Such an electron is called Auger electron.
- **Coster-Kronig transition**: In principle the same as an Auger transition but the vacancy is filled with an electron of the same principle quantum number and different orbital quantum number. The ejected electron is called Coster-Kronig electron.

Both - Auger and Coster-Kronig - transitions create a second vacancy and thus a cascade of events releasing several electrons and γ-rays - depending on atomic yields - can be started.

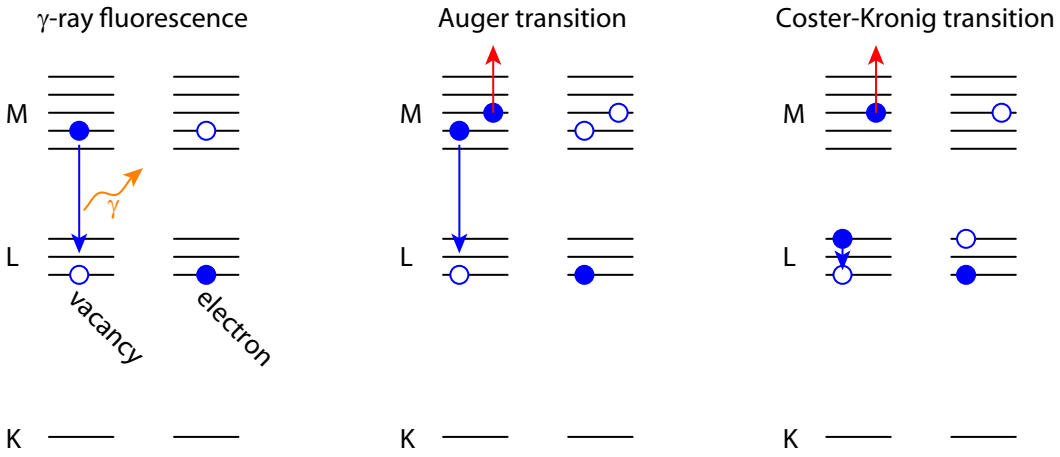

Figure 6.5: schematic overview of processes that could follow a L shell vacancy

6.4 Radon emanation in the pre-spectrometer

Measurements of the pre-spectrometer background characteristics revealed that Radon emanation is a significant background source in MAC-E filters (see chapter 5).

The Radon background process works the following way. Within the natural decay chains (see section 6.2) different Radon isotopes (^{219}Rn, ^{220}Rn and ^{222}Rn) are produced, which emanate from a thin surface layer (< 30 nm) into the volume of the pre-spectrometer where they decay. Electrons released in processes accompanying the α-decay can produce large numbers (>2000) of secondary background electrons depending on their initial energy:

- **Shake off electrons**: One or more of these electrons are produced in each α-decay (see figure 6.4). Because they have low energies (order of 10 eV) they create at maximum a few secondary background electrons via ionization of residual gas molecules. These electrons arrive at the detector as a non resolvable single event background (class *0* events).
- **Auger and Coster-Kronig electrons**: These electrons have energies in the order of 1 keV for a M shell vacancy created in an α-decay[5]. They have a good chance ($> 80\%$, see figure 5.3) to be magnetically trapped inside the pre-spectrometer and create several (order of 10) secondary electrons via ionization of residual gas molecules. The secondary electrons arrive at the detector on a ring like structure due to the magnetron motion of the trapped primary electron and are responsible for the observed class *I* events (see chapter 5).
- **Conversion electrons**: They appear with a probability of 3.25% for each ^{219}Rn decay (for ^{220}Rn and ^{222}Rn the probability is less than 0.1%) and can

[5]The probability that a M shell vacancy is created in an α-decay is between 2 and 4%, depending on the energy of the α-particle and thus on the Radon isotope.

have energies up to 501 keV whereas 178 keV (1.27%) and 254 keV (0.74%) are the most likely ones. The probability to be magnetically trapped is close to 100% and due to their high energy they create thousands of secondary electrons which are detected as class *II* and *III* events (see chapter 5). Depending on the pressure, the primary trapped electron can be stored on long time scales ($\approx$ 1 h for a pressure of 10^{-10} mbar).

In order to test the hypothesis of Radon induced background and to determine the activity of possible Radon sources, various measurements had been performed at the pre-spectrometer (see chapter 5). Measurements with different effective pumping speeds for Radon - and therefore different decay probabilities for Radon isotopes inside the pre-spectrometer (see table 5.17) - showed that the observed pre-spectrometer background is due to the Radon isotopes ^{219}Rn and ^{220}Rn. After removing the NEG pump, a significant reduction (see table 6.2) of the ^{219}Rn activity was observed. Anyhow, a measurable ^{219}Rn and ^{220}Rn activity remains. Hence it is concluded that there are three components: ^{219}Rn emanation from the getter material ($^{219}Rn_G$) and ^{219}Rn and ^{220}Rn emanation from one (or more) source(s) inside the pre-spectrometer test setup ($^{219}Rn_B$ and $^{220}Rn_B$). For a detailed discussion on possible sources see section 5.5.5.

Table 6.2: pre-spectrometer Radon (Rn) emanation results, *source*: Rn emanation from the getter pump ($^{219}Rn_G$) or from one (or more) source(s) inside the pre-spectrometer test setup ($^{219}Rn_B$ and $^{220}Rn_B$), *meas. activity*: measured Rn activity in the detectors field of view, *meas. background*: average measured background rate caused of Rn decays, *total activity*: calculated Rn activity in the total volume of the pre-spectrometer, *total background*: calculated average background rate for 100% flux tube

source	$^{219}Rn_G$	$^{219}Rn_B$	$^{220}Rn_B$
meas. activity [mBq]	0.55 $\pm$ 0.13	0.2 $\pm$ 0.15	2.4 $\pm$ 0.7
meas. background [mHz]	5.5 $\pm$ 1.2	1.8 $\pm$ 1.1	0.6 $\pm$ 0.11
total activity [mBq]	7.5 $\pm$ 1.8	2.4 $\pm$ 2.0	33 $\pm$ 9
total background [mHz]	19 $\pm$ 4	6 $\pm$ 4	2.1 $\pm$ 0.4

Table 6.2 shows the results of the pre-spectrometer Radon background measurements. For each source the measured activity (number of Radon decays observed in the detectors field of view) and average[6] background rate - for an effective pumping speed of 194 l/s (1 TMP) for Rn - is given. Assuming an isotropic distribution of the Radon decays (see figure 5.26) the total activity inside the pre-spectrometer and the background rate for 100% of the flux tube (the detector covers only 28.5% of the flux tube) were calculated. Due to the facts that ^{219}Rn has a shorter lifetime (5.7 s) compared to ^{220}Rn (80.5 s) - therefore ^{219}Rn has a larger decay probability

[6]The actual background behaviour is time dependent. Intervals of elevated rate following a Radon decay alternate with time intervals of almost no background events (e.g. see figure 5.10).

(factor 2.5 for one TMP) inside the pre-spectrometer - and that ^{219}Rn emits conversion electrons, the background rate is dominated from the ^{219}Rn contributions. In average a single ^{219}Rn decay produces about 20 times[7] more background events than a ^{220}Rn decay.

6.5 Implications for the main spectrometer

Measurements at the pre-spectrometer test setup, which acts as a prototype for the main spectrometer, showed that Radon (Rn) emanation is a considerable background source (see above). This section describes the implications of Radon emanation for the main spectrometer.

6.5.1 ^{219}Rn emanation from the main spectrometer NEG pump

The Rn induced background at the pre-spectrometer is dominated from ^{219}Rn emanation from the NEG (non-evaporable getter) material. For an estimate of the ^{219}Rn induced background at the main spectrometer, the following needs to be considered:

- **Getter material**: The main spectrometer NEG pump will use a low activity NEG material (see figure 5.2). In 2012 (the planned start date for the neutrino mass measurements) the specific activity of the low activity material will be about 2 Bq/kg which is a factor 2 lower compared to the standard material used for the pre-spectrometer at the time of the pre-spectrometer background measurements (2009 and 2010).
- **Getter length**: It is planned to use 3 km of NEG strips (about 30 times more than at the pre-spectrometer) at the main spectrometer in order to create the H_2 pumping speed needed (10^6 l/s) to achieve a pressure in the order of 10^{-11} mbar. Therefore the total ^{219}Rn activity of the main spectrometer NEG pump is about 120 Bq. Assuming the emanation efficiency measured at the pre-spectrometer (10^{-3}), the ^{219}Rn activity in the volume of the main spectrometer would be about 120 mBq (or 1 decay every 8 s).
- **Pumping system**: The main spectrometer pumping system has an effective Radon pumping speed of 5400 l/s [54]. Due to the large volume of the main spectrometer (1240 m^3), the pump out time is rather long (τ_p = 230 s) and therefore the ^{219}Rn decay probability inside the main spectrometer volume is close to 1 (97.6%). For the background rate at the detector only the flux tube volume ($\approx$ 750 m^3, this is about 60% of the main spectrometer volume) is relevant.

[7] This is specific for the pre-spectrometer and is not valid for the main spectrometer (see section 6.5).

- **Storage conditions**: The different electromagnetic configuration and geometry of the main spectrometer compared to the pre-spectrometer, changes the storage conditions for electrons considerably. The MAC-E filter limit for magnetic trapping (see section 5.2.1) at the main spectrometer is 0.93 eV (compared to 67 eV at the pre-spectrometer) and thus electrons with a few eV have already a good chance to be magnetically trapped. The cyclotron limit is about 170 keV (at this energy the cyclotron radius becomes larger than the main spectrometer radius). Therefore the ^{219}Rn conversion electrons with the largest probability (178 and 254 keV) are not stored in the main spectrometer. Simulations showed that the dominant conversion electron (37.5 keV, occurrence 0.4% of all ^{219}Rn decays) for energies < 170 keV has a 50% [25] chance to be trapped.

Taking everything mentioned above into account, the average background rate due to the decay of ^{219}Rn - emanating from the NEG pump - inside the main spectrometer can be estimated to ≈ 300 mHz. The time structure of Rn events at the detector will be different compared to the pre-spectrometer. Due to the expected low pressure of 10^{-11} mbar inside the main spectrometer the storage time of the primary electron increases (e.g. a class *I* event would last up to 300 s). Therefore more than 1 primary electron could be stored at the same time[8]. Most of the secondary electrons produced from the primary electron due to ionization of residual gas, are trapped magnetically. Because magnetic trapping is not stable on long time scales (see section 4.1.3) they will leave the main spectrometer after some time. This weakens the correlation between primary and secondary electrons and therefore a diffuse background rate is expected. Also the detection of distinct ring structures will be much more difficult (unless the pressure in the main spectrometer is artificially increased).

The estimated background rate is a factor of 30 larger compared to the background needed (10 mHz) in order to achieve the KATRIN sensitivity of 200 meV/c^2 on the neutrino mass. Therefore it is obvious that it is of high importance to prevent ^{219}Rn decays in the sensitive volume (flux tube) of the main spectrometer. Below three options are discussed.

- **Main spectrometer without NEG pump**
  The operation of the main spectrometer without NEG pump would remove the ^{219}Rn induced background in a trivial way. Anyhow, there are severe drawbacks of this option:
  - Without NEG pump the final pressure inside the main spectrometer would be $1.2{\cdot}10^{-9}$ mbar[9] [25] which is two orders of magnitude larger compared to the design value (10^{-11} mbar). The increased pressure could increase the background rate due to pressure dependent processes such as Penning discharges (see chapter 4).

[8] The probability that during a class I event a second class I event happens is 20%.
[9] Cooling the main spectrometer to 10°C could reduce the pressure to $7 \cdot 10^{-10}$ mbar.

  - The lack of pumping speed for hydrogen would also increase the partial pressure of tritium inside the main spectrometer. Simulations showed that at a T_2 partial pressure of 10^{-20} mbar an average background rate of 25 mHz is expected [80].

- **Dipole mode**
  The inner electrode system of the main spectrometer can be used to create an electric dipole field with a maximum voltage difference of 1 kV between the electrode segments. This dipole field can remove trapped particles via $\vec{E} \times \vec{B}$ drift from the volume of the main spectrometer and thus can be used to remove magnetically trapped secondary electrons from Rn decay events. Anyhow, the dipole field could also drift electrons into the flux tube which then could be trapped in this region after the dipole field is turned off. In order to obtain estimates on the efficiency of the dipole mode against Rn induced background detailed simulations are necessary.

- **LN2 cooled baffle**
  The idea of this solution is to install a liquid nitrogen (LN2) cooled baffle stage at the end of the pump ports in order to prevent ^{219}Rn (emanating from the NEG pump) to enter the main spectrometer flux tube volume and at the same time allow hydrogen to reach the NEG pumps. Due to a special geometry of the baffle a direct flight of Rn atoms into the main spectrometer is prohibited. Assuming that the sticking probability for Rn on the LN2 cooled surface of the baffle is unity [98], all ^{219}Rn atoms from the NEG pump would decay at the baffle (or inside the volume of the pump port). Vacuum simulations showed that hydrogen - coming from the main spectrometer volume - still is able to enter the pump port and thus reach the NEG pump. It is expected that the baffle will reduce the effective pumping speed of the NEG pump for hydrogen to values between 25% and 35% [54].

The baffle solution could prevent ^{219}Rn decays inside the sensitive volume of the main spectrometer and at the same time provide a sufficient pumping speed ($\approx 230 \cdot 10^3$ l/s [54]) for tritium in order to reduce background from tritium decays inside the volume of the main spectrometer. Additionally, the baffle acts as a cryopump and thus yields a further reduction of the final pressure. Therefore the baffle solution is the favoured solution. It is planned to install a LN2 cooled baffle at the pre-spectrometer in order to demonstrate that the concept is working and to test the technical feasibility.

6.5.2 ^{220}Rn emanation at the main spectrometer

Measurements at the pre-spectrometer showed that there is a considerable ^{220}Rn activity (33 ± 9 mBq, see table 6.2) inside the pre-spectrometer test setup. Because the source (or sources) of the ^{220}Rn is unknown at the time of this work, three different scenarios for the main spectrometer are discussed.

1. "**Pre-spectrometer specific**"
   ^{220}Rn emanates essentially from a material that is only present in the pre-spectrometer test setup (for a discussion of different Radon sources inside the pre-spectrometer test setup see section 5.5.5). In this case the radon emanation of the large inner surface (690 m^2) of the main spectrometer is dominant. Assuming that only a 30 nm thick surface layer[10] contributes to the Rn emanation, the released ^{220}Rn activity into the main spectrometer can be estimated to 12 mBq (using a specific activity of 71 ± 1 mBq/kg [86] for stainless steel). With this activity, an average background rate of 10 mHz is estimated (taking into account that ^{220}Rn has a decay probability of 74% inside the main spectrometer). In case the main spectrometer is equipped with the baffle solution (see above) the background rate could be reduced considerably to 1.4 mHz under the assumption that the baffle pump out time of the main spectrometer for ^{220}Rn is 10 s[11].
2. "**Point source**"
   In this scenario ^{220}Rn emanates from a local source e.g. a vacuum gauge or other devices attached to the pre-spectrometer which later on will also be present at the main spectrometer. Hence the expected ^{220}Rn activity would be on the same order of magnitude as in the pre-spectrometer (and would not scale with the dimensions of the main spectrometer). Assuming an activity of 33 mBq the estimated background rate would be 26 mHz or 4 mHz with the baffle solution.
3. "**Intrinsic source**"
   The observed ^{220}Rn emanation at the pre-spectrometer is an intrinsic property of the spectrometer material (stainless steel of type 1.4429). In this case the activity would scale with the surface area, resulting in an ^{220}Rn activity of 920 mBq inside the main spectrometer. The estimates for the background rate are 740 mHz or 110 mHz (baffle solution) which could be further reduced using the dipole mode.

6.5.3 ^{219}Rn emanation at the main spectrometer

The pre-spectrometer Radon background measurements showed that there is a ^{219}Rn component (activity 2.4 ± 2.0 mBq) which is not connected to the getter material and therefore has a different source (or sources). The implications for the main spectrometer can be estimated using the same scenarios discussed for the ^{220}Rn emanation (see section 6.5.2).

[10] This corresponds to about 160 g of material and is only $8 \cdot 10^{-7}$ of the total main spectrometer mass (200 t).

[11] In order to make more reliable estimates for the Rn reduction of the Baffle for Rn emanating within the spectrometer, this value needs to be measured with the baffle prototype at the pre-spectrometer and compared with corresponding vacuum simulations.

1. "**Pre-spectrometer specific**": Taking into account the ^{219}Rn activity of stainless steel (4 ± 0.2 mBq/kg [86]) an activity of 0.7 mBq is expected inside the volume of the main spectrometer. From this an average background rate of 1.4 mHz or 0.9 mHz (baffle solution) is expected.
2. "**Point source**": Assuming that the ^{219}Rn activity measured at the pre-spectrometer (2.4 ± 2.0 mBq, see table 6.2) is also present inside the main spectrometer, the expected average background rate can be estimated to 4.6 mHz or 3 mHz (baffle solution).
3. "**Intrinsic source**": If the ^{219}Rn activity scales with the surface of the spectrometer, a ^{219}Rn activity of 67 mBq is expected inside the main spectrometer. In this case the estimations for the average background rates are 140 mHz and 90 mHz (baffle solution) respectively.

6.6 Conclusion

Electrons released in processes accompanying the α-decay of different Radon isotopes (^{219}Rn, ^{220}Rn and ^{222}Rn[12]) are a major background component in MAC-E filters. Measurements performed at the KATRIN pre-spectromter showed that the average Radon induced background rate is 27 ± 6 mHz. Most of the background events are due to the decay of ^{219}Rn (in case of the pre-spectrometer[13] each ^{219}Rn decay produces about 20 times more background events than a ^{220}Rn decay). The NEG pump could be identified as the major ^{219}Rn source and the Radon emanation efficiency of the getter material could be determined to be in the order of 10^{-3}. For the KATRIN main spectrometer an average background rate - induced of ^{219}Rn emanating from 3 km (design value) of NEG getter strips - of 300 mHz is estimated. Because this is 30 times larger than the required background level of $\leq$ 10 mHz which needs to be achieved for the planned KATRIN sensitivity of 200 meV/c^2 on the neutrino mass, the installation of LN2 cooled baffles is proposed. The baffles could prevent ^{219}Rn from entering the sensitive volume (flux tube) of the main spectrometer and at the same time provide a sufficient effective pumping speed of the NEG pumps for hydrogen and tritium. Additionally, the baffles could reduce the background rate induced from Radon emanating from the main spectrometer vessel itself or devices attached to it.

[12] The isotope ^{222}Rn has a large lifetime (5.5 d) and therefore only a very small decay probability ($2 \cdot 10^{-4}$ for a pump out time $\tau_p = 100$ s) in the volume of a MAC-E filter if actively pumped.
[13] Due to different electromagnetic storage conditions at the main spectrometer, it is estimated that each ^{219}Rn decay produces about 2 to 3 times more background events than a ^{220}Rn decay.

7 KATRIN pre-spectrometer transmission characteristics

Adiabatic guidance on a meV level for electrons flying from the tritium source to the detector is important for the KATRIN experiment and therefore the transmission characteristics of each component has to be studied precisely. This chapter describes the transmission characteristics of the KATRIN pre-spectrometer at full magnetic field (4.5 T in the centre of each superconducting solenoid) and different configurations of the retarding potential. Section 7.1 describes the principle of MAC-E filters and gives a theoretical description of the transmission function. Afterwards the transmission function is simulated in detail for two different configurations of the retarding potential (see 7.2). The measurements of the transmission functions at the pre-spectrometer are presented in section 7.3. A summary of the measurements and a comparison with the simulations is given in section 7.4.

7.1 Transmission function

7.1.1 MAC-E filter

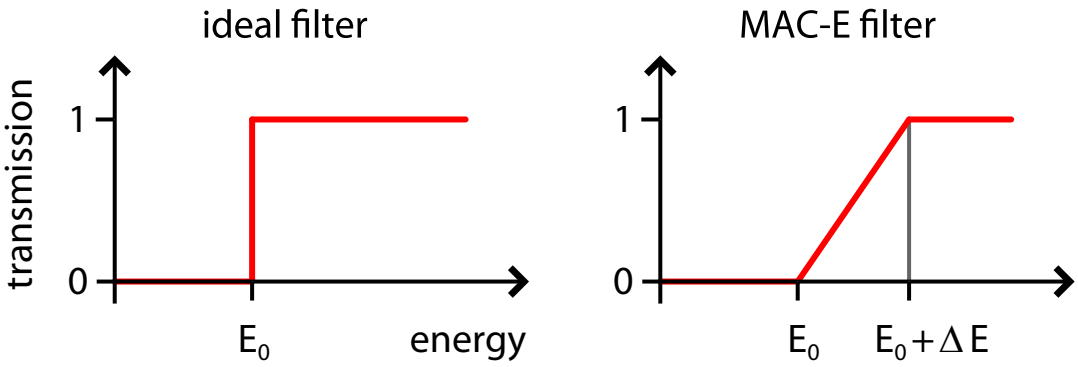

Figure 7.1: comparison between an ideal high pass filter (left) and a MAC-E filter (right)

In order to achieve a good energy resolution ΔE (0.93 eV for the main spectrometer) for a high flux (10^{10} 1/s) and a large accepted solid angle ($<2\pi$) of β-decay

electrons, the KATRIN spectrometers are designed as MAC-E[1] filters. A MAC-E filter works as an integrating high-pass filters with a retarding potential of U_0 and a magnetic guidance of the electrons. For a perfect filter the transmission of electrons with a kinetic energy $E \leq eU_0$ would be zero and for electrons with $E > eU_0$ maximum. MAC-E filters work similar, but there is a transition region where the transmission increases from zero to maximum (see figure 7.1). The width of this transition region is defined as the energy resolution ΔE of the spectrometer.

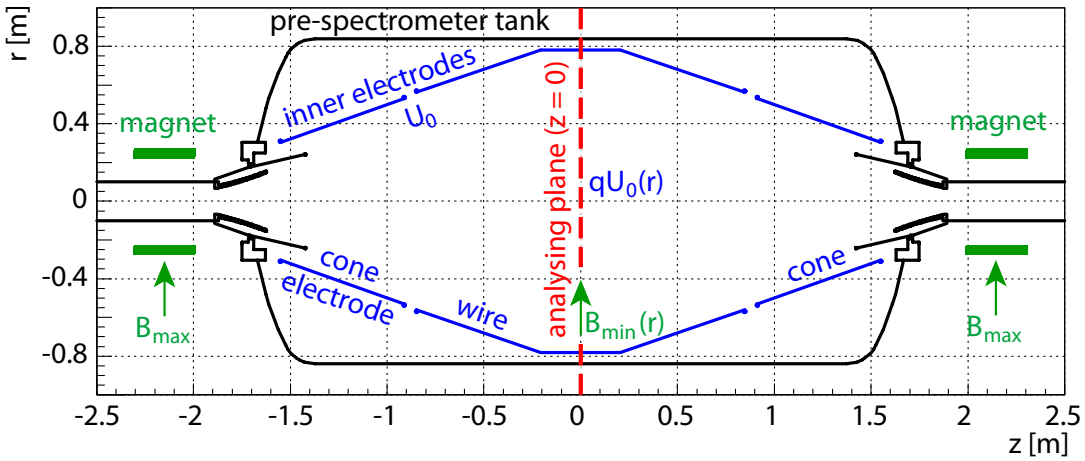

Figure 7.2: schematic drawing of the pre-spectrometer

The motion of an electron in a magnetic field $\vec{B}$ can be described as a superposition of two motions:

1. The transversal component of the electron momentum $\vec{p}_e$ forces the electron on a **cyclotron motion** with a radius r_c (see equation 7.1) and a frequency ω_c (see equation 7.2).
2. The longitudinal component of $\vec{p}_e$ results in **longitudinal motion** along a magnetic field line.

$$r_c = \frac{\gamma m v}{qB} \tag{7.1}$$

$$\omega_c = \frac{qB}{\gamma m} \tag{7.2}$$

$$\gamma = \frac{1}{\sqrt{1 - \left(\frac{v}{c}\right)^2}} \tag{7.3}$$

[1]**M**agnetic **A**diabatic **C**ollimation combined with an **E**lectrostatic Filter

For the design parameters of KATRIN the motion of the electrons is adiabatic. This means that electric potential and magnetic field are only changing slightly over the cyclotron period of the electron. In this case the product of Lorentz factor γ (see equation 7.3) and magnetic moment μ is constant:

$$\gamma \cdot \mu = const \tag{7.4}$$

The maximum γ for tritium β-electrons is 1.04, therefore equation 7.4 can be approximated with:

$$\mu = \frac{E_t}{B} = const \tag{7.5}$$

E_t is the transversal component of the total kinetic electron energy E_0, E_l the longitudinal component:

$$E_t = E_0 \cdot \sin^2(\Theta) \qquad E_l = E_0 \cdot \cos^2(\Theta) \tag{7.6}$$

Figure 7.2 shows a drawing of the pre-spectrometer as an example of a MAC-E filter. It consists of two superconducting solenoids to create a guiding magnetic field and an electrode system to generate a retarding potential. Let's assume an electron with energy E_0 starts at maximum magnetic field B_{max} in the centre of a magnet (z = -2.15 m) with a start angle Θ_0 (Θ is the angle between the magnetic field $\vec{B}$ and the momentum of the electron $\vec{p}$, see figure 4.4). As it moves towards the centre of the spectrometer (z = 0) the magnetic field decreases to B_{min}. According to equation 7.5 E_t has to decrease in the same way in order to keep μ constant. Hence there is an energy of $E_0 \cdot \sin^2(\Theta_0) \cdot \frac{B_{min}}{B_{max}}$ left in cyclotron motion that can not be analyzed by the retarding potential $q \cdot U_0$. This can be translated in transmission conditions for electrons with a fixed start angle (equation 7.7) or a fixed start energy (equation 7.8):

$$q \cdot U_0 \leq E_0 - E_0 \cdot \sin^2(\Theta_0) \cdot \frac{B_{min}}{B_{max}} \tag{7.7}$$

$$\Theta \leq \arcsin \sqrt{\frac{E_0 - qU_0}{E_0} \cdot \frac{B_{max}}{B_{min}}} \quad (= \Theta_0) \tag{7.8}$$

To derive an expression for the energy resolution ΔE the following two cases at a fixed start energy $E_0 = q \cdot U_0$ are contemplated:

- $\Theta_0 = 0$ °: The remaining transversal energy E_t at B_{min} ($E_{t,min}$) is zero. Because equation 7.7 is fulfilled, the electron is transmitted.
- $\Theta_0 = 90$ °: This is the maximum accepted angle of a MAC-E filter, the remaining transversal energy is $E_{t,min} = E_0 \cdot \frac{B_{min}}{B_{max}}$. In order to be transmitted, E_0 of the electron has to be larger by $E_{t,min}$.

The energy difference of those two cases gives the energy resolution:

$$\Delta E = \frac{B_{min}}{B_{max}} \cdot E_0 \tag{7.9}$$

For an isotropic source at B_{max} the number of electrons emitted in the solid angle $d\Omega$ is $sin(\Theta)d\Theta d\varphi$. After integration this results in the following equation:

$$\frac{\Delta\Omega}{2\pi} = 1 - \cos(\Theta) \tag{7.10}$$

Combining equation 7.8 with 7.10, an expression for the transmission function $T(E_0, U_0)$ can be derived:

$$T(E_0, U_0) = \begin{cases} 0 & E_0 - qU_0 < 0 \\ 1 - \sqrt{1 - \frac{E_0 - qU_0}{E_0} \cdot \frac{B_{max}}{B_{min}}} & 0 \leq E_0 - qU_0 \leq \frac{B_{min}}{B_{max}} \cdot E_0 \\ 1 & E_0 - qU_0 > \frac{B_{min}}{B_{max}} \cdot E_0 \end{cases} \tag{7.11}$$

Until now it was assumed that all electrons start at B_{max}, but in general the electrons can start at any magnetic field B_{start}. For the KATRIN experiment the magnetic field of the electron source (WGTS) is 3.6 T but B_{max} is 6 T. B_{max} defines a cut off angle Θ_{max}:

$$\Theta_{max} = \arcsin\sqrt{\frac{B_{start}}{B_{max}}} \tag{7.12}$$

Only electrons with $\Theta_0 < \Theta_{start}$ will arrive at the detector if B_{max} along their track is larger than B_{start}. For equation 7.11 an isotropic source was assumed. Due to equation 7.12 the angular distribution in B_{max} is not isotropic anymore and 7.11 needs to be modified to:

$$T(E_0, U_0) = \begin{cases} 0 & E_0 - qU_0 < 0 \\ \frac{1 - \sqrt{1 - \frac{E_0 - qU_0}{E_0} \cdot \frac{B_{start}}{B_{min}}}}{1 - \sqrt{1 - \frac{B_{start}}{B_{max}}}} & 0 \leq E_0 - qU_0 \leq \frac{B_{min}}{B_{max}} \cdot E_0 \\ 1 & E_0 - qU_0 > \frac{B_{min}}{B_{max}} \cdot E_0 \end{cases} \tag{7.13}$$

7.1.2 Transmission of a single electron

This section discusses the transmission of a single electron in a MAC-E filter in detail in order to show the basic principles of a MAC-E filter.

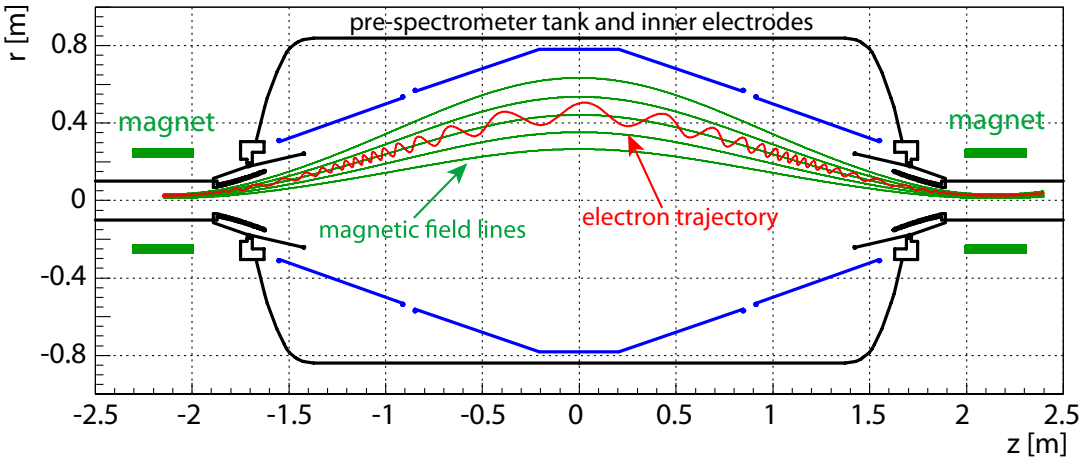

Figure 7.3: Trajectory of an electron in the pre-spectrometer, start conditions: z = -2.15 m, r = 0.0261 m, Θ = 89.9 °, E_0 = 18.145 keV, full magnetic field (4.5 T), retarding potential -18 kV. The electron mass is enhanced by a factor of 1000 for a better visualization of the cyclotron motion.

Figure 7.3 shows the trajectory of an electron in the pre-spectrometer. The electron starts at z = -2.15 m and r = 0.0261 m with a start energy E_0 = 18.145 keV and an angle Θ_0 = 89.9 ° at the centre of the magnet (B_{max} = 4.5 T). The retarding voltage (U_0) of the spectrometer is -18 kV (tank and all inner electrodes on the same potential). For better visualization of the cyclotron motion of the trajectory the electron mass is increased by a factor of 1000. The energy of the electron can be split in a transversal (E_t) and a longitudinal (E_l) component (see equation 7.6). Therefore the electron moves in a spiral track along a guiding magnetic field line with cyclotron radius r_c and frequency ω_c.

In the following the transmission of a single electron in the pre-spectrometer will be discussed in more detail. Let's assume an electron starts at z = -2.15 m, r = 0.0 in the centre of a pre-spectrometer magnet (B_{max} = 4.5T) with E_0 = 18.2keV and Θ_0 = 29.8 °. According to equation 7.6 E_0 can be split in a longitudinal (E_l) and a transversal (E_t) component as it is shown in figure 7.4. As the electron moves towards the analyzing plane (z = 0), the magnetic field B drops from B_{max} = 4.5 T to B_{min} = 16 mT. Due to the conservation of μ (see equation 7.5) E_t is transformed into E_l. E_l reaches its maximum at about z = -1.8 m and then drops by two orders of magnitude as the electric retarding potential increases. Between z = -1.0 and z = 0.0 E_t is further transformed into E_l. In the analyzing plane the retarding potential is maximal (qU_0) and B, E_l, E_t minimal. Because

$$E_0 - qU_0 \;\; (= \;\; 200 \; eV) > \frac{B_{min}}{B_{max}} \cdot E_0 \;\; (= \;\; 64.7 \; eV)$$

(see equation 7.13) the electron is transmitted. Between z = 0.0 m and z = 2.15 m

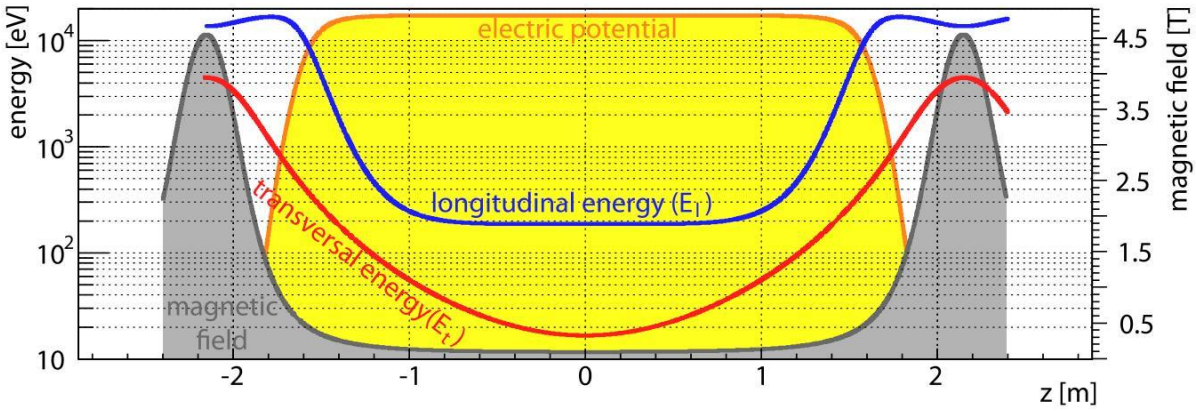

Figure 7.4: E_t and E_l of an transmitted electron in the pre-spectrometer, start conditions: z = -2.15 m, r = 0.0 m, E_0 = 18.2 keV, Θ_0 = 29.8 °, pre-spectrometer configuration: U_0 = -18 kV, B_{max} = 4.5T

B increases to B_{max} and therefore E_t is transformed again in E_l. As the electric potential drops around z = 1.6 m the electron is accelerated until it reaches E_0 at z = 2.15 m. The fact that the electron has almost the same energy before and after transmission[2] is very important for the KATRIN experiment. The pre-spectrometer is intended to work as a pre-filter at U_0 a few hundred volts below the tritium endpoint energy. The energy analysis of the β-decay electrons is done in the main spectrometer (see section 2.4.3). If the electrons loose energy as they are transmitted in the pre-spectrometer this would cause a systematic error of the neutrino mass measurement and therefore would reduce the sensitivity of the KATRIN experiment.

7.1.3 Radial dependence of transmission function

This section describes how the transmission characteristics of the pre-spectrometer depend on the radial start position of the electron.

Equation 7.13 describes the transmission function for fixed values of B_{start}, B_{max}, B_{min} and U_0. Due to technical reasons those values in general depend on the radial position r. Figure 7.5 shows the magnetic field in the pre-spectrometer for two different z-positions:

a) Magnetic field $B_{max}(r)$ in the centre of the pre-spectrometer magnet (z = -2.15 m). The field increases with r. This is expected because the coil has

[2]The mean free path of electrons at a pressure of 10^{-11} mbar is in the order of 10000 km (spectrometer length 4.3 m) therefore energy losses due to scattering with residual gas molecules can practically be neglected. Cyclotron radiation losses within the pre-spectrometer for a transmitted 18.5 keV electron (retarding potential configuration A, see below) are smaller than 10 meV (relative energy loss in the order of 10^{-7}).

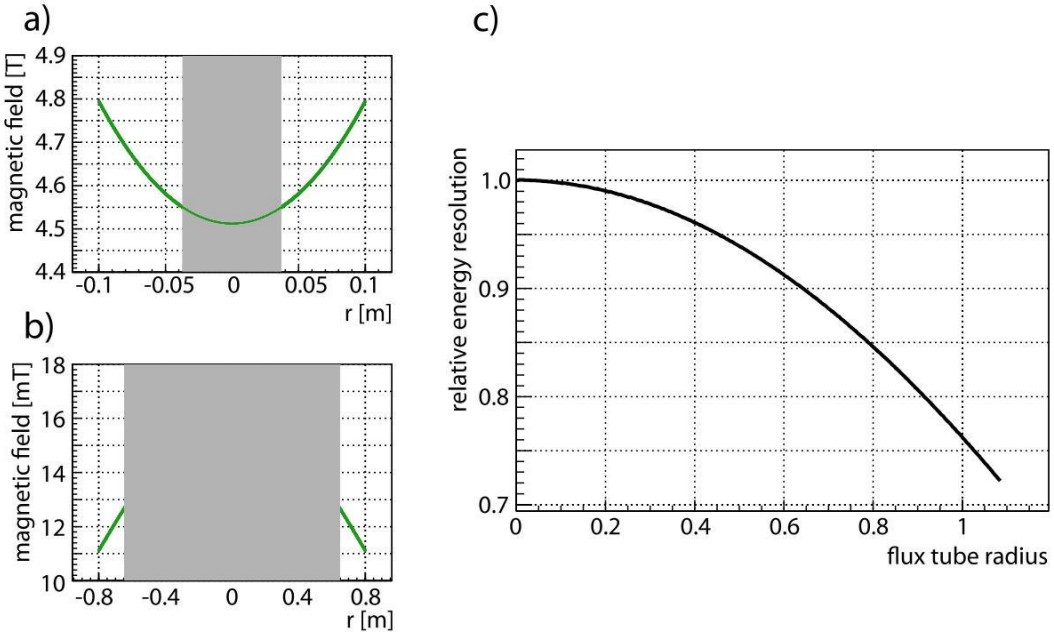

Figure 7.5: **a)** magnetic field inside pre-spectrometer coil (z = -2.15 m) **b)** magnetic field in analyzing plane ($z = 0$) **c)** radial dependence of relative energy resolution (normalized to $r = 0$)

only a length of 0.32 m at a diameter of 0.454 m. Hence the magnetic field is not homogeneous inside the magnet and increases closer to the coil.

b) Magnetic field $B_{min}(r)$ in the analyzing plane ($z = 0$). The field here is a superposition of the two solenoids. With increasing r the distance to the coils increases and hence $B_{min}(r)$ decreases.

The energy resolution ΔE of the spectrometer depends on the ratio of B_{min} and B_{max} (see equation 7.9). In **c)** the normalized[3] energy resolution $\Delta E(r_{ft})$ of the pre-spectrometer in dependence of the relative flux tube radius (r_{ft}, $1 \mathrel{\widehat{=}} 100\%$) is shown. $\Delta E(r_{ft})$ gets smaller with larger r_{ft}. This is mainly due to the radial decrease of $B_{min}(r)$.

The electric potential ($U_0(r)$) in the analyzing plane is shown in figure 7.6. As the spectrometer has no infinite length, there is still an influence of the ground electrodes in the analyzing plane of the spectrometer that causes an increase of the potential for smaller r values. This means that independent of Θ_0, E_0 has to be larger for electrons starting at larger r positions.

In order to receive an expression for the transmission function of the spectrometer for 100% flux tube equation 7.11 needs to be integrated over the relative flux tube radius r_{ft}:

[3] $\Delta E(r_{ft})/\Delta E(0)$

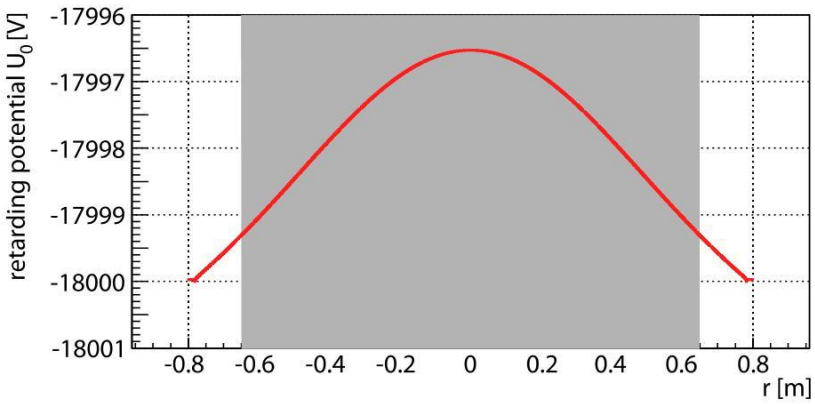

Figure 7.6: electric potential in the analyzing plane for $U_{tank} = U_{cone} = U_{wire} =$ -18 kV

$$T_{spec}(U_0, E_0) = \int_0^1 T(E_0, U_0) r_{ft} dr_{ft} \tag{7.14}$$

7.1.4 Dependence of the transmission function on the angular distribution of the source

The shape of the transmission function is also determined by the characteristics of the electron source and is not a property of the spectrometer alone. For the analytic expression of the transmission function in 7.11 an isotropic electron source at the centre of the pre-spectrometer magnet ($z = 2.15$ m) was assumed, but in general the angular distribution of the source could have any shape. For example, the electron gun (see section 3.2) that is used for the transmission function measurements described in section 7.3 has nonisotropic emission behaviour in favour of small angles.

In figure 7.7 three different angular distributions are shown:

- **isotropic:** The same number of electrons is emitted into each solid angle $\Delta\Omega$, or into each interval of $\cos(\Theta)$ (see left side of 7.7). An example of an isotropic source is the WGTS of KATRIN.
- **small angle:** The number of electrons as a function of $\cos(\Theta)$ increases linearly from zero to two times the value of the isotropic distribution.
- **large angle:** The number of electrons as a function of $\cos(\Theta)$ decreases linearly from two times the value of the isotropic distribution to zero.

The small/large angle distributions are defined completely arbitrarily without the need of having an electron source that could produce such distributions. They are only intended to show the effects of different angular distributions on the transmis-

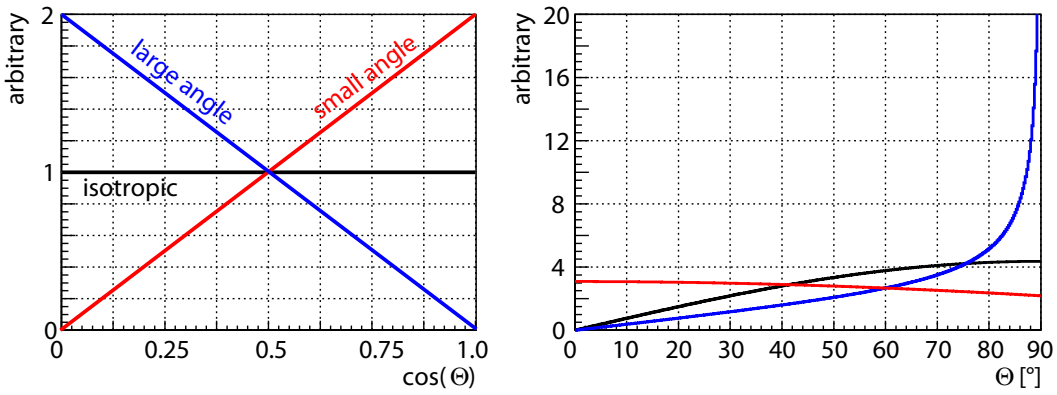

Figure 7.7: **left:** three different angular distributions as functions of cos(Θ), **right:** the same angular distributions as on the left side, but as a function of Θ

sion function.

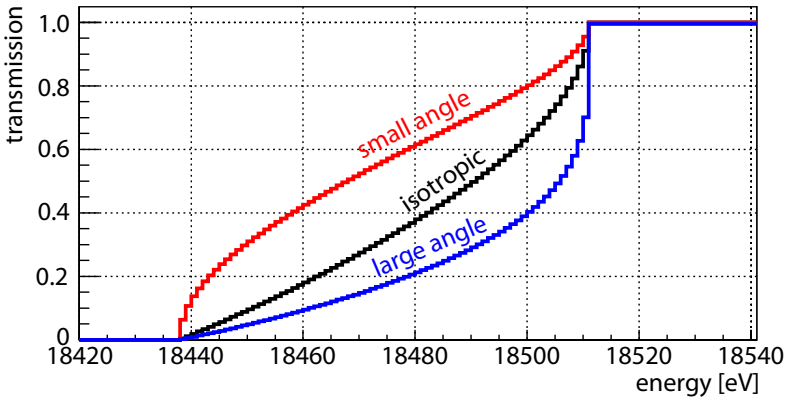

Figure 7.8: simulated transmission functions at the pre-spectrometer (B_{max} = 4.5T, U_0 = -18.5 kV) for the angular distributions described above (see figure 7.7)

As an example, the simulated transmission functions (for more information see section 7.2) of the pre-spectrometer for the angular distributions described above are shown in figure 7.8. For all three cases the transmission starts at around 18440 eV and reaches maximum transmission at around 18510 eV - the width ΔE is the same. This is expected because ΔE is a property of the spectrometer and independent of the angular distribution of the source. The transmission of the spectrometer starts with electrons that have small Θ_0, therefore the transmission function of the small angle distribution rises much faster compared to the large angle distribution. Electrons with large Θ_0 are transmitted close to the maximum of transmission, hence the transmission function of the large angle distribution increases very fast in this region.

7.2 Simulations of the pre-spectrometer transmission behaviour

In preparation of the measurements described in section 7.3 the transmission behavior of the pre-spectrometer was simulated for two different configurations of the retarding potential at full magnetic field B_{max} = 4.5 T:

A This potential distribution has the following parameters: pre-spectrometer tank U_{tank} = -18 kV, cone electrodes (east/west) U_{cone} = -18.3 kV, wire electrodes U_{wire} = -18.5 kV.

B All potentials have the same value: $U_{tank} = U_{cone} = U_{wire}$ = -18 kV.

The choice of these configurations is motivated from the background characteristics of the pre-spectrometer (for more information see chapter 4). In both cases a background level of < 0.01 events/s for each detector pixel is achievable. Configurations with optimized transmission conditions as proposed in [30] require a more positive cone electrode potential ($U_{cone} = U_{tank}$+1 kV), but corresponding measurements showed that the background level increases by more than 3 orders of magnitude due to the ignition of a Penning discharge.

The simulation of a transmission function was done in the following way: Electrons were started at z = -2.15 m (magnet centre) in B_{max} = 4.5 T. An isotropic angular distribution (see figure 7.7) of the polar start angle Θ_0 was used. The start energy E_0 was varied in 1 eV steps and for each step 1000 electrons were started. The trajectory of each electron was calculated with a modified[4] version of the tracking program traj [95]. The tracking was stopped if the electron reached z = 2.4 m (transmitted) or z = -2.4 m (reflected). The number of transmitted electrons as a function of E_0 gives the transmission function.

7.2.1 Transmission at -18.5 kV retarding potential

Figure 7.9 shows a simulated transmission function (e-gun position (0 °/0 °)). In addition, the analytically calculated transmission function according to equation 7.11 is shown. Up to an energy of E_0 = 18480 eV (or $\Theta_0 = 51.6°$) the agreement is very good. For larger E_0 the transmission function from the full tracking simulation reaches maximum transmission slower than the analytic calculation. The energy resolution ΔE for the analytic calculation is ΔE_{ana} = 67.3 eV and for the simulation ΔE_{sim} = 74 eV. This increase in ΔE can be explained with an early retardation of electrons (see figure 7.10). Early retardation can happen for two reasons:

- The maximum of the retarding potential $q \cdot U_0$ is not in the analyzing plane (z = 0 m). In case of the pre-spectrometer this can happen in the follow-

[4]The modifications only refer to the input and output parameters and not to the algorithms for tracking or field calculation.

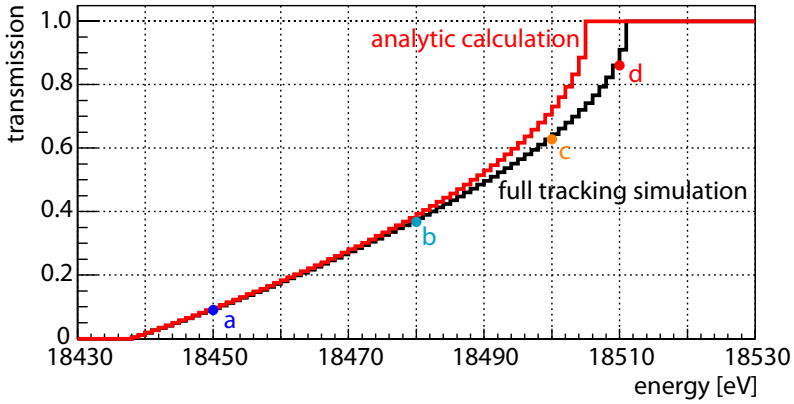

Figure 7.9: Comparison between analytically calculated and simulated transmission function with U_0 = -18437.5 V, B_{max} = 4.51 T, B_{min} = 16.4 mT. The longitudinal energy (E_l) of electrons transmitted in A to D is shown in figure 7.10.

ing configuration: $U_{cone} = U_{wire} < U_{tank}$. Because the wire electrode does not completely shield U_{tank}, the retarding potential in the centre of the pre-spectrometer decreases.

- The retarding potential increases too fast compared to the decrease in magnetic field B. According to equation 7.5 E_t is transformed into E_l. If $E_t - q \cdot U < 0$ for $z \neq 0$ m the electron is reflected even if equation 7.7 is fulfilled.

Both cases cause a broadening of the transmission function because the point where the electron is reflected is shifted to larger values of B and therefore ΔE (see equation 7.9) increases.

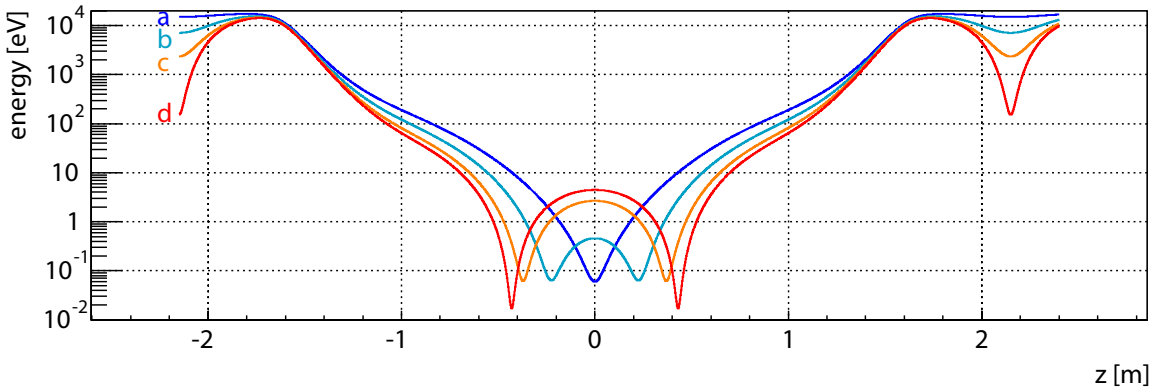

Figure 7.10: E_l for four electrons with the start parameters (E_0/Θ_0) at z = -2.15 m, B_{max} = 4.5 T: **a** (18450 eV/25.3 °), **b** (18480 eV/51.6 °), **c** (18500 eV/69.1 °) and **d** (18510 eV/84.3 °).

Figure 7.10 shows the longitudinal energy component (E_l) for electrons starting at different E_0 and Θ_0 within the transmission function shown in figure 7.9. The position of the minimum of E_l - that is in good approximation equal to the point where the electron is reflected if it had a slightly smaller E_0 (or slightly larger Θ_0) - is shifted from the analyzing plane (z = 0 m, B_{min} = 16.4 mT) towards larger absolute values of z and reaches a maximum shift of z = 0.43 m for electrons that start with maximum Θ_0 (90 °). The magnetic field B at this z position is 20.7 mT. The shift towards larger B with increasing transmission probability increases ΔE continuously and explains the deviation between ΔE_{ana} and ΔE_{sim} described above.

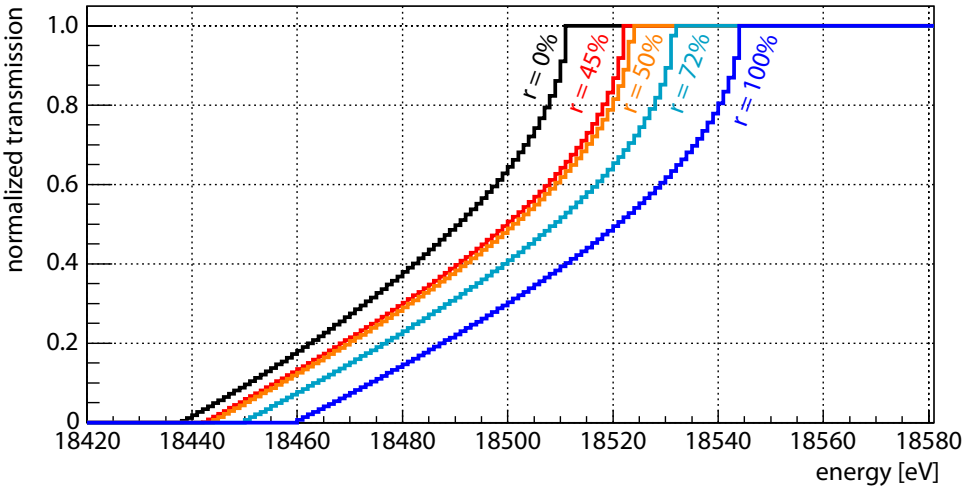

Figure 7.11: simulation (full tracking) of the transmission function at five different radii (see table 7.1)

Table 7.1: characteristics of simulated transmission functions: $r_{\%}$ radius of % enclosed flux tube, r_{start} radial start position at z = -2.15 m, r_{ap} radial position in analyzing plane, T_{start} start of transmission, ΔE energy resolution

$r_{\%}$	r_{start} [m]	r_{ap} [m]	T_{start} [eV]	ΔE [eV]
0	0.0	0.0	18438	73
45	0.0248	0.423	18442	80
50	0.0261	0.447	18444	80
72	0.0313	0.544	18450	82
100	0.0368	0.652	18460	84

In figure 7.11 the transmission functions for five different radial positions (0, 45, 50, 72 and 100 % enclosed flux tube) are shown. Corresponding characteristic values can be found in table 7.1. The shift of T_{start} is due to the radial increase of the retarding potential. The increase of ΔE is caused by early retardation of the electrons.

7.2.2 Transmission at -18 kV retarding potential

In this configuration all electrodes (U_{tank}, U_{cone}, U_{wire}) are at the same potential (-18 kV). The simulated transmission functions are shown in figure 7.12, characteristic values in table 7.2.

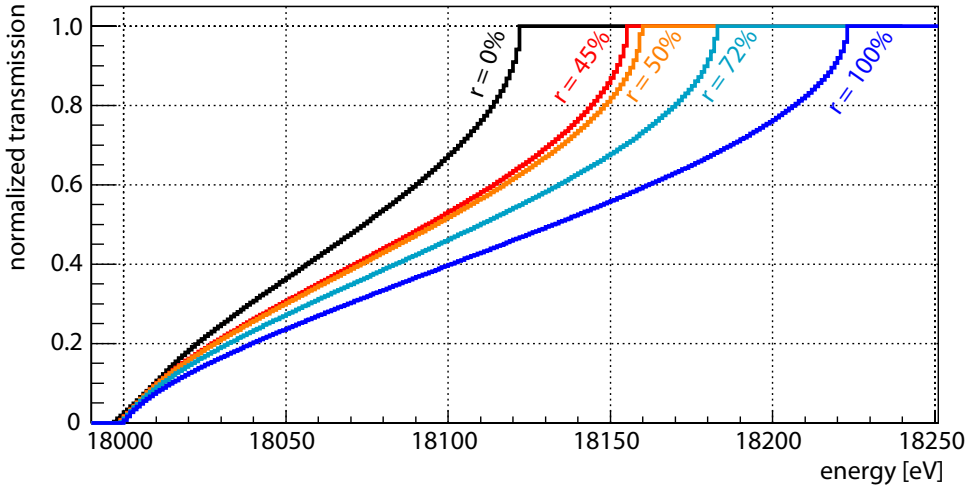

Figure 7.12: simulation (full tracking) of the transmission function at five different radii (see table 7.2)

Table 7.2: characteristics of simulated transmission functions: $r_{\%}$ radius of % enclosed flux tube, r_{start} radial start position at z = -2.15 m, r_{ap} radial position in analyzing plane, T_{start} start of transmission, ΔE energy resolution

$r_{\%}$	r_{start} [m]	r_{ap} [m]	T_{start} [eV]	ΔE [eV]
0	0.0	0.0	17997	125
45	0.0248	0.423	17999	156
50	0.0261	0.447	17999	161
72	0.0313	0.544	17999	184
100	0.0368	0.652	18000	223

Compared to the transmission functions for configuration **A** (see section 7.2.1) ΔE is up to 3 times larger. A calculation of E_l along the track of an electron starting at z = -2.15 m, r = 0.0368 m ($r_{100\%}$), E_0 = 18223 eV, Θ_0 = 89.94 ° shows that early retardation also happens in this configuration. The minimum of E_l is at z = -1.27 m in a magnetic field of 100 mT.

7.3 Transmission function measurements

The transmission characteristics (transmission functions) of the pre-spectrometer for electrons have been measured for the potential configurations **A** and **B** (see section 7.2) at different positions of the flux tube. First the experimental setup is described, afterwards the results of the single measurements are presented. For each measurement two characteristic values are determined: T_{start} and ΔE.

7.3.1 Experimental setup

In order to measure the transmission function a constant retarding potential configuration was applied to the pre-spectrometer. At the same time the voltage (U_{e-gun}) of the photoelectric electron source (e-gun) was varied in steps of 2 V [5] and the event rate R at the detector was measured. R as a function of U_{e-gun} gives the transmission function.

The transmission function measurements are organized in the following way:

- **Measurement:** Each measurement consists of 6 runs. The first run measures the transmission from zero to maximum transmission. In the second run the rate at maximum transmission is measured for 10 min. This run is used to normalize the transmission functions and to check the stability of the e-gun emission. Run three measures the transmission from maximum transmission to zero. Afterwards everything is repeated one time in order to check the reproducibility. The typical time for a measurement is 10 to 16 h, depending on the expected width of the transmission region.
- **Run:** In a run all experimental parameters except U_{e-gun} are kept constant. For each value of U_{e-gun} a separate subrun within the run is started.
- **Subrun:** In a subrun all experimental parameters are fixed. The duration of each subrun is adapted to the expected rate at the detector in order to have similar statistics for each subrun.

For each measurement an ORCA script was created that automatically changes U_{e-gun}. It also starts and stops the runs and subruns. For more information on the DAQ system see section 3.4.

Table 7.3 gives an overview of the transmission function measurements. Figure 7.13 shows the positions of the e-gun within the flux tube for the transmission function measurements. The axes correspond to the x (horizontal) and y (vertical) axis of the spectrometer. As the pre-spectrometer is a rotational symmetric system[6] the transmission properties should only depend on the radial position and therefore most of the measurements were done along the positive x axis. In order to check

[5] Because $E_0 = q \cdot U_{e-gun}$ this corresponds directly to a change of E_0 in 2 eV steps.
[6] This is true if the vertical gap between the electrodes is neglected.

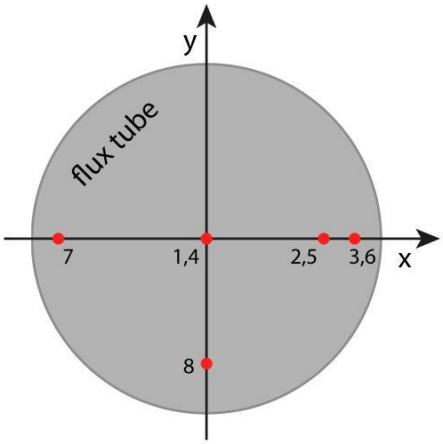

Figure 7.13: positions of the measured transmission functions within the flux tube

the rotational symmetry measurements 7 and 8 were done.

Table 7.3: overview of the transmission function measurements, number: measurement number, e-gun (x/y) [°]: horizontal/vertical position of the e-gun in degree, 64PD (x/y) [cm]: horizontal/vertical position of the detector in cm, configuration: retarding potential configuration according to section 7.2, runs: run numbers within the measurement

number	e-gun (x/y) [°]	64PD x/y [cm]	configuration	runs
1	0/0.2	-0.3/0.35	B	10437 - 10442
2	15/0.2	-2.5/0.5	B	10445 - 10450
3	19/0.2	-2.5/0.5	B	10456 - 10461
4	0/0.2	-2.5/0.5	A	10494 - 10499
5	15/0.2	-2.5/0.5	A	10477 - 10482
6	19/0.2	-2.5/0.5	A	10484 - 10489
7	-19/0.2	1.2/0.5	A	10504 - 10509
8	0/-16	-1.0/-0.7	A	10515 - 10520

For all measurements presented below, the following experimental parameters were used:

- full magnetic field: east magnet current 157 A (4.5 T), west magnet current 157 A (4.5 T)
- pressure p inside pre-spectrometer: 10^{-10} mbar (In order to keep the background level low, all vacuum gauges inside the pre-spectrometer were turned off during the measurement. p was measured before and after the transmission measurements.)
- U_{tank} = -18 kV, active high voltage stabilization turned on.

- e-gun shutter 0.4 mm, rate at maximum transmission (R_0) about 4 kHz.
- detector (64PD) z-position at 40 cm (-2.3 m in pre-spectrometer coordinates), 28.5 % flux tube visible

The following parameters were varied for the individual measurements:

- (x/y) position of the e-gun in order to measure at different positions of the flux tube (see figure 7.13)
- (x/y) position of the detector to compensate a shift of the e-gun
- U_{cone} and U_{wire} to adjust the retarding potential configuration to **A** or **B**

7.3.2 Systematic effects

The systematic effects of the transmission function measurements are listed below:

- **Stability of U_{e-gun}**: U_{e-gun} was monitored with the internal voltage readout of the e-gun high voltage supply. For each subrun U_{e-gun} was stable within 1 V which is the accuracy of the readout.
- **Start energy (E_0) distribution of electrons**: The width of this distribution is 2.1 ± 0.2 eV [41] and is caused by the continuous spectrum of the UV lamp.
- **E-gun UV lamp stability**: The rate of electrons produced at the e-gun is correlated with the intensity of the UV lamp (I_{UV}). I_{UV} was monitored with a photo diode in order to check for fluctuations.

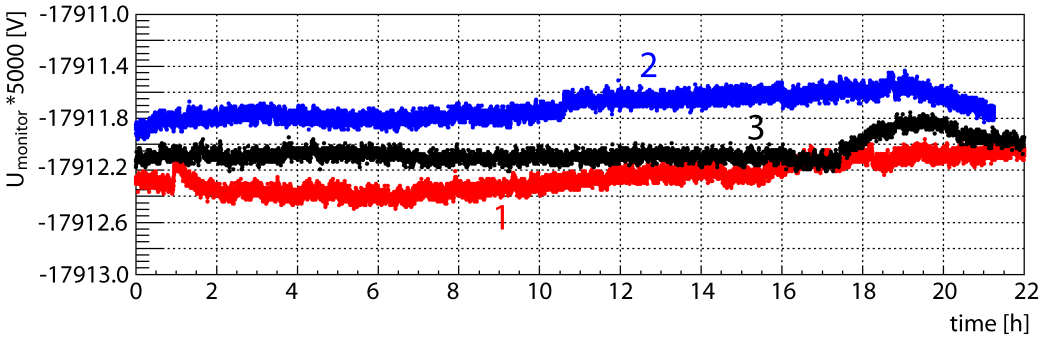

Figure 7.14: Stability of U_{tank} for the measurements 1 to 3.

- **Stability of U_{tank}**: The active high voltage stabilization reduces fluctuation of U_{tank} below 100 mV (at U_{tank} = -18 kV) on time scales of minutes. In order to monitor the long term drift of U_{tank} a second Julie Research KV-50 voltage divider (divider ratio 1:5000) was attached to the pre-spectrometer tank and read out with a Fluke 8846A voltmeter ($U_{monitor}$). Figure 7.14 shows

$U_{monitor}$*5000 during the measurements 1 to 3[7]. Whether the change of $U_{monitor}$ is due to a drift of U_{tank} or due to drifts of the HV divider characteristics can not be distinguished. Anyhow it is reasonable to claim that U_{tank} is stable within 0.5 V in time periods of several hours and the reproducibility of U_{tank} for different measurements is better than 1 V.

- **Scattering on residual gas**: At a pressure of 10^{-10} mbar is the mean free path for electrons in the order of 1000 km. The path length for electrons from the e-gun tip to the detector is between 6 and 10 m depending on the e-gun position and Θ_0. Hence the probability of a scatter event for a single electron is in the order of 10^{-5}. Therefore scattering can be neglected compared to other systematic effects.
- **Magnetic field**: The transmission characteristics are sensitive on the ratio of B_{min} and B_{max} and not on the absolute value of B[8], therefore a precise monitoring of the magnetic field is not necessary. Anyhow, magnetic materials (e.g. steel in the ground) close to the spectrometer could disturb B, especially close to B_{min}. This could lead to a non rotational symmetric transmission behaviour and shows the importance of measurement 7 and 8.
- **DAQ dead time**: The counting efficiency of the IPE3 electronics at R_0 (about 4 kHz) is 98 % [70]. In the analysis of the data this effect is corrected.
- **Penning trap between e-gun and pre-spectrometer**: In order to investigate the transmission characteristics of the spectrometer with a photoelectric electron source it is unavoidable to create a "vacuum to cathode" type Penning trap between spectrometer and e-gun (for more information on Penning traps see chapter 4). The ignition of this trap could create a time dependent background and therefore disturb the measurement significantly. An 8 h measurement (Run 528) with U_{e-gun} slightly below U_{tank} showed no increase in rate at the detector and therefore no evidence for the ignition of the trap. Also, the very good agreement of count rate within different runs of the measurements presented below indicates that no major ignition of a Penning discharge occurred.

7.3.3 Transmission function with -18 kV retarding potential

This section contains all measurements with retarding potential configuration **B**. For each measurement R as a function of U_{e-gun} is shown for the complete transmission region and the region close to maximum transmission.

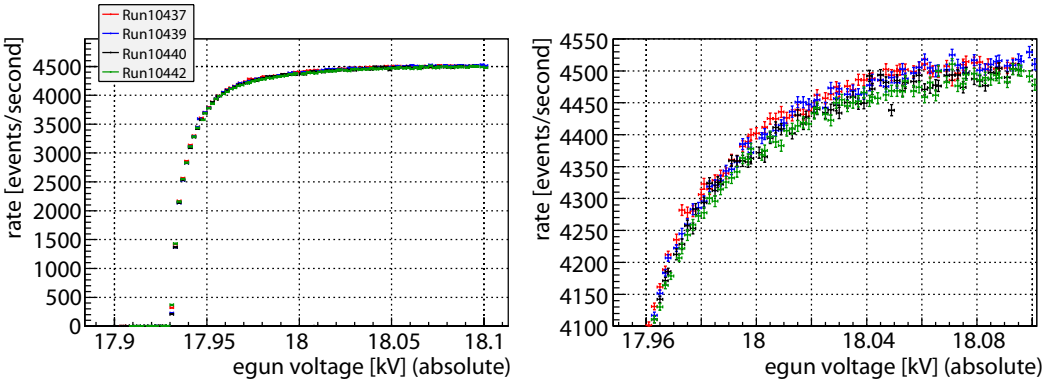

Figure 7.15: measured transmission function, configuration **B**, e-gun at x = 0°, (measurement 1)

Electron gun at centre position (measurement 1)

The transmission starts very steep at $U_{e-gun} = 17931 \pm 1$ V and reaches maximum transmission at 18060 ± 20 V[9] (see figure 7.15). All four runs show excellent agreement with each other.

Electron gun at x = 15° (measurement 2)

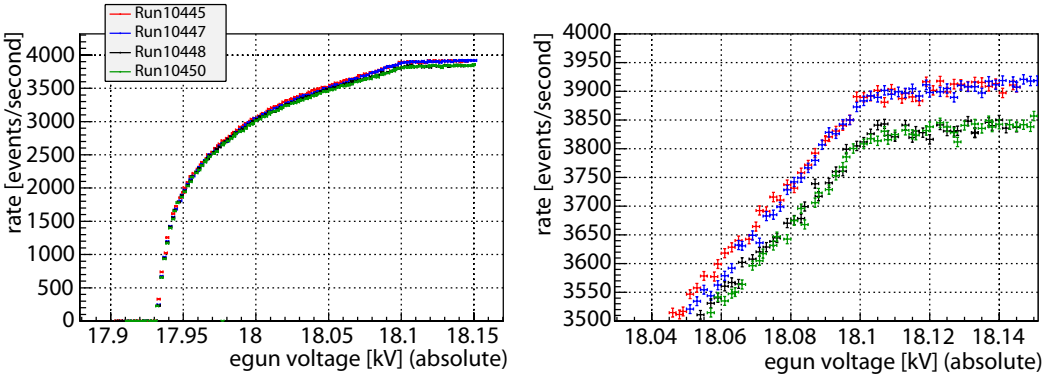

Figure 7.16: measured transmission function, configuration **B**, e-gun at x = 15°, (measurement 2)

For this measurement the e-gun was moved to x = 15°. The start of transmission is at $U_{e-gun} = 17933 \pm 1$ V and maximum transmission is reached at 18099 ± 1 V (see figure 7.16). Run 10445 and run 10447 are in good agreement with each other,

[7] Measurements 4 to 8 show similar behaviour.
[8] This is true as long as the electrons are guided adiabatic.
[9] Unlike all other measurements, no pronounced kink in rate is observed, therefore there is a large uncertainty about the point where maximal transmission is reached.

also run 10448 and 10450. Nevertheless run 10448 & 10450 are systematically about 2 % below run 10445 & 10447. This behaviour could be explained with a shift in R_0. The shape of the transmission function indicates that the e-gun preferably emits electrons with small Θ_0 (see figure 7.8). Especially the very slow rise of R between 18000 V and 18100 V shows that only very few electrons with large Θ_0 are emitted.

Electron gun at x = 19° (measurement 3)

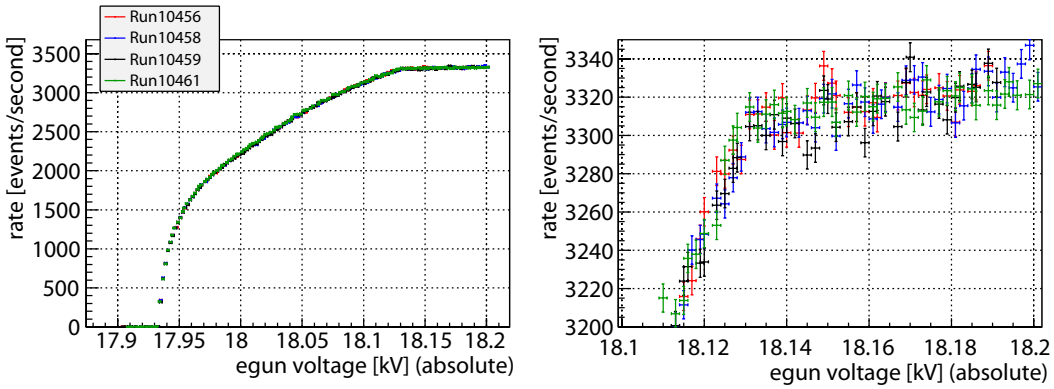

Figure 7.17: measured transmission function, configuration **B**, e-gun at x = 19°, (measurement 3)

Here the e-gun was at x = 19°. The transmission starts at $U_{e-gun} = 17935 \pm 1$ V and reaches maximum transmission at 18131 ± 1 V (see figure 7.17). The agreement of all four runs is very good.

7.3.4 Transmission function with -18.5 kV retarding potential

This section contains all measurements with retarding potential configuration **A**. For each measurement R as a function of U_{e-gun} is shown for the complete transmission region and the region close to maximum transmission.

Electron gun at centre position (measurement 4)

The transmission starts at $T_{start} = 18440 \pm 1$ V and reaches maximum transmission at 18506 ± 1 V (see figure 7.18). The shape of the transmission function is similar compared to the ones measured at retarding potential configuration **B**.

Electron gun at x = 15° (measurement 5)

The e-gun position for this measurement was x = 15°. The start of transmission is at 18448 ± 1 V and maximum transmission is reached at 18520 ± 1 V (figure 7.19).

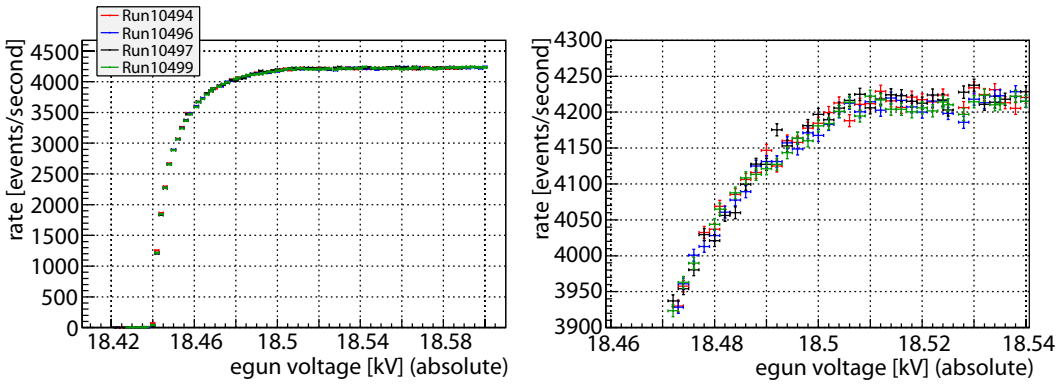

Figure 7.18: measured transmission function, configuration **A**, e-gun at x = 0°, (measurement 4)

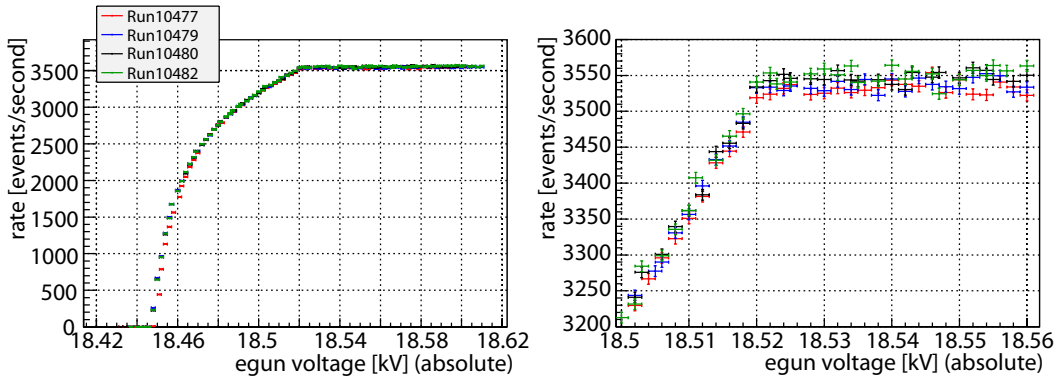

Figure 7.19: measured transmission function, configuration **A**, e-gun at x = 15°, (measurement 5)

Electron gun at x = 19° (measurement 6)

Here the e-gun was at x = 19°. The transmission starts at U_{e-gun} = 18454 ± 1 V and reaches maximum transmission at 18530 ± 1 V (see figure 7.20).

Electron gun at x = -19° (measurement 7)

For this measurement the e-gun was moved to x = -19° which corresponds to the same radial position as in measurement 6. The start of transmission is at U_{e-gun} = 18454 ± 1 V and maximum transmission is reached at 18530 ± 1 V (see figure 7.21). For a detailed comparison between measurement 6 and 7 see figure 7.27.

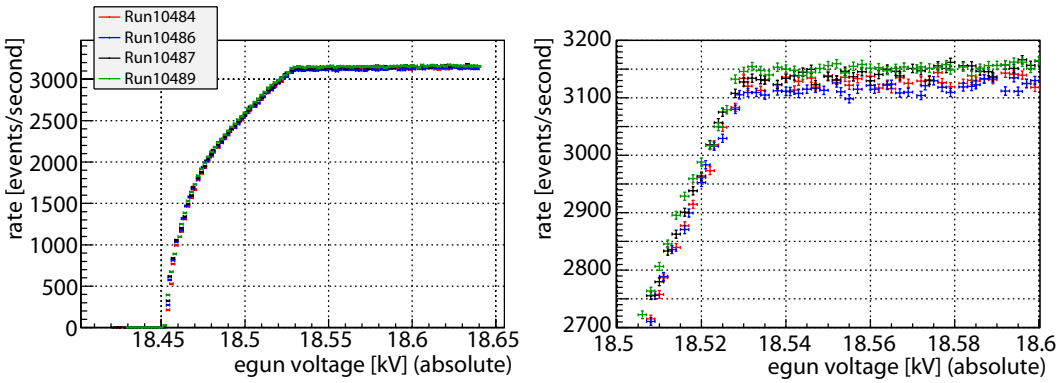

Figure 7.20: measured transmission function, configuration **A**, e-gun at x = 19°, (measurement 6)

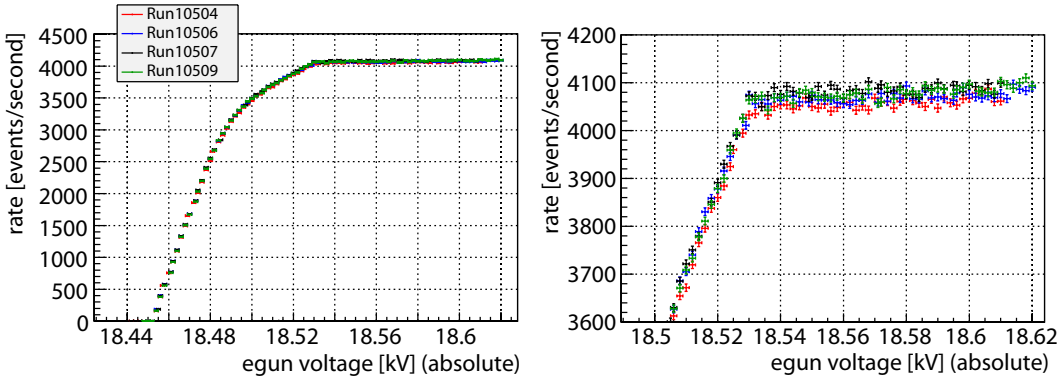

Figure 7.21: measured transmission function, configuration **A**, e-gun at x = -19°, (measurement 7)

Electron gun at y = -16° (measurement 8)

Here the e-gun was at y = -16°. The transmission starts at U_{e-gun} = 18448 ± 1 V and reaches maximum transmission at 18520 ± 1 V (see figure 7.22).

7.3.5 Stability of transmission at low excess energies (< 100 eV)

In this paragraph the stability of the maximum transmission at low excess energies (up to 100 eV) is discussed. The stability of the transmission in this region is of high importance for the KATRIN experiment because here the β-decay electrons that will be used for neutrino mass measurements are transmitted. Any deviations from a constant transmission could result in systematic effects on $m_{\overline{\nu}_e}$.

Figure 7.23 shows the deviation (for each run) of each measurement point (subrun) to a constant rate value R_0 in units of the standard deviation σ of each subrun.

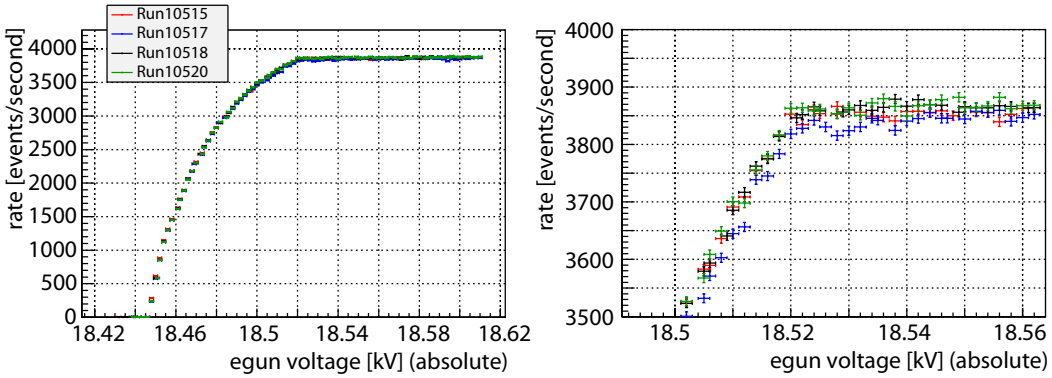

Figure 7.22: measured transmission function, configuration **A**, e-gun at y = -16°, (measurement 8)

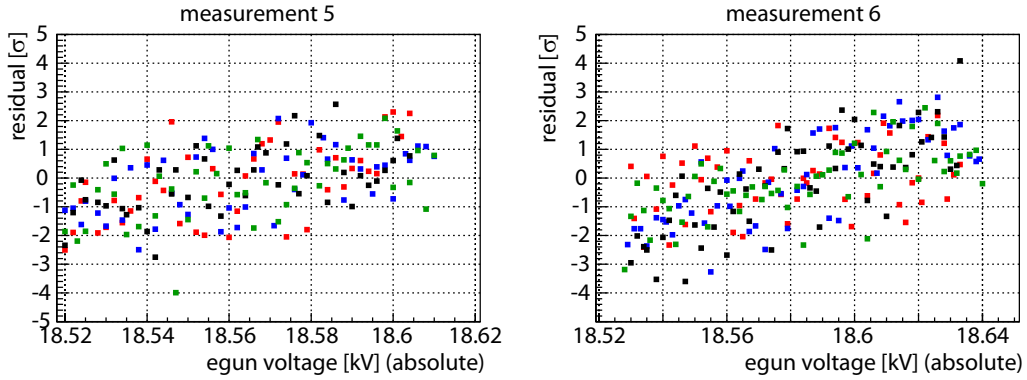

Figure 7.23: Deviation from R_0 in units of σ for each subrun in the region of maximum transmission. Left: measurement 5, right: measurement 6

R_0 had been determined before by fitting the data in the region of maximum transmission to a constant value. All values scatter within 4 σ[10] around R_0. Anyhow, a small increase of the mean value of the residuals is observed towards larger U_{e-gun}. An independent measurement of the dependence of the e-gun rate on U_{e-gun} at maximum magnetic field (B_{max}) and zero tank potential showed that the e-gun rate increases with 203 ± 18 Hz/keV (for -18.3 kV > U_{e-gun} > -18.7 kV). The increase in rate in the region of maximum transmission (for each run) is within 1 σ compatible with the voltage dependent increase of the rate. Therefore it is concluded that there is no statistical significant evidence for a non constant transmission behaviour at low excess energies.

[10]The relative error for 1 σ is 0.23 % in the region of maximum transmission.

7.3.6 Transmission at high excess energies (> 100 eV)

The test of the stability of maximum transmission described above was only investigated up to excess energies (E_e = E_0 - $q \cdot U_0$) of 100 eV. One possible operating scenario of the pre-spectrometer in the final KATRIN setup is the operation at zero retarding potential. In this case the maximum transmission has to be stable (the magnetic guiding of β-decay electrons has to be adiabatic) for E_e up to the endpoint energy of tritium β-decay.

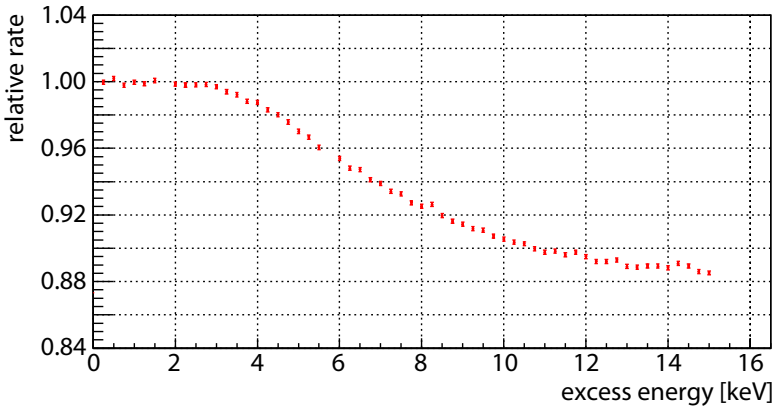

Figure 7.24: relative rate (normalized to R_0) as a function of the electron excess energy in the analyzing plane

The transmission at high E_e was measured with a constant e-gun potential $U_e - gun$ = -18.5 kV while ramping down the spectrometer potential (configuration **A**) in steps of 250 V and thus increasing E_e. All other experimental parameters were identical with measurement 7. Figure 7.24 shows the relative rate r (normalized to the rate at maximum transmission and small E_e) as a function of E_e. The decrease of r for $E_e > 3$ keV could be identified as a systematic effect of the measurement: Backscattered electrons from the 64PD are normally reflected from the retarding potential U_0 or the increasing magnetic field. As U_0 is lowered stepwise more and more backscattered electrons fulfill equation 7.7 and are transmitted to the e-gun. Due to magnetron drift the electrons move in azimuthal direction and hit the ground electrode of the e-gun and therefore are not registered at the detector - the count rate decreases. Simulations of this effect show good agreement with the measurements [75]. A detailed investigation of the transmission properties at high excess energies can be found in [67].

7.4 Result

7.4.1 Overview of transmission functions

Figure 7.25 shows the transmission functions (measurements 1 to 3) for retarding potential configuration **B**. All runs are normalized to relative transmission $r = R/R_0$ for better comparison. R_0 is determined from the e-gun stability runs of each measurement. All three transmission functions increase steeply at the beginning and then increase slowly until maximum transmission is reached. ΔE increases as the e-gun moves to larger x values. This is expected because of early retardation of the electrons in this configuration (for more information on early retardation see section 7.2).

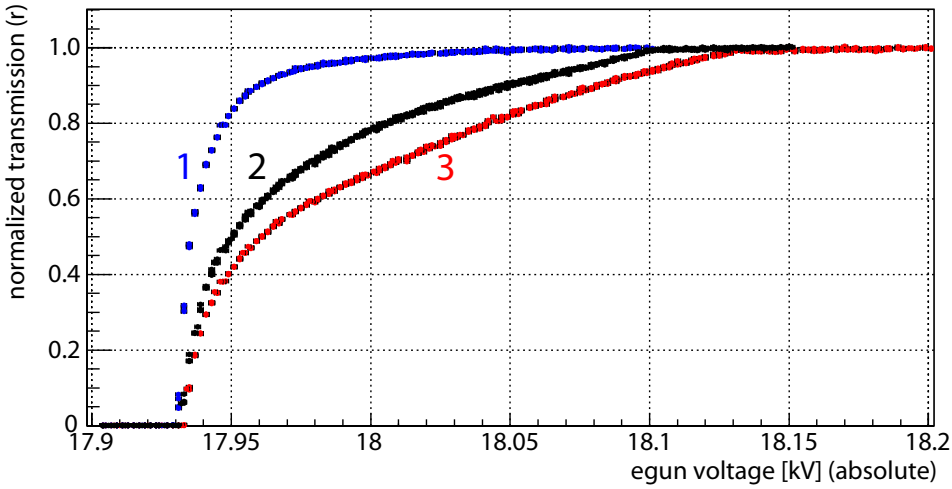

Figure 7.25: normalized transmission functions (measurements 1 to 3) for retarding potential configuration **B**

The normalized transmission functions for measurements 4 to 6 are shown in figure 7.26. The relative rate r rises steeply at the beginning of the measurements and reaches maximum transmission with a medium slope. The shape of the transmission functions is comparable with the ones in figure 7.25 but ΔE is more than a factor two smaller. The start of the transmission shifts to larger U_{e-gun} with larger x values of the e-gun position.

The normalized transmission functions for measurement 6 and 7 are shown in figure 7.27. Both were measured at the same radial position of the flux tube and because the pre-spectrometer is a rotational symmetric system a good agreement between each other is expected.

The comparison shows that the start positions of the transmission and the point where maximum transmission is reached are matching very well. The shape of the

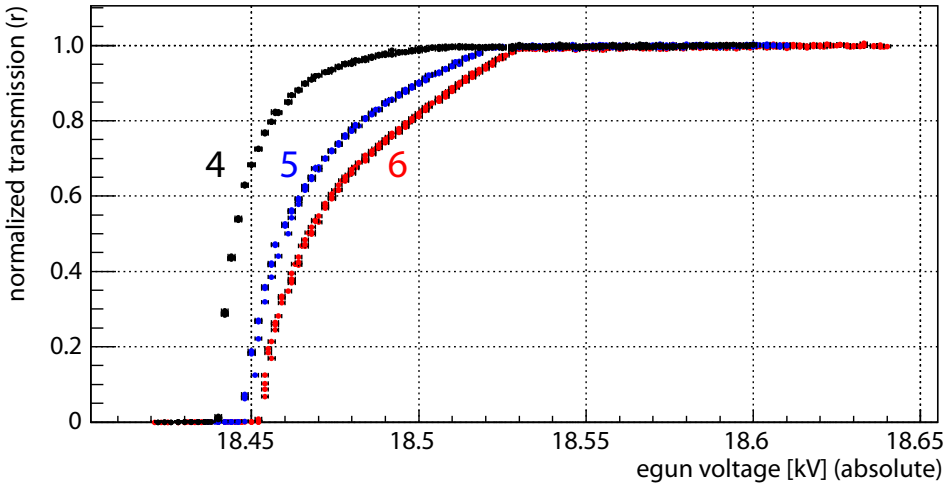

Figure 7.26: normalized transmission functions (measurements 4 to 6) for retarding potential configuration **A**

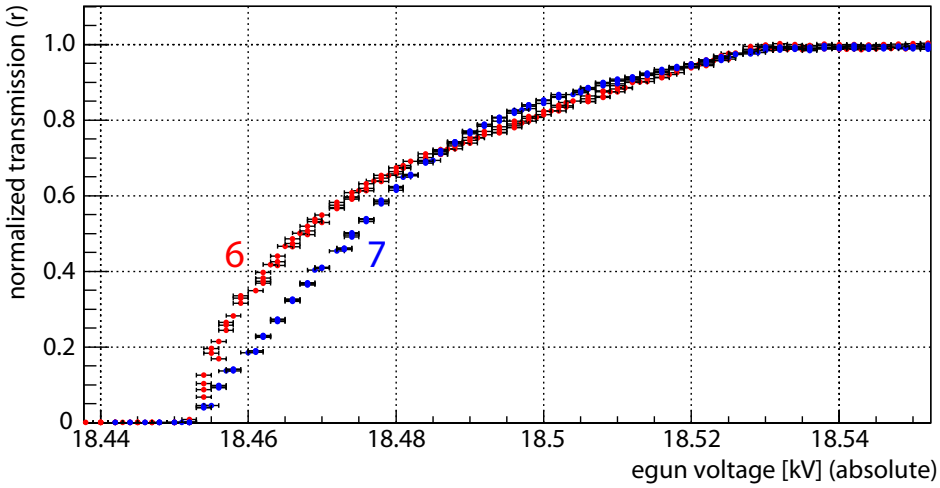

Figure 7.27: normalized transmission functions (measurements 6 & 7) for retarding potential configuration **A**, comparison between e-gun position x = ± 19°

transmission functions is significantly different. As described in section 7.1.4 the shape is mainly determined from the angular distribution of the electron source. Different shapes point out that the emission characteristics of the e-gun depend on the absolute e-gun position and not only on the radial position. Another observed effect is that the rate of the e-gun at maximum transmission R_0 is different for the two x positions: $R_0 = 3150 \pm 3$ 1/s ($x = 19°$), $R_0 = 4049 \pm 4$ 1/s ($x = -19°$).

A possible explanation of this behaviour could be a misalignment of the e-gun ground electrode or the e-gun tip or both (for a detailed description of the e-gun setup see section 3.2). This would cause differing angles between magnetic and electric field (α_{me}) in the acceleration region of the e-gun dependent on the absolute e-gun position. Even small changes of α_{me} could have a large effect on the angular distribution of the e-gun because the magnetic field at the e-gun $B_{e-gun} = 38$ mT is much smaller than $B_{max} = 4.5$ T ($\sin(\Theta) \propto \sqrt{B}$ and therefore Θ increases with B).

Another effect that could cause the observed behaviour is a varying thickness of the gold layer at the e-gun tip. The number of electrons emitted would dependent on the start region at the tip and therefore R_0 would depend on the absolute e-gun position.

7.4.2 Comparison between measurements and simulations

Table 7.4: comparison between measured and simulated transmission functions, number: measurement number, $T_{start,m}$: start energy of transmission, ΔE_m: measured energy resolution (width of transmission function), $T_{start,sim}$: simulated start energy of transmission, ΔE_{sim}: simulated energy resolution

number	$T_{start,m}$ [eV]	ΔE_m [eV]	$T_{start,sim}$ [eV]	ΔE_{sim} [eV]
1	17931 ± 1	130 ± 20	17997	125
2	17933 ± 1	166 ± 1.4	17999	156
3	17935 ± 1	196 ± 1.4	17999	184
4	18440 ± 1	66 ± 1.4	18438	73
5	18448 ± 1	72 ± 1.4	18442	80
6	18454 ± 1	76 ± 1.4	18450	82
7	18454 ± 1	76 ± 1.4	18450	82
8	18448 ± 1	72 ± 1.4	18444	80

Table 7.4 shows the results of the transmission function measurements $\Delta E, T_{start}$ and the corresponding simulations. The agreement of energy resolution ΔE between simulation and measurement is better than 10%. It needs to be considered that the simulations were performed with a rotational symmetric system whereas the pre-spectrometer shows deviations from rotational symmetry. There is a vertical gap in the inner electrode system of about 5 cm. Also, the cone electrodes are shifted

(compared to the symmetry axis of the pre-spectrometer) in the order of cm [41]. Therefore a perfect agreement between simulations and measurements can not be expected. It seems that for potential configuration **B** (measurements 1 to 3) the simulated value for ΔE is systematically below the measured value whereas it is opposite for potential configuration **A**. There is an offset of about 70 V between the measured value of T_{start} and the simulation for potential configuration **B**. Anyhow, more important than the absolute value of T_{start}[11] is the difference in T_{start} between the single measurements (for one potential configuration) because this corresponds to the inhomogeneity of the potential in the analyzing plane (see figure 7.6). For potential configuration **B** there is a good agreement of the difference in T_{start} between measurement and simulation within the uncertainties of the measurements. Comparing measurements 4 and 6 (potential configuration **A**) also a good agreement is seen.

7.4.3 Electron gun angular distribution

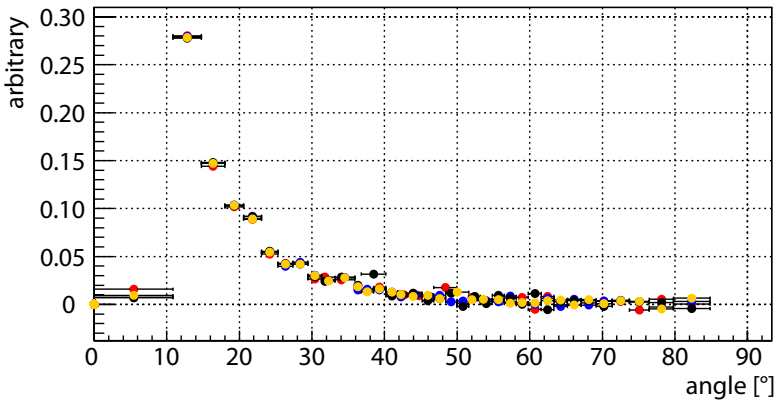

Figure 7.28: e-gun angular distribution at B_{max}, determined from measurement 4

Figure 7.28 shows the angular distribution of electrons starting at the e-gun, in the centre of the east magnet ($B_{max} = 4.5$ T). The distribution was obtained from the transmission function measurement 4. Each voltage step (i) of U_{e-gun} (2 V) corresponds to a specific range of angles ([Θ]). From the increase in rate (R) - compared to the previous value of U_{e-gun} - the rate within ([Θ]) can be determined: $[\Theta](i) = R(i) - R(i-1)$. Thus the angular distribution from 0 to 90 ° can be obtained.

The e-gun emits preferably electrons with small angles (the maximum of the angular distribution at B_{max} is between 10 and 20 °). This is expected of the actual

[11] In case of the main spectrometer the precise knowledge of the absolute value of T_{start} is essential for the neutrino mass measurements.

e-gun geometry [19] because the magnetic and electric field in the acceleration region of the e-gun are almost parallel and the electrons only gain little transversal energy.

7.4.4 Conclusion

The following conclusions from the detailed investigation of the pre-spectrometer transmission characteristics can be made:

- All examined retarding potential configurations show an early retardation of the electrons and therefore an increased energy resolution. Other configurations with optimized transmission properties create Penning traps which produce - after ignition of a Penning discharge - background electrons in the flux tube at a rate in the order of 100 1/s. In the final KATRIN setup these electrons are trapped between main and pre-spectrometer and could boost the ignition of the Penning trap in this region. The pre-spectrometer will be used as a pre-filter for the neutrino mass measurements and therefore early retardation has no negative effect.
- Within the statistical uncertainties no evidence of a non constant transmission at low excess energies (< 100 eV) is observed (stability better 1%).
- The good agreement between simulations and measurements demonstrates that the methods used for electric and magnetic field calculation are working well.
- The emission characteristic of the e-gun depends on its absolute position. The angular distribution of the e-gun could be reconstructed from the shape of the transmission function for different e-gun positions.

8 Conclusions and outlook

Neutrino oscillation experiments showed that neutrinos are massive particles. Until now there is only a lower limit (0.04 eV/c^2 [10]) and an upper limit (2 eV/c^2 [10]) on the neutrino mass. Because the neutrino mass is an important parameter for the large scale structure formation in the universe and neutrinos contribute to dark matter, it is of high interest to determine the absolute mass scale of neutrino masses. The KATRIN experiment, which is presently being set up at Karlsruhe Institute of Technology (Germany), aims to measure the neutrino mass with a sensitivity of 200 meV/c^2 by investigating the kinematics of tritium β-decay. In order to achieve this sensitivity, the background rate R_{BG} at the detector should not exceed a value of 10 mHz.

A major component within the KATRIN experiment is the electrostatic pre-spectrometer which will act as a pre-filter for β-electrons in the final setup. Presently it is being operated in a test setup as a prototype for the main spectrometer (see chapter 3) and is used for background investigations to test and refine the new electromagnetic design of the KATRIN spectrometers. Additionally, new technologies such as active high voltage (HV) stabilization are tested and developed within the test setup.

Within this thesis the background characteristics of the pre-spectrometer test setup were studied. It could be shown that there are two major background processes in MAC-E filters:

- **Penning discharge**
  A Penning trap is a special configuration of electromagnetic fields that allows the storage of electrically charged particles. The ignition of a Penning discharge can yield large background rates at the detector. A Penning discharge from a Penning trap between ground electrode and 500 mm flange (U_{trap} = 5 kV, volume $\approx$ 10 l) in the initial pre-spectrometer design caused a breakdown of the pre-spectrometer HV in presence of a magnetic field and thus prevented the operation of the pre-spectrometer at its design values of U_{tank} $\approx$ -18 kV and B_{max} = 4.5 T. The installation of an additional pair of electrodes (shielding electrode) and a modification of the ground electrode geometry could successfully remove the initial Penning trap. After the modification the pre-spectrometer could be operated at the design parameters, but R_{BG} was in the order of kHz. Extensive measurements and simulations could identify small-volume local Penning traps (U_{trap} = 0.9 kV, volume $\approx$ 10 cm^2) at the ground electrode to be the most likely sources of the background. A

ground electrode designed to follow the magnetic field lines could remove all Penning traps and after installation no Penning discharge related background was observed anymore.
The experience gained from the pre-spectrometer have yielded important constraints and guiding principles for the design of the main spectrometer electrodes in the region of the ground electrode. Deviations of the optimal electrode shape on a mm level can increase the background by many orders of magnitude. Therefore a very careful design, precise manufacturing and mounting of the electrodes on a mm level is required for the main spectrometer electrodes in the region of the ground electrode.
At the intended operational parameters of KATRIN, a large ($U_{trap} \approx 18$ kV) unavoidable Penning trap (vacuum to vacuum type) between the main and pre-spectrometer is created. In order to investigate the behaviour of this trap a main spectrometer mockup will be installed at the pre-spectrometer. This setup is intended to simulate conditions similar to the final setup and will be used to test technologies (particularly a sweeping wire [7]) preventing a possible Penning discharge.

- **Radon decay**
  Radon (Rn) atoms, which emanate from materials inside the vacuum region of the KATRIN spectrometers are able to penetrate deep into the magnetic flux tube so that the final α-decay of Rn contributes to the background. Of particular importance are electrons emitted in processes accompanying the Rn α-decay such as shake off, internal conversion of excited levels in the Rn daughter atoms and Auger electrons. While low-energy electrons directly contribute to the background in the signal region, high-energy electrons can be stored magnetically inside the volume of the spectrometer. Depending on their initial energy, they are able to create thousands of secondary electrons via subsequent ionization processes of residual gas molecules thus creating a time dependent background rate at the detector. For the pre-spectrometer test setup an average Rn induced background rate of 27 ± 6 mHz was determined (see chapter 5 and 6). The emanation of ^{219}Rn from the getter material was determined to be 7.5 ± 1.8 mBq thus being responsible for a large fraction (19 ± 4 mHz) of the average background rate. After removing the NEG pump at the pre-spectrometer one (or more) source(s) for ^{219}Rn (2.4 ± 2.0 mBq) and ^{220}Rn (33 ± 9 mBq) remained within the test setup.
  Based on the results from the pre-spectrometer, estimates for the Rn induced background at the main spectrometer can be made. If the main spectrometer is equipped with 3 km (design value) of getter strips, an average background rate - induced of ^{219}Rn emanating from the getter material - of about 300 mHz is expected. The source(s) of Radon (which is not emanating from the getter material) at the pre-spectrometer test setup is unknown at the time of this thesis[1]. Therefore the estimates for the average background rate (induced of

[1]Most recent measurements revealed that a large fraction of the ^{220}Rn activity is due to a (not

Rn not emanating from the getter material) at the main spectrometer range between 14 and 1100 mHz (see chapter 6). In order to reduce the Rn induced background, the installation of LN2 cooled baffles is proposed. The baffles could prevent ^{219}Rn (emanating from the NEG pumps) from entering the sensitive volume (flux tube) of the main spectrometer and at the same time provide a sufficient effective pumping speed of the NEG pumps for hydrogen and tritium. Additionally, the baffles could reduce the background rate induced from Radon emanating from the main spectrometer vessel itself or devices attached to it. In order to experimentally determine the Radon suppression efficiency of a LN2 cooled baffle and to test the technical feasibility, a baffle will be installed at the pre-spectrometer test setup.

Adiabatic guidance on a meV level for electrons flying from the tritium source to the detector is important for the KATRIN experiment and therefore the transmission characteristics of each component has to be studied precisely. Within this thesis the transmission functions of the pre-spectrometer for different flux tube positions and two different retarding potential configurations (**A** U_{tank} = -18 kV, U_{cone} = -18.3 kV, U_{wire} = -18.5 kV and **B** $U_{tank} = U_{cone} = U_{wire}$ = -18 kV), were measured and compared with corresponding simulations (see chapter 7). The agreement between simulations and measurements is better than 10%. For both retarding potential configurations the effect of early retardation was observed, especially for configuration B is the width of the transmission function (which corresponds to the energy resolution ΔE of a MAC-E filter) a factor of about 3 larger than expected from equation 7.9. The pre-spectrometer will be used as a pre-filter for the neutrino mass measurements (the actual energy analysis of the β-decay electrons is done at the main spectrometer) therefore early retardation has no negative effect. The measurements showed that the stability of the transmission for low excess energies ($E_e < 100$ eV) is better than 1%. The measured transmission functions also yield information about the electron source (e-gun). The angular distribution of the e-gun could be reconstructed from the shape of the measured transmission functions.

yet identified) removable device ("point source").

Acknowledgments

At this point I want to thank all people who supported me during the time of my PhD thesis. Especially I want to thank

Prof. Dr. G. Drexlin for giving me the opportunity to work at the KATRIN pre-spectrometer and for his support and advice during the time of my PhD thesis

Prof. Dr. W. de Boer who agreed to act as second reviewer.

Dr. L. Bornschein for his continuous strong support, advice and for proofreading my thesis. I also want to thank him for the many sweets that were always available during the time when we shared an office.

Dr. F. Glueck, his electromagnetic field calculation code was the basis of all simulations presented here. I also want to thank him for many discussions and for proofreading parts of my thesis.

The pre-spectrometer test setup is a complex system, therefore I want to thank several people who helped with their expertise to answer many questions on different aspects of the system: Dr. J. Wolf, Dr. T. Thümmler, Dr. M. Steidl, Dr. K. Schlösser and Dr. J. Bonn.

Furthermore I want to thank my colleagues of the pre-spectrometer task Dr. F. Habermehl, S. Görhardt, M. Lammers and P. Renschler for their support.

I am grateful for many fruitful discussions and continuous support of the pre-spectrometer group by our colleagues from University of Münster: Prof. C. Weinheimer, Dr. K. Valerius, K. Hugenberg and M. Zacher.

In order to deal with the complex slow control, DAQ and HV systems I am grateful for the help and support of Dr. S. Wüstling, A. Beglarian, Dr. T. Bergmann and Dr. A. Kopmann. I also want to thank M. Howe for his always prompt replies on ORCA related issues.

The numerous hardware modifications of the pre-spectrometer test setup were only possible with the strong support of our technical staff: B. Bender, H. Frenzel, M. Kuhl, N. Lohr, L. Schäfer, B. Schüssler, H. Skacel and H. Weingardt. At this point

I also want to thank M. Mark for his efforts to make the pre-spectrometer a safe place to work.

Bibliography

[1] A. Monfardini et al.: The microcalorimeter arrays for a rhenium experiment (MARE): A next-generation calorimetric neutrino mass experiment. In: *Nuclear Instruments and Methods in Physics Research Section A: Accelerators, Spectrometers, Detectors and Associated Equipment* 559 (2006), Nr. 2. http://dx.doi.org/DOI:10.1016/j.nima.2005.12.006. – DOI DOI: 10.1016/j.nima.2005.12.006

[2] Aalseth, Craig E. ; et al.: Comment on "'Evidence for Neutrinoless Double Beta Decay"'. In: *Modern Physics Letters A* 17 (2002), Januar, S. 1475–1478

[3] Abdurashitov, J. ; et al.: Solar neutrino flux measurements by the Soviet-American gallium experiment (SAGE) for half the 22-year solar cycle. In: *Journal of Experimental and Theoretical Physics* 95 (2002), Nr. 2, S. 181–193. http://dx.doi.org/10.1134/1.1506424. – DOI 10.1134/1.1506424

[4] al., C. A.: Bolometric Bounds on the Antineutrino Mass. In: *Phys. Rev. Lett.* 91 (2003), Nr. 16. http://dx.doi.org/10.1103/PhysRevLett.91.161802. – DOI 10.1103/PhysRevLett.91.161802

[5] Bahcall, John N. ; Pena-Garay, Carlos: Solar models and solar neutrino oscillations. In: *New Journal of Physics* 6 (2004), Nr. 1, 63. http://stacks.iop.org/1367-2630/6/i=1/a=063

[6] Bahcall, John N. ; Pinsonneault, M. H. ; Basu, Sarbani: Solar Models: Current Epoch and Time Dependences, Neutrinos, and Helioseismological Properties. In: *The Astrophysical Journal* 555 (2001), Nr. 2. http://dx.doi.org/DOI:10.1086/321493. – DOI DOI: 10.1086/321493

[7] Beck, M. ; Valerius, K. ; Bonn, J. ; Essig, K. ; Glück, F. ; Ortjohann, H.-W. ; Ostrick, B. ; Otten, E. W. ; Thümmler, Th. ; Zboril, M. ; Weinheimer, C.: Effect of a sweeping conductive wire on electrons stored in a Penning-like trap between the KATRIN spectrometers. In: *The European Physical Journal A - Hadrons and Nuclei* 44 (2010), Nr. 3, S. 499–511. http://dx.doi.org/10.1140/epja/i2010-10959-1. – DOI 10.1140/epja/i2010–10959–1

[8] Bohr, Nils: Faraday lecture. Chemistry and the quantum theory of atomic constitution. In: *J. Chem. Soc.* (1932), S. 349–384

[9] Brun, R. ; Rademakers, F.: ROOT - An object oriented data analysis framework. In: *Nuclear Instruments and Methods in Physics Research A* 389 (1997), Februar, S. 81–86

[10] C. Amsler et al.: The Review of Particle Physics. In: *Physics Letters* B667 (2008)

[11] C. Arnaboldi et al.: Physics potential and prospects for the CUORICINO and CUORE experiments. In: *Astroparticle Physics* 20 (2003), Nr. 2, S. 91 – 110. http://dx.doi.org/DOI:10.1016/S0927-6505(03)00180-4. – DOI DOI: 10.1016/S0927–6505(03)00180–4

[12] Ch Kraus, B. Bornschein, L. Bornschein, J. Bonn, B. Flatt, A. Kovalik, B. Ostrick, E. W. Otten, J. P. Schall, Th Thümmler and Ch Weinheimer: Final results from phase II of the Mainz neutrino mass searchin tritium β decay. In: *Eur. Phys. J. C* 40 (2005), Nr. 4, S. 447–468. http://dx.doi.org/10.1140/epjc/s2005-02139-7. – DOI 10.1140/epjc/s2005–02139–7

[13] Chadwick, James: Possible Existence of a Neutron. In: *Nature* (1932), S. 312

[14] Cryogenic Limited: *Cryogen Free Magnet (CFM) systems*. http://www.cryogenic.co.uk/downloads/brochures/cfm.pdf. Version: 2002

[15] D. Larson et al.: Seven-Year Wilkinson Microwave Anisotropy Probe (WMAP) Observations: Power Spectra and WMAP-Derived Parameters. In: *ArXiv Astrophysics - Cosmology and Extragalactic Astrophysics* (2010)

[16] Drexlin, Guido: *KATRIN handout.ppt*. private communication,

[17] European Commission, Joint Research Centre: *Nucleonica*. www.nucleonica.net

[18] EXO Collaboration: EXO: an advanced Enriched Xenon double-beta decay Observatory. In: *Nuclear Physics B - Proceedings Supplements* 138 (2005), Januar, S. 224–226. http://dx.doi.org/10.1016/j.nuclphysbps.2004.11.054. – DOI 10.1016/j.nuclphysbps.2004.11.054

[19] F. Fraenkle: *Simulation of different e-gun geometries*. http://fuzzy.fzk.de/bscw/bscw.cgi/d363139/egun_simulations.pdf. Version: 2007

[20] F. Fraenkle: Measurements with the KATRIN pre-spectrometer test setup. In: *XV KATRIN collaboration meeting* C1 (2008). http://fuzzy.fzk.de/bscw/bscw.cgi/d477683/95-TRP-4532-C1-FFraenkle.pdf

[21] F. Fraenkle: Measurements with the KATRIN pre-spectrometer test setup. In: *XIV KATRIN collaboration meeting* 7 (2008). http://fuzzy.fzk.de/bscw/bscw.cgi/d443841/95-TRP-4456-S7-FFraenkle.ppt

[22] F. Fraenkle: KATRIN pre-spectrometer. In: *XVI KATRIN collaboration meeting* 2 (2009). http://fuzzy.fzk.de/bscw/bscw.cgi/d539549/95-TRP-4608-S2-FFraenkle.ppt

[23] F. Fraenkle: KATRIN pre-spectrometer: Latest measurements. In: *EMDS Meeting Muenster (15.04. - 17.04.2009)* (2009). http://fuzzy.fzk.de/bscw/bscw.cgi/d542402/emd_fraenkle.ppt

[24] F. Fraenkle, F. Glueck, F. Habermehl, K. Valerius: east trap, west trap, ion trap. In: *KATRIN pre-spectrometer elog* 306 (2008). http://www-ik.fzk.de:8080/pre-spectrometer/306

[25] F. Fraenkle, F. Glueck, W. Kaefer, S. Mertens, N. Wandkowsky and J. Wolf: *Implications of Radon-219 emanation from NEG strips for the KATRIN measurements.* 2009

[26] F. Fraenkle, F. Habermehl, F. Glueck: Pressure dependance of SPD rate. In: *KATRIN pre-spectrometer elog* 373 (2008). http://www-ik.fzk.de:8080/pre-spectrometer/373

[27] F. Fraenkle, M. Lammers: wire comb design finished. In: *KATRIN pre-spectrometer elog* 443 (2009). http://www-ik.fzk.de:8080/pre-spectrometer/443

[28] F. Glück: Penning traps in the pre-spectrometer. In: *EMD meeting in Fulda* (2006). http://fuzzy.fzk.de/bscw/bscw.cgi/d344884/FGlueck_Penningtraps.ppt

[29] F. Glück: *The Penning discharge.* http://fuzzy.fzk.de/bscw/bscw.cgi/d354775/The_Penning_discharge_(F._Glueck).pdf. Version: 2007

[30] F. Glück, K. Hugenberg, K. Valerius, Ch. Weinheimer: *Simulations of a pair of additional electrodes to shield the Penning trap at the cone regions of the KATRIN pre-spectrometer.* BSCW, 2007
http://fuzzy.fzk.de/bscw/bscw.cgi/d354857/report-simulations-addelectrode.pdf

[31] F. Glück, L. Bornschein, F. Fränkle, F. Habermehl, K. Hugenberg, M. Leber and K. Valerius: *Penning discharge experiments with the KATRIN pre-spectrometer.* http://fuzzy.fzk.de/bscw/bscw.cgi/d357468/Penning_experiments_with_pre-spectrometer.pdf. Version: 2007

[32] F. Glück, S. Mertens, A. Osipowicz, P. Plischke, J. Reich, N. Wandkowsky: *Air Coil System and Magnetic Field Sensor System.* http://fuzzy.fzk.de/bscw/bscw.cgi/d530439/Air%20Coil%20System%20and%20Magnetic%20Field%20Sensor%20System.pdf. Version: 2009

[33] F. Habermehl, F. Glueck, K.Valerius: Test of new Penning electrodes after system modification. In: *KATRIN pre-spectrometer elog* 269 (2007). http://www-ik.fzk.de:8080/pre-spectrometer/269

[34] Feedman, Melvin S.: Ionization by nuclear transitions. In: *Conference: Summer course in atomic physics, Carry-le-Rouet, France* (1975)

[35] Fermi, Enrico: Versuch einer Theorie der β-Strahlen. In: *Zeitschrift fuer Physik A* 88 (1934), S. 161–177

[36] Fite, Wade L. and Stebbings, R. F. and Hummer, David G. and Brackmann, R. T.: Ionization and Charge Transfer in Proton-Hydrogen Atom Collisions. In: *Phys. Rev.* 119 (1960), Jul, Nr. 2, S. 663–668. http://dx.doi.org/10.1103/PhysRev.119.663. – DOI 10.1103/PhysRev.119.663

[37] Florian Fraenkle: discharges inside e-gun. In: *KATRIN pre-spectrometer elog* 187 (2007). http://www-ik.fzk.de:8080/pre-spectrometer/187

[38] Florian Fraenkle: e-gun @ -12kV + UV light. In: *KATRIN pre-spectrometer elog* 201 (2007). http://www-ik.fzk.de:8080/pre-spectrometer/201

[39] Florian Fraenkle: connection between e-gun background and high B-field background. In: *KATRIN pre-spectrometer elog* 378 (2008). http://www-ik.fzk.de:8080/pre-spectrometer/378

[40] Florian Fraenkle: *KATRIN Pre-Spectrometer Run Descriptions.* http://www-ik.fzk.de/~katrin/interna/ps/rundescriptions.html. Version: 2008

[41] Fraenkle, Florian: *Erste Messungen der elektromagnetischen Eigenschaften des KATRIN Vorspektrometers.* Diploma thesis, 2006 http://fuzzy.fzk.de/bscw/bscw.cgi/d347227/dth-fraenkle.pdf

[42] Fraenkle, Florian: *Pre-Spectrometer measurements with new electrodes.* BSCW, 2009 http://fuzzy.fzk.de/bscw/bscw.cgi/d578612/95-TRP-4709-S3-FFraenkle.ppt

[43] G Beamson, H Q Porter and D W Turner: The collimating and magnifying properties of a superconducting field photoelectron spectrometer. In: *Journal of Physics E: Scientific Instruments* 13 (1980), Nr. 1. http://stacks.iop.org/0022-3735/13/i=1/a=018

[44] Gaillard, Mary K. ; Grannis, Paul D. ; Sciulli, Frank J.: The standard model of particle physics. In: *Rev. Mod. Phys.* 71 (1999), Nr. 2, S. S96. http://dx.doi.org/10.1103/RevModPhys.71.S96. – DOI 10.1103/RevModPhys.71.S96

[45] GALLEX Collaboration: GALLEX solar neutrino observations: results for GALLEX IV. In: *Physics Letters B* 447 (1999), Februar, S. 127–133

[46] Glueck, Ferenc: *Insulator Penning trap.* private communication,

[47] Goldhaber, M. ; Grodzins, L. ; Sunyar, A. W.: Helicity of Neutrinos. In: *Phys. Rev.* 109 (1958), Nr. 3, S. 1015–1017. http://dx.doi.org/10.1103/PhysRev.109.1015. – DOI 10.1103/PhysRev.109.1015

[48] H. Tawara et al.: In: *J. Phys. Chem. Ref. Data* 19 (1990), 617 S.

[49] H. V. Klapdor-Kleingrothaus and I. V. Krivosheina: The Evidence for the Observation of $0\nu\beta\beta$ Decay: The Identification of $0\nu\beta\beta$ Events from the full Spectra. In: *Modern Physics Letters A* 21 (2006), Nr. 20, S. 1547–1566. http://dx.doi.org/10.1142/S0217732306020937. – DOI 10.1142/S0217732306020937

[50] Habermehl, Florian: *Electromagnetic measurements with the KATRIN pre-spectrometer.* PhD thesis, 2009 http://fuzzy.fzk.de/bscw/bscw.cgi/d640281/phd_F_Habermehl.pdf

[51] Hamamatsu Photonics: *Circular MCP and assembly series.* http://sales.hamamatsu.com/assets/pdf/catsandguides/MCP-circular.pdf

[52] Howe, M.A. ; Cox, G.A. ; Harvey, P.J. ; McGirt, F. ; Rielage, K. ; Wilkerson, J.F. ; Wouters, J.M.: Sudbury neutrino observatory neutral current detector acquisition software overview. In: *IEEE Transactions on Nuclear Science* 51 (2004), Nr. 3, S. 878 – 883. http://dx.doi.org/10.1109/TNS.2004.829527. – DOI 10.1109/TNS.2004.829527

[53] Hugenberg, Karen: *Design of the electrode system for the KATRIN main spectrometer.* Diploma thesis, 2008 http://fuzzy.fzk.de/bscw/bscw.cgi/d454711/dth-hugenberg.pdf

[54] J. Wolf: Optimized pumping schemes for the spectrometers. In: *XVIII KATRIN collaboration meeting* A2 (2010). http://fuzzy.fzk.de/bscw/bscw.cgi/d631028/95-TRP-4837-A2-JWolf.ppt

[55] Johannes Goullon: *Simulation of Rn-emanation from NEG-Getter strips.* http://fuzzy.fzk.de/bscw/bscw.cgi/d629582/95-TRP-4835-A1-JGoullon.ppt. Version: 2010

[56] K Hirata et al.: Real-time, directional measurement of $B8$ solar neutrinos in the Kamiokande II detector. In: *Phys. Rev. D* 44 (1991), Nr. 8, S. 2241–2260. http://dx.doi.org/10.1103/PhysRevD.44.2241. – DOI 10.1103/PhysRevD.44.2241

[57] K. Hugenberg, F. Fraenkle, F. Glueck: high B-field background at low potentials. In: *KATRIN pre-spectrometer elog* 380 (2008). http://www-ik.fzk.de:8080/pre-spectrometer/380

[58] K. Mueller: 320-DWG-011-10 (CPS Overview). Version: 2007. http://fuzzy.fzk.de/bscw/bscw.cgi/d429808/320-DWG-011-10%20(CPS%20Overview).pdf. 2007. – Forschungsbericht

[59] KATRIN Collaboration: KATRIN Design Report 2004 / Forschungszentrum Karlsruhe. 2005 (FZKA 7090). – Forschungsbericht

[60] Kazachenko, O. ; Bornschein, B. ; Bornschein, L. ; Eichelhardt, F. ; Kernert, N. ; Neumann, H.: TRAP - a cryo-pump for pumping tritium on pre-condensed argon. In: *Nuclear Instruments and Methods in Physics Research Section A: Accelerators, Spectrometers, Detectors and Associated Equipment* 587 (2008), S. 136 – 144. http://dx.doi.org/DOI:10.1016/j.nima.2007.12.024. – DOI DOI: 10.1016/j.nima.2007.12.024

[61] Knauer, W.: Mechanism of the Penning Discharge at Low Pressures. In: *Journal of Applied Physics* 33 (1962), Nr. 6, S. 2093–2099. http://dx.doi.org/10.1063/1.1728902. – DOI 10.1063/1.1728902

[62] L. Bornschein, Ch. Day, F. Habermehl, X. Luo and J. Wolf: Outgassing measurements with a prototype for a large UHV spectrometer, AIP, 2006

[63] Lammers, Melanie: *Untersuchung der Untergrundrate des KATRIN Vorspektrometers im Bereich hoher Feldstaerken*. Diploma thesis, 2009 http://fuzzy.fzk.de/bscw/bscw.cgi/d578755/dth-lammers.pdf

[64] Landau, L.: In: *J. Physics (USSR)* 8 (1944), 201 S.

[65] Leber, Michelle: *Monte Carlo Calculations of the Intrinsic Detector Backgrounds for the Karlsruhe Tritium Neutrino Experiment*. PhD thesis, 2010 http://fuzzy.fzk.de/bscw/bscw.cgi/d642437/phd-M_Leber.pdf

[66] Leiber, Benjamin: *Non-axially symmetric field and trajectory calculations for the KATRIN-experiment*. Diploma thesis, 2010

[67] M. Prall, A. Beglarian, L. Bornschein, S. Görhardt, F. Glück, F. Fränkle, S. Mertens, P. Renschler, S. Wüstling: The Transmission Function of the Pre-Spectrometer at Large Surplus Energies. In: *XVIII*

KATRIN collaboration meeting 3 (2010). http://fuzzy.fzk.de/bscw/bscw.cgi/d626455/95-TRP-4810-S3-Prall.pdf

[68] M. Zacher: Steep cone design and Penning traps. In: *XVI KATRIN collaboration meeting* A2 (2008). http://fuzzy.fzk.de/bscw/bscw.cgi/d540129/95-TRP-4629-A2-MZacher.pdf

[69] MAJORANA Collaboration: The MAJORANA Project. In: *Journal of Physics: Conference Series* 173 (2009), Nr. 1. http://stacks.iop.org/1742-6596/173/i=1/a=012007

[70] Michelle Leber: Time distribution of lost events in Energy Mode. In: *KATRIN UW elog* 69 (2008). http://ewiserver.npl.washington.edu:8080/KATRIN+Electronics/69

[71] Monreal, Benjamin ; Formaggio, Joseph A.: Relativistic Cyclotron Radiation Detection of Tritium Decay Electrons as a New Technique for Measuring the Neutrino Mass. In: *Phys. Rev.* D80 (2009). http://dx.doi.org/10.1103/PhysRevD.80.051301. – DOI 10.1103/PhysRevD.80.051301

[72] Nagy, Sz. ; Fritioff, T. ; Björkhage, M. ; Bergström, I. ; Schuch, R.: On the Q-value of the tritium β-decay. In: *EPL (Europhysics Letters)* 74 (2006), Nr. 3, S. 404. http://dx.doi.org/10.1209/epl/i2005-10559-2. – DOI 10.1209/epl/i2005–10559–2

[73] P. Benetti et al.: Measurement of the specific activity of 39Ar in natural argon. In: *Nuclear Instruments and Methods in Physics Research Section A: Accelerators, Spectrometers, Detectors and Associated Equipment* 574 (2007), Nr. 1, S. 83 – 88. http://dx.doi.org/DOI:10.1016/j.nima.2007.01.106. – DOI DOI: 10.1016/j.nima.2007.01.106

[74] P. Doe: Status of the focal plane detector (FPD). In: *XVI KATRIN collaboration meeting* 3 (2009). http://fuzzy.fzk.de/bscw/bscw.cgi/d539582/95-TRP-4611-S3-PDoe.ppt

[75] P. Renschler, G. Drexlin, F. Glück, S. Mertens, M. Steidl: Simulations of transmission at high surplus energies. In: *XVIII KATRIN collaboration meeting* 3 (2010). http://fuzzy.fzk.de/bscw/bscw.cgi/d626464/95-TRP-4811-S3-PRenschler.ppt

[76] Pauli, Wolfgang: Offener Brief an die Gruppe der Radioaktiven bei der Gauvereinstagung zu Tuebingen (datiert 4. Dez. 1930), wiedergegeben in:. In: *R. Kronig and V. Weisskopf, Collected Scientific Papers* 2 (1964), S. 1316–1317

[77] Reines, F. ; Cowan, C. L.: Detection of the Free Neutrino. In: *Phys. Rev.* 92 (1953), Nov, Nr. 3, S. 830–831. http://dx.doi.org/10.1103/PhysRev.92.830. – DOI 10.1103/PhysRev.92.830

[78] Renschler, Pascal: *Inbetriebnahme und Charakterisierung der 64fach segmentierten PIN-Diode*. Diploma thesis, 2007
http://fuzzy.fzk.de/bscw/bscw.cgi/d421547/dth-renschler.pdf

[79] S. Görhardt: The KATRIN Pre-Spectrometer - selected pre-spectrometer results. In: *XVIII KATRIN collaboration meeting* A1 (2010). http://fuzzy.fzk.de/bscw/bscw.cgi/d629537/95-TRP-4830-A1-SGoerhardt.ppt

[80] S. Mertens: Background from Tritium decay in the main and pre-spectrometer. In: *XVIII KATRIN collaboration meeting* 3 (2010). http://fuzzy.fzk.de/bscw/bscw.cgi/d626482/95-TRP-4813-S3-SMertens.pdf

[81] S. Schönert et al.: The GERmanium Detector Array (Gerda) for the search of neutrinoless $\beta\beta$ decays of 76Ge at LNGS. In: *Nuclear Physics B - Proceedings Supplements* 145 (2005), S. 242 – 245. http://dx.doi.org/DOI:10.1016/j.nuclphysbps.2005.04.014. – DOI DOI: 10.1016/j.nuclphysbps.2005.04.014

[82] S. Wuestling: Recent Electronics & Signal Processing Task Activities. In: *XVI KATRIN collaboration meeting* 3 (2009). http://fuzzy.fzk.de/bscw/bscw.cgi/d539618/95-TRP-4620-S3-SWuestling.pdf

[83] S. Wüstling, T. Armbrust, M. Steidl and S. Zadorozhny: A large, 64-pixel PIN-diode detector for low-energy beta-electrons. In: *Nuclear Instruments and Methods in Physics Research Section A* 568 (2006), Nr. 1. http://dx.doi.org/DOI:10.1016/j.nima.2006.06.029. – DOI DOI: 10.1016/j.nima.2006.06.029

[84] SAES company: *Getter alloy ST707*. http://www.saesgetters.com/default.aspx?idpage=212

[85] SAES company: *St707 Strips*. http://www.saesgetters.com/default.aspx?idPage=185

[86] Schwamm, Frank: *Untergrunduntersuchungen fuer das KATRIN-Experiment*. PhD thesis, 2004
http://fuzzy.fzk.de/bscw/bscw.cgi/d145302/phd-Frank_Schwamm.pdf

[87] SNO collaboration: Measurement of the Total Active 8B Solar Neutrino Flux at the Sudbury Neutrino Observatory with Enhanced Neutral Current Sensitivity. In: *arXiv:nucl-ex* (2004)

[88] Sturm, M.: *Aufbau und Test des Inner-Loop-Systems der Tritiumquelle von KATRIN*. PhD thesis, 2010

[89] Szucs, S. ; Delfosse, J. M.: Charge Spectrum of Recoiling $Po216$ in the α Decay of $Rn220$. In: *Phys. Rev. Lett.* 15 (1965), Jul, Nr. 4, S. 163–165.

http://dx.doi.org/10.1103/PhysRevLett.15.163. – DOI 10.1103/PhysRevLett.15.163

[90] T. Araki et al.: Experimental investigation of geologically produced antineutrinos with KamLAND. In: *Nature* 436 (2005), S. 499–503. http://dx.doi.org/10.1038/nature03980. – DOI 10.1038/nature03980

[91] Th Thümmler, R Marx and Ch Weinheimer: Precision high voltage divider for the KATRIN experiment. In: *New Journal of Physics* 11 (2009), Nr. 10. http://stacks.iop.org/1367-2630/11/i=10/a=103007

[92] The Office of Health, Safety and Security: *Use of Tungsten Welding Rods Containing Thorium*. http://www.hss.doe.gov/

[93] Theisen, Ch. ; Lopez-Martens, A. ; Bonnelle, Ch.: Internal conversion and summing effects in heavy-nuclei spectroscopy. In: *Nuclear Instruments and Methods in Physics Research Section A: Accelerators, Spectrometers, Detectors and Associated Equipment* 589 (2008), Nr. 2, S. 230 – 242. http://dx.doi.org/DOI:10.1016/j.nima.2008.02.044. – DOI DOI: 10.1016/j.nima.2008.02.044

[94] Thümmler, Thomas: *Entwicklung von Methoden zur Untergrundreduzierung am Mainzer Tritium-β-Spektrometer*. Diploma thesis, 2002 http://fuzzy.fzk.de/bscw/bscw.cgi/d25072/dth-thuemmler1.pdf

[95] Valerius, Kathrin: *Spectrometer-related background processes and their suppression in the KATRIN experiment*. PhD thesis, 2009 http://fuzzy.fzk.de/bscw/bscw.cgi/d594832/phd-K_Valerius.pdf

[96] W. Hassenmeier, H. Baumeister, K. Valerius, K. Hugenberg: new pictures from egun tip - update. In: *KATRIN pre-spectrometer elog* 171 (2007). http://www-ik.fzk.de:8080/pre-spectrometer/171

[97] WMAP Science Team: Internal Linear Combination Map. In: *Legacy Archive for Microwave Background Data Analysis* http://lambda.gsfc.nasa.gov/product/map/current/m_images.cfm

[98] X. Luo: Influence of LN2 baffles on pre-spec NEG pump. In: *XVIII KATRIN collaboration meeting* A2 (2010). http://fuzzy.fzk.de/bscw/bscw.cgi/d629596/95-TRP-4836-A2-XLuo.ppt

[99] Y. Fukuda et al.: Evidence for Oscillation of Atmospheric Neutrinos. In: *Phys. Rev. Lett.* 81 (1998), Nr. 8, S. 1562–1567. http://dx.doi.org/10.1103/PhysRevLett.81.1562. – DOI 10.1103/PhysRevLett.81.1562

[100] Zadorozhny, S.: *Search for neutrino mass in tritium beta decay. Data acqusition system and preliminary data analysis.* PhD thesis, 2004 http://fuzzy.fzk.de/bscw/bscw.cgi/d125612/phd-zadorozhny.ps